51

INTERNAL SHELF TIDES AND WIND-DRIVEN MOTIONS IN DEEPENING THE SURFACE MIXED LAYER

John L Largier

Submitted
in fulfillment of the requirements
for the degree of
Doctor of Philosphy
in the Faculty of Science
University of Cape Town

INTERNAL SHELF TIDES AND WIND-DRIVEN MOTIONS IN DEEPENING THE SURFACE MIXED LAYER

John L Largier
National Research Institute for Oceanology
P O Box 320
Stellenbosch
South Africa

ABSTRACT

Thermistor string data, collected off Cape Point (South Africa), exhibit temporal and spatial structures characteristic of the internal wave field on a continental shelf. This internal wave field is investigated in order to develop a predictive model of thermocline erosion events.

Analysis of these thermistor data is by means of graphical representations, spectral analysis and empirical orthogonal function analysis. The temporal and horizontal structures are dominated by energy at the inertial and tidal frequencies with a local energy peak at near-buoyancy frequency. Vertical structure is predominantly first mode (internal tide) with some second mode energy. Estimates of tidal energy imply a transfer of 20 to 25% of the barotropic energy to the baroclinic component.

Both empirical knowledge of the study area and theoretical discussion support the adoption of a two-layer approximation. Within this context, models of shelf-edge generation of internal tides are reviewed. A simple, two-layer, linear model is developed in order to account for the presence of a submarine canyon at the shelf-edge. Resonant generation, across the canyon, is probable and partially explains the anomalously large internal tide amplitudes recorded at the Cape Point mooring. Wind-driven inertial oscillations and Ekman transport are similarly modelled with a two-layer structure.

Turbulent breakdown of the thermocline is predicted for either super-critical tidal shear or super-critical wind-driven shear at the interface. A Richardson number argument is extended to account for the effect of shear due to a vector-sum of tidal and wind-driven components. Within the definition of the bulk Richardson number, the depth scale is chosen to be equally dependent on the depths of the upper and lower layers in a shallow sea.

Mixed layer deepening events, recorded off Cape Point, are discussed and hind-casted in terms of the rescaled model. The inclusion of tidal shear and rescaling of total interfacial shear are especially crucial to understanding and predicting deep mixed layers (of the order of 100 m) on the continental shelf. The two-layer representation, assumed for the sake of simplicity and predictability, is shown to be realistic and to provide reasonable numerical values.

PREFACE

The study of the ocean, by necessity, is a co-operative and multidisciplinary pastime. Good empirical oceanography is characterized by experimental and intellectual interaction. Very few investigations can be exclusively credited to one person.

This thesis originated with a paper given by Grev Nelson and Vere Shannon (both of the Sea Fisheries Research Institute) at the 5th National Oceanographic Symposium in 1983. Under the supervision of Grev and through the hard work of Carl Wainman (SFRI) and his colleagues, thermistor strings were deployed off Cape Point for May 1983 to May 1984. Anastasia Polito (SFRI) read the data and was continually of assitance in accessing these or other data. Most of the Landsat imagery was generously supplied by Vere Shannon. Supported to such an extent by SFRI, the research developed within an ecological perspective. Many of the SFRI personnel were consulted but in particular I would like to thank Grev Nelson for his advice on topics ranging from instrumentation through to data processing, fluid dynamics and ecology.

Initially, I was employed by the Institute of Maritime Technology where I worked under Ryno Buys. He was instrumental in initiating the project as an M.Sc. study and allowed me more than my fair share of freedom and flexibility in order to pursue this work. At present, I am employed by the National Research Institute for Oceanology where I have worked under Eckart Schumann and Marten Gründlingh. They allowed me continued freedom and, together with my other colleagues at the NRIO, have always been encouraging, interested and helpful. In particular, my association with Vincent Swart and Robin Carter (Agulhas Bank Coastal Dynamics Experiment) has broadened my knowledge and developed my approach to oceanography. Vincent assisted me specifically in the field of time-series analysis.

During this time (1984-1986), I was registered as a student in the Department of Oceanography at the University of Cape Town where Frank Shillington, Dirk van Foreest and Geoff Brundrit were always ready to advise and to appraise. Geoff, my thesis supervisor, provided invaluable assistance with the mathematics and linguistics of the work.

The project commenced, in late 1983, as an M.Sc. study with two objectives. Firstly, to review reports of internal waves on continental shelves, and secondly, to analyse and interpret the thermistor data. Although a report was written, it was never published following the recommendation of my supervisor (Geoff Brundrit). It was decided to publish the theory review separately and to convert the empirical results into a Ph.D. thesis. The literature review (Largier, 1986) now forms a general theoretical background to the empirical/theoretical work which is presented in this thesis.

Since then, the data have undergone further interpretation. Theoretical models relevant to the observed dynamics were altered, and in some cases developed, in order to produce more easily applicable, predictive expressions. The results of this endeavour are reported in the following chapters. Notwithstanding the generous and useful assistance of Geoff Brundrit and Grev Nelson, this research is essentially my own.

The final manuscript was produced at the NRIO, thanks to the combined efforts of the publications section. Most of all, I am indebted to Marthie Els, who worked to deadlines which I had no right to impose. Although the M.Sc. thesis was never submitted, I would like Lesley Elley to know that it has been put to good use and her effort is no less appreciated.

For reminding me that oceanography does not rule the waves, I thank Joy. I am most grateful for her understanding, support and perseverance throughout this 'giving of birth.' Finally, I would like to dedicate this work to Tutu who still hopes to read for his Ph.D. - he made me realize how fortunate I was to be able to study.

JOHN LOUIS LARGIER DECEMBER 1986

CONTENTS

CONTENTS (continued)

CHAPTER 1
INTRODUCTION

> "It is a curious situation that the sea, from which life first arose, should now be threatened by the activities of one form of that life. But the sea, though changed in a sinister way, will continue to exist; the threat is rather to life itself" (Carson, 1950).

The economically valuable and accessible shelf seas, which encircle the continents feel the greatest threat. These seas support a vast ecosystem which includes both man and woman. The wise management of the oceans, in general, and the continental shelf ocean, in particular, is dependent on perceptive, honest studies leading to practical and understandable theories. However, the application of this wisdom, in management and exploitation of the ecosystem, depends on the wishes and action of corporate mankind as expressed in economic and political structures. Unfortunately, in the eco-political arena 'good' science is usually impotent and discarded if found to be in opposition to that which is considered to be economically or politically expedient. This thesis has developed an honest, and I hope perceptive, study into what is considered to be an important component of continental shelf ecosystems. While the thesis may contribute to our corporate wisdom, we should not forget that the fruits of our increasing wisdom will only be borne by incessant political effort to counteract the opposing forces of expediency and ultimately to ensure continuation of healthy life.

Light and nutrients, the limiting factors for primary production, are relatively well-supplied in shelf seas. A significant portion of the water column is contained in the latently-productive euphotic zone which is not far removed from the nutrient-rich sediment-water interfacial zone. In temperate to tropical latitudes the upward transport of nutrients is frequently inhibited by a stably-stratified seasonal thermocline. The intention is to provide insight into the subject of stratified flows and, in particular, ecologically-significant vertical exchange. The study was initiated by the question: What role do internal waves play in mixing deeper nutrient-rich water across the seasonal thermocline into the euphotic zone on the continental shelf? This originated from Nelson and Shannon (1983) who observed clear surface expressions of internal waves over the Cape shelf. It was anticipated that the saturated internal wave field on the shelf (Gordon, 1978) would be the major agent for diapycnal nutrient fluxes. As such, a predictive estimate of the mixing effect would be an essential component of our understanding of the ecosystem and it would further our attempts to tackle the broader issues outlined above.

Within this perspective and from these beginnings the thesis has grown into a more directed study of the principal internal tide and inertial frequency signals. Under certain circumstances these two dynamic signals interfere constructively and enhanced vertical exchange occurs as a result of turbulent mixing across the thermocline. The importance of these events lies in the premise that these two processes are dominant at the base of the pre-existing mixed layer and that mixed layer deepening events over the continental shelf can be accounted for in terms of these processes. Thus attention is focussed on the active dynamic role of internal waves, not only as a significant reservoir of energy, but more importantly as an efficient mechanism for transport and transfer of momentum and energy from larger scale forcing to smaller scale stirring.

The Internal Wave Field. Since 1762, when Benjamin Franklin made notes on the oscillation of oil over water, the phenomenon of internal waves has been studied. Two-layer theory developed by Stokes (1847) was extended to continuously stratified fluids by Rayleigh (1883). The first conscious observation of internal waves in the ocean (Nansen, 1902) was substantiated by Ekman (1904). Since then oceanographers have become aware of internal waves on a wide spectrum of scales. The three-dimensional interior of the ocean, analogous to the irregularly deformed two-dimensional sea surface, was found to be in continual motion owing to the random superposition of an infinite set of internal waves. Defant (1961) reviewed the steadily expanding inventory of internal wave observations and Cox (1962) pioneered the idea of a frequency continuum, which led to the milestone work of Garrett and Munk (1972). Followed by an update (Garrett and Munk, 1975), they developed an empirical space-time model which accounted for many deep ocean observations in terms of a randomly and weakly interacting wave field. Energy is smeared over all horizonal and vertical wavenumbers and over frequencies between the inertial and buoyancy frequencies. The 'universal' spectral shape suggested by these statistical arguments is accounted for in terms of an equilibrium spectral shape for which the time constant is much longer than the time between generation events (Garrett and Munk, 1979). The energy input during a generation event 'tops up' the equilibrium spectrum and the remainder is dissipated within a few days. The dissipation time scale for the equilibrium spectrum is of the order of months to years, allowing the deep ocean to be both spatially and temporally uniform. McComas and Müller (1981) find that internal wave energy is usually generated at low vertical wavenumbers and dissipated at high vertical wavenumbers.

This universal spectrum has also become a valuable model for the 'base state' of the internal wave field in the upper ocean and on continental shelves (Roth et al., 1981 and Levine, 1983). Whitening of the red Garrett-Munk spectrum is found by Pinkel (1981) due to the proximity of the surface. Roth et al. (1981)

find that "deviations" from the base state correspond to higher energy values indicative of a source which is both local in space and time. These deviations are greatest and most common at the inertial frequency, the tidal frequency and in a high-frequency band preceding the change in spectral slope at the buoyancy frequency (Levine, 1983). These three signals, which will be discussed in turn, and their associated anisotropy are studied in the shelf seas.

The Internal Tide. Foremost is the internal tide which has frequently been observed through bands of modulated surface roughness propagating shoreward from a generation site at the shelf-edge. Apel et al. (1975) report a Landsat image of 6 consecutive tidal packets approaching the Namibian coast. Fu and Holt (1982) present a selection of Seasat SAR images, most of which are nearshore and represent shoreward propagating internal wave packets. They report significant activity for the Gulf of California (also Fu and Holt, 1984), the east coast of USA from Florida to Nova Scotia, the west coast of USA off Oregon and Washington, the Mexican coast and in the Labrador Sea. These wave packets, which are a non-linear symptom of the internal shelf tide, partially account for the energy peak often observed near the buoyancy frequency. Although large areas are covered in short time, satellite observations provide no information on the three-dimensionality of the internal wave field. Further, only those waves effective in modulating the surface wave field will be detected.

Nevertheless, these images strongly support the concept of internal tides propagating shoreward, each packet corresponding to a successive flood tide at the shelf-edge. Initially investigated by Zeilon (1912, 1934), various analytical models of the internal shelf tide have been developed. Rattray (1960) developed modally-decomposed expressions for the internal tide by matching across a step between a constant-depth, two-layered shelf and a constant-depth, two-layered ocean. Weigand et al. (1969) include the effect of friction. Rattray et al. (1969)

extend the model to a continuously stratified ocean. Prinsenberg et al. (1974) develop the solution for a shoaling continental shelf and account for viscous dissipation of the internal tide. Prinsenberg and Rattray (1975) are the last in this series of papers; they cater for a finite continental slope and variable buoyancy frequency (a function of depth). Meanwhile Baines (1973, 1974) used the method of characteristics to determine the response of a continuously stratified ocean to barotropic tidal flow over 'flat' and 'steep' topography, respectively. A synthesis of these linear generation models is presented by Baines (1982) who separates the solution into an interfacial mode and a ray theory integral for waves in a sub-thermocline continuum. Over the continental shelf the interfacial mode dominates, owing to strong dissipation of motion with higher vertical wavenumbers. Therefore it appears to be preferable to consider a simple interfacial model of internal tide generation. Simplicity facilitates practical application of the model in order that it may be used to **predict** internal shelf tides.

Internal tides have been monitored by ship-board profiling or moored instruments on the NW Australian shelf (Holloway, 1983, 1984, 1985), the Nova Scotian shelf (Petrie, 1975; Sandstrom and Elliott, 1984), Georges Bank (Marsden, 1986), NW African shelf (Gordon, 1979; Huthnance and Baines, 1982), Bay of Biscay (Gould and McKee, 1973), British shelf (James, 1982, Pingree and Mardell, 1985 and De Witt et al., 1986), the shelf off Cape Cod (Wunsch and Hendry, 1972) Southern California (Cairns, 1967) and Massachusetts Bay (Halpern, 1971; Chereskin, 1983). Wunsch (1975) reviews oceanic internal tides and refers to some further data from the Californian and New England shelves. The features are essentially the same: intermittent signal with a high noise level, first mode internal tides with high-frequency waves superimposed on the crests or troughs; uni-directional large-amplitude (Holloway, 1983, reports 50 m from crest to trough) motions with crests parallel to isobaths; generation at shelf-edge and strong dissipation over the shelf; increasing intensification and dissipation contend with each other as the water shoals.

Inertial Motions. At the low frequency limit of the internal wave spectrum, wind-driven currents provide a second equally important signal. Following Levine et al. (1983), inertially-oscillating currents are energetic in upper ocean records. The generation of these rotating currents, and the associated Ekman transport, has been accounted for in terms of sea-surface wind stresses (Pollard, 1970). This model of wind-generated baroclinic currents has been confirmed by the observations of Pollard and Millard (1970), Kundu (1976), Blackford (1978), Jensen (1982), Pollard (1980), Krauss (1981) and D'Asaro (1985a), amongst others. These currents have a first mode structure with strong velocity shear across the seasonal thermocline. Wind events may be such that this thermocline shear overcomes the stabilizing buoyancy forces and turbulent mixing deepens the surface mixed layer. Pollard et al. (1973) model this process with a critical Richardson number control. One-dimensional models of the mixed layer (Niiler, 1977; Niiler and Krauss, 1977) employ an energy budget to confirm that deepening of a pre-existing mixed layer is largely due to these wind-driven mean currents. In addition to its simplicity, the model of Pollard et al. (1973) results in expressions which may be used remarkably successfully in **predicting** the deepening of the mixed layer.

High-frequency Internal Waves. The third consistent deviation from the 'base' state occurs at high frequencies, typically 0,5 to 5,0 cph (Levine, 1983), near to the buoyancy frequency. This energy peak is the result of non-linear transfer of energy from lower frequency waves, in particular from the energetic internal tide (Levine et al., 1983). These high-frequency waves provide increased shear at the thermocline and are always available as a trigger for a marginally stable lower frequency flow.

Theoretical Approach. To obtain a complete model of the effect of internal waves on the thermocline, one would need to adopt statistical methods (cf. Garrett and Munk, 1972b; Gargett and Holloway, 1984) in order to describe the continuous field of

randomly interfering (linearly) and interacting (non-linearly) internal waves. But, in doing this, one may lose sight of the physical processes. It is suggested that the effect of continuous, small-scale processes such as non-linear wave-wave interaction, viscous attenuation (Reynold's stresses) and bottom friction are adequately described by a statistically or empirically derived parameter (e.g. eddy viscosity or e-folding time). For the larger-scale dynamics, however, an attempt should be made to address the instability and breakdown as identifiable events. Therefore, while cognizance is taken of the dissipative effect of small-scale dynamics, attention is focussed on analytical models of internal tide generation, its interference with baroclinic wind-driven motions and subsequent deformation of the seasonal thermocline.

From the analysis and interpretation of mooring data from the study area off Cape Point (Section 2.2), it has been possible to characterize the vertical and temporal structures of the local internal tide. With the assistance of Landsat imagery, the horizontal wavelengths and direction of propagation perpendicular to the isobaths have been determined. In order to explain these observations a simple linear two-layer model of topographic generation was developed. Within its specified context, this easily applicable model is as representative as the previous more complicated models from which it receives justification. An interfacial model seems particularly appropriate for the investigation of thermocline dynamics and this approach is favoured throughout the thesis. However caution should be shown in extrapolating from an interfacial model to study dynamics away from a quasi-interfacial thermocline.

Although little information on horizontal inertial motions is contained in the data from the thermistor mooring, the detailed model of Pollard (1970) and the two-layer simplification of Pollard and Millard (1970) allow thorough interpretation of the vague indications of inertial motion. The subsequent extension to shear-driven mixed layer deepening (Pollard et al., 1973)

completes the trio of two-layer models for internal tide, wind-driven motion and deepening events. These sub-inertial, irreversible deformations of the thermocline are well represented in the thermistor data collected off Cape Point. However, some of these events involve horizontal advective dynamics and cannot be interpreted fully in terms of one-dimensional models of deepening.

Objectives. The thesis thus develops as an application of theory to a practical problem; where theory is insufficient or too complicated, assumptions are suggested and adopted with the purpose of obtaining managable expressions which retain their representivity. The criteria of simplicity, applicability and representivity guide the discussion and development of theory.

Models, generally, are not developed as a simultation of reality but rather as an investigation of a single, hypothetically isolated process or mechanism. In this case the key features of three such models have been extracted, subject to the conditions discussed in the previous more detailed investigations. These are arranged into a consistent, linear model which addresses the question: In what circumstances do the combined dynamics of internal tide and wind-driven motion result in penetration of the quasi-interfacial seasonal thermocline?

The thesis as a whole has a two-fold objective. The data from Cape Point are analysed and interpreted in terms of internal wave theory. The dominant internal tide signal is modelled in order to account for its magnitude and its character. Secondly, a combined model is developed in order to determine the effect of simultaneous internal tides and wind-driven motion in eroding a quasi-interfacial thermocline.

Structure of the Thesis. In the following chapter (Chapter 2), background is provided through a review of reports concerned with the hydrology of the study area and adjacent areas. The

fundamental internal wave equations are discussed indicating the variety of frequencies and modes which may occur. Although the constant-N approximation is considered, it is the two-layer ideas and formulation which are developed in Section 2.3.

Chapter 3 concerns itself with the origin, nature and quality of the mooring data and satellite imagery. These data are analysed and partially interpreted in Chapter 4. The emphasis is on the digital data from the moorings. Information on two-dimensional, horizontal variation is extracted from Landsat views of the sea-surface (Section 4.1). The following sections, which discuss graphical plots of the temporal and vertical structure, respectively, are supported by more rigorous quantitative analysis in Sections 4.4 (spectral analysis) and 4.5 (empirical orthogonal function analysis). The remainder of Chapter 4 is used to estimate the energy content of the internal wave field and of the internal tide, in particular.

This tidal signal is interpreted in terms of a model for shelf-edge generation and subsequent propagation onto the shelf. The generation off Cape Point is peculiar in that it is enhanced by a long-shelf canyon (Section 5.4). The energy of this internal tide is compared with reported values from other continental shelf regions (Section 5.5).

Section 6.1, which considers theory concerned with the wind generation of inertial and Ekman motions, allows interpretation of the indications of inertial activity which are contained in the data. Section 6.2 reviews the ideas of one-dimensional mixed layer models and describes a developed version of the wind-driven deepening model of Pollard et al. (1973). Application of this model underestimates the rapid response of the thermocline to a strong wind event.

One-dimensional models of the thermocline (e.g. Niiler and Krauss, 1977) generally balance energy input at the surface with energy dissipation and storage at the thermocline. Kantha

(1977), however, suggests that the entrainment rate at the thermocline could be enhanced by interfacial waves that have been generated elsewhere. Turner (1981), after reviewing surface-driven external turbulence, similarly suggests that mixing resulting from internal waves and internal shear may be significant in accounting for rapid change of the density profile observed at depth. This is the approach adopted in the penultimate chapter. The effects of internal tide shear are considered in isolation and then in combination with shear due to non-turbulent, wind-driven motions in the upper layer (Sections 7.1 and 7.2). The effect of including internal tides can be gauged by comparing the results of Section 7.3 with those in Secion 6.2, where only wind-driven shear is accounted for. As might have been expected, these internal tides are found to be significant (and occasionally dominant) in the case of large amplitudes and/or deep thermoclines.

The concluding chapter (Chapter 8) is used to draw the various ideas, models and results together and to review the successes and inadequacies of the thesis. Attention is returned to the broader issues presented at the beginning of this introduction.

CHAPTER 2
A BRIEF REVIEW OF BACKGROUND KNOWLEDGE

2.1 The Cape Point Study Area

The study area, based on the Cape Point mooring site CP (Fig. 2.1), extends seaward to the shelf-edge. The historical data and the dynamics in an area between lines off Slangkop and Cape Hangklip are considered relevant. To a limited extent, some of the results of this study may be extrapolated further towards Cape Columbine and Cape Agulhas. This three-tier system loosely delimits the area of interest. Inshore of the 100 m isobath the structure and dynamics are expected to be symptomatic of a coastal boundary zone. These regions, in particular False Bay, are not discussed further than to assume them to be a passive boundary to the shelf dynamics which are being studied. Incident energy may be reflected or absorbed, but it is assumed that no new energy has its source in this coastal region.

The study area (situated around 34,5°S and 18,5°E) lies partially within the Southern Benguela upwelling system which is part of one of the four major eastern boundary current regions of the world (Shannon, 1985). At these latitudes the coastal upwelling, which is driven by equatorward longshore winds, is strongly seasonal. In summer the South Atlantic Anticyclone ridges south of a continental trough and strong surface pressure gradients give rise to persistent and strong south-easterly winds. These winds are modulated by the periodic passage of east-moving mid-latitude cyclones, and associated coastal lows, such that a recurrent wind sequence is induced (Nelson and Hutchings, 1983). During winter the South Atlantic Anticyclone moves north and westerlies due to the mid-latitude cyclones generally dominate the local wind record. The winds recorded at Cape Point lighthouse (Fig. 2.2) clearly display this seasonal cycle.

Three distinct upwelling sites may influence the study area. The Cape Peninsula plume, a semi-permanent feature during the

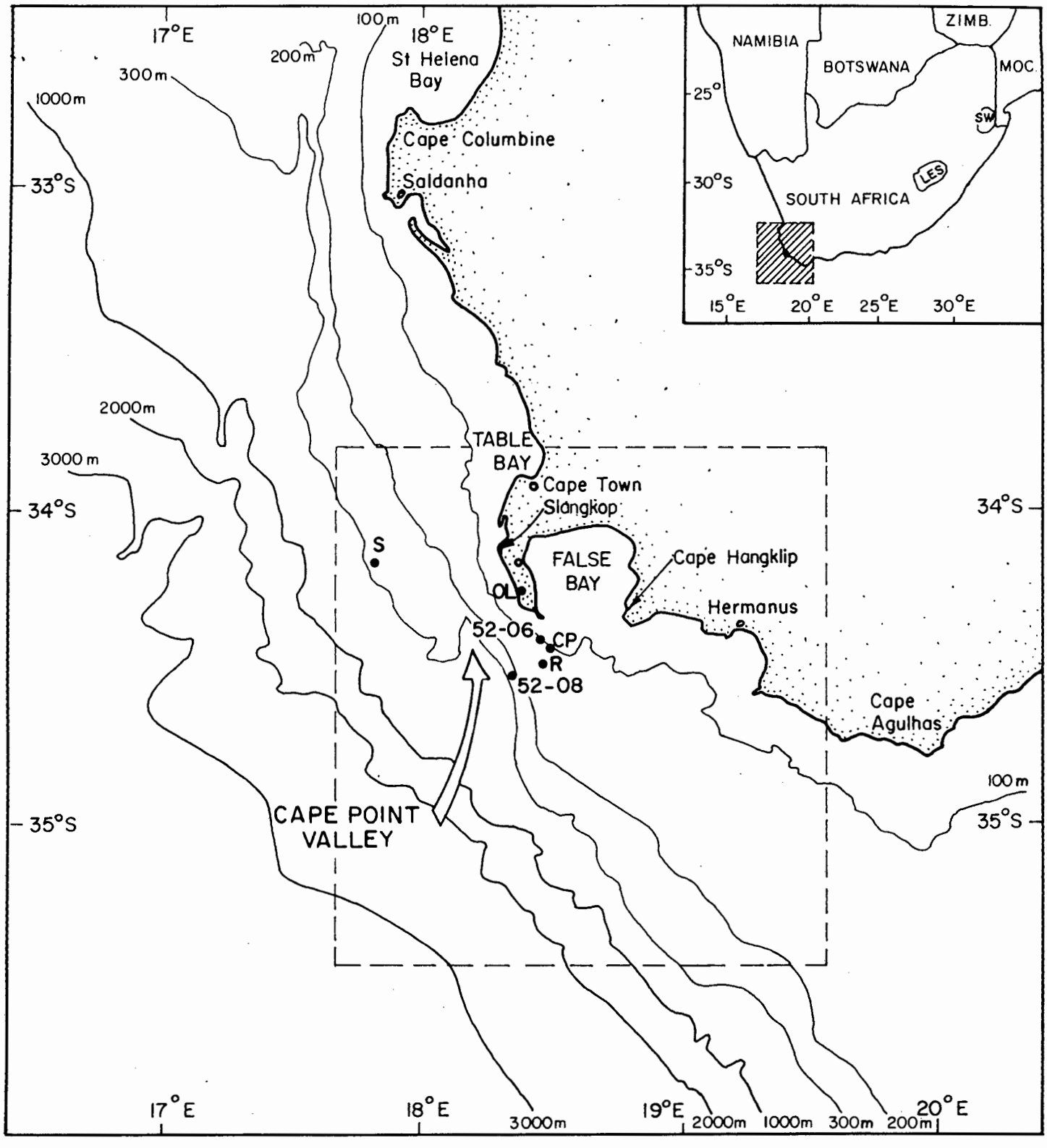

FIGURE 2.1: The Cape Point Study Area. The continental shelf, which extends to 200 or 300 m, is intersected by Cape Point Valley directly seaward of the thermistor string mooring at CP. A current meter (S), was moored off Slangkop, and an anemometer (OL), was erected at Olifantsbos. Monthly temperature profiles were measured at the routine stations R in 1958 and 1959 and at the Coastal Egg and Larval Program (CELP) stations 52-06 and 52-08 in 1977 and 1978. The square depicted by a dashed line indicates the approximate coverage of a single Landsat image.

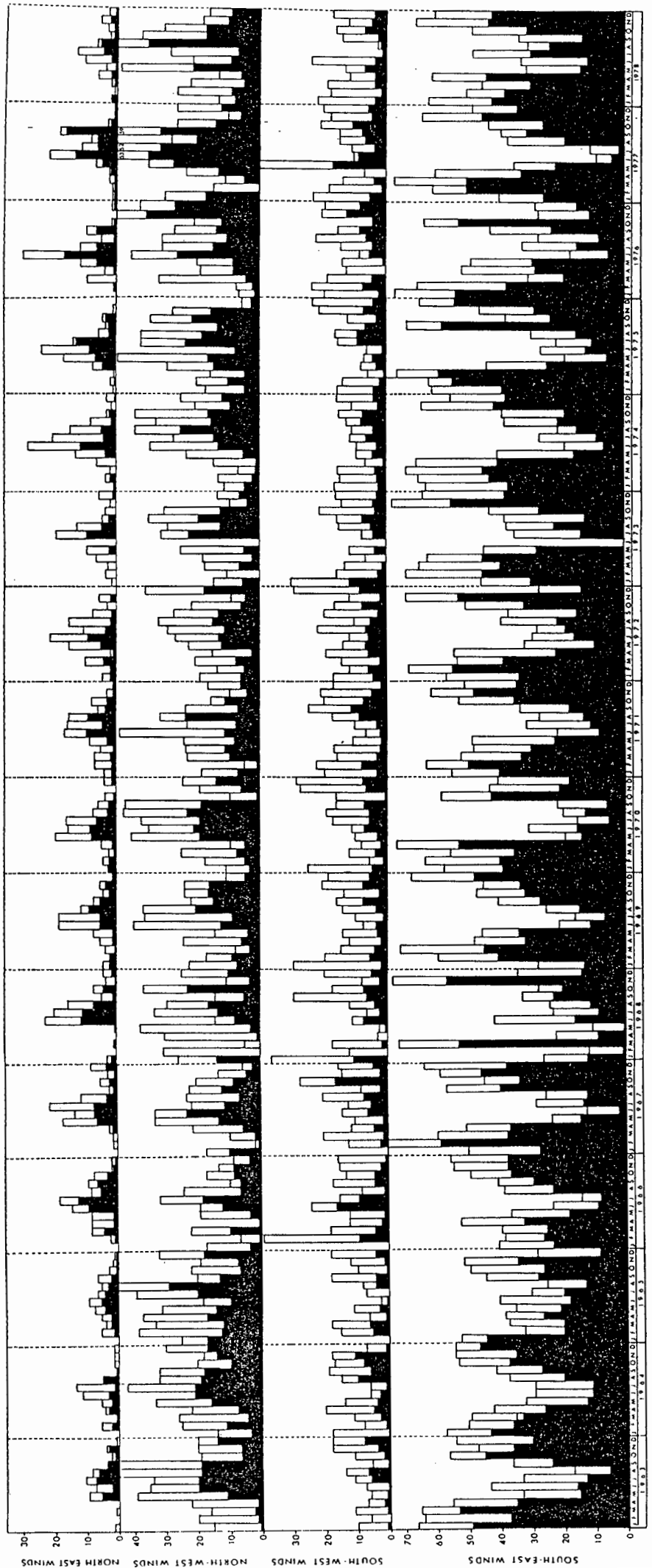

FIGURE 2.2: Monthly wind averages at Cape Point Lighthouse. Percentage occurrence of moderate (1,5 to 7,5 ms^{-1}, shaded bar) and strong (>8 ms^{-1}, unshaded bar) winds in each quadrant, where south-east includes southerlies and easterlies and north-west includes northerlies and westerlies [from Andrews and Hutchings, 1980].

summer months (Andrews and Hutchings, 1980), extends northwards from Cape Point (Fig. 2.3). At depth, the mooring site may experience cold water as it is drawn in from the south. During decay of the plume, north-westerly winds may advect cold water past the mooring site (Shannon, et al., 1981, Fig. 7; Jury, 1984, Fig. 9). The small Hangklip plume (Fig. 2.3) is relatively insignificant but, under certain conditions, may also introduce anomalously cold water into the study area (Jury, 1984, Fig. 20). The extended Cape Agulhas plume, when well-developed, may include the mooring site inshore of the upwelling front (Fig. 2.3). Such events are readily seen on NOAA thermal imagery (Shannon, 1985, Fig. 35) and from historic data (Shannon, 1966, Fig. 30, 32, inter alia, Shelton, 1986, Fig. 2.1.2, 2.1.4 and Boyd et al., 1985, Fig. 8). Two upwelling events can be identified in Fig. 2.4(a) and (b): February 1959 and November 1977.

A further upwelling-related intrusion is that of very cold Atlantic Ocean Central Water (less than 8°C) onto the shelf during spring (Nelson and Hutchings, 1983). Nelson (1983) reports 5°C water moving up Cape Point Valley. Current-meters at the head of the valley recorded sharp reversals of current indicating to-and-fro movement of this water onto the shelf with a time-scale of a few days. Shannon et al. (1981) suggest that these intrusions are controlled by atmospheric forcing on a scale significantly larger than that forcing local upwelling. During September and October 1977, such cold water was found on the shelf (Fig. 2.4).

To the east lies the Agulhas Bank and, beyond that, the Agulhas Current which is one of the major western boundary currents of the world (Gründlingh, 1980). Both warm Agulhas Current Water and cold Indian Ocean Central Water are advected west as a two-layer structure from the current-shelf interaction zone (Swart and Largier, 1986). It is not clear whether this bottom water (temperature 9° or 10°C) remains on the bank and enters the study area or whether the cold water off Cape Point all originates from the Atlantic. The warm surface water which is advected

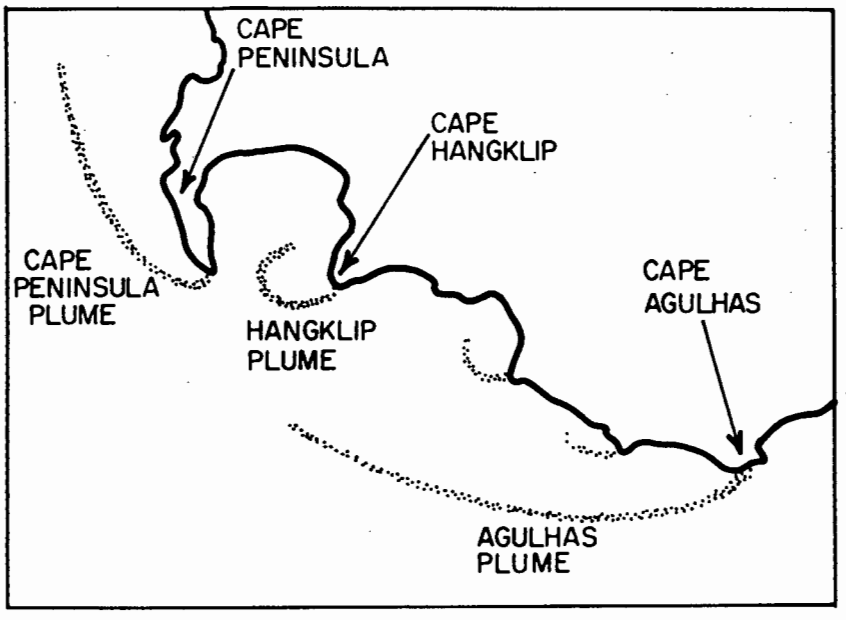

FIGURE 2.3: A schematic of upwelling plumes which may influence the Cape Point Study Area.

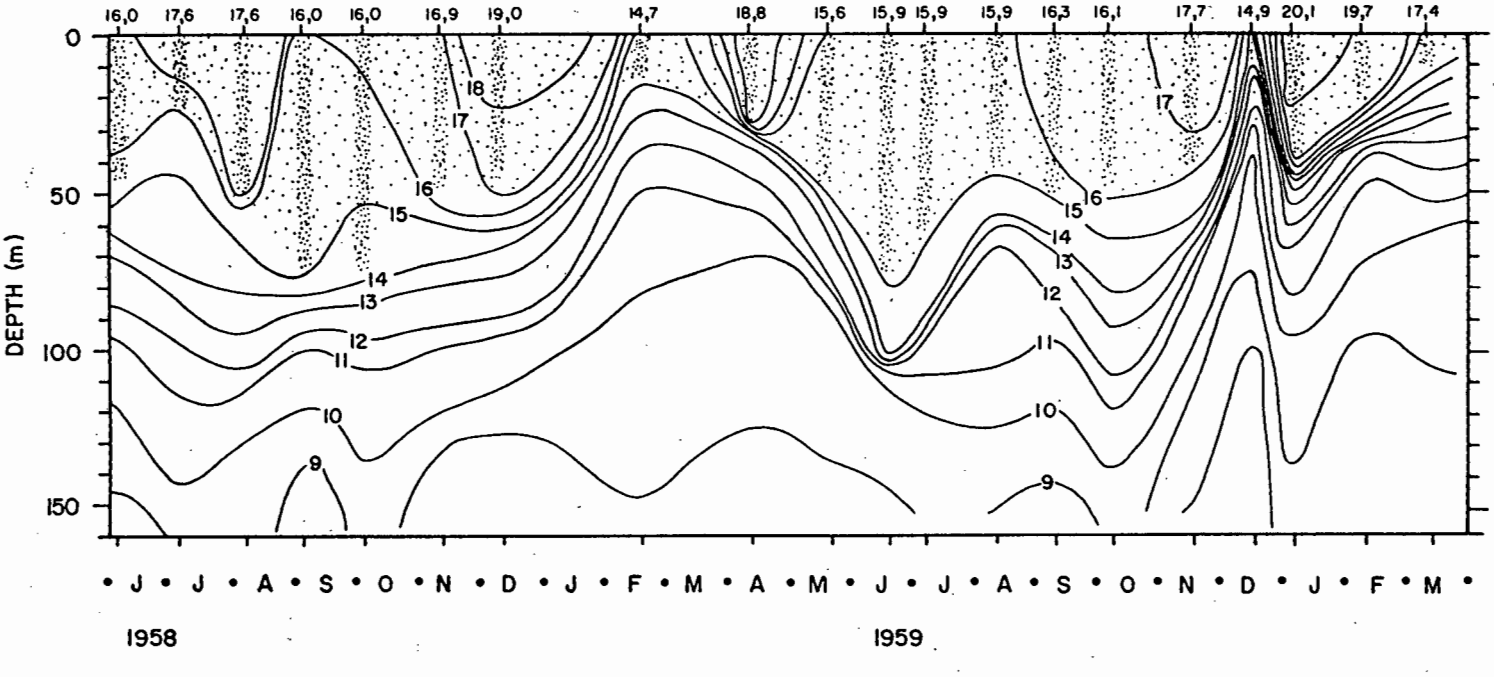

FIGURE 2.4(a): Seasonal variation in thermal structure at station R (Fig. 2.1). Single profiles were recorded as indicated on the upper horizontal axis. The approximate mixed layer depth is shaded.

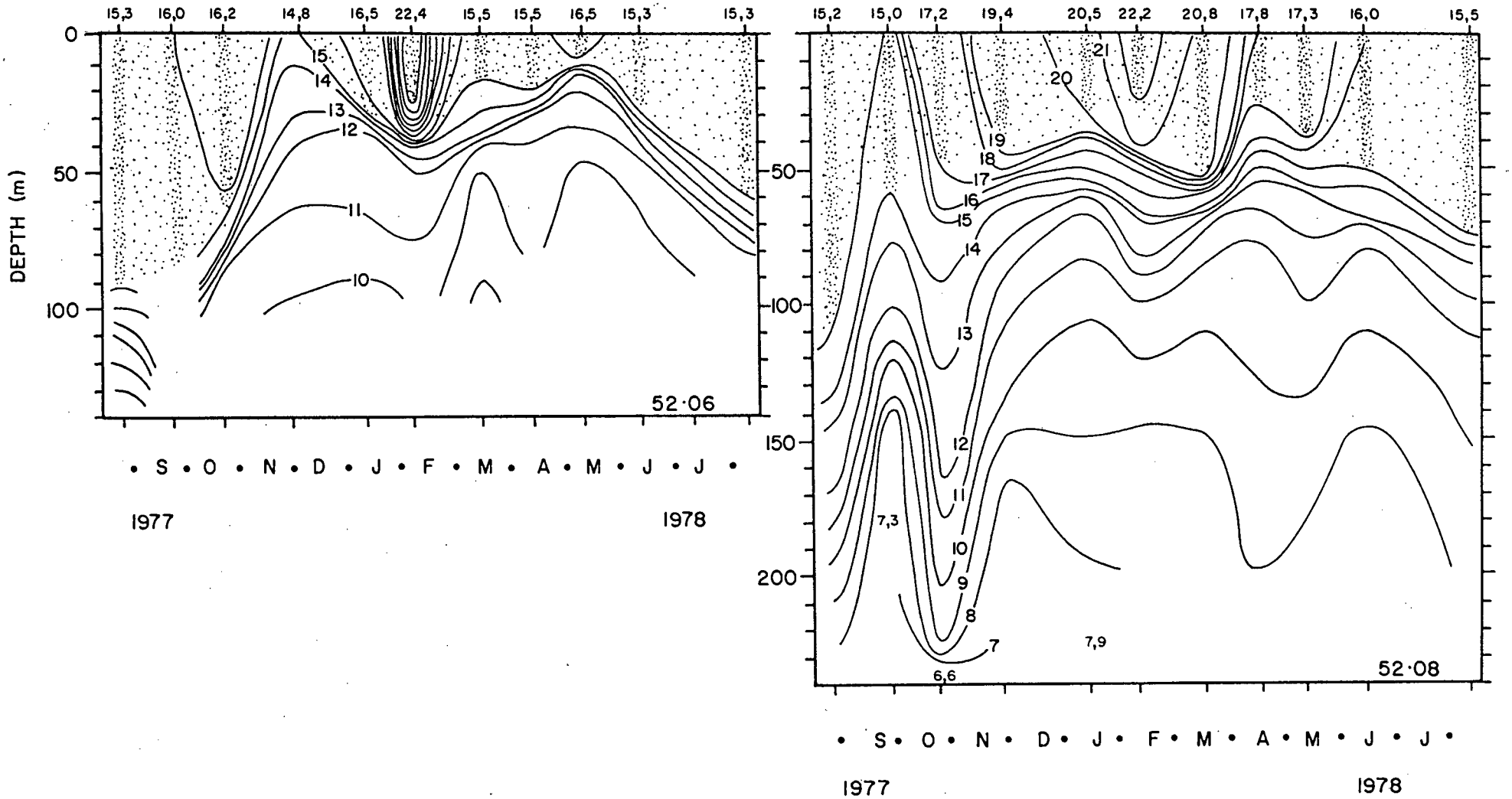

FIGURE 2.4(b): Seasonal variation in thermal structure at stations 52-06 and 52-08 (Fig. 2.1). Single profiles were recorded as indicated on the upper horizontal axes. The approximate mixed layer depth is shaded.

past Cape Point originates from frontal eddies shed from the cyclonic front of the Agulhas Current. These patches of warm water may intrude into the study area or even into False Bay (Wainman et al., 1986) during periods of weak or absent upwelling (Boyd, 1986). One such event was found during February 1978 (Fig. 2.4). When upwelling is active these patches of warm water will intensify horizontal gradients across the upwelling front. The longshore currents offshore of the front will carry this water further west and north.

Strong north-westward transport also occurs as a permanent baroclinic jet which exists over the line of steepest gradient on the shelf-edge (Nelson, 1983, 1985). Earlier drift-card work by Duncan and Nell (1969) has been confirmed by Bang (1973) and Bang and Andrews (1974), who suggested currents of the order of 1 m/s. Shannon (1985) has discussed further observations and studies of this topographically-controlled equatorward flow. Associated with this flow is a thermocline, which generally slopes upward to the coast. The shelf-edge front, corresponding to the shelf-edge jet, may match up with the local upwelling front as shown by Shelton and Hutchings (1982). This shelf-edge front appears to be a permanent feature which weakens in winter owing to a decrease in upwelling favourable winds. It is clearly displayed by Boyd et al. (1985, Fig. 9) and can be inferred from comparison of the structure of stations 52-06 and 52-08 as plotted in Fig. 2.4(b).

Dynamics on the time-scale that is addressed in this thesis have received little attention. Inertial and tidal currents have been analysed by Schumann and Perrins (1982) for moorings adjacent to the study area. Strong inertial motions (up to 0,2 m/s) and weaker tidal currents (up to 0,04 m/s) were recorded off Slangkop (mooring S, Fig. 2.1) by the Sea Fisheries Research Institute (Grev Nelson, unpublished data, 1985). In False Bay, inertial currents (up to 0,2 m/s) and tidal currents (up to 0,1 m/s) have been reported by Wainman et al. (1986). At the head of the Cape Point Valley, tidal currents of the order

of 0,05 m/s were observed (Shannon, et al., 1981). Further to the above, internal waves and tides have been observed with Landsat (Apel et al., 1975 and Nelson and Shannon, 1983) off the west and south-west coasts. The latter report, which addresses some of the slick patterns discussed in Chapters 3 and 4, is the forerunner to this extended investigation.

The local wind field has been extensively described by Jury (1980, 1984). The winds offshore in the study area appear to be stronger than those recorded at Olifantsbos, a coastal automatic weather station (OL in Fig. 2.1). Winds up to 20 ms^{-1} are recorded at Olifantsbos for both the winter north-westerlies and summer south-easterlies.

In order to obtain an idea of the ambient seasonal structure at the Cape Point mooring site, historical temperature data (collected by the Sea Fisheries Research Institute) are plotted in Fig. 2.4. Similar plots by Boyd et al. (1985, Fig. 5), Shelton (1985, Fig. 2.1.18) and Nelson (1985, Fig. 6), for stations in the study area, are also considered. In each survey, instantaneous profiles were taken once a month. Although intended to follow seasonal changes each profile is subject to a spectrum of intra-seasonal variation. In particular, the episodic events described above can be accounted for, but internal waves combine with possible instrument error to the extent that one cannot expect a resolution of better than a few metres. Since the temperature-salinity character of the area usually approximates a well-defined T-S curve (Shannon, 1985), the temperature data alone may be considered as a reasonable expression of density (refer to Section 4.6 and Bang, 1973).

The most important feature is that the structure is clearly more relaxed in winter. The sub-surface front and westward jet weaken, the surface fronts disappear and the thermocline deepens and weakens. Above the thermocline a well-mixed layer extends to the surface, below the thermocline the stratification is usually weak and uniform. With the approach of summer and the

increase in SE winds, cold water is fed onto the shelf (e.g. September and October 1977 at station 52-08), coastal upwelling is initiated and the sub-surface front is strengthened. Simultaneously more Agulhas water is advected westward from the bank and the temperature gradients near Cape Point, due to the emergent surface fronts, are enhanced. Boyd et al. (1985) and Shelton (1986) also discuss these dynamics. The oceanography of the area to the north and west of Cape Point is well described as part of reviews on the Southern Benguela system (e.g. Andrews and Hutchings, 1980; Nelson and Hutchings, 1983 and Shannon, 1985). In Fig. 2.4 upwelling and advective events are seen to interrupt the underlying seasonal pattern. The thermocline generally rises to about 20 to 30 m in summer and is deepened to about 80 or 90 m in winter. The offshore profiles consistently record deeper thermoclines consistent with a semi-permanent sub-surface front. In winter the difference is less, indicative of a weakening front. For this thesis, valid data is returned for the months May to November of 1983; these data should exhibit the deepening of the mixed layer, a deep weak winter thermocline and spring resurrection of the shallow strong thermocline (Section 4.2).

2.2 The Theory of Internal Waves

Any density-stratified fluid may support baroclinic oscillations or internal waves. The vertical displacements associated with these waves have sub-surface maxima and distort the surface negligibly. At higher frequencies a disturbance is restored mostly by gravity, therefore $\sigma<N$ where σ is the frequency of the wave and N is the Brunt-Väisälä or buoyancy frequency. At lower frequencies a disturbance is restored mostly by rotation, therefore $\sigma>f$ where f is the local Coriolis or inertial frequency.

Recent texts by Defant (1961), Krauss (1966), Turner (1973), Roberts (1975), Phillips (1977), Le Blond and Mysak (1978) and Gill (1982) provide a good introduction to internal waves in the ocean. Recent specialist reviews are on internal tides (Wunsch,

1975; Hendershott, 1981), internal waves and small scale processes (Gregg and Briscoe, 1979; Munk, 1981) inertial oscillations (Fu, 1981) and the internal wave field (Briscoe, 1975; Garrett and Munk, 1979; Olbers, 1983; Levine, 1983). The general theory of internal waves presented in this section is extracted from Largier (1986).

Considering a Boussinesq, incompressible fluid one may write linearized equations to describe the free behaviour of a perturbation from rest:

$$\rho_o\left(\frac{\partial}{\partial t}\underline{u} + \underline{f} \times \underline{u}\right) = -\nabla p' - \rho' g\hat{\underline{z}} + \rho_o \nu \nabla^2 \underline{u} \qquad \text{momentum}$$

$$\frac{\partial}{\partial t}\rho' + w\frac{\partial}{\partial z}\rho_o = 0 \qquad \text{conservation of mass}$$

$$\nabla \cdot \underline{u} = 0 \qquad \text{continuity} \qquad (1)$$

where (x,y,z) are a right-hand set of spatial axes with z vertical upwards

$\underline{u} = (u,v,w)$ are the component velocities of a material volume element relative to the rotating reference frame

t is time

$\underline{f} = (0,0,f)$ is the local Coriolis acceleration, taken as constant for the limited horizontal scales of internal waves ($f>0$ for the Northern Hemisphere; $f<0$ for the Southern Hemisphere).

$p=p_o(z)+p'(x,y,z,t)$ is pressure

$p_o(z)$ is the pressure in hydrostatic equilibrium

$p'(x,y,z,t)$ is the dynamic pressure (due to perturbation)

$\rho=\rho_o(z)+\rho'(x,y,z,t)$ is density

$\rho_o(z)$ is the density in hydrostatic equilibrium

$\rho'(x,y,z,t)$ is the density anomaly (due to perturbation)

g is acceleration due to gravity

ν is the kinematic viscosity

Excluding viscous effects, these equations of motion may be reduced to a single equation in a single variable:

$$\left(\frac{\partial^2}{\partial t^2} + f^2\right) \nabla^2 w + N(z)^2 \nabla_h^2 w = 0 \qquad (2)$$

where $N(z)^2 = \frac{-g}{\rho_o} \frac{\partial \rho_o}{\partial z}$

∇_h is the horizontal gradient $\left(\frac{\partial}{\partial x}, \frac{\partial}{\partial y}\right)$

For constant depth, this equation is separable if N is taken constant or if the long-wave approximation is made.

For $w(x,y,z,t) = h(z) \cdot \tilde{w}(x,y,t)$
one obtains a horizontal-time wave equation

$$\left(\frac{\partial^2}{\partial t^2} + f^2\right) \tilde{w} - \frac{s^2}{N^2} \left(\frac{\partial^2}{\partial t^2} + N^2\right) \nabla_h^2 \tilde{w} = 0 \qquad (3)$$

and a vertical eigen-value equation

$$\frac{d^2}{dz^2} h + \frac{N^2}{s^2} h = 0 \qquad h=0 \text{ at } z=0, -H \qquad (4)$$

where s is a separation constant (dimensions of velocity)
H is the depth of water
and a rigid-lid approximation is adopted (Gill, 1982).

For constant N, Eq. 3 and 4 are satisfied by a plane wave solution

$$w(x,y,z,t) = W \exp[i(kx+ly+mz-\sigma t)] \qquad (5)$$

where $\underline{K} = (k,l,m)$ is the wave-number and $k_h^2 = k^2+l^2$.
The dispersion relation is

$$\sigma^2 = \frac{m^2}{K^2} \cdot f^2 + \frac{k_h^2}{K^2} \cdot N^2 \qquad (6)$$

therefore internal waves may only exist for frequencies $f \leq \sigma \leq N$. The same solution is obtained for slowly-varying N(z) by extended asymptotic methods (Gill, 1982). As a vertically propagating wave of frequency σ approaches a depth where $N(z)=\sigma$, it will be reflected (this is the 'turning depth').

These and subsequent general expressions may be simplified by the non-rotating approximation as $\sigma \to N$ or by the hydrostatic approximation as $\sigma \to f$. In this thesis, attention is mostly given to internal tides and inertial motions, which are both long waves ($k_h << m$), and the hydrostatic (or long-wave) approximation is adopted. Thus $m \sim K$ and

$$\sigma^2 = f^2 + \frac{k_h^2}{m^2} N^2 \tag{7}$$

The eigen-solutions to Eq. 4 (corresponding to discrete, positive values of s^2) describe the possible modes or depth structures in a stratified ocean. An ocean with n interfaces may support n modes and a continuously stratified ocean may support an infinite number of discrete modes. Empirically, the majority of energy is found in the simpler lower order modes.

For a disturbance of given frequency σ, the response will be characterized by modes with

$$\begin{aligned}
&\text{phase speeds} && c_n = \left[\frac{f^2}{K^2} + \frac{k_h^2}{K^2 m^2} N^2\right]^{0,5} \\
&\text{horizontal phase speeds} && (c_h)_n = \left[\frac{f^2}{k_h^2} + \frac{N^2}{m^2}\right]^{0,5} \\
&\text{group velocity} && (\underline{c}_g)_n = \frac{N^2}{\sigma\, m^2} \left(k, \ell, \frac{-k_h^2}{m}\right) \\
&\text{where} && \underline{c}_g \cdot \underline{K} = 0 \\
\text{and} \quad &\text{aspect ratio} && \alpha = \frac{k_h}{m} = \left(\frac{\sigma^2 - f^2}{N^2}\right)^{0,5}
\end{aligned} \tag{8}$$

As σ approaches f, the inertial frequency, the disturbance becomes more horizontally polarized so that $\underline{c}_g$ is horizontal for pure inertial motion ($\sigma = f$).

Returning to constant-N, it can be seen that wavelength and phase speed are inversely proportional to mode number n.

Having solved for w as in Eq. 5, one can derive expressions for the remaining dependent variables:

$$
\begin{aligned}
p' &= \frac{-N^2 \rho_o}{\sigma\, m}\, w \\
u &= \frac{k\sigma + i\ell f}{\sigma^2 - f^2}\, \frac{1}{\rho_o}\, p' \\
v &= \frac{\ell\sigma - ikf}{\sigma^2 - f^2}\, \frac{1}{\rho_o}\, p' \\
\rho' &= \frac{i\rho_o\, N^2}{\sigma g}\, w
\end{aligned}
\tag{9}
$$

From a scalar product of $\underline{u}$ with the momentum equations, the energy equation is obtained

$$
\frac{\partial}{\partial t}\left[\frac{1}{2}\,\rho_o(\underline{u}_H \cdot \underline{u}_H + N^2\,\zeta^2)\right] + \nabla \cdot p\underline{u} = 0 \tag{10}
$$

where ζ is the vertical displacement $\frac{w}{i\sigma}$.

Kinetic energy (KE) and potential energy (PE), expressed by the first two terms in Eq. 10, are not equally partitioned in a rotating system (Gill, 1982):

$$
\frac{KE}{PE} = \frac{\sigma^2 + f^2}{\sigma^2 - f^2} \tag{11}
$$

Equation 10 equated the rate of change of energy density E with the energy flux E_f, which can be simply obtained as $E \cdot \underline{c}g$.

2.3 The Two-Layer Approximation

At latitudes where the net heat flux is into the ocean, the density stratification tends to take a two-layer character in the presence of wind. The warm surface layer, mixed by the wind, overlies a seasonal thermocline. Below the thermocline, temperature decreases slowly with depth. On the continental shelf this bottom layer is often partially mixed such that the whole structure may be approximated by two homogeneous layers separated by an interface. In particular the historical data (Section 2.1) and contemporary data (Section 3.3) off Cape Point

indicate that this is the case seaward of the coastal mixed boundary layer. Generally the thermocline is shallow and strong in summer/autumn and weak and deep in winter/spring. This thermal structure may be strengthened or weakened by salinity distribution.

Although simplistic, the two-layer approximation is very attractive in that it may be solved exactly and so allows one to easily and clearly perform an analytical investigation of various concepts and processes. This approximation will be used frequently throughout the thesis to model the internal tide and inertial motions. Justification and/or limitations in these two special cases are presented in Chapters 5 and 6, respectively. Essentially the first mode, which has a form $h(z) = \sin \frac{\pi}{H}(z+H)$ in a constant-N ocean, is assumed dominant and is approximated by $h'(z)= -\frac{z}{H_1}$ for $z > -H_1$ and $h'(z) = \frac{H+z}{H-H_1}$ for $-H_1 > z > -H$, where H_1 is the depth of the interface and H is the water depth. The constant-N approximation complements the two-layer approximation in that the former is the smoothest profile and the latter is the sharpest profile for a given gross density difference $[\rho(-H)-\rho(0)]$. It is expected that real stratification will be characterized by solutions lying between the above two extrema. This work, which chooses the two-layer approximation because of the stratification of the study-area, would be extended and complemented by work based on the constant-N approximation.

Considering the two-layer system depicted in Fig. 2.5, linearized equations of motion (cf. Eq. 1) can be written for an inviscid, incompressible, homogeneized, Boussinesq fluid with the hydrostatic approximation describing the vertical dimension.

$$\text{Layer 1} \qquad \begin{aligned} &\partial_t u_1 - f v_1 = -g \partial_x a \\ &\partial_t v_1 + f u_1 = -g \partial_y a \\ &p_1 = \rho_1 g (a - z) \\ &\partial_t (a-\zeta) + \partial_x (H_1 u_1) + \partial_y (H_1 v_1) = 0 \end{aligned} \qquad (12)$$

Layer 2

$$\partial_t u_2 - f v_2 = -(\rho_1/\rho_2) g \partial_x a - g' \partial_x \zeta$$
$$\partial_t v_2 + f u_2 = -(\rho_1/\rho_2) g \partial_y a - g' \partial_y \zeta$$
$$p_2 = \rho_1 g (H_1 + a - \zeta) + \rho_2 g (\zeta - H_1 - z)$$
$$\partial_t \zeta + \partial_x (H_2 u_2) + \partial_y (H_2 v_2) = 0 \qquad (13)$$

where $\partial_x \equiv \frac{\partial}{\partial x}$, $\partial_t \equiv \frac{\partial}{\partial t}$, $\partial_y \equiv \frac{\partial}{\partial y}$

a is the surface displacement

ζ is the interface displacement

$g' = \frac{\Delta\rho \cdot g}{\rho}$ is the reduced gravity

1 refers to the upper layer (Fig. 2.5)

2 refers to the lower layer (Fig. 2.5)

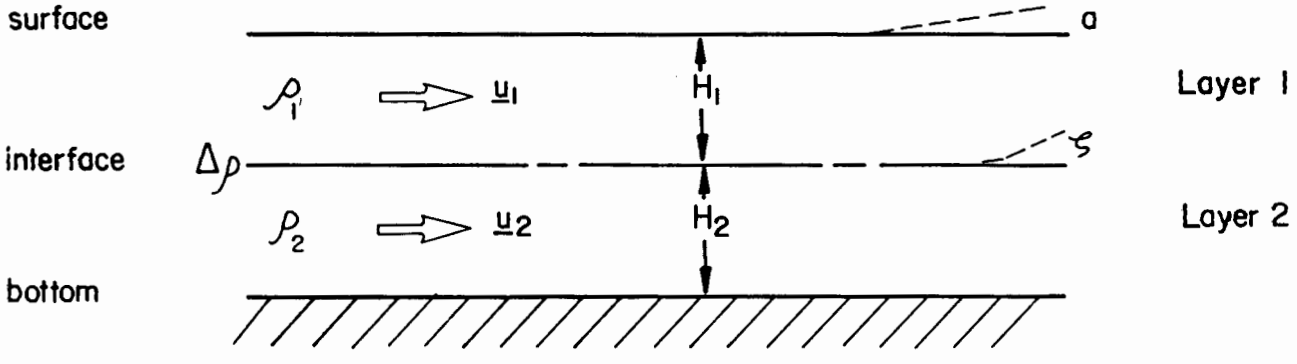

FIGURE 2.5: The two-layer model.

A single, composite equation in terms of a and ζ can be developed from Eq. 12 and Eq. 13 for layer 1 and layer 2, respectively. Two solutions are found, corresponding to a barotropic and a baroclinic mode, as expected. With this foresight, the barotropic mode is modelled through taking $\rho_1 = \rho_2 = \rho$:

$$\begin{aligned} \partial_t u - fv &= -g\partial_x a \\ \partial_t v + fu &= -g\partial_y a \\ \partial_t a + \partial_x(Hu) + \partial_y(Hv) &= 0 \end{aligned} \tag{14}$$

Assuming slowly-varying depth, that is $\frac{1}{H} \cdot \partial_x H << \frac{1}{u} \cdot \partial_x u$ and $\frac{1}{H} \partial_y H << \frac{1}{u} \partial_y u$, the above equations may be reduced to a single equation in a single variable.

$$\partial_t^2 a + f^2 a = c_o^2 \nabla^2 a \tag{15}$$

where $c_o^2 = gH$.

∇ for this 2-layer case is the horizontal operator ∇_h

The baroclinic mode is modelled as a difference between Eq. 12 and 13, assuming a rigid-lid surface ($a << \zeta$), constant H_1 and slowly-varying depth H.

$$\begin{aligned} \partial_t \hat{u} - f\hat{v} &= g'\partial_x \zeta \\ \partial_t \hat{v} + f\hat{u} &= g'\partial_y \zeta \\ -\left(\frac{H}{H_1 H_2}\right)\partial_t \zeta + \partial_x \hat{u} + \partial_y \hat{v} &= 0 \end{aligned} \tag{16}$$

This is reduced to a single equation in ζ

$$\partial_t^2 \zeta + f^2 \zeta = c_1^2 \nabla^2 \zeta \tag{17}$$

where $\hat{u} = u_1 - u_2$, $\hat{v} = v_1 - v_2$

$$c_1^2 = g' \frac{H_1 H_2}{H}$$

Adoption of this two-layer approximation anticipates that the solutions of Eq. 15 and 17 closely approximate the solutions of the exact, continuously-stratified system. If the depth is not slowly-varying, one would need to include topographic terms, which involve a, in the baroclinic equation. Therefore, in the presence of significant topography, the barotropic solution will force a baroclinic response. These barotropic-to-baroclinic topographic coupling terms depend on the size of $\frac{1}{H} \partial_x H$ and $\frac{1}{H} \partial_y H$ In contrast, baroclinic-to-barotropic coupling has negligible effect on the barotropic solution.

Eq. 15 and 17 are rotationally modified wave equations describing free barotropic and baroclinic waves. Assuming $\partial_y H \sim 0$, $\partial_y a \sim 0$ and $\partial_y \zeta \sim 0$, the system is reduced to two-dimensions and has a barotropic solution.

$$\begin{aligned} a &= A \exp\left[i(\sigma t \pm k_b x)\right] \\ u_b &= U_b \exp\left[i(\sigma t \pm k_b x)\right] \end{aligned} \qquad (18)$$

with dispersion relation $\sigma^2 = f^2 + gHk_b^2$

where A is the amplitude of the barotropic wave

$$U_b = \frac{gk_b\sigma}{\sigma^2 - f^2} A$$

$$c_b = \pm \left(\frac{\sigma^2}{\sigma^2 - f^2}\right)^{0,5} (gH)^{0,5} \qquad \text{phase speed}$$

$$(c_g)_b = \pm \left(\frac{\sigma^2 - f^2}{\sigma^2}\right)^{0,5} (gH)^{0,5} \qquad \text{group speed}$$

and a baroclinic solution

$$\begin{aligned} \zeta &= T \exp\left[i(\sigma t \pm kx)\right] \\ \hat{u} &= \hat{U} \exp\left[i(\sigma t \pm kx)\right] \end{aligned} \qquad (19)$$

with dispersion relation $\sigma^2 = f^2 + g' \frac{H_1 H_2}{H} k^2$

where T is the amplitude of the baroclinic wave

$$\hat{U} = -\frac{g'k\sigma}{\sigma^2 - f^2} T = \left(\frac{\sigma^2}{\sigma^2 - f^2} \cdot \frac{g'H}{H_1 H_2}\right)^{0,5} T$$

$$c = \pm \left(\frac{\sigma^2}{\sigma^2 - f^2}\right)^{0,5} \left(g' \frac{H_1 H_2}{H}\right)^{0,5} \qquad \text{phase speed}$$

$$C_g = \pm \left(\frac{\sigma^2 - f^2}{\sigma^2}\right)^{0,5} \left(g' \frac{H_1 H_2}{H}\right)^{0,5} \qquad \text{group speed}$$

Introducing the additional constraint that depth-integrated baroclinic transport is zero (Gill, 1982),

$$u_1 = \frac{H_2}{H} \hat{u} \qquad \text{and} \qquad u_2 = -\frac{H_1}{H} \hat{u}$$

where u_1 and u_2 are the baroclinic velocities in layer 1 and layer 2 respectively.

CHAPTER 3
DATA COLLECTION AND OBSERVATION

Internal wave activity is reflected in a wide variety of oceanographic data sets. Consequently evidence is readily obtainable of such activity (given that the waves are present). The continental shelf surrounding southern Africa is no exception to internal wave ubiquity. However, in order to quantitatively analyse the internal wave field it is necessary to have a data set appropriate for this purpose. For a complete analysis of the full internal wave spectrum, using conventional mooring systems, one would require data on the variation of current and temperature with time at a variety of spatially-separated points. The time or spatial interval between two data provides an indication of the lower limit to resolution in that dimension. The total time or spatial range between the first and last data points of a set provides an upper limit to the period or wavelength determinable in that dimension.

Although few authors (Bang, 1972, 1973, 1974; Apel et al., 1975; Nelson and Shannon, 1983) have referred to internal wave activity in southern African waters, there are a number of historical data sets (bathythermograph, CTD, current-meter and thermistor) which indicate the ubiquity of internal waves in these waters. In an attempt to measure the internal waves reflected via surface slicks on Landsat imagery, a thermistor string was moored south of Cape Point during 1983. The research effort which is reported in this thesis, had its genesis in the analysis of these thermistor data. Certain other ancillary data were available, mostly through the Sea Fisheries Research Institute, but they were collected simultaneously as part of a separate research effort (e.g. current data and wind data). Since 1983 further useful data sets (current meter and thermistor string) have been collected by the Sea Fisheries Research Institute, the University of Cape Town and the National Research Institute for Oceanology in the course of their individual research efforts. Nevertheless, the 1983 Cape Point thermistor data set forms the empirical core of this thesis.

3.1 Thermistor String Data

An Aanderaa thermistor string (temperature profiler) was deployed and recovered successfully on three occasions. A fourth deployment, consisting of a triangular array of thermistor strings, during the summer of 1983/84 unfortunately produced no data. This was partially the result of a mid-latitude storm of record strength and intensity (Subsection 7.3.2). Current meters included on the moorings were deployed simultaneously but as part of a separate research effort. The current data are, therefore, not analysed as part of this work but are referred to at a later stage. The position of the initial mooring (Fig. 3.1) was chosen predominantly to fulfill its role as the most southerly of a series of west coast sub-thermocline current meter moorings. A secondary objective was to locate it within the area in which banded sea-surface structures had been recorded by Landsat (Section 3.3). The majority of the instrumentation was the property of the Sea Fisheries Research Institute (SFRI) and the remainder belonged to the Institute of Maritime Technology (IMT). The moorings were deployed and recovered by the SFRI.

The data records are summarized in Table 3.1. The thermistor string data constitute a semi-continuous temperature record from May 1983 through winter and spring to November 1983. These data are generally of a very high standard. Certain obviously incorrect data were replaced by interpolated values. However, near the end of the tape, where tape stretch started to affect the recording performance of the data logger, increasingly bad data were recorded. When more than 0,5% of the values required replacement, the remaining data were abandoned. The earlier data were characterized by a replacement rate which was at least one order of magnitude better than the above rate. In the first deployment 4 893 good recordings were made; the second and third deployments contain 4 524 and 3 568 good recordings, respectively.

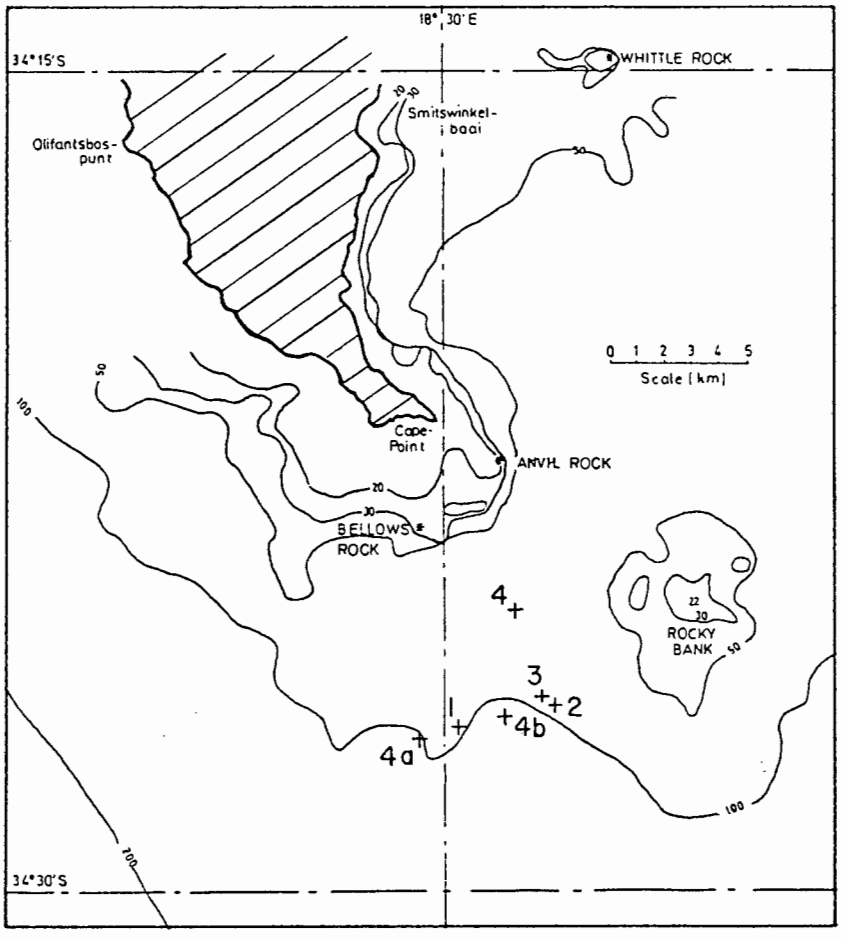

FIGURE 3.1: Locations of the consecutive thermistor string moorings at Cape Point. 1. First deployment (May-July 1983) 40 m string; 2. Second deployment (Aug-Sept 1983) 20 m string; 3. Third deployment (Oct-Nov 1983) 20 m string; 4. Fourth deployment (a) 40 m string; (b) 20 m string; (c) surface mooring. See Table 3.1 for details.

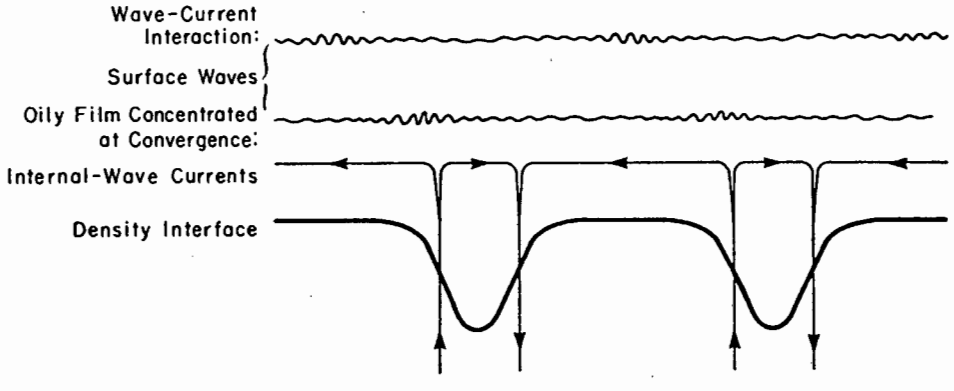

FIGURE 3.2: Schematic showing the expected modulation of short surface waves due to a first mode internal wave. The upper trace respresents wave-current interaction and the lower trace represents damping by surfactents [from Sawyer, 1983].

	INSTRUMENT	DURATION OF RECORD (TIME INTERVAL)	DEPTH RANGE (SEPARATION)	LOCATION
*	Thermistor String	17/05-0/07/83 (15 min)	55-95 m (4 m)	34°27,0'S 18°30,3'E
x	Current Meter	17/05-24/07/83	100 m	"
*	Thermistor String	10/08-27/09/83 (15 min)	57-77 m (2 m)	34°26,6'S 18°32,5'E
x	Current Meter	10/08-20/10/83	85 m	"
*	Thermistor String	20/10-26/11/83 (15 min)	64-84 m (2 m)	34°26,4'S 18°32,2'E
	Current Meter	20/10-18/12/83	62 m	"
	Current Meter	20/10/83-21/01/84	89 m	"
+	Thermistor String (no data)	3/02/84 (15 min)	50-70 m (2 m)	34°26,8'S 18°31,4'E
	Current Meter	3/02-10/05/84	76 m	"
	Current Meter	3/02-18/05/84	103 m	"
+	Thermistor String (no data)	4/02/84 (5 min)	38-78 m (4 m)	34°27,2'S 18°29,4'E
	Current Meter	4/02-7/05/84 (15 min)	89 m -	" "
+	Thermistor String (no data)	10/02/84 (2 min)	20-40 m (5 m)	34°25'S 18°32'E

TABLE 3.1: Summary of deployments associated with the Cape Point study (see also Fig. 3.1). The data obtained from those deployments marked with an asterisk (*) were analysed and interpreted in detail. The data indicated by a cross (x) were not analysed but reference has been made to them. The deployments marked by a plus-sign (+) yielded no data.

In retrospect, a better mooring location could have been chosen. The shelf topography, along a line normal to the isobaths, is not easily described by a simple shape (Fig. 1.1). This complicates attempts to model the internal tide generation. Further, the lack of summer/autumn data is a severe inadequacy which restricts comment on the seasonality of the internal wave spectrum. [Partly to address these issues, a series of three moorings have been deployed across the shelf west of Agulhas. They were deployed in December 1986 and will be recovered in January 1987]. Further restrictions are imposed on the data by the limited vertical range covered by the thermistors (Table 3.1) as well as by the coarseness of the sample intervals (15 minutes in time and 2 m or 4 m in depth).

3.2 Landsat Imagery

It has been known for a long time that sub-surface internal wave activity may produce a surface signature. For winds well below white-capping strength the surface ripples (capillary to ultra-gravity section of spectrum) may be modulated by surface velocities induced by the internal waves. Bands of relatively smooth sea (specular reflection) alternate with bands of rippled sea (diffuse scattering). Dependent on the angle of the sun, either band may appear brighter. Two mechanisms have been proposed. Ewing (1950) proposed that, in the presence of internal waves, convergent surface velocities would compact oily organic substances into a continuous surface layer which would inhibit deformation of the surface, causing surface slicks (Fig. 3.2). Verification has been provided by La Fond and La Fond (1967) and further support was given by the work of Ermakov and Pelinovsky (1984). The second mechanism was postulated by Gargett and Hughes (1972). Short surface waves will be alternately lengthened and diminished or shortened and enhanced by currents induced parallel or opposed, respectively, to the direction of propagation of the surface waves (Fig. 3.2). Sawyer (1983) discusses the relative merits of these two mechanisms.

These banded signatures have been recorded previously by Landsat, as reported by Apel, et al. (1975); Apel et al. (1976); Baines (1981) and others. A perusal of nearly cloud-free images of the SW Cape area between 1978 and 1985 yielded twelve images of interest to an internal wave study. Two of these images are shown in Fig. 3.3 and discussed in Section 4.1. The long Landsat repeat cycle of 18 or 16 days, the dependence on angle of the sun relative to the observer and the need for cloud-free images conspire to make this an exercise low in dividends. Therefore, it should be realized that these few images give little indication of the continual activity on the thermocline.

The following images, centred at about 24,5°S and 19,0°E, were obtained from the Satellite Remote Sensing Centre at Hartebeeshoek. With a resolution of about 80 m these images were all obtained in the 500-600 nm or the 600-700 nm spectral bands. Interesting images were obtained for 1 December 1978; 19 December 1978; 6 January 1979; 11 February 1979; 19 October 1981; 24 November 1981; 16 September 1982; 3 November 1982; 6 January 1983; 7 February 1983; 10 February 1984 and 23 October 1984. Line drawings of eight of these images are presented in Fig. 3.4.

3.3 Further Observations

In addition to the satellite images and the thermistor data, which are extensively analysed, many other data were referenced or used.

Historical BT and CTD data, mostly unreported, were inspected in order to obtain an idea of the variation in thermocline depth, strength and shape. However, these individual profiles contain a large uncertainty owing to the presence of an unknown internal wave field. In Section 2.1, some of the data were discussed in terms of seasonality and episodic events. For a study of internal waves, coarsely-spaced vertical profiles over a limited depth, as provided quarter-hourly by the thermistor strings, are more reliable and more interesting.

a.

b.

FIGURE 3.3: LANDSAT images of surface slick patterns (a) 1 Dec. 1978: Semi-parallel, white bands in the south-west are clouds; packets of short, parallel slicks near Cape Point are probably due to local generation of internal tides and waves at Rocky Bank; long, diffuse lines near the coast are conceivably due to mixing internal tides (b) 10 Feb. 1984: Five successive tidal crests are identifiable. The oldest tides have reached shallow water and they are strongly scattered. The central tide has a very clear signature, with the longest and strongest crest leading the packet. The subsequent tide is heading for the mooring position CP.

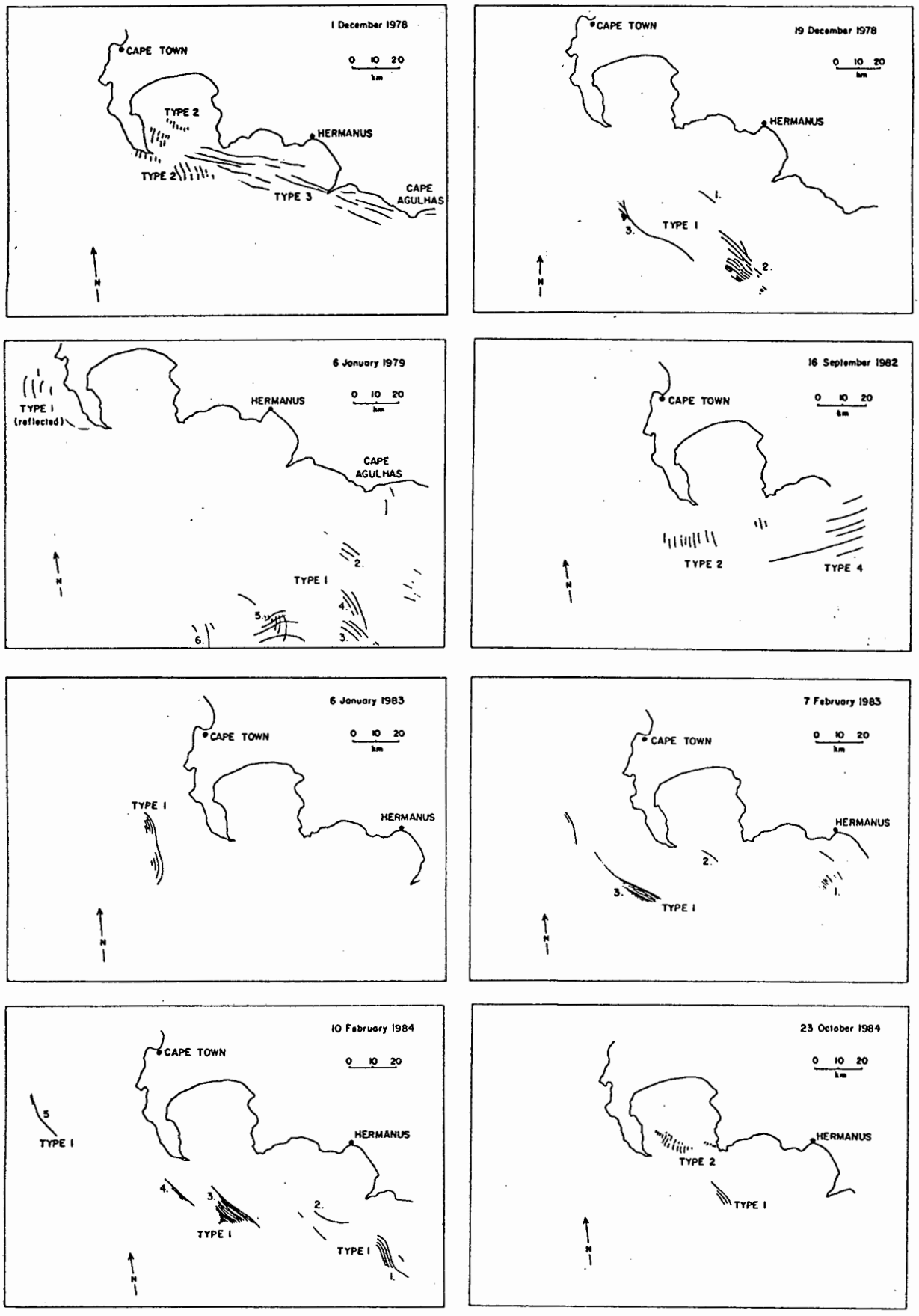

FIGURE 3.4: Line drawing interpretations of eight of the clear LANDSAT images. The three types are discussed in Section 4.1

Current-meter data, listed in Table 3.1, were scrutinized and they have been referred to in later chapters. These records, obtained from the SFRI, are the subject of a separate study and were not available for quantitative analysis.

A continuous, quarter-hourly record of wind at Olifantsbospunt (Fig. 2.1) was also made available by the SFRI. Although a coastal station, Olifantsbos falls within the Cape Point Study Area. This was the only relevant quantitative data available. Daily synoptic charts, obtained from the South African Weather Bureau, presented a meteorological context within which the wind record could be interpreted.

Other useful information was extracted from tables of tidal sea level (South African Navy), a detailed bathymetric chart (Dingle, Moir, Bremner and Rogers, 1977) and weekly mean sea surface temperature charts (GOSSTCOMP) provided by U.S. National Oceanic and Atmospheric Administration.

CHAPTER 4
DATA ANALYSIS (PROCEDURES AND RESULTS)

In this chapter the data, described in Chapter 3, are inspected and analysed in order to extract the essence of the dynamics represented by them. Various procedures are used to determine the theoretically reproducible **signal** and thereby to class, with justification, the residual variation as background **noise.** Simultaneously the characteristics of the components of the signal are revealed.

The first three sections of this chapter provide empirical information on the horizontal, temporal and vertical structure, respectively, of the local internal wave field. This information is obtained directly through inspection, in turn, of the Landsat imagery, the temperature time series for given depths and the temperature-depth profiles for given times. Having derived the full benefit of direct study, the data are subjected then to statistical manipulations in order to compare the mean strengths of the principal temporal and vertical structures. In Section 4.4 a spectral analysis is performed and the resultant frequency spectra are presented. In Section 4.5 an empirical orthogonal function analysis is performed and a comparison is made of the relative strengths of increasingly complex vertical structure. In the final section of this chapter, estimates are derived for the energy of the semi-diurnal internal tide.

4.1 Landsat Imagery

Four types of banded structure were identified in the twelve images, of which eight are presented in Fig. 3.4. The one type consisted of very long (~100 km) diffuse curved bands which appeared to follow the atmospheric isobars. This type, atypical of internal wave slicks, is probably of atmospheric origin and is not discussed. The remaining three types are interpreted below.

Type 1: Packets of long slightly-convex slicks, aligned roughly parallel to the isobaths, are typical of internal tides (Apel et al., 1975; Apel et al., 1976; Baines, 1981). These slicks, with wavelengths of 1 to 3 km, occur in groups or packets separated by 10 to 35 km. Each packet corresponds to a crest of the internal tide. The slicks themselves correspond to higher-frequency waves which are characteristically found superimposed on the internal tide. These waves are generally found with a frequency near to the local Brunt-Vaisäla frequency (Levine, 1983). It appears that these packets propagate shoreward with a group speed equal to the phase speed of the internal tide, which has a semi-diurnal frequency. Within each packet the wavelength, crest-length and pronunciation of the slick decrease from front to rear. This is consistent with the expectation that a packet of solitons will be led by the largest amplitude wave (Apel, 1981). The interpacket separation (internal tide wavelength), intercrest or intrapacket separation (high-frequency wavelength), maximum crest length, angular-spread of packet and mean direction of propagation are measurable on six of the images and are summarized in Table 4.1. All of the six images are obtained during mid-summer when the thermocline is typically shallower.

The internal tide over the deeper shelf (200 m) has a wavelength of about 25 to 30 km. Over the shallower shelf (100 m) the wavelength has reduced to about 10 to 15 km. This corresponds to a horizontal phase speed of about 0,6 m/s over the outer shelf decreasing to about 0,3 m/s over the inner shelf. Where two consecutive tidal packets appear on the same image (e.g. 10 December 1984), the generation site can be estimated by retracing the path of the incident internal tide. However, in the presence of irregular topography these internal waves may be scattered owing to bathymetric refraction. One particularly interesting packet of slicks is observed heading towards the shelf edge, presumably after reflection from the 'steep' topography (Baines, 1982) to the west of Olifantsbospunt (Fig. 3.4, 6 January 1979).

DATE	PACKET NUMBER	INTERPACKET SEPARATION (km)	INTRAPACKET SEPARATION (km)	MAX. CREST LENGTH (km)	NUMBER OF SLICKS	ANGULAR SPREAD (RADIUS OF CURVATURE)	BEARING OF TIDAL PROPAGATION
Dec '78	(1)	-	-	11	1	-	036°
	2	10	0,8 to 2,0	32	12	14° (80km)	036°
	3	19	0,5 to 1,3	48	6	30° (30km)	030°
Jan '79	1	-	4,1	14	4	-	274°
	2	-	2,2	11	3	-	042°
	3	26	2,1	13	3	-	052°
	4	-	1,7 to 2,9	21	3	-	071°
	5	34	1,2 to 3,1	14	6	-	096°
	6	32	2,5	20	3	-	088°
Feb '79	1	-	1,0	27	4	-	040°
	2	50	0,7 to 1,2	23	7	-	070°
Jan '83	1	-	0,5 to 1,9	35	5	40° (18km)	085°
Feb '83	1	-	0,8 to 2,0	17	8	28° (29km)	082°
	(2)	35	-	8	1	-	053°
	3	10	0,5 to 1,0	45	7	6°	034°
Feb '84	1	-	0,9 to 1,5	25	5	-	060°
	2	12	-	14	1	-	050°
	3	17	0,5 to 1,0	35	11	14°	050°
	4	12	1,0	25	3	9° (120km)	047°
	(5)	11	1,5	25	2	-	057°

BLE 4.1: Summary of type 1 internal tidal slicks observed over the south-west Cape shelf. Packets are numbered in sequence from the leading packet (furthest northeast). The authenticity of those numbers in brackets is questionable.

Type 2: Packets of short-crested slicks around the entrance to False Bay appear to emanate from an isolated relic wave-cut terrace (Rocky Bank, Fig. 3.1) situated in the mouth of the bay. The three clear images are all from early summer (September to December). It is suggested that the internal waves are generated by tidal shear flow over Rocky Bank. The mechanism has been clearly postulated by Maxworthy (1979) and Maxworthy, Chabert d'Hieres and Didelle (1984). A similar phenomenon in Massachusetts Bay has been well documented by Halpern (1971), Chereskin (1983) and Haury, Wiebe, Orr and Briscoe (1983) amongst others. In order that the mechanism works the thermocline must be shallower than the crest of the bank (about 30 m) and weak enough that the tidal flow over the crest may become supercritical and give rise to an internal hydraulic jump and lee wave - these dual conditions are probably satisfied in early summer only. In view of the fact that no relevant thermistor data is available, this rather local phenomenon has not been fully investigated. The review presented by Largier (1986) provides further background to this theory. The packets have from 3 to 11 crests of lengths up to 7 km. Wavelengths vary from 1 to 3 km. If the period were of the order of 20 to 30 minutes, then the expected horizontal phase speeds of between 0,5 and 2,5 m/s would be consistent with the group speeds estimated from the imagery.

Type 3: Semi-parallel bands, which were observed close to the coast between Cape Point and Cape Agulhas, appear to be due to enhanced biological activity (Nelson and Shannon, 1983). This feature is only found in a single image. The associated physical structure cannot be conclusively ascribed to any particular dynamics, but the foremost candidate is internal tide mixing induced by the shoaling topography. The inter-band spacing agrees with an expected tidal wavelength for these shallow depths. If this interpretation is correct, it then becomes very important to determine whether this event is a rare or a frequent occurrence.

4.2 Temperature Time-series

The temporal structure of the thermistor data is largely revealed by simple graphical plots of the data. For each deployment, the eleven parallel records are plotted alongside each other on a common time axis (Fig. 4.1). Amongst other uses, this plot allows one to pick out any phase differences between the records within one deployment. Most features are clearly simultaneous. In order to estimate the vertical displacements giving rise to these temperature fluctuations, the data were interpolated and isotherms were constructed as a function of depth and time (Fig. 4.2). This interpolation was performed on hourly data, after having applied a simple triangular running-mean formula (with three weights). Expecting free internal waves at only those frequencies above the local inertial frequency (about 0,048 cph at 35° latitude), the records were demeaned, detrended and filtered. A Lanczos-cosine filter (with 96 weights) was applied with a quarter-amplitude point at 0,04 cph such that internal wave periods (less than 21 hr.) were separated from longer period fluctuations (Fig. 4.3). Having identified excessively energetic spectral bands at high frequency (near the Nyquist frequency) and near the semi-diurnal tidal frequency, the time structure was split further (Fig. 4.4). The second application of a 96-weight Lanczos-cosine filter, with a quarter-amplitude point at 0,10 cph, displays a better response function (Fig. 4.4). The choice of a split at a 10 hr-period is supported by the spectra presented in Section 4.4. Each application of the filter truncates the input time-series by 96 points at each end (that is, about 5% of the data is sacrificed each time).

Interpretation of the variation of temperature T with time is based on the conservation of temperature (heating and cooling neglected):

$$\frac{\partial T}{\partial t} = \frac{\partial T}{\partial x} u + \frac{\partial T}{\partial y} v + \frac{\partial T}{\partial z} w$$

For horizontally homogeneous and/or non-advective oceans the temperature variations are solely due to vertical displacements. In the real ocean the product of horizontal velocity with temperature gradient is generally an order of magnitude less than recorded temperature changes (e.g. Holloway, 1984). Making this assumption for Cape Point, the recorded temperature time-series is interpreted as an expression of vertical displacement.

$$\Delta z = \left(\frac{\partial T}{\partial z}\right)^{-1} \cdot \Delta T$$

4.2.1 General Features of Temporal Structure

A large variety of frequencies appear to be present. This quarter-hourly data is incapable, however, of resolving any fluctuations with a period of less than half an hour (the Nyquist period). [But shorter period fluctuations may appear as longer super-Nyquist period fluctuations. This frequency aliasing is fully discussed by Bendat and Piersol (1971)]. An abundance of activity is evident at high frequencies near to the Nyquist frequency. This high frequency signal is modulated with a tidal period (Fig. 4.3) and generally occurs on the crest of the internal tide wave, that is, in the troughs of the tidal temperature record (Fig. 4.1 and Appendices). These packets of waves, which also may occur in the trough of the tidal wave, are characteristically led by the largest wave in the packet. Following Levine, et al. (1983), the time scale of amplitude modulation indicates the period of the mesoscale features from which this high frequency energy is derived. This transfer occurs via a non-linear wave-wave interaction (McComas and Bretherton, 1977, Djordjevic and Redekopp, 1978). From a tidal perspective, this continual energy loss can be considered as a damping factor. Expecting a period of the order of half an hour and a wavelength of the order of 1 km (Section 4.1), the phase speed of these high frequency waves is of the order of 0,5 m/s which compares with the group speed of the internal tide on the inner shelf as estimated in the previous section.

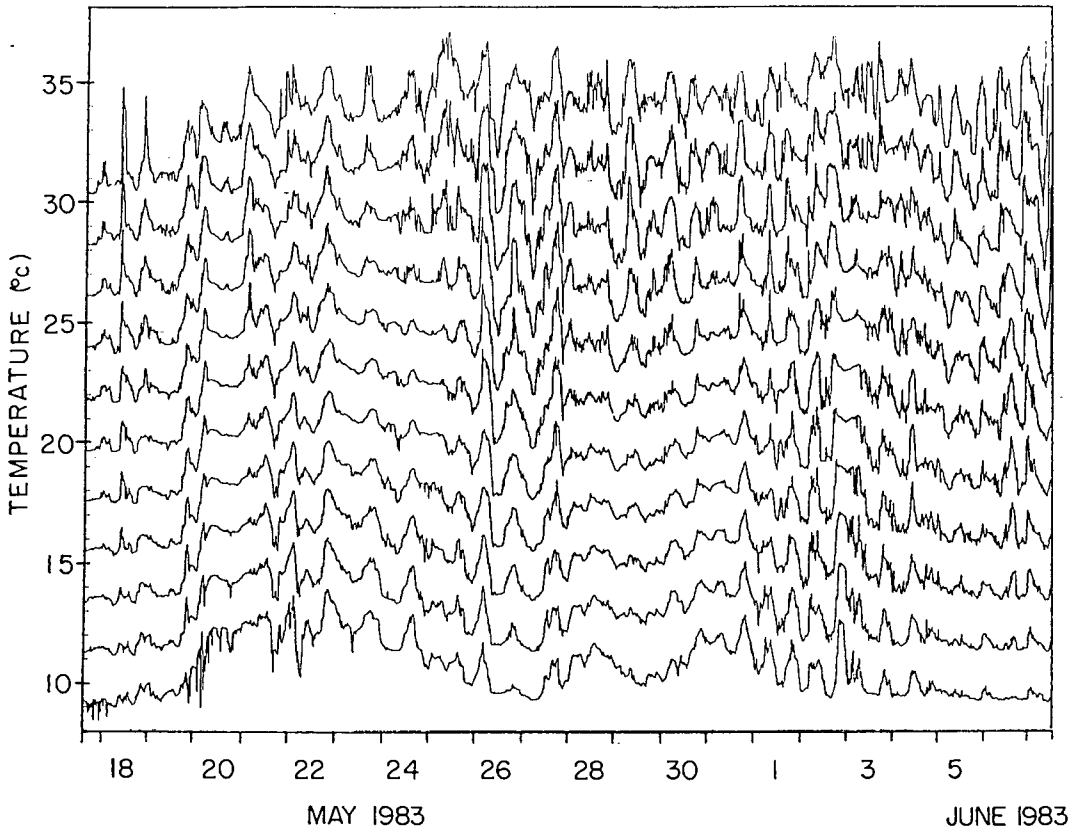

FIGURE 4.1: A parallel time-series plot of temperature. Quarter-hourly values are plotted for each thermistor over a period of about 21 days from the start of the first deployment. The full data sets are presented in the appendices. The deepest record (95 m) is plotted at its correct position relative to the vertical temperature axis. Each shallower record is off-set by 2°C upwards so that the shallowest record (55 m) overreads by 20°C (10°C is read as 30°C).

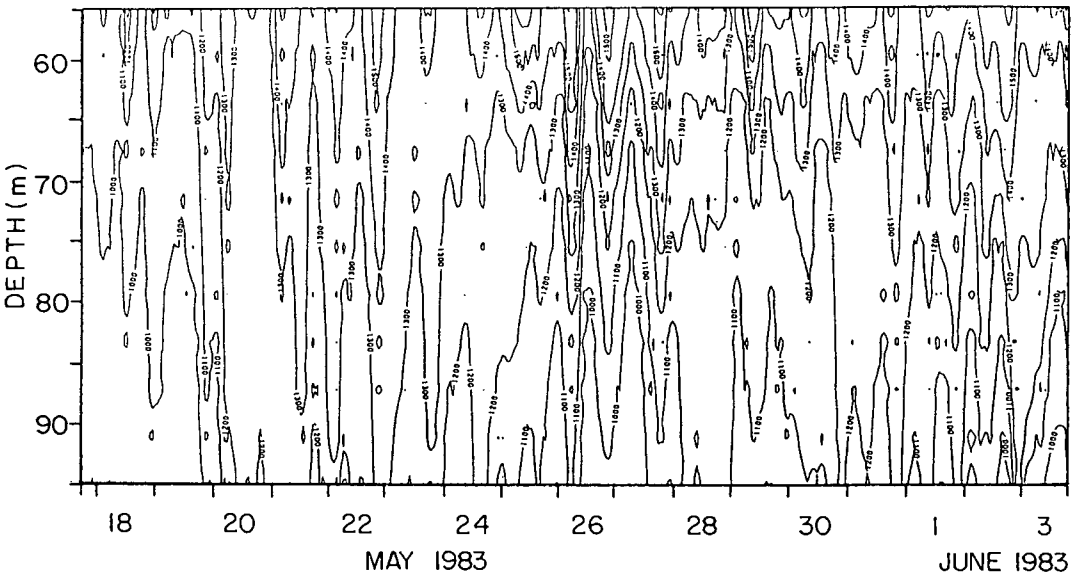

FIGURE 4.2: Isotherm depth as a function of time. The data presented in Fig. 4.1 were hourly averaged and interpolated. Treating temperature as a quasi-conservative property, the vertical migrations of these isotherms indicate the amplitude of the vertical displacemnt of water. This plot covers the first 17 days of the first deployment; the full plot is included in appendix (g).

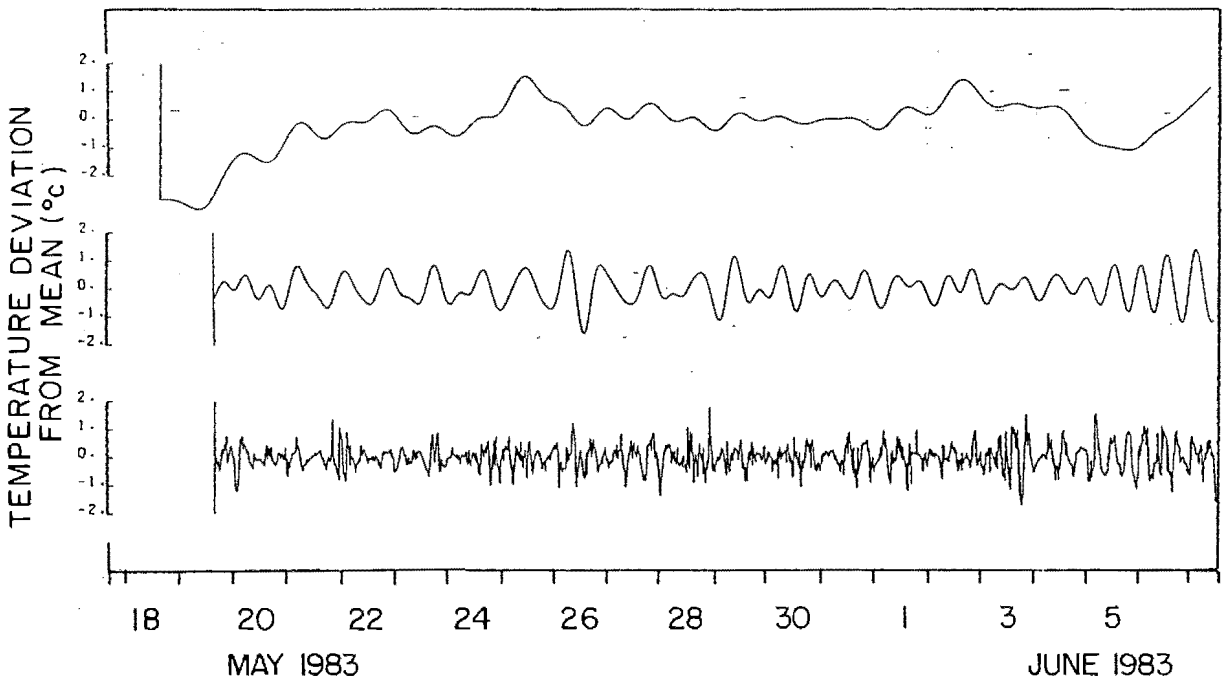

FIGURE 4.3: Filtered temperature variations for the shallowest thermistor at the start of the first deployment. Two Lanczos low-pass filters were applied: the first, with a quarter-amplitude point at 25 hr period, separated off sub-inertial fluctuations; the second, with a quarter-amplitude point at 10 hr period, separated the inertial-tidal band from the high-frequency waves. The full data sets are presented in the appendices.

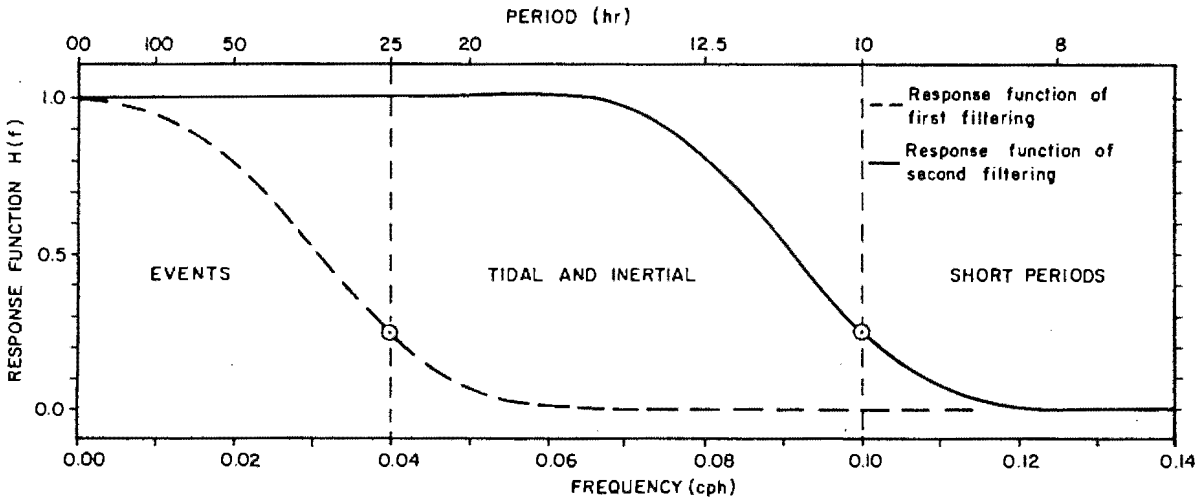

FIGURE 4.4: Response functions of Lanczos filtering in the frequency domain. Quarter-amplitude points at 0,04 cph and 0,10 cph roughly split the time-series into long-period events, tidal and inertial signals and short period signals.

Further abundant activity is evident at tidal frequency. These semi-diurnal (12,4 hr) waves are clearly described by the quarter-hourly data. They are generated at the shelf-edge (Rattray, 1960) and propagate shoreward in association with the high frequency packets described above. Temporal variations in amplitude are observed (Figs 4.1, 4.2 and 4.3). These are primarily ascribed to variations in the ambient stratification; but variations in barotropic tidal amplitudes, wave-wave interactions and dissipative processes may also affect the internal tide amplitude. The shape of the tidal temperature record is also of interest, particularly for the second deployment. In places the record displays a sinusoidal shape, as one would expect for a small-amplitude wave; in other places the trace is flat-crested and sharp-troughed, as one would expect for a finite amplitude, flat-troughed and sharp-crested wave found in the presence of a lower boundary (Le Blond and Mysak, 1978). However, even a sinusoidal wave shape may produce a strongly asymmetrical record in the presence of a sharp thermocline. Vertical displacement of well-mixed water past the thermistor produces little response, but as the thermocline moves past the fixed thermistor and back again a strong, sharp temperature response is recorded.

Internal waves of periods longer than semi-diurnal contain a decreasing component of vertical motion (Largier, 1986). In the limit $\sigma=f$, pure inertial waves consist of purely horizontal motion ($u\neq o$, $v\neq o$, $w=o$). In order that such pure inertial waves could be reflected in the temperature record, a vertical front ($\frac{\partial T}{\partial x} \neq o$ or $\frac{\partial T}{\partial y} \neq o$) would be required. In practice however, these motions usually occur at a frequency slightly higher than the inertial frequency f (Pollard, 1980) such that the small component of vertical motion (see Eq. 9 and Section 6.1.1) is sufficient to account for a temperature signal without the need for non-zero horizontal temperature gradients. Some of these signals are weakly but unmistakably present. At similar times a modulated signal, due to interference between the tidal and inertial signals, is observed. This signal has a period of 15,5 hr and a modulation period of 64 hr.

4.2.2 Specific Events

In addition to signals of internal wave frequencies, some interesting sub-inertial frequency, forced events were recorded. The thermocline, initially recorded in the season of deepening, deepened from less than 55 m in May to about 85 m in July and then shoaled to about 70 m in November (Section 4.3). As reported by Krauss (1981) for the Baltic, deepening occurred as a series of discrete events or steps, each step apparently correlating to a particular wind event.

The first such step is indicated by a general warming from 19 May to 22 May (Fig. 4.1 and Appendix (a)). The deepest thermistor records a 3°C increase from 9,0°C and the shallowest thermistor (55 m) records a 2°C increase from 10,5°C. Given a sea-surface temperature (GOSSTCOMP) of about 19°C, a thermocline must exist and at a depth less than 55 m. Before this event, a large amplitude internal tide was recorded at 55 m as a spike (from 10,5°C to about 14,5°C) in the temperature trace. The interpolated plot indicates an amplitude of well over 5 m which implies that the thermocline has a mean depth of about 45 to 50 m. Therefore, mixing across this thermocline will be recorded as a warming by the thermistors, which were all initially below the thermocline. This event appears to be caused by strong winds (maximum of 40 knots recorded at Olifantsbospunt).

The thermocline partially recovers its strength, through weak solar heating and advection, before it is hit by another strong NW wind heralding the arrival of the winter cold fronts. The thermocline, initially at about 50 m on 20 June, is eroded and deepened to 95 m or deeper on 21 and 22 June (Appendix (a), also Fig. 6.4). The temperature at the shallowest thermistor, initially above the thermocline, decreases by about 2°C whereas the temperature at the deepest thermistor, initially well below the thermocline, increases by about 3°C. For a few days an isothermal structure is recorded. The deepening takes place on 22 June, during winds at Olifantsbospunt of up to 40 knots.

Inertial period fluctuations, in the sub-thermocline layer after the event, are hinted at by the deepest thermistor. A current meter at 101 m depth clearly displays an inertial current component from 23 June to 26 June. This information strongly suggests that the thermocline breakdown occurred as a result of wind-driven velocity shear as described by Pollard (1970) and Pollard, et al. (1973); these ideas are discussed fully in Chapter 6. Following a wind event on 3 and 4 July, inertial period signals are again recorded by the thermistors. The deepest thermistor, which lags the shallowest thermistor by 3 or 4 hr, itself leads an inertial signal at the current meter by about 15 hr.

Tidal crest-to-trough heights of 30 to 40 m were recorded in this first deployment; later deployments (shorter thermistor strings) could only explicitly record wave heights of 20 m or less. These largest waves correspond to mean vertical velocities of 0,15 to 0,20 cm/s and maximum vertical velocities of up to 1 cm/s. Together with a 5 m amplitude high-frequency wave, the combined effect may temporarily displace water particles by 50 m. Vertical displacements of this magnitude have a severely deformed shape in a shallow continental shelf environment and are an unlikely occurrence.

The second thermistor string (57 m to 77 m) is mostly above the seasonal thermocline. The deployment is characterized by a quiet isothermal structure invaded from below by tidal crests which lift the thermocline to thermistor depths. These tidal fluctuations appear as asymmetrical waves in the temperature time-series. An isolated, large-amplitude tidal crest on 16 August (Fig. 4.5), suggests that internal tides are possibly better described as consecutive non-linear solitary waves rather than as a linear wave train.

An interesting event in early September (Appendix (b)) has been interpreted as follows. In response to a four-day (6 to 10 September) SE wind (10 to 30 knots), summer-type upwelling is initiated west of the Cape Peninsula (Fig. 2.3). Cold water

(<10°C) is drawn up beneath the thermistors. Simultaneously the water above the new advectively imposed thermocline is pushed up and mixed, destroying the old thermocline (originally at about 80 m). A drop of 1°C in GOSSTCOMP temperatures is paralleled by a 1°C drop (15° to 14°C) in mean temperature at all the thermistors (8 and 9 September). This is due to the mixing in of a significant amount of old sub-thermocline water. The new sharp 4°C thermocline, upwelled to about 80 m, produces a strong tidal temperature signal indicating internal tide amplitudes of 10 m and more (10 and 11 September). The new thermocline appears to have a short life, being removed by the advective input of a new quasi-isothermal water mass (12,3°C to 13,0°C). By 14 September the thermistors are again displaying weak stratification (12,5°C to 14,5°C). The initial winter-type deep thermocline (at about 80 m) is eventually restored. During this event, and elsewhere in the deployment (e.g. 22 September), there is evidence of inertial motions during the mixing processes.

The third thermistor string (64 m to 84 m) spans the decaying winter thermocline which rises from about 80 m initially to about 70 m finally. The GOSSTCOMP sea surface temperatures increase from 16°C to over 18°C over the 37 days considered. The temperatures at the shallowest thermistor are generally significantly lower than those at the surface, particularly as summer approaches. A mean temperature difference of 6°C in later November indicates the existence of a new shallower thermocline. In contrast to the previous deployment, the later part of this deployment is characterized by invasion from above by the new thermocline (similar to the first few days of the first deployment). A large tide on 24 November (Appendix (c)) produces a sharp temperature response as the tidal trough brings the thermocline into contact with the uppermost thermistor. This tide with a vertical displacement of over 30 m brings the 15°C isotherm down to 65 m. This would suggest a temperature gradient of over 3°C in the upper 45 m.

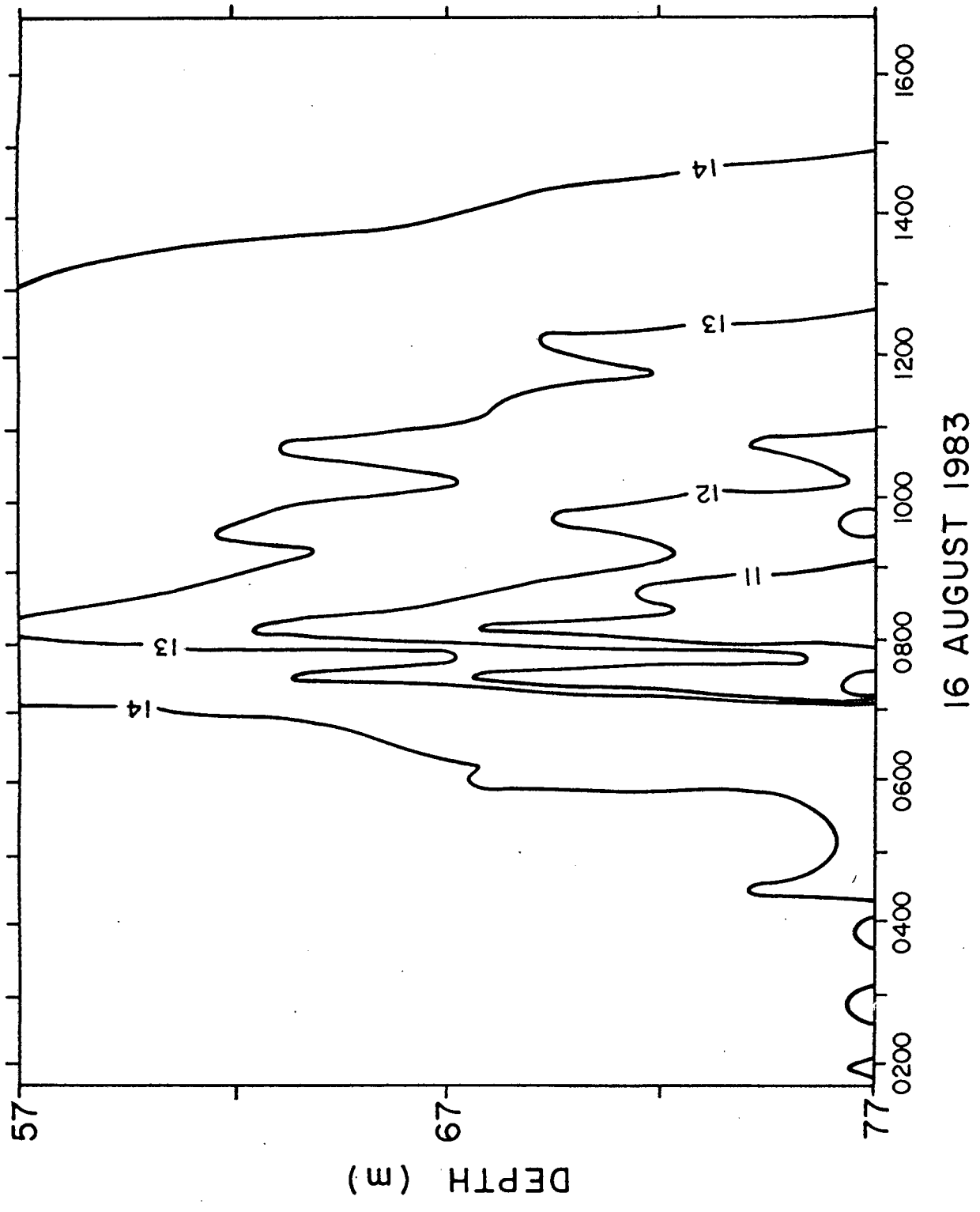

FIGURE 4.5: A solitary tidal crest with an amplitude in excess of 10 m. The isothermal mixed layer is invaded from below by the thermocline.

A burst of SE wind on 26 and 27 October generates clear inertial motions. These horizontal motions are detected in the presence of a temperature front probably created by the SE wind upwelling response. An extended SE wind (30 October to 2 November) subsequently mixes the weakly stratified layers at the thermistor depths. This is made obvious by an abundance of high frequency energy. An isothermal layer (64 m to 84 m) of 14,5°C is recorded in the tidal trough on 3 November. A 3°C temperature gradient occurs below this layer and a 2°C temperature gradient occurs between this layer and the surface. Similarly, a general temperature decrease on 6 and 7 November (Appendix (c)) implies another wind-driven mixing event. The water either side of the old thermocline is mixed together to produce this recorded decrease. But how can surface-driven dynamics be responsible for mixing across deeper stratification while shallower stratification is left intact? There are two possible answers. Firstly, the change in structure could be due to advective processes; the wind event is incidental. Alternatively, internal tides on the lower thermocline may be more susceptible to breakdown. Either alone or owing to interaction with the wind-driven motions, the tide could bring about mixing across only this deeper thermocline.

4.3 Temperature-depth Profiles

Two types of temperature-depth data are available. The first consists of continuous CTD or BT profiles collected as part of mesoscale grids. On the time and space scales of internal motions, these profiles are usually incoherent. It is impossible to determine to what extent the internal waves have transiently deformed the profile from the mean, ambient structure. The second type consists of temporally coherent profiles provided directly by the thermistor strings. Unfortunately these data are discretely sampled with depth and, further, do not extend over the full depth range.

A perusal of available CTD and BT profiles over the far western Agulhas Bank reveals a typical seasonal thermocline. Owing to the complications introduced by incessant internal wave deformations, this data set has not been analysed. All that can be

stated is that the profiles are not inconsistent with the classical shelf thermocline picture: shallow, sharp and strong in summer; eroded in autumn; deep, gradual and weak in winter; recover in spring.

Expecting the first mode structure to dominate (Chapters 2 and 5), the thermistor string profiles can be manipulated in order to provide an accurate indication of the mean thermocline depth. In conjunction with this, an idea of the thermocline shape is obtained from an inspection of a number of individual profiles. First mode internal waves have a maximum vertical displacement at the thermocline. Given also that the temperature gradients at the thermocline are sharpest, the mean thermocline depth will be unequivocally marked by the depth of the time-series with the maximum variance. A sample mean temperature profile over the same chosen period produces a smoothed indication of the absolute temperatures involved. A corollary of the above variance argument is that if the second, or any other, mode were dominant over the chosen period, then the profile of variance would display or attempt to display two, or more, peak values. This would be dependent on the ambient thermocline depth being sufficiently constant. The following variance profiles provide evidence of first mode dominance. This dominance is also obvious from a visual inspection of the combined time-series plots (for example, Fig. 4.1). All temperature fluctuations on an internal wave time scale appear to be in phase; higher modes would be characterized by phase reversals across or adjacent to the thermocline.

Variance profiles have been plotted (Fig. 4.6) for the first two-thirds (17 May to 20 June) and last third (23 June to 7 July) of the first deployment, the full second deployment (10 August to 28 September) and the full third deployment (20 October to 26 November). The two profiles for the first deployment describe the mean structure before and after the major storm which deepened the mixed layer between 20 and 23 June. Altogether the four profiles roughly indicate how the thermocline, initially above 55 m, deepens to over 95 m during June, remains at depth during winter and recovers to about 50 m, during spring.

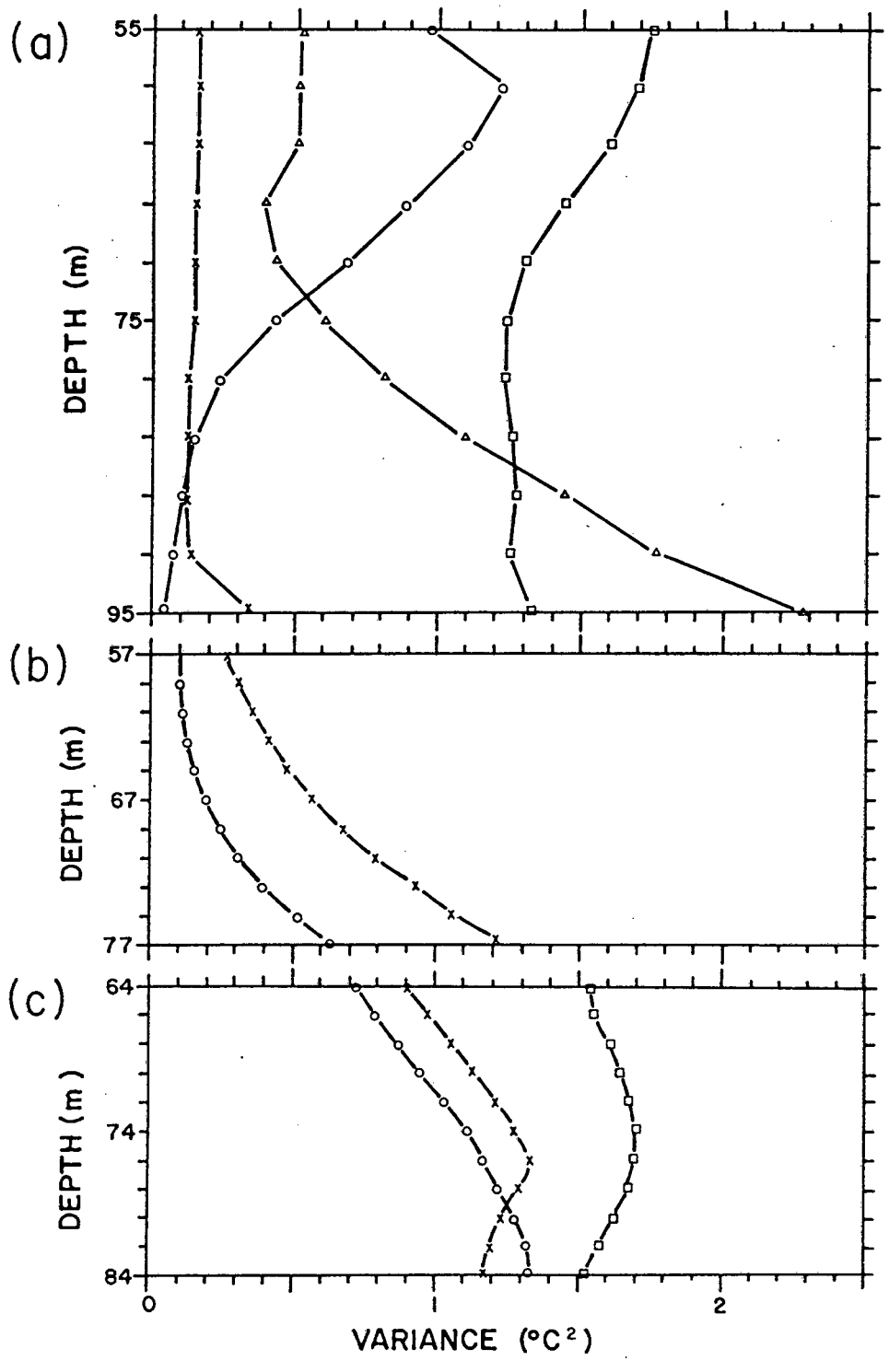

FIGURE 4.6: Variance of temperature records plotted as a function of depth. (a) First deployment: □——□ time steps 3-3302 (preceding June storm), △———△ time steps 3501-4892 (following June storm), o——o time steps 2800-3200 (immediately preceding June storm), X——X time steps 3501-3900 (immediately following June storm). (b) Second deployment: X———X time steps 3-4624 (complete record), o——o time steps 3-2702 (preceding September south-easter event). (c) Third deployment: □——□ time steps 3-3568 (complete record), X——X time steps 3-1002 (preceding storm at end October), o——o time steps 1301-2700 (following October event, preceding November event).

For more accurate determination of thermocline depth, it is advisable to consider shorter periods (Fig. 4.6). Low frequency temperature fluctuations, which also contribute to the variance, may provide a false impression of internal wave vertical structure. The variances of the deepest five time-series during the period 17 May to 20 June are falsely enhanced by a significant low frequency signal at that depth. It is preferable to consider, for example, the four days preceding the June storm. The variance plot for this period (Fig. 4.6) is a true and more definite indication of the ambient thermocline depth. Ideally this exercise should be performed on a period short enough that the ambient thermocline depth remains fairly constant. Taking a longer period, which includes changes in the ambient thermocline depth, will result in a broad, diffuse indication of an average depth. For example, the variance plot for the 37 day-period from 20 October to 26 November is characteristically smooth such that it can only be concluded that the ambient thermocline had a mean depth between about 70 and 80 m. In contrast, the variance plot for 20 to 31 October indicates a thermocline consistently found around 76 m. In a sense the depth, at which peak variance occurs, indicates the mean thermocline depth and the sharpness, of the variance profile, indicates the standard deviation of the suggested mean.

In summary, these profiles provide good evidence in support of the allegation that the first mode is dominant. Further, they are effective, as anticipated, in determining the low frequency variation in thermocline depth. Initially at about 45 m, the thermocline is deepened to below 60 m at the end of May. The major NW storm in late June deepens it further from about 60 m to deeper than 95 m (Fig. 4.6). The variance profile for 23 to 26 June displays isothermal character with a hint of thermocline activity below the deepest thermistor. The profile for 23 June to 7 July indicates a restoration of the thermocline. The combined time-series plots suggest that the thermocline is at about 80 m during the last days of the first deployment. This is consistent with the variance profile for the stable second

deployment. The thermocline depth of about 76 m for 20 to 31 October (Fig. 4.6) increases beyond 84 m during 3 to 17 November (Fig. 4.6) and decreases again before the end of the third deployment.

4.4 Spectral Analysis

4.4.1 The Technique

In order to investigate the spectral structure of the temperature signal, the data are manipulated with a spectral analysis technique. Three such techniques are now well-known: autocorrelation, fast Fourier transform and maximum entropy. Autocorrelation, although the oldest and most basic technique, was used because it is more immediately understandable, more instructional and therefore easier to program and debug. A further advantage is its robustness against round-off errors (Yuen, 1979). Ultimately, the method was justified through its results which clearly indicate all the essential spectral features of the data.

Having inspected the time-series, it is obvious that the data is largely deterministic with a small random contribution. However, sufficient components are present that the total signal may be considered as a sample function of a pseudo-random process. Further, the data are assumed to be ergodic. It is also necessary that the data are stationary, or time invariant. This is shown to be the case in that the statistical properties, computed over sub-intervals, do not vary 'significantly' from one interval to the next; that is, the same 'type' of data is being dealt with throughout each analysis.

The following short description of the method is fully covered in any major text on time-series analysis (e.g. Bendat and Piersol, 1971). The data are initally demeaned and detrended (in this study, however, no evidence could be found for a component of period longer than the record length and consequently no trend was removed). The spectral functions, continuous integrals over the full record, are approximated by

summations for discretely-sampled data. The auto-correlation function calculates the correlation between two versions of the same data, the one separated from the other by a specified time lag. For discretely-sampled data, auto-correlation estimates $\hat{R}_m$ can be calculated only for time lags $\tau = m \cdot \Delta t$ where Δt is the sampling interval (15 minutes) and m is an integer.

$$\hat{R}_m = \frac{1}{N-m} \sum_{n=1}^{N-m} T_n \cdot T_{n+m} \qquad (20)$$

where T_n is the temperature after n time steps
N is the total number of time steps.

Each such value estimates the dependence of the temperature at one time on the temperature at the other time. For a monochromatic signal of period $m \cdot \Delta t$, the estimate will take a value equal to the mean square temperature of the record. In real data, periodic signals will be indicated by enhanced auto-correlation estimates.

The Fourier transform of this auto-correlation function, the autospectral density function, describes the frequency composition of the data. From this two-sided function, a one-sided power spectral density (PSD) function is obtained as a function of frequency. An estimate of the PSD function $\hat{G}_\ell$ is obtained for discretely-sampled data,

$$\hat{G}_\ell = 2 \cdot \Delta t \left[\hat{R}_o + 2 \sum_{m=1}^{M-1} \hat{R}_m \cos \frac{\pi m \ell}{M} + \hat{R}_M \cos M\pi \right] \qquad (21)$$

where $\ell = 0,1,2,\ldots,M$
$M \cdot \Delta t$ is the maximum period investigated.

This is plotted against values of frequency $\sigma_\ell = \frac{\ell}{2M \cdot \Delta t}$; each estimate $\hat{G}_\ell$ describing the intensity of the data in a frequency band $\Delta\sigma = \frac{1}{2M \cdot \Delta t}$. A time step Δt thus only allows resolution of components below the Nyquist or folding frequency $\sigma_c = \frac{1}{2 \cdot \Delta t}$

(in this study σ_c = 2cph). As mentioned in Section 4.2, some of the energy at higher frequencies ($2n\sigma_c \pm \sigma$), where n = 1,2,3,..., will be aliased (folded) so that it is added to the power spectral density estimate for $\sigma \leq \sigma_c$.

A plot of these raw PSD estimates proves to have very erratic fluctuations. It is necessary to apply a 'lag window' in the time domain or the equivalent 'frequency window' in the frequency domain. The boxcar function, applied by default in obtaining the raw PSD estimates, weights the autocorrelation estimates as follows:

$$W_m = 1 \qquad \text{for} \quad m = 0,1,2...,M$$
$$= 0 \qquad \text{for} \quad m<0, m>M.$$

The sudden cut-off at m = 0 and m = M causes 'leakage' by spreading the peaks of the PSD function and by adding an infinite number of side lobes for each peak. In preference to this, the Hanning window was applied (Bendat and Piersol, 1971) and the autocorrelation estimates are weighted:

$$W_m = \frac{1}{2}\left(1 + \cos\frac{\pi m}{M}\right) \qquad \text{for } m = 0,1,2,...,M \qquad (22)$$
$$= 0 \qquad \text{for } m>M.$$

This is equivalent to a frequency smoothing of the raw estimates $\hat{G}_\ell$ to give smoothed estimates G_ℓ:

$$G_o = \frac{1}{2}\hat{G}_o + \frac{1}{2}\hat{G}_1$$
$$G_\ell = \frac{1}{4}\hat{G}_{\ell-1} + \frac{1}{2}\hat{G}_\ell + \frac{1}{4}\hat{G}_{\ell+1} \qquad (23)$$
$$G_m = \frac{1}{2}\hat{G}_{M-1} + \frac{1}{2}\hat{G}_M$$

The continuous frequency window functions for the box-car and Hanning procedures are compared in Fig. 4.7. Although the main lobe has spread out, the side lobes have been decreased significantly. For a unit PSD estimate at the tidal frequency (0,081 cph), the negative lobes occur with a magnitude of 0,024

at 0,068 cph and 0,093 cph and the positive lobes occur with a magnitude of 0,008 at 0,063 cph and 0,098 cph. This windowing results in a smaller confidence interval (more reliable estimates) but a poorer frequency resolution.

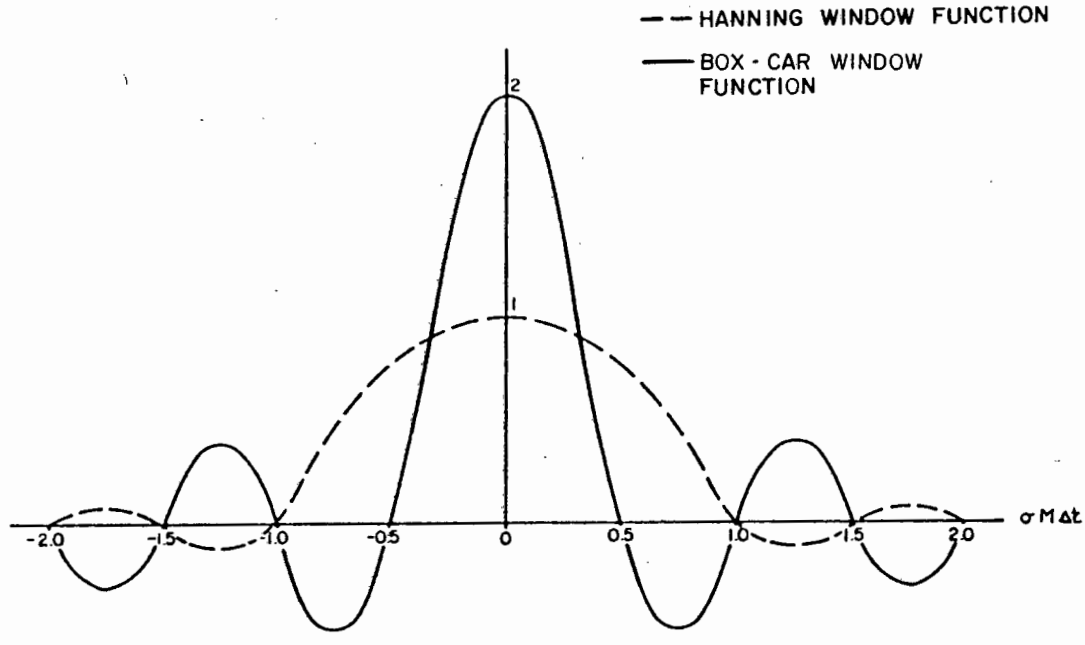

FIGURE 4.7: Box-car and Hanning window functions [from Bendat and Piersol, 1971].

Various parameters are defined in order to describe the spectrum. The bandwidth $B_e = \frac{1}{M \cdot \Delta t} = 2\Delta\sigma$ gives the frequency resolution. The degrees of freedom are given by $\nu_f = \frac{2N}{M}$. The maximum lag number M = 400 is chosen to be roughly 0,1 N for each of the three deployments. The bandwidth is thus 0,01 cph and there are about 20 degrees of freedom. The confidence intervals are given by Jenkins and Watts (1968) for a known number of degrees of freedom. These multiplicative factors can be represented by a constant length on log-log spectral plots. A 99% confidence interval means that there is a 99% chance that the true value will fall within the indicated interval from the estimate.

Further frequency smoothing was sometimes applied in order to remove the jaggedness of the high frequency spectrum. A bell-shaped cosine function was chosen

$$g_j = \frac{1}{2}\left(1 + \cos\frac{\pi j}{J}\right) \qquad j = 0,1,\ldots,J$$

such that a well-smoothed estimate

$$\bar{G}_\ell = g_o\, G_\ell + \sum_{j=1}^{J} g_j \left(G_{\ell-j} + G_{\ell+j}\right) \tag{24}$$

is obtained. This results in increased confidence (increased $\nu_f = \frac{2JN}{M}$) but decreased resolution, $B_e = \frac{J}{M \cdot \Delta t}$.

4.4.2 General Features of Spectral Structure

A lot of the information extracted by this method is the same as that discovered in Section 4.2.1 (General features of temporal structure), except that this analysis is more quantitative and is presented in the frequency domain.

Choosing M = 400 is a trade-off between decreased bandwidth and increased degrees of freedom. The Hanning window is applied to data with N~4000 and Δt = 15 min. This gives a frequency resolution of 0,01 cph and a 95% confidence interval extending from 0,63 to 2,0. The lowest frequency estimate is at 0,005 cph ($8^1/_3$ day period) and the cut-off frequency is 2,0 cph ($^1/_2$ hour period).

In all of the spectra a shoulder rises at sub-inertial frequencies due to the events described in Section 4.2.2. This energy is particularly obvious in the filtered time-series (Fig. 4.3). Although the spectral structure at frequencies well outside of the internal wave band is not of importance to this thesis, it is necessary to briefly investigate the possibility of a diurnal signal in the temperature record. As already shown in Section 2.2 (Eq. 6), free diurnal internal tides do not exist polewards of 30° latitude. Diurnal barotropic tides, although

significant off southern Africa (Schumann and Perrins, 1982) provide negligible vertical displacement of the thermocline (of the order of 0,1 m). Internal Kelvin waves, which may exist at the diurnal frequency, are trapped against the coast with an offshore e-folding length of the order of 5 km. These waves would need to have exceptional amplitudes in order to be significant at the Cape Point mooring and over the bulk of the continental shelf. This is unlikely since no obvious diurnal forcing exists in the absence of large, longshore topographic steps. Internal Kelvin waves are generally associated with coastal upwelling (Gill, 1982) and they have much smaller frequencies.

The spectra (Figs 4.8, 4.10 and 4.11) confirm this absence of a strong diurnal temperature signal. A broad peak around the near-inertial frequency is clearly centred on the spectral value for ℓ=10 (σ = 0,87 × 10^{-4} s^{-1}) and falls off sharply towards the spectral value for ℓ=8 (σ = 0,70 × 10^{-4} s^{-1}). Separated by a bandwidth (B_e = 0,17 × 10^{-4} s^{-1}), the near-inertial signal (σ~0,88 × 10^{-4} s^{-1}) is distinct and much more energetic than the combined diurnal signals (σ~0,70 × 10^{-4} s^{-1} to 0,73 × 10^{-4} s^{-1}). Following from the above, diurnal dynamics contribute negligibly to current shear across the thermocline; consequently they are considered no further and discussion is focussed on the internal wave spectrum.

Within the internal wave frequency band, the log-log spectral plot is expected to approximate a line of constant lope (Garrett and Munk, 1972). This is as a result of energy saturation and a

continual energy cascade. Garrett and Munk (1975) suggest a slope of about -2. On the shelf, in the near-field of a variety of internal wave sources, one does not expect a spectrum to take such an ideal shape. Significant deviations may be ascribed to particular sources (or sinks) of energy in the internal wave field. Three peaks seem common to all the data.

(1) An inertial peak is found close to the expected frequency (Pollard, 1980), which is about 5% greater than f~0,047 cph (at latitude 34° 30'S). The precise frequency of this peak is poorly resolved due to large bandwidth at lower frequencies. The size of the peak depends on the number and intensity of effective wind events during the period analysed.

(2) A semi-diurnal tidal peak is found centred at about 0,08 cph. As expected from the time-series plots, this usually dominates the spectrum. Apart from poor frequency resolution, this peak is spread further by Doppler shifts. An ambient current of 0,1 m/s enables the 0,081 cph wave to be recorded at frequencies between 0,066 cph and 0,095 cph. It is not possible to resolve the exact tidal frequency.

(3) A shoulder at high frequencies near the Nyquist frequency is elucidated by application of the second smoothing procedure with J = 8. It is not possible to ascertain to what extent this shoulder is due to the expected cusp at the buoyancy frequency (Levine, 1983). The non-linear dissipative process desribed in Section 4.2.1 appears to account for this broad band feature. The frequencies reported in other studies (Brekhovskikh, et al., 1975; Curtin and Mooers, 1975; Osborn and Burch, 1981; Apel, 1981) suggest that this energy, apparent between 1,4 cph and 2,0 cph, is actually folded from super-Nyquist frequencies (eg. between 2,0 cph and 2,6 cph).

4.4.3 Interpretation of Particular Spectra

The eleven spectra from the first deployment are plotted in Fig. 4.8 on a common log-log set of axes (spectral density $^{o}C^{2}\cdot hr$ as a function of frequency cph). The lowest spectrum, corresponding to the deepest thermistor, is correctly placed with respect to the vertical axis. The shallower spectra are each displaced upwards by 1,0 on the log-axis so that the shallowest spectrum overreads by 10^{10} times the correct value.

A constant slope of -2,0±0,1 seems to be representative of the internal wave dynamics during this deployment. The sub-inertial frequency events have more active temperature records at depth (refer to Section 4.2.2 and Fig. 4.6). The inertial peak, found at 0,05±0,005 cph, is significant at 95% confidence. A slight decrease in spectral density is found at the middle thermistors. The tidal peak, found at 0,08±0,005 cph, is significant at 99% confidence. The amplitude of the tidal peaks are plotted against depth in Fig. 4.9. Expecting the variation with depth to be exclusively due to stratification, this provides a clear estimate of the mean thermocline depth and strength (as discussed in Section 4.3). This can be compared to the profiles of Fig. 4.6, which are contaminated by the inclusion of other frequencies. The shoulder at high frequency (1,5 to 2,0 cph) is significant at 95% confidence. The estimate of excess energy contained in this band is strongly sensitive to the choice of a straight-line fit.

In the uppermost 9 thermistor records there is some consistent indication of the modulated signal (0,065) due to interference of inertial and tidal signals. Side lobes of the tidal peak may appear towards the lower energy high-frequency side of the spectrum. A bump at about 0,143 cph is possibly one such lobe or alternatively due to non-linearities in the internal tide generation. In order to investigate stationarity, the temperature record from the 75 m thermistor of this first deployment was split into four separate sub-intervals (n = 1 to 2048, n = 901 to 2948, n = 1801 to 3838, n = 2701 to 4748). Insofar

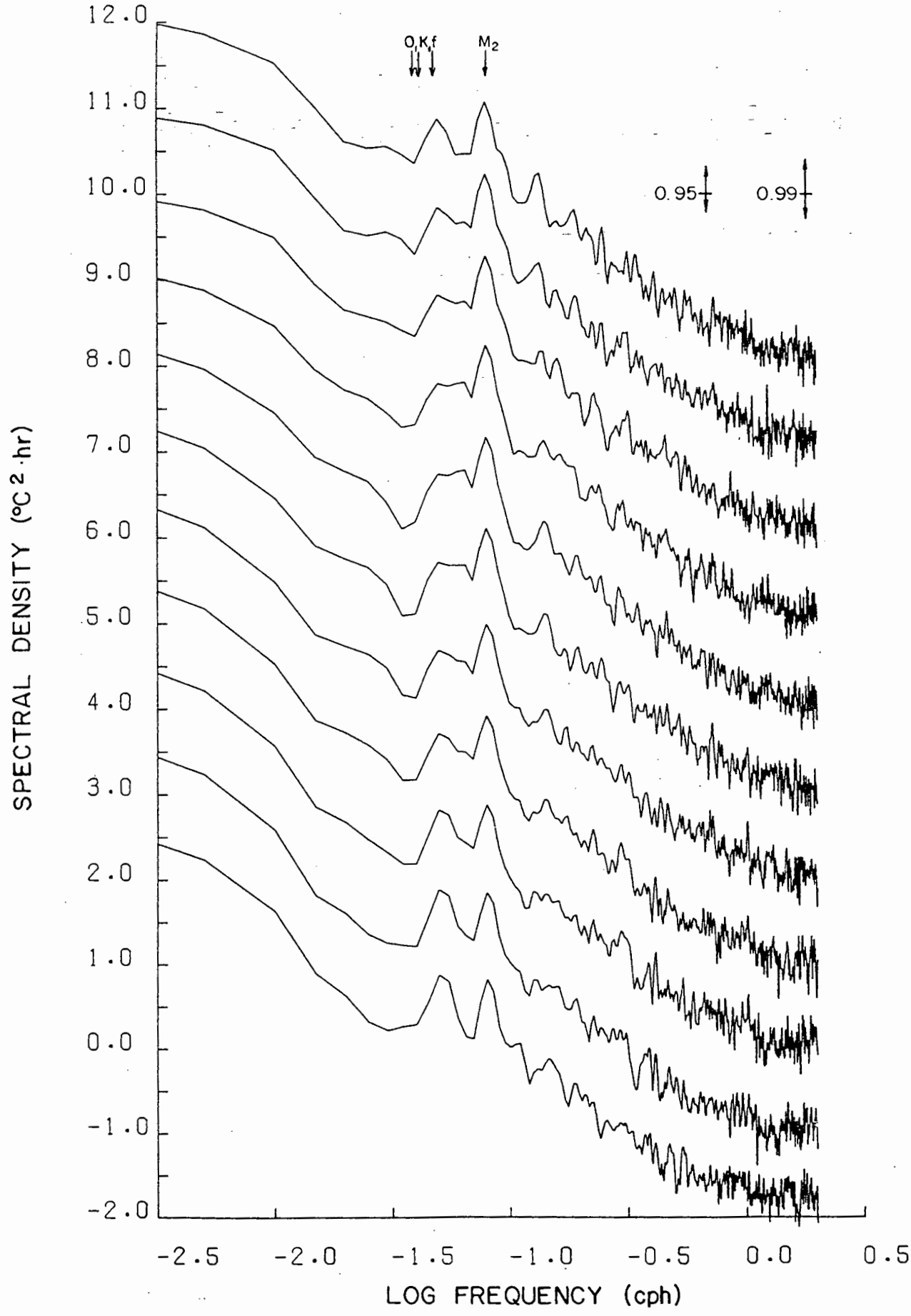

FIGURE 4.8: Spectra for the eleven records of the first deployment. The deepest record is correct relative to the vertical axis; the shallower records each overread by a single unit on the vertical log-axis. The 95% and 99% confidence intervals are shown in the upper right-hand corner. The bandwidth is 0,01 cph.

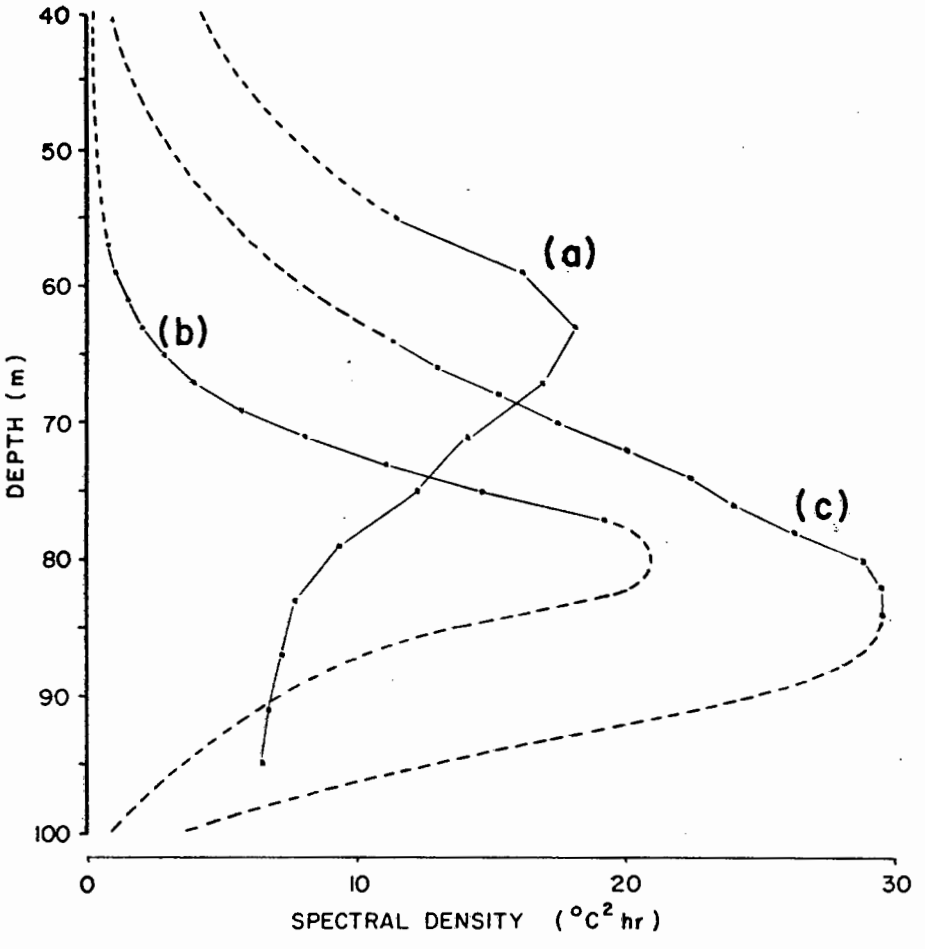

FIGURE 4.9: Plot of the size of the spectral peak, at the tidal frequency, as a function of depth. Extrapolated as would be expected for a first mode wave, the thermocline depth is indicated. Compare with Fig. 4.6. (a) First deployment (b) Second deployment (c) Third deployment.

as the data displayed a common slope, a high-frequency shoulder, a tidal peak and a low-frequency shoulder, the data are considered stationary. Nevertheless there are variations, particularly in the wind-driven low-frequency and inertial wave energy.

The eleven spectra obtained from the second deployment, are plotted in Fig. 4.10. The saturated spectrum appears to have more high-frequency energy and less low-frequency energy with a linear slop of -1,7±0,2. This whitening of the spectrum is also reported by Pinkel (1981) for oceanic spectra nearer the surface. The proximity of the surface, turning depths or bottom have a greater damping effect on larger-scaled waves. The tidal peak, significant at 99%, increases dramatically with depth (Fig. 4.9). The inertial peak, although weak, is confirmed by its consistent presence at all depths. The high-frequency shoulder is significant at 99% confidence.

The multiple-spectra plot for the third deployment approximates a line with a slope of -1,9±0,1 (Fig. 4.11). The inertial and tidal peaks are both significant at 99% confidence. The profile of the tidal spectral density function is included in Fig. 4.9. The high-frequency shoulder is only significant at 95% confidence for this period.

4.5 Empirical Orthogonal Function Analysis

In the way that spectral analysis (Section 4.4) provided a quantitative confirmation of the discussion of temporal structure (Section 4.2) so empirical orthogonal function analysis (or principal components analysis) is applied in this section in order to provide a quantitative confirmation of the discussion of vertical structure (Section 4.3). But this statistical procedure is applied objectively to the data - no pre-determined curve fitting or hypothesis proposals are required. The data from each deployment are separated into orthogonal spatial and temporal eigen-functions ranked according to their contribution to the total variance (Aubrey and Emery, 1983). If the first few eigen-functions alone account for the vast majority of the variance, then the lesser components may be neglected and the effective dimensionality of the system is reduced. These principal components are subjectively studied to determine whether they have a physical analogue or interpretation which

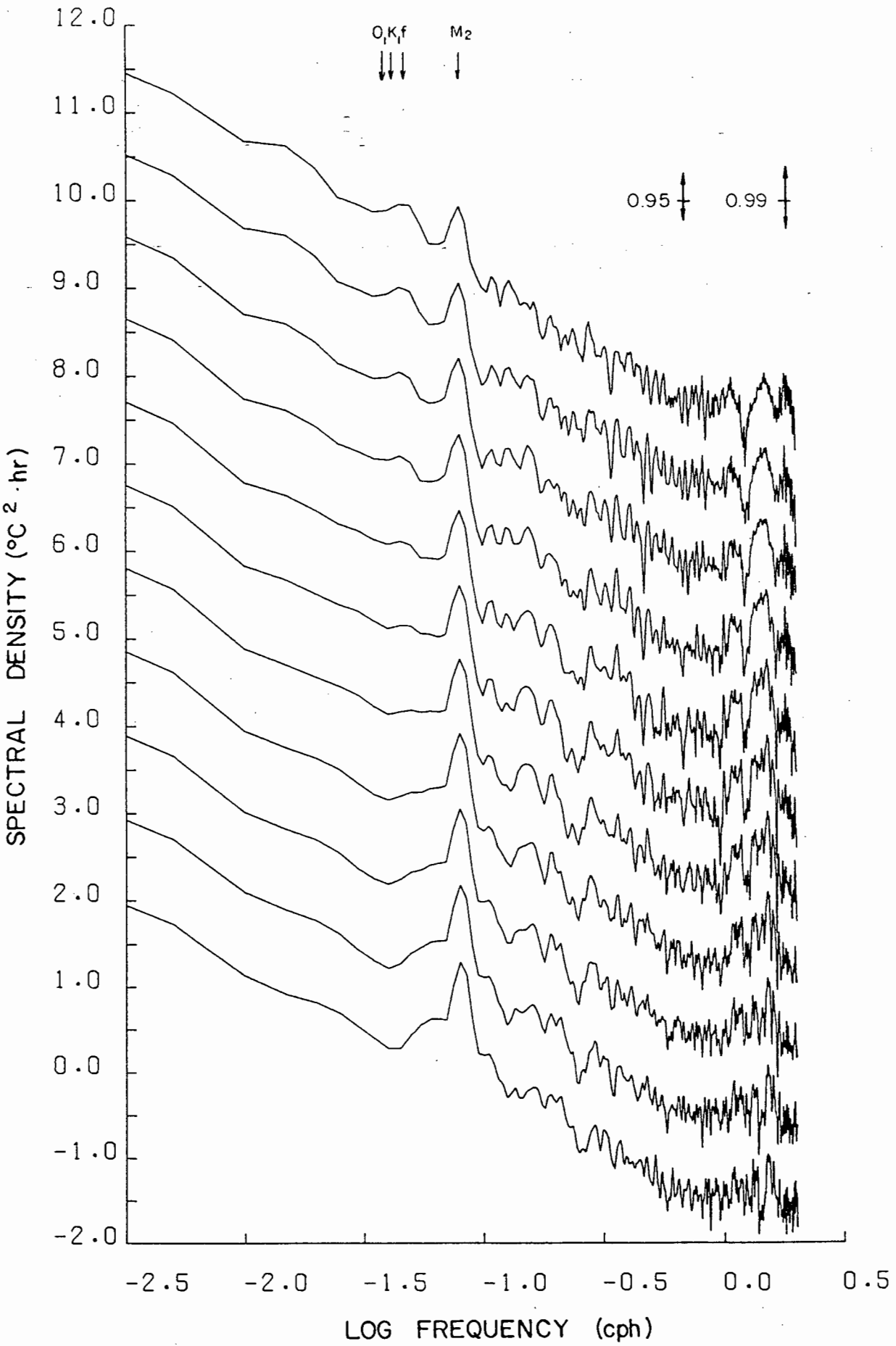

FIGURE 4.10: Spectra for the eleven records of the second deployment. The deepest record is correct relative to the vertical axis; the shallower records each overread by a single unit on the vertical log-axis. The 95% and 99% confidence intervals are shown in the upper right-hand corner. The bandwidth is 0,01 cph.

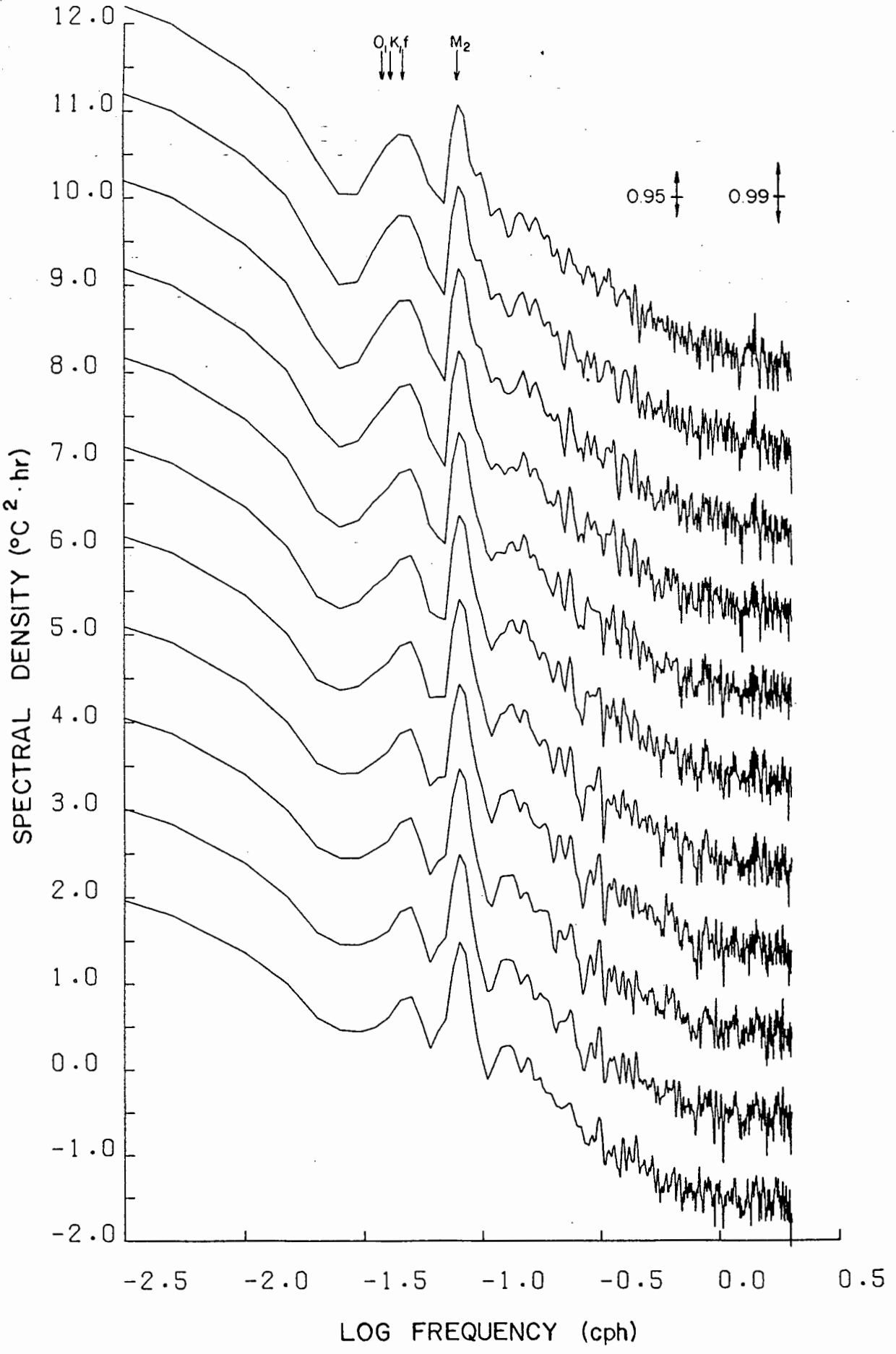

FIGURE 4.11: Spectra for the eleven records of the third deployment. The deepest record is correct relative to the vertical axis; the shallower records each overread by a single unit on the vertical log-axis. The 95% and 99% confidence intervals are shown in the upper right-hand corner. The bandwidth is 0,01 cph.

may provide an insight to the dominant forcing of the real system. Such an interpretation may not exist or, if it exists, may not be taken as proof of any causality within the system.

4.5.1 The Technique

The data were collected simultaneously from eleven vertically separated thermistors at N temporally separated instants. The original time-series T are demeaned and linearly combined to create new combinational time-series ϕ

$$\phi_{q_n} = \sum_{p=1}^{11} f_{qp} \, (T_{p_n} - \bar{T}_p) \qquad (25)$$

where f_{qp} is the weighting applied to original time-series T_p when calculating new time-series ϕ_q,

T_{p_n} is the temperature after n time steps.

$\bar{T}$ is the mean temperature of time-series T_p

The weights are chosen such that, for each q,

$$\sum_{p=1}^{11} f_{qp}^2 = 1 \qquad (26)$$

These new time-series are designed to be orthogonal and in an order such that the variance of each is maximized consecutively (Browne, 1983). This is done by maximizing an objective function which describes the variance and contains the restriction on f_{qp}. The following eigen-value problem provides the optimal solution:

$$\sum_{p=1}^{11} f_p \, C_{kp} - \lambda \, f_k = 0$$

where k = 1,2,...,11.

This is also written in matrix form

$$\underline{C}\,\underline{f} - \lambda\,\underline{f} = 0 \qquad (27)$$

where $\underline{C}$ is the symmetric covariance matrix
$\underline{f}$ is the weighting vector
λ is the eigenvalue.

There are eleven distinct eigen-solutions (λ_q, $\underline{f}_q$) corresponding to eleven new time-series.

Towards this end, the original data are demeaned and an 11 × 11 covariance matrix is constructed. Solution of Eq. 27 yields eleven orthogonal eigen-solutions such that λ_q describe the variances, $\underline{f}_q$ describe the orthonormal vertical structures and the new time-series ϕ_q are uncorrelated. The total variance, although conserved

$$\sum_{q=1}^{11} \lambda_q = \sum_{p=1}^{11} C_{pp},$$

is reallocated such that the first eigen-solutions contain nearly all the information. The variance, which describes the mean square value of the demeaned time-series, is a measure of the potential energy of the internal wave field (refer to Section 4.6).

This exploratory procedure helps one to discover trends or relationships in the data. It is invaluable in determining which time-series may be redundant, dependent or predictive and can also help one to detect 'bad' data (that is, data which is consistently uncharacteristic). However, only linear trends will be revealed because the procedure is linear.

The analysis delineates clusters of time-series over which variation is coherent. For the first component, all eleven records fall into a single mutually coherent cluster. In retrospect, this is expected since the original time-series plots (Fig. 4.1) appear strongly positively correlated. The

second component consists of two clusters over which variation is coherent, and so it continues till the eleventh component. The shapes of these vertical structures (as given by $\underline{f_q}$) are reminiscent of the physical eigen-modes which describe the vertical dependence of an internal wave. If this is a valid interpretation, then this analysis provides support for the expectation that lower modes are more important over the continental shelf (Chapter 1). Huthnance and Baines (1982) interpreted an empirical orthogonal analysis in the same way.

Alternatively, if this procedure split the variance between components in either the temporal or horizontal domains, then one would expect the first component to provide a simple band-filtered plot of the internal tide (which has been shown to be the most energetic signal). This is not the case.

4.5.2 Application and Interpretation

The technique described above was applied to the whole or part of the data set from each deployment. The percentage contributions to variance are plotted for the eigen-solutions for each deployment (Fig. 4.12).

Because of the strong mixing event 20 to 23 June (Section 4.2.2), only the first 3 300 time steps of the first deployment were analysed. The first three components account for 69%, 24% and 4%, respectively, of the variance. The eigenvector structures, plotted in Fig. 4.13, suggest that the first principal component PC1 is composed largely of mode 1, PC2 of mode 2 and PC3 of mode 3. The phase of PC2 changes at about the same depth as the maxima of PC1 and PC3; this is the pattern for the first three modes, given a thermocline at that depth. However, the thermocline may migrate vertically such that for a thermocline shallower than 55 m or deeper than 95 m, a second mode wave would be viewed as a first mode wave (all thermistor records in phase). This is a rare occurrence for the first deployment.

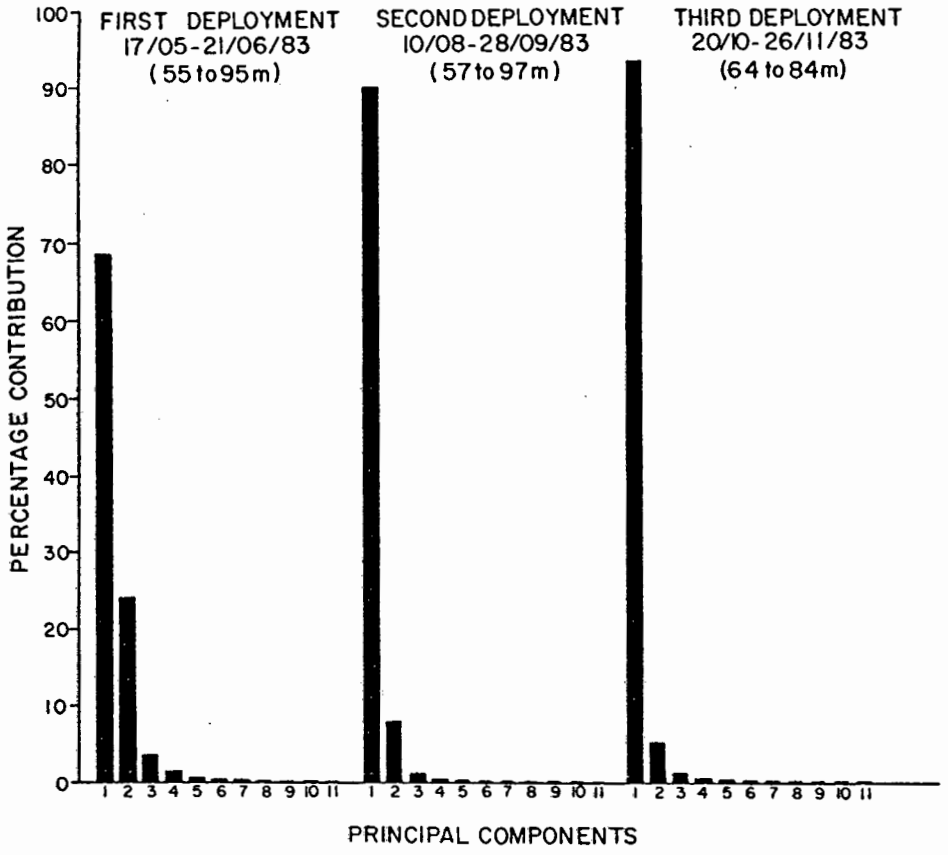

FIGURE 4.12: Bar chart displaying the percentage contribution of each principal component to the total variance.

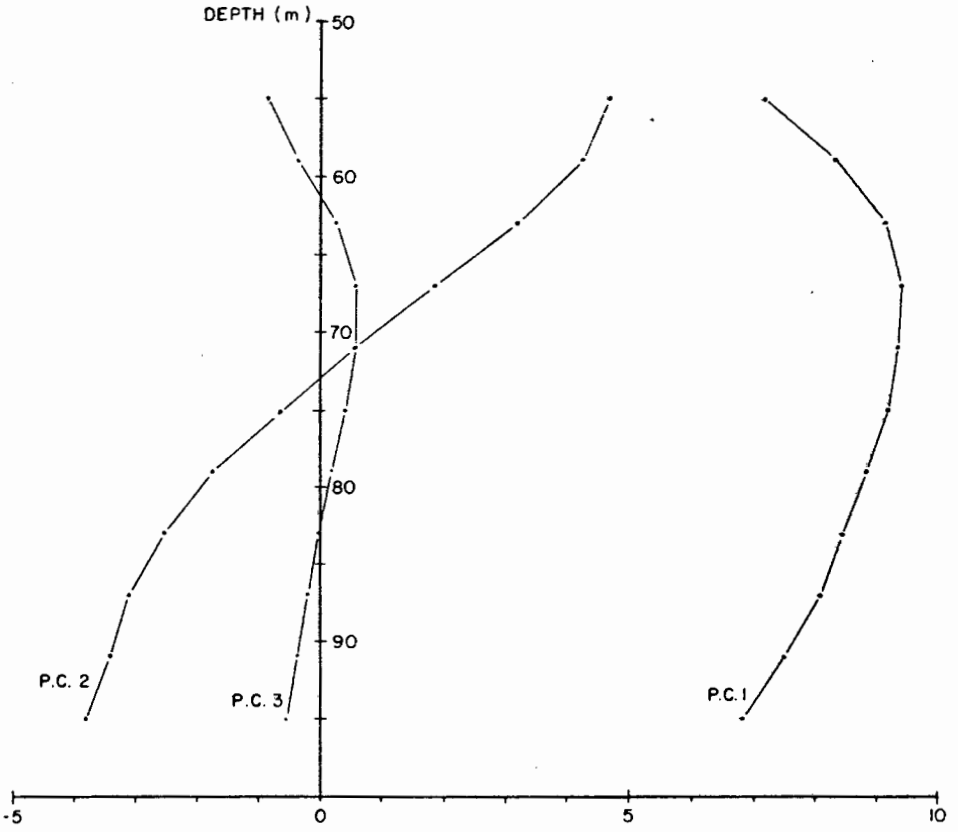

FIGURE 4.13: Plots of the three principal depth eigen-vectors for the first 3 300 time steps of the first deployment (i.e. preceding the major June storm). The shape and relative sizes are important.

The above interpretation is further supported by a spectral analysis of the first and second new combinational time-series. The first component has a large tidal peak and negligible inertial energy. The second component has relatively less tidal energy, much more inertial energy and large low-frequency energy. Both inertial energy and low-frequency events have temperature signals which change phase across the thermocline (Chapter 6). The first component (PC1) is probably due to the first mode alone.

The second deployment is equally interesting. The full records are analysed and the first three components account for 90%, 8% and 1%, respectively. Caution must be shown in interpreting the structures which are plotted in Fig. 4.14. From Section 4.3 it is clear that the thermocline is below the thermistors. Consequently, mode 2 produces a correlated signal over all 11 thermistors and contributes its energy to PC1. Likewise, both modes 3 and 4 produce a signal with the shallower thermistors out of phase with the deeper thermistors (PC2). And so it continues for higher modes. A contrived sketch of anticipated modal structures for this deep thermocline are shown diagrammatically to combine to give the same shapes and relative sizes as do the principal components (Fig. 4.15).

The above discussion is a bit idealized because the thermocline, assumed to be continually below 77 m, is not at rest. If the thermocline is raised above 77 m (by a tide or an event), then second mode fluctuations will change phase above the deepest thermistor at 77 m. Their energy will be contributed to PC2. The opposite (mode 3 contributes to PC1) may also happen, but to a lesser degree. Therefore the principal components, which are expressions of the energy of mono-polar or bi-polar vertical dynamics, are sums of the contributions to their particular dynamics irrespective of mode. For a thermistor string long compared to the mean thermocline displacement, one can tentatively relate certain modes to certain components. A string spanning the full depth will have the principal modes unequivocally related to the principal components, in a one to one correspondence.

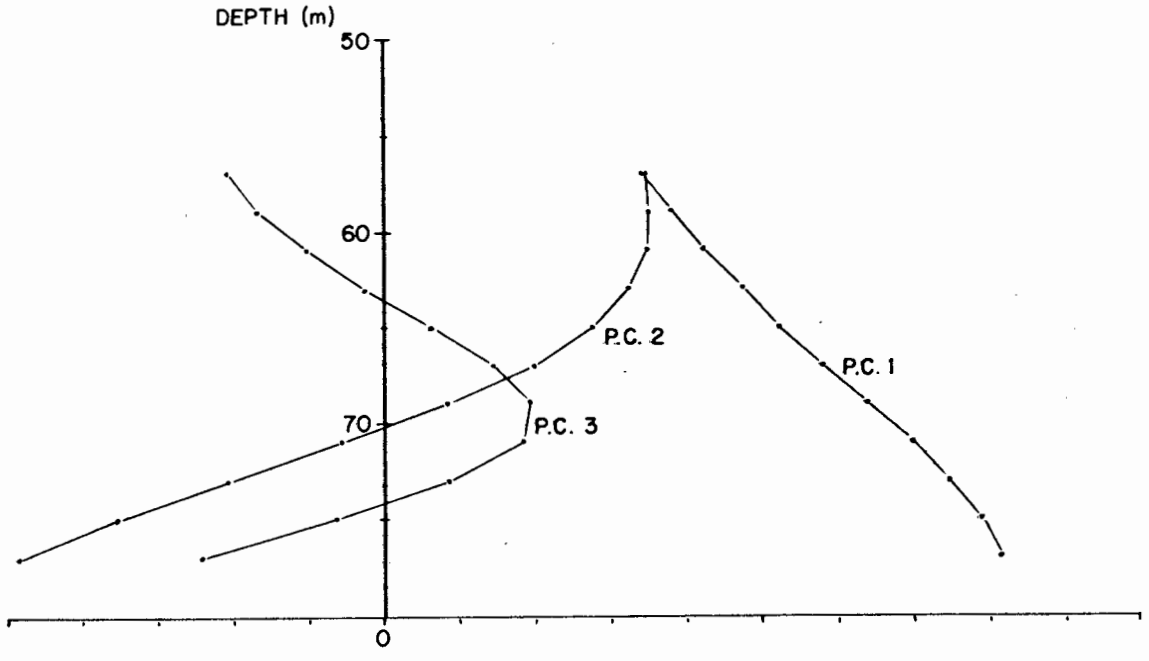

FIGURE 4.14: Plots of the three principal depth eigen-vectors for the second deployment. The shape and relative sizes are important.

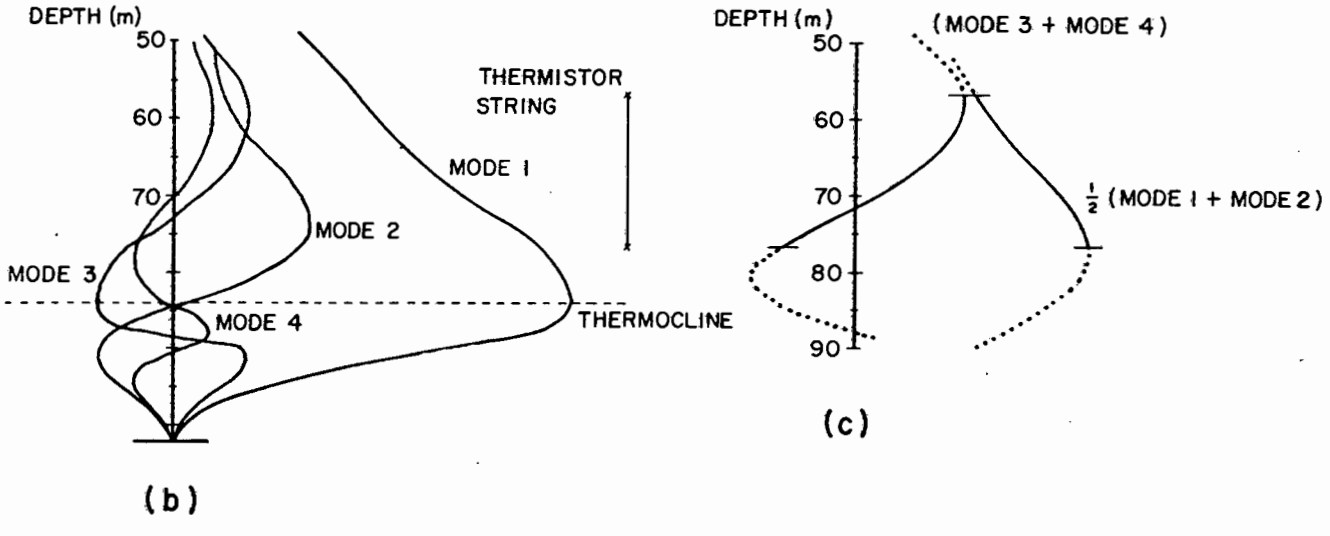

FIGURE 4.15: A schematic suggesting the relation between physically-real vertical modes and statistically-created depth eigen-vectors. Taking a thermocline at 84 m, the first four modes are sketched with typical shapes and relative sizes. The thermistor string, extending from 57 to 77 m, sees both first and second modes as vertically coherent. The proportionate sum of these two modes produces vertical structure similar to that of the first principal component. Likewise for modes 3 and 4 and component PC2.

The first three eigen-vector structures are plotted in Fig. 4.16 for the first 500 time steps and also for the full duration of the third deployment. Three points are noted. The full record has PC2 and PC3 structures about 2 m shallower owing to a general rising of the thermocline later in the record. The upper thermistors are more energetic for the full record. This is also due to the rise in thermocline and the consequent rise in structure. The short record has a sharper PC1 structure which implies a more precisely defined thermocline depth (a smaller standard deviation).

4.6 Energy Content of Dominant Components

In this section an attempt is made to determine the energy contained in this measured internal wave field. The temperature spectra presented in Section 4.4 are interpretable as energy spectra. The technique and assumptions are discussed in Section 4.6.1. The energy of any particular spectral band thus may be estimated (Section 4.6.2). Estimates of internal tide energy are calculated also from formulae derived in the cases of two-layered or linearly stratified structure (Section 4.6.3). In the next chapter, these estimates, which are summarized in Table 4.3, are compared with some values found in the literature.

4.6.1 A Spectral Analysis Procedure

The vertical axis of the spectral plots (Figs 4.8, 4.10 and 4.11) has the dimensions of temperature squared per frequency. The temperature data analysed are temperature differences, ΔT, from a mean or background temperature. It is shown that ΔT can be simply but cautiously related to corresponding density differences $\Delta\rho$ (Wahl and Teague, 1983) and, in turn, $(\Delta\rho)^2$ can be related to a corresponding energy density E.

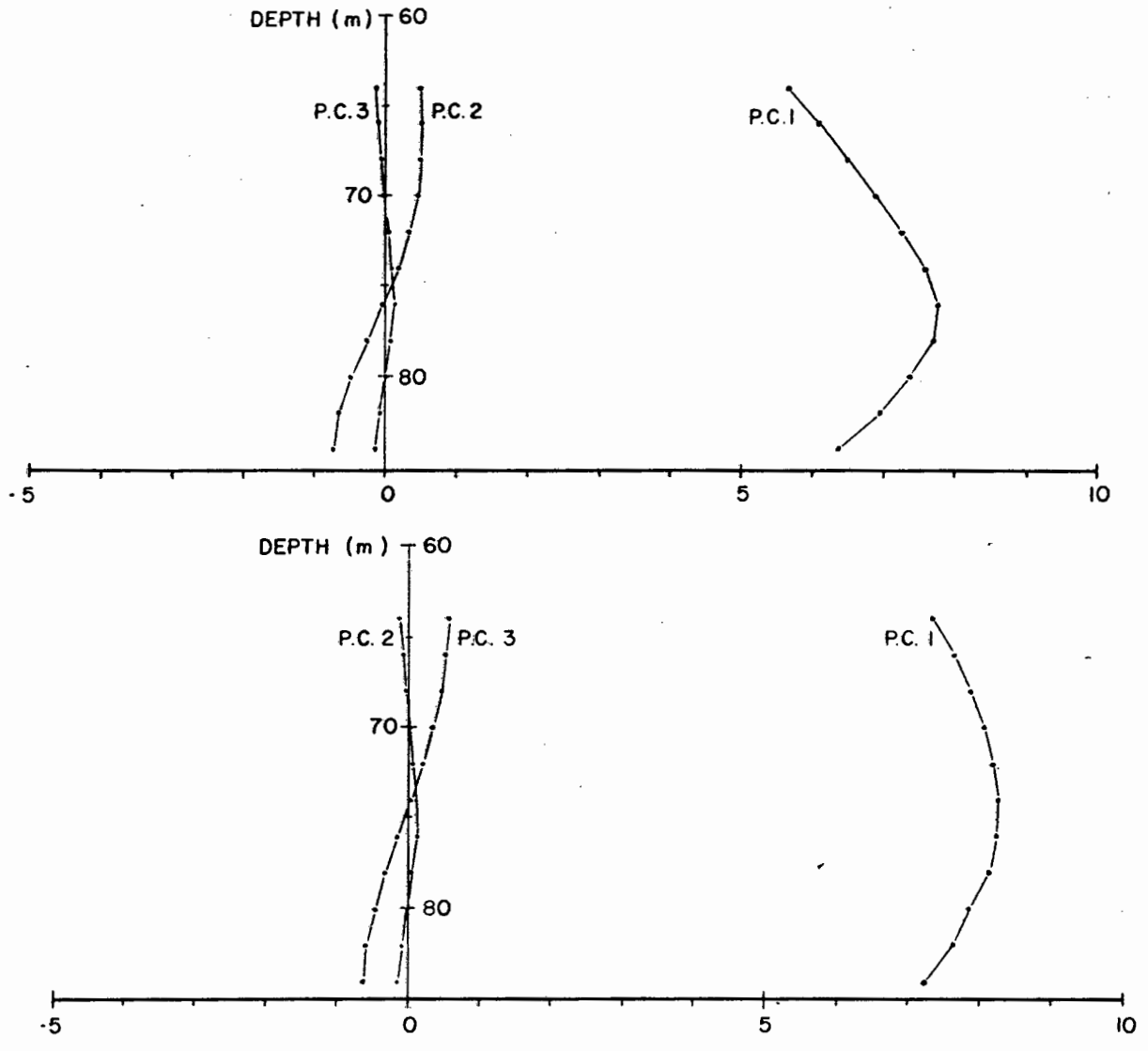

FIGURE 4.16: Plots of the three principal depth eigen-vectors for the first 500 time steps (above) and for the complete third deployment (below). The shape and relative sizes are important.

In Fig. 4.17 a mean temperature-salinity curve, for the region 30° to 35°S and 10° to 20°E (Shannon, 1985), is well approximated by a linear relationship over the range of temperatures recorded by the thermistors at Cape Point. Where salinity S is measured in $^{o}/_{oo}$ and temperature T is measured in °C:

$$S \simeq 0{,}08\ T + 33{,}97 \qquad (28)$$

Using this relation, density was plotted against temperature (and implicitly salinity) in Fig. 4.18. Assuming a linear relation between density and temperature, density differences are related to temperature differences through the coefficient of thermal expansion α.

$$\alpha = \frac{1}{\rho}\frac{\partial \rho}{\partial T} \text{ and } \quad \Delta\rho = \rho \cdot \alpha\ \Delta T \qquad (29)$$

From Fig. 4.18 it can be seen that this assumption is valid over limited ranges. A value of $1/7_{\rho}$ is taken for the range 10°C to 15°C and $1/8_{\rho}$ for the range 8°C to 12°C; the coefficient is larger for warmer water. Using this approach a temperature spectrum is thus easily interpreted as a density spectrum.

Expecting the recorded changes in temperature or density to be solely due to vertical displacements of a passive stratified structure (Section 4.2), the density spectrum can be interpreted as a potential energy spectrum describing the energy of these vertical displacements. Assuming that the thermistor is sufficiently removed from the boundaries (to exclude two-dimensional orbits) and, initially neglecting rotation, the particles oscillate vertically with their energy shared equally between potential and kinetic forms (Eq. 11).

If F(r) is the force acting on a particle removed a distance r from its rest level (r = 0), then the potential energy at separation h is expressed as

$$V(h) = -\int_0^h F(r)\cdot dr \qquad (30)$$

where $V(0) = 0$

The restoring force (per unit volume) is due to an imbalance between buoyancy and gravity forces.

$$\underline{F}(r) = g\{(\rho_o - \int_0^r \frac{\partial \rho}{\partial z}\, dz) - \rho_o\}\hat{\underline{z}} \qquad (31)$$

Therefore, the potential energy (per unit volume) of particles displaced a distance h from their rest position, is

$$V(h) = -\int_0^h \int_0^r g\cdot \frac{\partial \rho}{\partial z} \cdot dz \cdot dr \qquad (32)$$

If the density gradient $\frac{\partial \rho}{\partial z}$ can be assumed constant, $[\frac{\partial \rho}{\partial z}]_o$, over the local depth $-h_{max} \leq r \leq +h_{max}$, then the potential energy is given as

$$V(h) = \frac{1}{2}\, g\, h^2 \cdot [\frac{\partial \rho}{\partial z}]_o, \qquad (33)$$

where h can be given by the recorded density changes

$$\Delta\rho = h \cdot [\frac{\partial \rho}{\partial z}]_o. \qquad (34)$$

The time-series of temperature changes $\Delta T(t)$ provides a time-series of density changes $\Delta\rho(t)$ which can be interpreted (conditionally) as a time-series of vertical displacements h(t). This vertical displacement corresponds to a time-series of potential energy V(t). Similarly the power spectral density function of dimensions $[(\Delta T)^2/\sigma]$ provides a PSDF of dimensions $[(\Delta\rho)^2/\sigma]$ and a PSDF of dimensions $[V/\sigma]$, the average potential energy of a cycle of given frequency. This average V(t) equals $\frac{1}{2}\, V_{max}$. In the absence of rotation, $V(\sigma, z_o, t) = \frac{1}{2}\, E(\sigma, z_o, t)$ where E is the total energy density of a signal of frequency σ recorded at depth z_o and time t. The values of the temperature PSDF provide values of the energy PSDF:

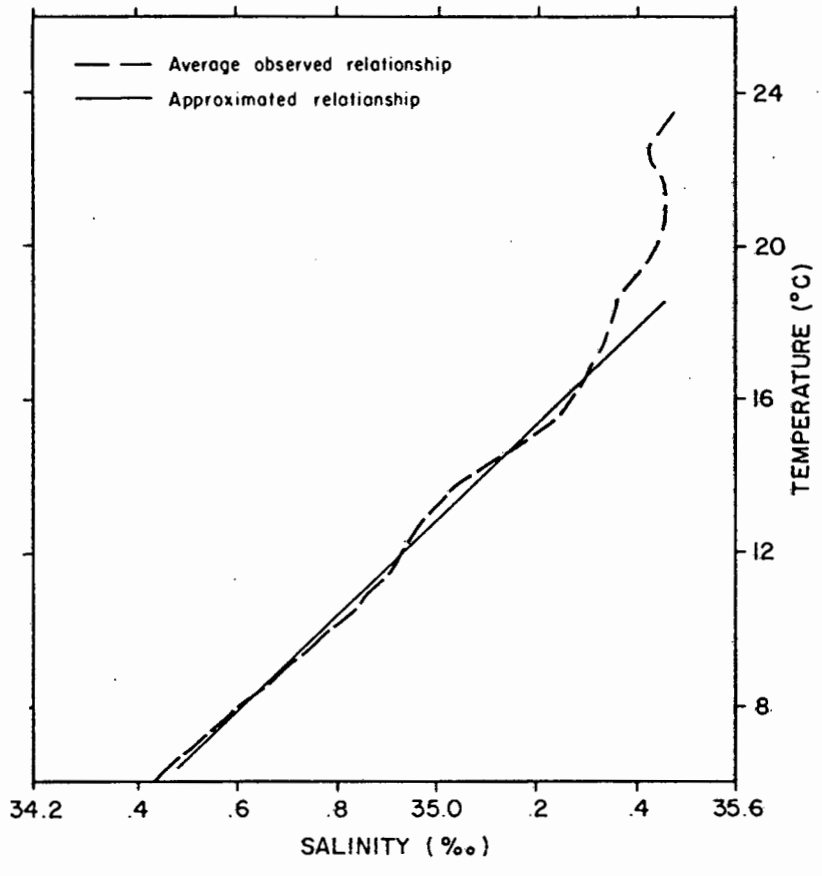

FIGURE 4.17: The mean temperature-salinity relationship obtained by Shannon (1985) from 10^5 observations in the region 30° to 35°S and 10° to 20°E is displayed by the dashed line. The solid line is an acceptable linear approximation for temperatures below 18°C.

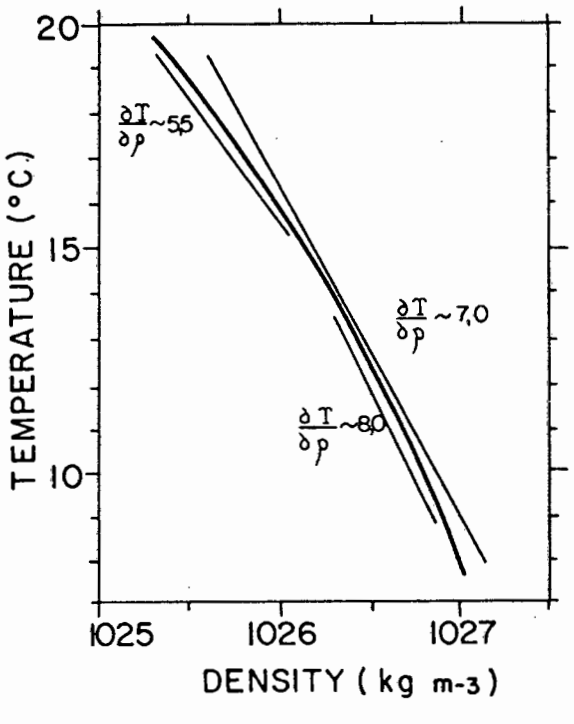

FIGURE 4.18: The relation between temperature and density obtained by assuming a constant temperature-salinity curve (Fig. 4.17). This relation approximates a linear function over a limited temperature range.

$$\frac{E(\sigma)}{\sigma} = \frac{g\cdot[\Delta\rho(\sigma)]^2}{\left[\frac{\partial\rho}{\partial z}\right]_o\cdot\sigma} = g\rho\alpha\cdot\left[\frac{\partial T}{\partial z}\right]_o^{-1}\cdot\frac{[\Delta T(\sigma)]^2}{\sigma} \qquad (35)$$

The total energy density E of a given frequency band σ_1 to σ_2 is given by the integral

$$E = \int_{\sigma_1}^{\sigma_2}\frac{E(\sigma)}{\sigma}\,d\sigma \qquad (36)$$

The equi-partition of energy, accepted for vertical displacements of high-frequency waves, is not valid at lower frequencies where rotation is significant. The particles describe a more horizontal path and less potential energy is available (Eq. 11). With this partition of energy, the total energy density PSDF can be approximated by

$$\frac{E(\sigma)}{\sigma} = \left(\frac{\sigma^2}{\sigma^2-f^2}\right) g\alpha\rho\left[\frac{\partial T}{\partial z_o}\right]^{-1}\frac{[\Delta T(\sigma)]^2}{\sigma} \qquad (37)$$

at frequencies near to the inertial frequency. It is clear, however, that a pure inertial signal, recorded as a result of the displacement of horizontal gradients, will be interpreted as potential energy (due to vertical displacement) and multiplied by an infinitely large correction factor. In other words, the presence of horizontal gradients leads to an overestimation of the energy of sub-tidal motions. It is assumed that such gradients are absent.

4.6.2 Spectral Estimates of Energy

It is now possible to obtain a value for the energy contained in any spectral band. This is done by integrating the energy PSDF with frequency; in this case of discrete spectral estimates, the estimates are summed and multiplied by the frequency interval $\Delta\sigma = \frac{1}{2M\cdot\Delta t} = 0{,}005$ cph (where M as in Section 4.4) between successive estimates. This is now done for the full internal wave spectrum ($f<\sigma<\sigma_c$, where σ_c is the Nyquist frequency), for the semi-diurnal tidal band ($0{,}075<\sigma<0{,}085$ cph) and for high-frequency motion ($1{,}0<\sigma<2{,}0$ cph).

In order to convert the spectra obtained in Section 4.4 (Figs 4.8, 4.10 and 4.11) to energy spectra, the vertical axes are rescaled by choosing a representative mean density gradient $[\frac{\partial \rho}{\partial z}]_o$ for the period analysed. The choice of this gradient introduces a significant error into the estimate of energy (cf. Levine et al., 1983), nevertheless a comparison of energy in different spectral bands is independent of this choice. The spectral estimates near inertial frequency were corrected for the non-equipartition of energy through multiplying by $\frac{\sigma^2}{\sigma^2-f^2}$. However, the signals at the inertial frequency are multiplied by an infinitely large correction factor as $\sigma \to f$. Therefore, low frequency estimates ($f<\sigma<0,065$ cph) were rather taken at mean levels according to the theory of a saturated spectrum with a power function shape $\frac{E(\sigma)}{\sigma} \propto \sigma^{-q}$ where q is a constant value (determined in Section 4.4.2). Unfortunately this obscures the detected peak at inertial frequency.

By plotting the size of the tidal peak versus depth (Fig. 4.9), a vertical profile of energy is obtained. This profile may be extrapolated by anticipating the shape of a simple first mode tide (Section 4.5). Although a subjective process, this procedure can provide a realistic estimate of the vertically integrated energy density at the mooring. High-frequency motions will have a sharper wave-guide (where $\sigma<N$). The depth integral is estimated by the product of the peak energy and an appropriate depth factor. The results, obtained by investigating the most energetic record of each deployment, are presented in Table 4.2.

4.6.3 Other Estimates of Tidal Energy

As an alternative to estimating the energy content from spectral densities (variance), one can obtain an estimate of the energy content from an estimate of the root-mean-square amplitude of a wave of given frequency. These estimates are also based on a calculation of potential energy and thus suffer from increasing error at lower frequency due to the non-equipartition of energy (Section 4.6.1). Since the tidal signal has been identified as most energetic (Section 4.4 and Table 4.2), estimates are made of this signal alone.

	FIRST DEPLOYMENT	SECOND DEPLOYMENT	THIRD DEPLOYMENT
Depth of most energetic record	63 m	77 m	82 m
Mean density gradient ($kg.m^{-4}$)	0,016	0,006	0,006
High-frequency shoulder			
Energy density ($J.m^{-3}$)	0,2	0,6	0,4
Depth factor (m)	35	20	25
Integrated energy density ($J.m^{-2}$)	7	12	10
Percentage of total	2	5	3
Tidal peak			
Energy density ($J.m^{-3}$)	4,2	5,2	7,2
Depth factor (m)	40	22	30
Integrated energy density ($J.m^{-2}$)	168	115	216
Percentage of total	46	51	53
Full spectrum (σ>f)			
Energy density ($J.m^{-3}$)	9,2	10,2	13,6
Depth factor (m)	40	22	30
Integrated energy density ($J.m^{-2}$)	368	224	408

TABLE 4.2: Estimates of mean energy density as calculated from spectra of temperature fluctuations. Values, which are calculated for the particular thermistor ($J.m^{-3}$) and for the depth-integrated water column ($J.m^{-2}$), provide a fair comparison between different spectral bands of the same deployment but the uncertainty is large in comparison between different spectra.

The simplest method is to calculate the energy of an interfacial wave between two homogeneous layers. Such a scheme is suggested by the results of Section 4.5. The potential energy expression leads to the following vertically integrated estimate of energy density (see Eq. 10 and 11):

$$E = \frac{1}{2} \frac{\sigma^2}{\sigma^2 - f^2} \cdot g \cdot \Delta\rho \cdot T^2 \qquad (38)$$

where T is the wave amplitude

$\Delta\rho$ is the interfacial density discontinuity

The vertically integrated energy flux E_f, which is horizontal and shoreward, is estimated by a product of energy density E with group speed c_g. The group speed may either be calculated theoretically for an interfacial system (Eq. 19) or may be estimated from satellite images of actual slick patterns. The separation between packets (Table 4.1) indicates phase speed c which is related to group speed:

$$c_g = \frac{\sigma^2 - f^2}{\sigma^2} \cdot c \qquad (39)$$

It is obvious that the values of E and E_f are dependent on the choice of values for T and $\Delta\rho$. Values of k_h may be extracted from satellite imagery, but it should be noted that these values are usually for shallow summer thermoclines. The values chosen and the typical results obtained are presented in Section 5.5 (Table 5.1).

Alternatively a constant-N profile could be assumed. The real system falls between this approximation and the previous one (Section 2.3). The fundamental mode internal wave has an energy density per unit volume (Gill, 1982).

$$E = \frac{1}{2} \rho_o \frac{N^2}{\sigma^2 - f^2} W^2 = \frac{1}{2} \rho_o \frac{m^2}{k_h^2} W^2 \qquad (40)$$

where W is the amplitude of the vertical velocity

In such a linearly stratified fluid $W(z) \propto \sin m(z+H)$ and, for the first mode, $m = \frac{\pi}{H}$ (Section 2.2). Vertical integration is achieved by multiplying $E_{max}(z)$ by a depth factor $\frac{1}{2}$ H. Therefore, the integrated energy density is approximated by

$$E = \frac{1}{4} \rho_o H \frac{\sigma^2}{\sigma^2 - f^2} N^2 T^2 \qquad (41)$$

which is equivalent to the two-layer result if $N^2 \equiv \frac{g \cdot \Delta\rho}{\rho_o \cdot H/2}$. Similar to the two-layer approximation, the horizontal group speed may be calculated

$$[c_g]_h = \left(\frac{\sigma^2 - f^2}{N^2}\right)^{0,5} \cdot \frac{N^2 H}{\sigma\pi} \qquad (42)$$

or estimated from phase speeds extracted from satellite imagery, using Eq. 39 which is valid for constant-N.

For a linearly stratified ocean, the values of E and E_f depend on the choice of typical values of T and N^2. These values are calculated and tabulated in Section 5.5 (Table 5.1). The formulae (Eq. 41 and 42) used to calculate E and c_g, in the absence of satellite information, are equivalent to the expressions used by Wunsch (1975). However, Wunsch calculates the sum of energy due to all the modal contributions where mode n has energy flux

$$(E_f)_n \propto \frac{1}{n} T_n^2 \qquad (43)$$

where T_n is the amplitude of mode n
A mode 2 wave with $T_2 \sim \frac{1}{2} T_1$ will have $[E_f]_2 \sim \frac{1}{8} [E_f]_1$.

For a known bulk density gradient $\frac{\rho(-H)-\rho(0)}{H}$, a two-layer model with $\Delta\rho = \rho(-H)-\rho(0)$ and a constant-N model with $N^2 = \frac{g(\rho(-H)-\rho(0)}{\rho H}$ will over-estimate and underestimate, respectively, the actual energy density due to a wave of measured amplitude T. Energy densities obtained from these models provide an upper and a lower limit to the estimate of actual energy density. The

sharper the stratification, the closer is the actual value to the 2-layer limit, and vice-versa. The profiles, which were measured at Cape Point, appear to be better represented by a 2-layer profile than a linear profile. Irrespective of the choice of profile, these energy estimates (Eq. 38 and 41) are most sensitive to the choice of T.

Finally, it is interesting to compare the average energy density and flux with estimates of available barotropic energy (Section 5.5). The mean surface tide energy density is approximated by

$$E_b \simeq \frac{1}{2\pi} \int_o^{2\pi} \frac{1}{2} \rho g (A \sin \theta)^2 \, d\theta = \frac{1}{4} \rho g \cdot A^2 \qquad (44)$$

where A is the amplitude of surface tidal elevation.

CHAPTER 5
THE TIDAL SIGNAL

In the previous chapter, it became obvious that the 'noisy' internal wave field is dominated by particular spatial and temporal structures over the continental shelf. Spectral peaks, representing enhanced energy levels, in Fig. 4.8, 4.10 and 4.11 were interpreted in terms of local internal wave sources, such as wind and tide. In the near-field of inertial oscillations and internal tides these anomalous perturbations survive the non-linear dynamical tendency to diffuse into the base-state Garret-Munk spectrum (Roth et al., 1981, compare similar upper ocean spectra to the Garrett-Munk model).

In this chapter the dominant tidal dynamics are discussed. Models of shelf-edge generation are reviewed and dissipation of tidal energy, on propagating shorewards, is parametrized. In Section 5.4 the internal tide, monitored at the Cape Point mooring, is theoretically estimated. Finally energy density is discussed and compared with values reported for other continental shelves.

5.1 Summary of Results

The strong tidal signal and the poorly-resolved, tidally-modulated, high-frequency signal are apparent in time-series plots of the data. These two clear signals are quantitatively confirmed in the spectra presented in Figs 4.8, 4.10 and 4.11. The packets of high-frequency waves, discussed in Sections 4.2.1 and 4.4.2, are also evident in the Landsat imagery (Section 4.1). Their association with the internal tide is obvious. Although these high-frequency waves may assume the proportions and thus the non-linear nature of solitary waves (Fig. 5.1), as reported by Osborne and Burch (1980), Sandstrom and Elliott (1984) and Pingree and Mardell (1985), these high-frequency dynamics have not been addressed further than to treat them as a dissipative

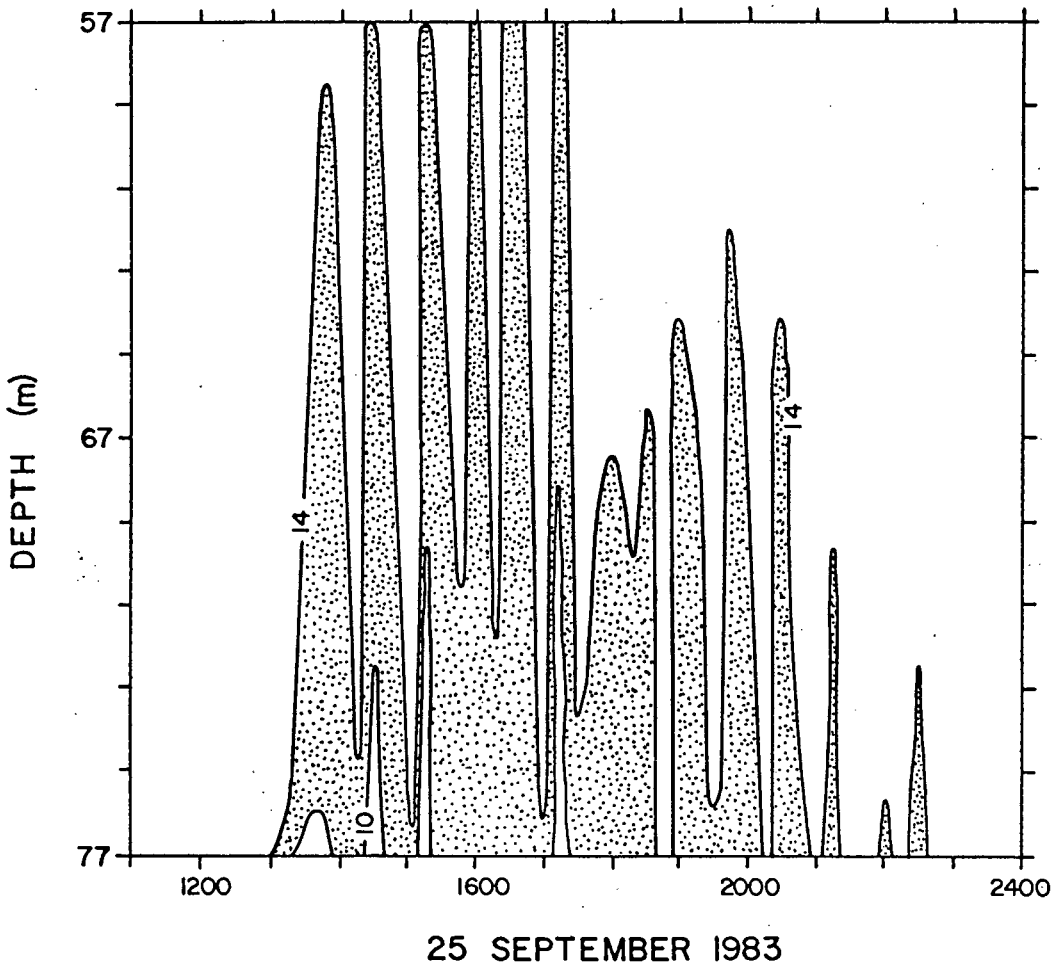

FIGURE 5.1: A tidal packet of large amplitude high-frequency waves recorded during the second deployment at Cape Point. The thermocline region, between 10°C and 14°C, has been shaded in order to accentuate the displacement of the isotherms; the 14°C isotherm is displaced as much as 20 m in 15 min ($W \sim 0{,}02\ ms^{-1}$).

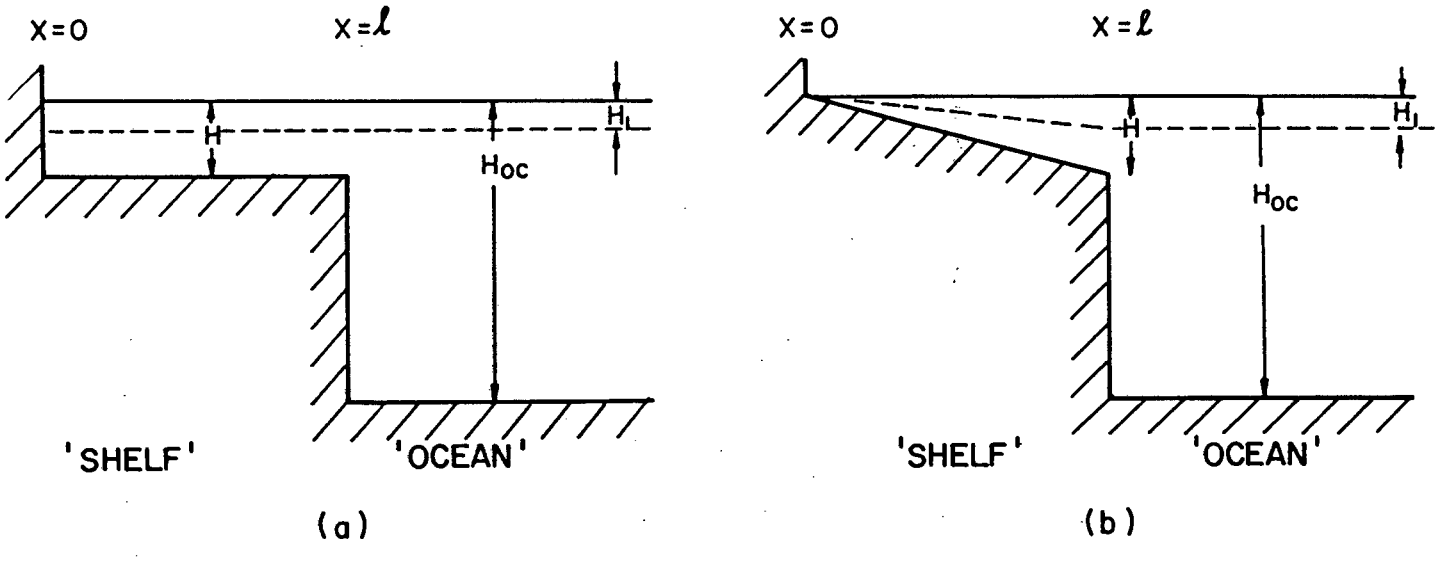

FIGURE 5.2: Simple models of step-like continental shelf topography (a) Constant depth ocean, constant depth shelf, constant depth thermocline (b) Constant depth ocean, sloping shelf and thermocline (for $x<\ell$).

mechanism contributing significantly to internal tide damping rates. The non-linear effects leading to steepening of the tide, and transfer of energy to high-frequency waves, are stronger in shallower shelf areas. The subsequent dissipation of this high-frequency energy, due to bottom and internal stresses, is also enhanced in shallower water (Le Blond, 1966). The high rates of tidal dissipation (e-folding length of about one wavelength) observed on the NW Australian shelf (Holloway, 1983) and the Scotian shelf (Petrie, 1975 and Sandstrom and Elliott, 1984) contrast with the lower rates (e-folding length of several tidal wavelengths) observed by Osborne and Burch (1980) and Apel et al. (pers. comm., cited by Sandstrom and Elliott, 1984) in the deeper Andaman and Sulu Seas. In conclusion, the high-frequency energy emerges as an alternate form of some of the internal tide energy. Notwithstanding the insufficient resolution of super-Nyquist frequencies, this appears to be the case in Fig. 4.1 where larger amplitude high-frequency waves (solitons) correspond to smaller amplitude tidal waves.

The spectral estimates of energy (Table 4.2) indicate that the tidal frequency band accounts for a mean 50% of the energy in the internal wave field. (It should be remembered, however, that the energy of the inertial frequency band was poorly estimated and, it is suspected, underestimated; see Chapter 6). The mean contribution from the high-frequency band is about 5%, but this mean value conceals individual solitons which would account for a much greater proportion during their momentory presence. If the above analysis were accepted, then the tide accounts for 55% of internal wave energy, on average. With the possible exclusion of inertial motions, waves of non-tidal frequencies are less important and can be considered as an amorphous weakly interacting background to the clear tidal signals.

In Section 4.5, an empirical orthogonal function analysis singles out the lower mode waves as the principal components (that is, most energetic). The first component contributed 69%, 90% and 93% of the variance in the respective deployments. From

an investigation of these components (Section 4.5.2), it can be concluded that the first mode internal waves are responsible for about two-thirds (>60%) of the total internal wave energy at the mooring. The internal tide energy, generated at the shelf-edge as mode 1, does not easily leak to higher order modes (Baines, 1982). Therefore, it can be expected that the internal tide is dominated to even greater extent by the first mode - the data presented in this thesis suggest that a value of about 70% would be representative (in other words, the first mode internal tide accounts for about 40% of the energy in the entire internal wave field). This strengh of the first mode internal tide has been reported in many continental shelf studies (e.g. refer to Wunsch, 1975, Huthnance and Baines, 1982, Holloway, 1983, 1984 and Sandstrom and Elliott, 1984).

5.2 Theory of Shelf-edge Generation

It is now well accepted that the astronomically-forced barotropic tide forces a baroclinic tide through blocking action at the shelf-edge. The internal (baroclinic) tidal energy radiates towards the ocean as well as towards the coast. In particular, the internal tide that propagates up the continental shelf is investigated. First demonstrated by Zeilon (1934), this shelf-edge generation has been addressed by numerous models. Largier (1986) reviews two major branches of development. The one group of researchers (latest report: Prinsenberg and Rattray, 1975) developed a modally decomposed solution by matching, at the shelf break, of separable solutions in the constant depth shelf and oceanic regions. The second model (latest report: Baines, 1982) treats a variable-depth, non-separable problem via the method of characteristic variables. Sandstrom (1976) provides a similar treatment to Baines. The experimental/conceptual work by Maxworthy (1979) and Maxworthy, Chabert d'Hieres and Didelle (1984), for internal tide generation over a sill, also provides interesting comment on the shelf-edge generation process. However, this model involves supercritical flow ($Fr = \frac{U_b}{c} > 1$)

over the sill, an internal hydraulic jump and an internal lee wave. This situation is less common at the shelf-edge (Huthnance, 1981) and inappropriate for the shelf off Cape Point. Baines and Fang (1985) investigate the limitations of linear generation models by comparing results with a laboratory experiment. In this section, these models are used in order to predict the internal tide energy (amplitude), given the essential information on barotropic tide, topography and stratification.

5.2.1 Models of Interfacial Tides

Rattray (1960) formulates a 2-mode, 2-layer system in the presence of a shelf-edge and a coast. The cross-shelf transport vanishes in each layer at the coast (x = 0). At the shelf-edge (x = ℓ), the total transport, the transport in each layer and the pressure must be continuous. With zero friction and total reflection at the coast, a standing wave solution is obtained over the shelf and the solution displays resonances. In reality, friction will strongly damp the wave propagating shoreward (Weigand, et al. 1969) and negligible reflection occurs at the coast. For a step shelf of uniform depth H, adjacent to an ocean of uniform depth H_{oc} (Fig. 5.2a), the first mode internal tide amplitude over the shelf T, is given by Rattray (1960) in terms of the barotropic tide amplitude A:

$$T = H_1 \left(\frac{1}{H} - \frac{1}{H_{oc}}\right) \left(\frac{1 + k_2^2 \ell^2}{\cos^2 k_1 \ell + \frac{k_2^2}{k_1^2} \sin^2 k_1 \ell} \right)^{0,5} A \qquad (45)$$

where $$k_1^2 = \frac{(\sigma^2 - f^2)}{g'} \frac{H}{H_1 H_2}$$

$$k_2^2 = \frac{(\sigma^2 - f^2)}{g'} \frac{H_{oc}}{H_1 (H_{oc} - H_1)} .$$

For a linearly sloping shelf (Fig. 5.2b), a similar relation is obtained. Interface depth is H_1 in the ocean and $\frac{H_1 x}{\ell}$ over the shelf.

$$T = H_1 \left(\frac{1}{H} - \frac{1}{H_{OC}}\right) \left(\frac{1 + k_2^2 \ell^2}{[Jo(2k_1\ell)]^2 + \frac{k_2^2}{k_1^2}[J_1(2k_1\ell)]^2} \right)^{0,5} A \quad (46)$$

where k_1 and k_2 are as above.

In this case, the amplitude will grow as the wave propagates into shallower water towards the coast. In both cases T tends to increase with increasing A, increasing ℓ, increasing $(H_{OC}-H)$, decreasing $\Delta\rho$ and increasing H_1. Typical amplitude ratios range from about 1 to in excess of 10. A peculiar feature of this frictionless, standing-wave model is that $\frac{T}{A}$ displays local extrema as ℓ increase relative to a wave length-scale

$$\ell_w = \left(\frac{g' H_1}{\sigma^2 - f^2}\right)^{0,5}. \quad (47)$$

These local extrema correspond to resonance and anti-resonance conditions.

Rattray, et al. (1969) extend the theory to a frictionless, continuously stratified ocean but do not solve their model for T. Prinsenberg, et al. (1974) continue the development and suggest that

$$T_{OC} = \frac{\alpha \ell H_{OC}}{2H(H_{OC}-H)} A \quad (48)$$

where T_{OC} is the amplitude of the oceanward wave (due to all the modes) in the absence of reflection at the coast.

$\alpha = \left(\frac{\sigma^2 - f^2}{N^2 - \sigma^2}\right)^{0,5}$ is the slope of the semi-diurnal tidal characteristic in the ocean.

The final paper in this group, Prinsenberg and Rattray (1975), addresses the case of variable buoyancy frequency N(z).

The ray theory approach used by Baines (1973) for flat topography ($\delta<\alpha$ everywhere, where δ is the topographic slope) and by Baines (1974) for steep topography ($\delta>\alpha$ over the continental slope), is combined with interfacial models in order to develop a more realistic model which is easily used to calculate theoretical amplitudes (Baines, 1982). In this 'composite' model waves may be generated both on the interface and in a stratified continuum below it. The model density profile corresponds to

$$\begin{aligned} N^2 &= 0 && -H_1<z<0 \\ N^2 &= N_o^2(z) + \frac{g\Delta\rho_o}{\rho_o}\,\delta(z+H_1) && -H<z<-H_1 \end{aligned} \qquad (49)$$

where δ is the Dirac delta function (in this equation alone)
$\Delta\rho_o$ is the density difference across $z=-H_1$
N_o is constant or slowly-varying.

From this, two special cases are identified. For shallow, weaker interfaces, the effect of the upper layer and interface on motions below may be negligible. This is approximated by allowing the stratified continuum to extend up to the rigid surface. For deeper, strong interfaces, a particular mode associated with the interface may be isolated. The stratified continuum then extends to the interface which may be taken as rigid for all motion other than the interfacial mode. This interfacial mode is closely approximated by a two-layer form if

$$R > (1+\frac{\pi}{2}\,S^{0,5})^{-1} \qquad (50)$$

where $R = \dfrac{H_1}{H}$ relative depth of interface

$S = \dfrac{g\Delta\rho_o}{H_1\rho_o(N_o^2-\omega^2)}$ relative strength of interface

In Fig. 5.3 the regions of validity of the above approximations are shown in R, S space.

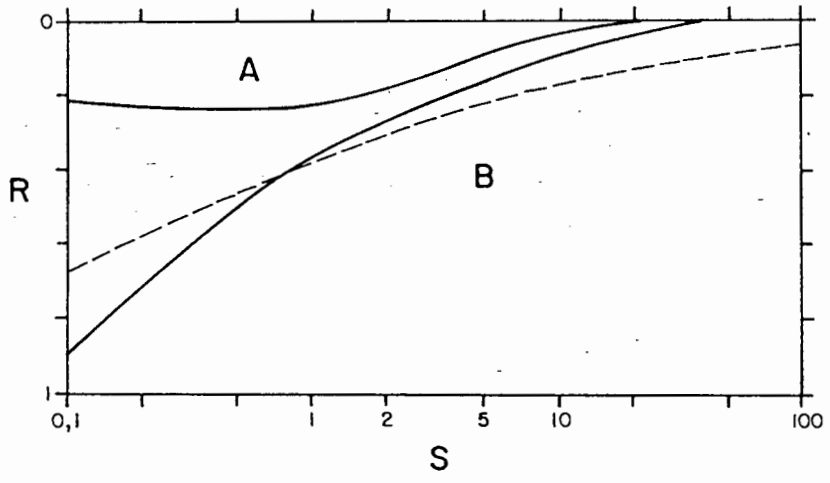

FIGURE 5.3: Regions of R-S space where either the motion in the stratified continuum is well approximated by taking a rigid lid at the sea surface (region A) or by taking, firstly, a rigid lid at the interface and, secondly, an interfacial mode (region B). The interfacial mode approximates to a two-layer wave for the region below the dashed curve, which is described by Eq. 50 [from Baines, 1982].

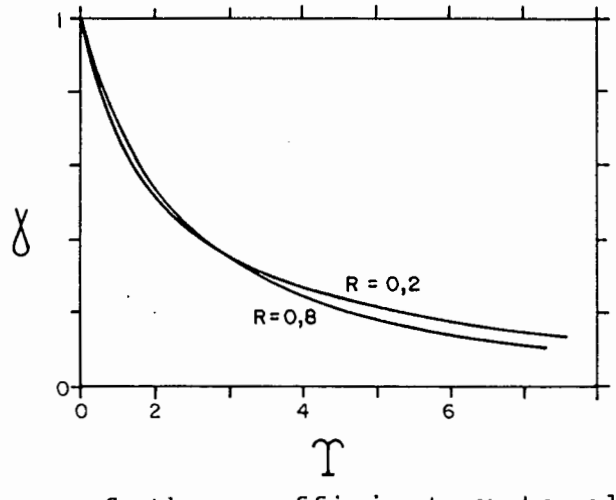

FIGURE 5.4: Values of the coefficient γ to allow for finite slope δ as expressed by T (Eq. 51) [from Baines, 1982].

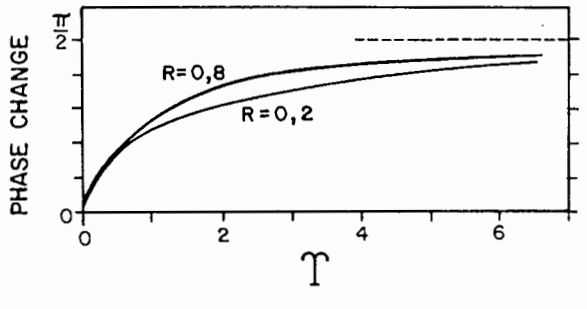

FIGURE 5.5: The phase change experienced at the top of the slope as a result of the centre of the generating force spreading seaward, away from the top of the slope, for finite slope δ expressed by T (Eq. 51) [from Baines, 1982].

The interfacial approximation is generally valid for the density profiles recorded. Further, Baines (1982) concludes that, for this case, the part of the solution due to higher order modes, in the stratified continuum, is generally negligible on the shelf. The seaward propagating solution behaves differently. Bearing in mind the conditions discussed by Baines (1982), the internal tide over the continental shelf may be modelled as a simple, first mode (interfacial) wave.

Taking $0<R<1$ and assuming a linear continental slope δ, the solution is characterized by the parameters R, S and T, where

$$T = \frac{H(\sigma^2-f^2)^{0,5}}{(g'H_1)^{0,5}\delta} \qquad (51)$$

The interface displacement ζ is given by:

$$\zeta = \frac{Q(\sigma^2-f^2)^{0,5}}{\sigma(g'\frac{H_1H_2}{H})^{0,5}} \; D_o \; e^{-i\theta} \; e^{-i\sigma t} \qquad (52)$$

where Q is the barotropic volume flux (approximated by $A\sigma\ell$ for both Poincaré and Kelvin tides; see Baines 1973 and Battisti and Clarke 1982))

A is the barotropic tidal amplitude

ℓ is the shelf-width

$$\theta = x \frac{g'\frac{H_1H_2}{H}^{-0,5}}{(\sigma^2-f^2)}$$

x is the horizontal co-ordinate (x = 0 at the shelf-edge; x<0 over the shelf)

$$D_o = \frac{\gamma H_1(\frac{1}{H_{oc}} - \frac{1}{H})}{1 + \frac{H_{oc_2}}{H_{oc}} \cdot \frac{H}{H_2}^{0,5}}$$

$H_2 = H-H_1$

$H_{oc_2} = H_{oc}-H_1$

γ is a coefficient allowing for finite δ (Fig. 5.4 relates γ to T and R)

The associated horizontal velocity is given by:

$$u = \frac{QD_o}{H_1} e^{-i\theta} e^{-i\sigma t} \qquad -H_1 < z < 0$$
$$= \frac{-QD_o}{H_2} e^{-i\theta} e^{-i\sigma t} \qquad -H < z < -H_1 \tag{53}$$

As the slope δ of the step decreases from infinity, the generating body force is spread out so that it does not all act with the same phase relative to the resultant waves. A corresponding phase change is consistent with the centre of the generating force moving seaward from the shelf-edge. This phase difference, at the shelf-edge, is related to T in Fig. 5.5.

The internal tide generating body force is easily derived by subtracting the equations of motion for barotropic flow from the general equations of motion for a rotating, stratified, inviscid fluid. The problem is reduced to two dimensions (x,z). Introducing Q, the barotropic volume flux, the body force for arbitrary N(z) is given by Baines (1982):

$$\underline{F} = - \frac{QN^2}{\sigma} \frac{z \frac{\partial H}{\partial x}}{H^2} \sin \sigma t \cdot \hat{\underline{z}} \tag{54}$$

where the vertical velocity due to the barotropic tide is

$$w_b = \frac{Qz \frac{\partial H}{\partial x}}{H^2} \cos \sigma t \tag{55}$$

The amplitude of F is strongly concentrated at the top of the slope. Contours of this body force are drawn for constant-N for the shelf profile directly seaward of the mooring site (Fig. 5.6a). Large values of F are found not only at the crest of the continental slope but also above the sides of Cape Point Valley. The same plot of F is made for a transition layer profile as shown in Fig. 5-6b. In Section 5.4 this multiple generation is investigated and shown to enhance the internal tide under certain phase conditions.

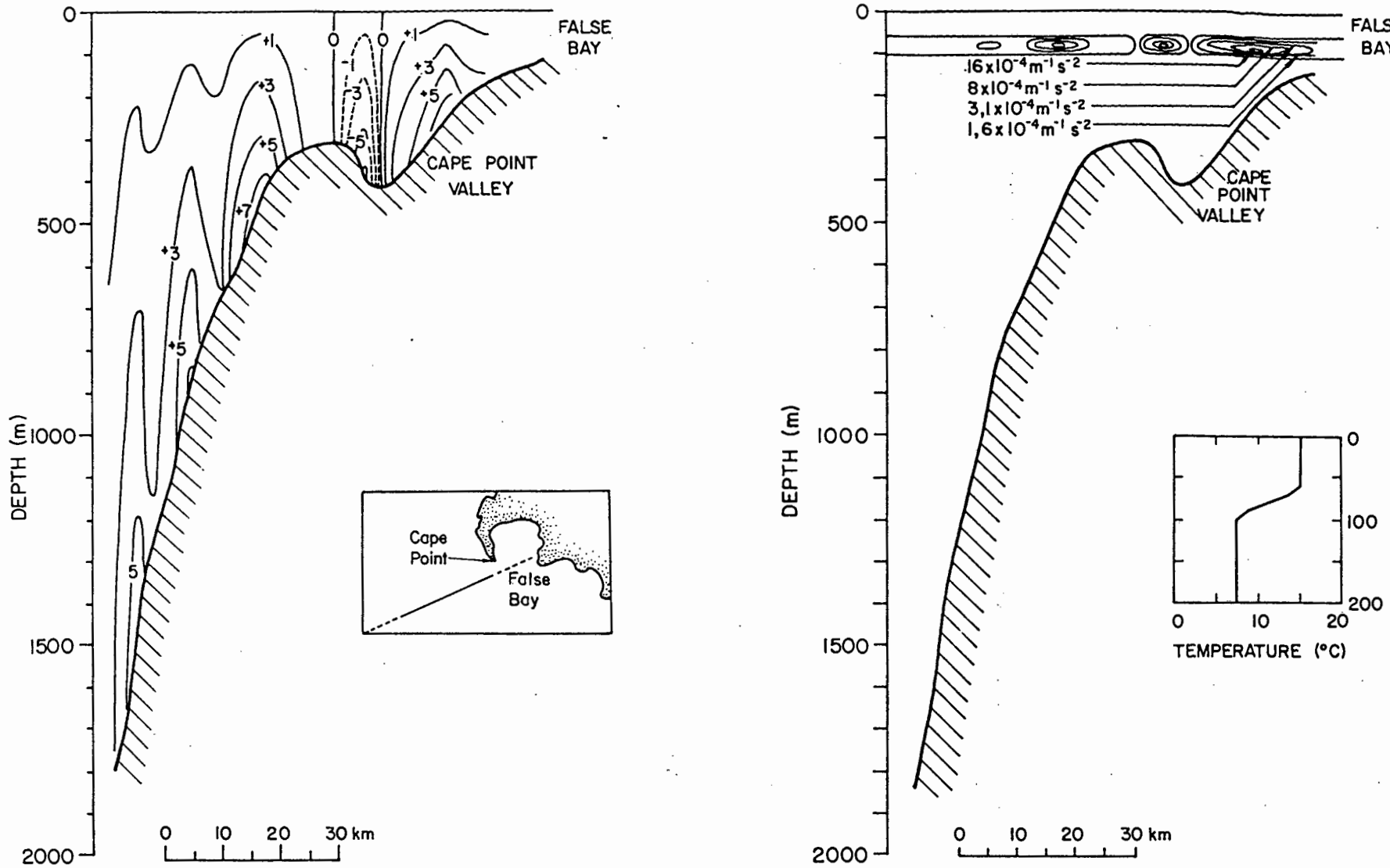

FIGURE 5.6: Distribution of the generating force F as a function of depth and stratification (Eq. 54) along a cross-section as shown in the inset. (a) Scalar values of $10^5 \cdot \sigma F/QN^2 = 10^5 \cdot z\ \partial_x H/H^2$ are plotted. This indicates the generation centres in the hypothetical case of constant-N stratification. Contours are drawn for 1, 3, 5 and 7. Negative values for the seaward valley wall imply a phase shift of π. (b) Scalar values of $\sigma F/Q = zN^2\ \partial_x H/H^2$ are plotted for a simple thermocline profile as displayed in the inset. The generating force is zero in the upper and lower mixed layers and over the flat topography at the crest of the hill and in the bottom of the valley.

Given the wisdom of the preceding internal tide generation models, and considering that two-layer structure is both representative (Chapter 2) and justifiable (Fig. 5.3), a very simple model of two-layer flow over topographic steps is developed. Symbols are used as in Sections 2.3 and 5.2.1.

5.2.2 A Simple Predictive Model for Interfacial Tides

Formulation. It is known that the depth discontinuity forces a compensatory adjustment in the interface depth. As the flow varies with time, the interface changes depth and a disturbance travels away from this localized source as a wave. A generalized barotropic flow perpendicular to the step is modelled by a long surface wave incident on a step in an unbounded ocean. There is negligible variation in the y-dimension parallel to the step: $L_y = \frac{H}{\delta_y} >> \lambda$, $v_b \sim 0$ and $\partial_y u_b \sim 0$. The step is such that $L_x = \frac{H}{\delta_x} << \lambda$ and L_x may be taken as zero. The barotropic flow $U \cdot \exp(i\sigma t) \cdot \exp(ik_b x)$ is such that $\sigma > f$ and $k_b^{-1} >> \lambda >> L_x$.

The barotropic wave (Eq. 18), incident on the step, is partially transmitted and partially reflected. But without a coupled baroclinic response (Eq. 19), the barotropic waves cannot be matched at the depth discontinuity (Fig. 5.7). Baroclinic velocities $u_1 = \frac{H_2}{H} \hat{u}$ and $u_2 = \frac{-H_1}{H} \hat{u}$ are obtained for zero net baroclinic transport (Gill, 1982). Matching surface displacement, interface displacement and transport in each layer at x=0 with x>0 over the shelf region (Fig. 5.7):

$$A_i + A_r = A_t \tag{56}$$

$$A_t = \frac{2c_{b_-}}{c_{b_-} + c_{b_+}} A_i \tag{57}$$

$$T_t = T_r = \Delta(H_1, H_-, H_+) \cdot \phi(\Delta\rho, H, \sigma, f) \cdot \Psi \tag{58}$$

where i,r,t refer to the incident, reflected and transmitted waves

b refers to the barotropic wave

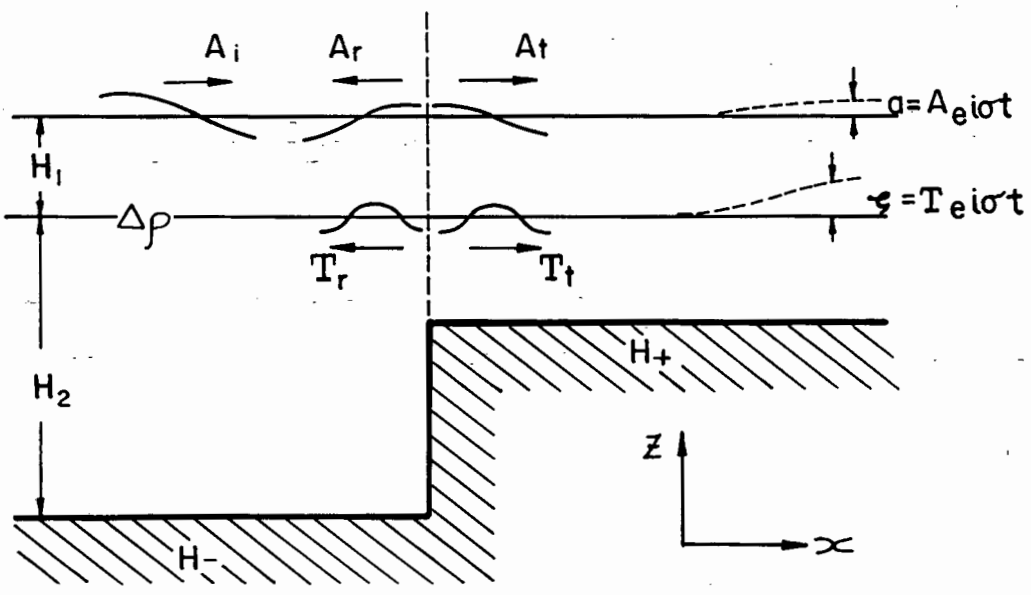

FIGURE 5.7: An incident surface wave A_i is reflected, A_r, and transmitted, A_t, on encountering the step. A coupled baroclinic response, T_r and T_t, is required in order to match transports and vertical displacements at the depth discontinuity (x = 0).

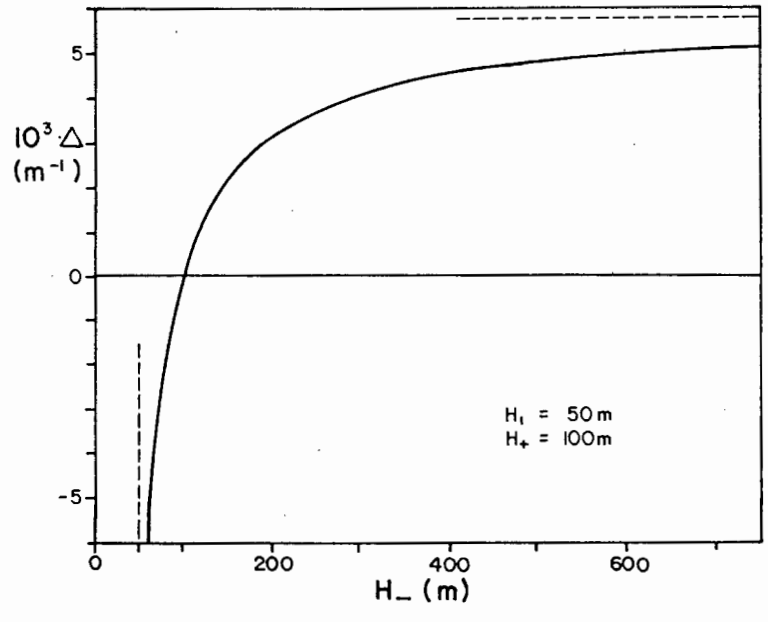

FIGURE 5.8: The topographic coefficient Δ plotted as a function of water depth H_- for x<0, given a fixed depth H_+ for x>0. When $H_- = H_+$ there is no response. For $H_- >> H_1$ the dependence of Δ on H_- is small. For $H_- \sim H_1$ the dependence grows without bound.

$$\Delta(H_1,H_-,H_+) = \frac{H_+^{-1} - H_-^{-1}}{(1-R_+)^{0,5}+(1-R_-)^{0,5}}$$ topographic coefficient

$$\phi(\Delta\rho,H_1,\sigma,f) = \left(\frac{H_1(\sigma^2-f^2)}{g'\sigma^2}\right)^{0,5}$$ stratification coefficient

$\Psi = c_{b_+} A_t = U_b H_+$ barotropic forcing

H_1 is an ambient value, uniform over the step.

The topographic coefficient Δ may be multiplied by the slope coefficient γ (see Eq. 52), which was introduced by Baines (1982) to account for a non-vertical continental slope.

Barotropic-to-Baroclinic Coupling. This result should be investigated. Firstly, symmetrical generation is predicted with equal amplitude interfacial waves propagating towards the ocean and towards the coast. In other words, the same expression would describe the interfacial response for a barotropic wave incident on a 'step-down' ($H_+<H_-$). The full solution of Baines (1982) reduces to the same symmetrical form for an interfacial tide generated at a step. Eq. 52 only differs from Eq. 58 in its more general expression for barotropic forcing. Although Fig. 5.7 suggests that forcing is due to a barotropic Poincaré wave, the result is general for any oscillatory barotropic flow at a topographic step, given the conditions of subcritical flow ($Fr<1$), step-like topography ($L_x<<\lambda$) and two-layer structure ($\frac{\pi}{2} S^{0,5} > \frac{1}{R} - 1$).

For $H_+>H_-$, the interfacial response T is in phase with barotropic forcing U_b. Its magnitude depends on the topography (H_-, H_+, δ), the stratification ($\Delta\rho$, H_1) and the barotropic forcing (U_b, σ). For a given shelf depth H_+, the topographic coefficient is positive for $H_->H_+$ and negative for $H_-<H_+$. The dependence on H_- increases as H_- decreases: $\partial_{H_-}(\Delta)\to 0$ for $H_-\to\infty$ and $\partial_{H_-}(\Delta)\to\infty$ for $H_-\to H_1$ (Fig. 5.8). The dependence of the stratification coefficient ϕ on $\Delta\rho$ and H_1 is given in Fig. 5.9. It is larger for smaller $\Delta\rho$ and larger H_1 with $\partial_{\Delta\rho}(\phi)\to\infty$ for $H_1\to 0$. Taken together, the barotropic-to-baroclinic coupling is stronger for larger steps in shallower water and for weaker interfaces nearer to the bottom (Fig. 5.10).

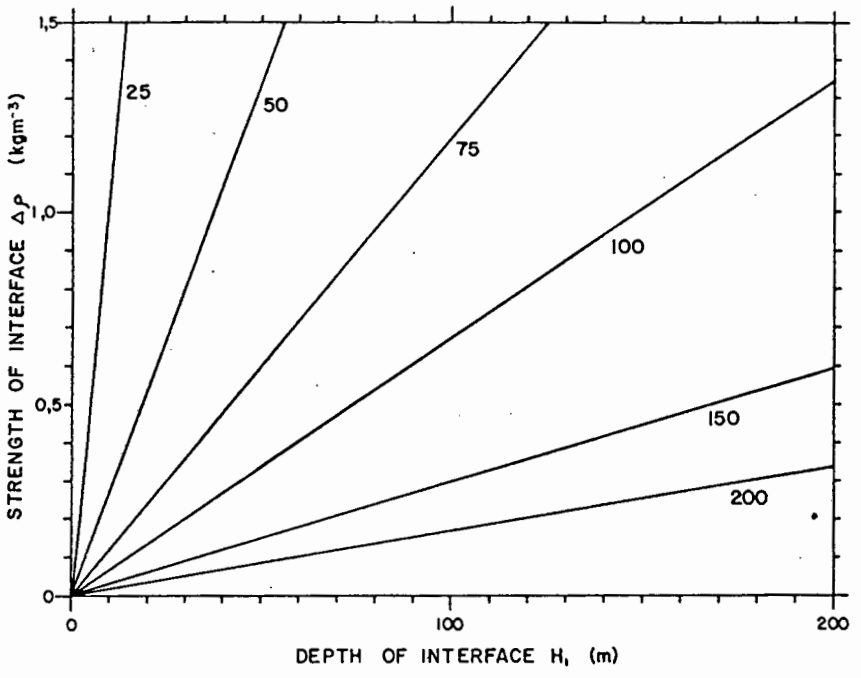

FIGURE 5.9: The stratification coefficient ϕ plotted as a function of interface depth H_1 and interface strength $\Delta\rho$; given semi-diurnal frequency $\sigma = 1,41 \times 10^{-4} s^{-1}$.

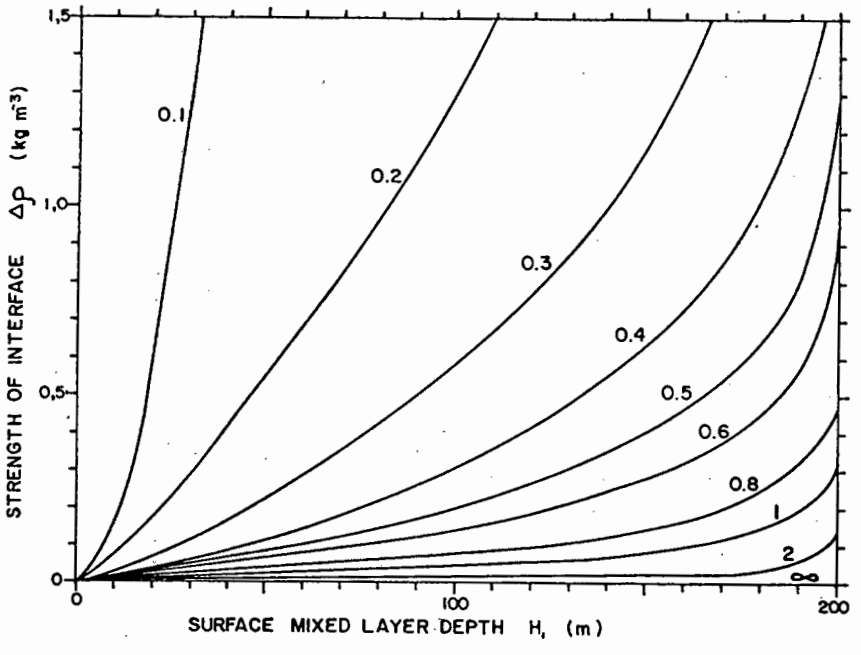

FIGURE 5.10: The interfacial tidal amplitude T plotted as a function of interface depth H_1 and interface strength $\Delta\rho$; given unit barotropic flow $\psi=1 m^2 s^{-1}$, semi-diurnal frequency $\sigma=1,41\times10^{-4} s^{-1}$, ocean depth $H_1=3\ 500$ m and shelf depth $H_+=200$ m. For real values of ψ (typically of the order of 10 $m^2 s^{-1}$), the interfacial amplitude shown here is multiplied by ψ.

Eq. 58 displays singularities in the interfacial wave as $H_1 \rightarrow H$ and as $\Delta\rho \rightarrow 0$. The linear model predicts very large amplitude (i.e. non-linear) waves near to these singularities. As T increases from zero, the linear formula (Eq. 58) loses validity but is retained as a first approximation for interfacial waves $T \lesssim 0{,}1$ H. Beyond this limit the waves are strongly non-linear and they are poorly described by linear theory. Finite-amplitude waves have a distorted wave shape with flattened crests or troughs near to an upper or lower boundary, respectively. The retention of second-order and third-order terms in the original formulation changes the theoretical orbits of the water particles and results in a steady, horizontal drift analogous to 'Stokes drift' for surface waves (Turner, 1973). Further, the group velocity increases proportional to wave amplitude. Apel (1981) accounts for the linearly decreasing wavelength, decreasing crest length and exponentially decreasing amplitude towards the rear of a packet (Section 4.1) in terms of non-linear theory.

Application on the Shelf. The above model was specifically derived in order to predict interfacial tides generated at the shelf-edge, irrespective of whether the barotropic forcing Ψ is due to Kelvin or Poincaré tides. The best results would be obtained with empirical on-the-spot data but, except for bathymetry, this data is usually not available and it is impracticable or unaffordable to measure it. Correct estimates of $\Delta\rho$, H_1 and U_b, which are crucial for credible prediction of internal waves, must be derived from historical data and analytical models. Stratification, by its nature, is horizontally extensive but it may change significantly with time. Areas characterized by quasi-interfacial structure usually exhibit clear seasonal trends. Since T depends weakly on $\Delta\rho$ and H_1 (unless $H_1 \rightarrow H$), adequate confidence can be shown in the use of historical CTD, BT and other temperature profile surveys. Nevertheless due regard should be given to contemporary wind-driven mixing events which impart a stepped shape to the seasonal trend (Section 6.2.1).

The barotropic tidal flow, in contrast, exhibits a deterministic time-dependence but is subject to spatial variation, particularly on a non-smooth shelf such as off Cape Point. In the absence

of local, historical data, one can only estimate tidal currents from models. Introducing the presence of a coast, a Poincaré barotropic tide is considered incident on the coast-shelf oceanic boundary, it is reflected and the resultant barotropic velocity at the shelf-edge is due to a vector sum of the velocities due to the incoming and outgoing waves. For zero or weak damping (e.g. Redfield, 1958), this results in a standing wave with amplitude 2A' and zero velocity at the coast. Surface elevation is given by $2A' \cos \sigma t \cos k \Delta x$ and velocity is given by $2\frac{c_b A'}{H} \sin \sigma t \sin k_b \Delta x$ at a location Δx from the coast. Generally $k\Delta x << 1$ so the maximum velocity is $\frac{c_b 2A'}{H} \cdot k_b \Delta x$ and is out of phase with the surface elevation. The same expression is given for Kelvin barotropic tides by Baines (1973), Petrie (1975) and Huthnance (1981) who relate the mass flux across the shelf to the amplitude of the tide at the coast. Thus

$$\Psi = U_b H = c_{b+} A_t k_b \Delta x = A_t \sigma \Delta x \qquad (59)$$

where $2A' \equiv A_t$

The dependence of Ψ on surface tide amplitude A and distance from the coast Δx is plotted in Fig. 5.11.

Battisti and Clarke (1982), following their own work (Clarke and Battisti, 1981), extend the classical canal theory of tides on the shelf to include the effects of longshore gradients and rotation. Nevertheless, the theory is developed for smooth continental shelves where long-shelf scales are much longer than cross-shelf scales. For non-broad shelves, the cross-shelf velocity U_b is given by Eq. 59 and long-shelf velocity is

$$V_b = \frac{A_t}{\frac{ir}{(1-\sigma H)}} \left(\frac{\Delta x \cdot f}{H} - \frac{g \cdot \partial y a}{\sigma \cdot a}\right) \qquad (60)$$

where r = Cu and C is the bottom drag coefficient. For broad shelves (large ℓ, small H) or short long-shelf scales, more complicated expressions are found for U_b and V_b (Battisti and

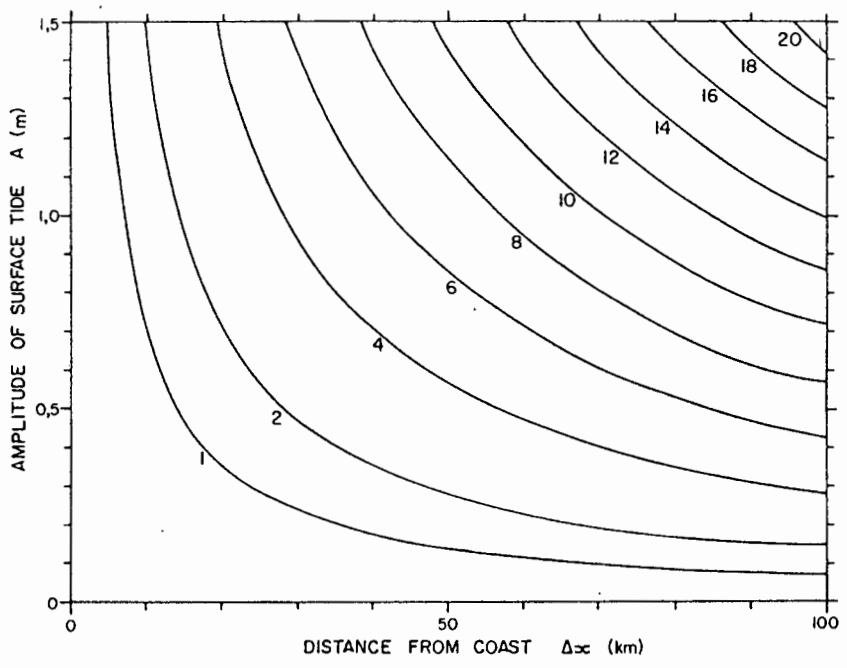

FIGURE 5.11: The cross-shelf barotropic transport ψ ($m^2 s^{-1}$), for a long smooth shelf, plotted as a function of surface tide amplitude on the shelf, A, and distance from the coast Δx; given semi-diurnal frequency $\sigma = 1{,}41 \times 10^{-4}$ s^{-1}.

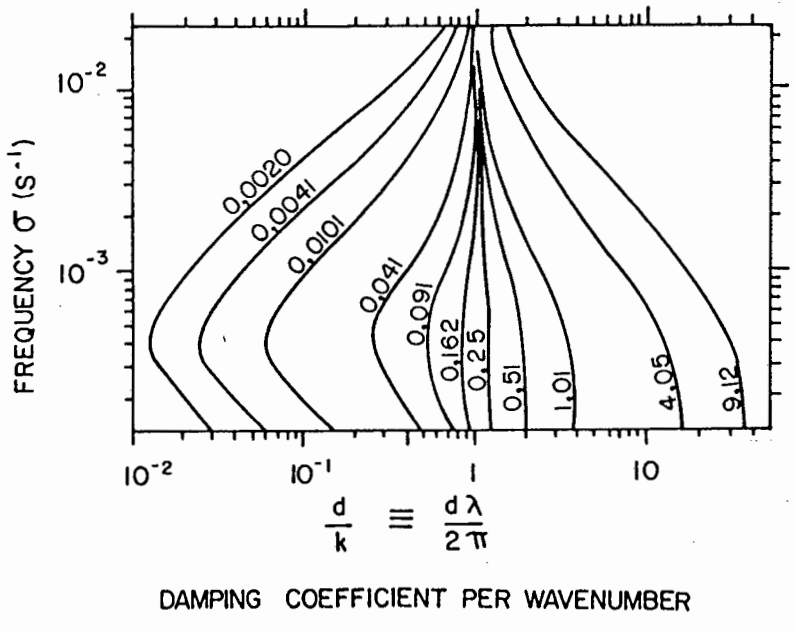

FIGURE 5.12: Damping of first mode waves, in a constant-N fluid, as a function of frequency for different values of the vertical eddy viscosity ν decreasing from 9,12 s^{-1} to 0,002 s^{-1}; given water depth H = 100 m and linear stratification $N^2 = 5 \times 10^{-4}$ s^{-2} [from Prinsenberg et al., 1974].

Clarke, 1982: Eq. 3.6, 3.7, 3.8 and 3.9). Confidence in this model is provided by good agreement with observed tides on both the east and west coasts of North America.

Although the Cape shelf is generally suitable for Eq. 59 and 60, the short long-shelf scales and irregularly curved edge in the Cape Point Study Area are not suitable for these expressions.

This interfacial shelf tide model, as a whole, is simple and correctly models the gross character of the internal tide. Confidence is gained from previous theoretical work, especially Baines (1982). Unfortunately, as for all internal shelf tide models to date, the energetic detail and background noise introduce large uncertainty to any prediction of amplitude. Largier (1987) has used this model to obtain a first approximation of the generation of internal tides at canyons on the continental shelf.

5.3 Propagation and Dissipation

In theory, it is now possible to determine the energy transfer to internal tides at the shelf-edge. However, in order to obtain values away from the shelf-edge, it is necessary to investigate how these waves propagate up a shoaling shelf. Three features are considered: continuous damping, wave intensification and wave breaking. Dissipation is thus accounted for as a combination of small-scale parametric mixing (damping) and larger-scale semi-deterministic events (internal tide breaking).

Damping. Damping, that is energy loss without structural breakdown, is understood to include the continuous mechanisms of viscous attenuation, bottom friction, non-linear wave-wave interactions and interaction with turbulence. Conventionally, the parameters of eddy diffusivity and eddy viscosity are used to describe the ability of the fluid to transfer properties and momentum, respectively. Since these fluxes are considered to be due to Reynolds stresses (eddy diffusion) the parameters should

be a function of the flow and not specific for a fluid. This inadequacy in the eddy coefficient approach is manifest in the wide range of values suggested in research reports. Further, these coefficients generally describe viscous attenuation only. Le Blond and Mysak (1978) obtain an expression which indicates that damping increases as the wavelength and buoyancy frequency decrease. Using a numerical scheme, Crampin and Dore (1970) relate relative damping lengths to wavenumber for particular density profiles, but only short waves are considered, in order that rotation may be neglected, and the results are inappropriate for internal tides. Prinsenberg et al. (1974) drew diagrams interrelating damping, wave-number and frequency for different modal numbers and different values of the horizontal eddy viscosity. Fig. 5.12 displays damping, expressed by a damping coefficient d, as a function of frequency and mode number. This result was derived for viscous attenuation in a constant-N, non-shelf environment. Damping is proportional to n/H, so higher modes in shallower water are damped more strongly. Le Blond (1966), who included an estimate due to bottom friction, found that, for weak continuous stratification, long waves in shallow basins (~100 m) are rapidly damped (e-folding length of about one wavelength).

The approach adopted in this thesis is that a damping coefficient d can be found to describe the gross, combined effect of damping mechanisms on the internal tide propagating coastward

$$T(x_2) = T(x_1)\, e^{-d(x_2-x_1)} \qquad \text{where } x_2>x_1 \qquad (61)$$

Although insufficient local data is available, d can be estimated from other reports of internal tides on the shelf. [A cross-shelf line of three moorings has been deployed east of False Bay, December 1986 to January 1987, in order to calculate a local value of d].

Rattray (1957) uses such a coefficient to describe the effect of friction on an interfacial wave in the ocean. Assuming a constant eddy viscosity ν, he obtains an expression for d for a long wave on a rotating earth.

$$d = \left(\frac{\nu}{2g'}\right)^{0,5} \left(\frac{H}{H_1 H_2}\right)^{1,5} \left(\frac{(\sigma-f)^{1,5} + (\sigma + f)^{1,5}}{4\sigma}\right) \qquad (62)$$

In this 2-dimensional model, ν is actually a vertical eddy viscosity and thus could realistically take values from $10^{-1}m^2s^{-1}$ in a breaking wave environment to $10^{-4}m^2s^{-1}$ in a quiescent environment (Rattray, 1957; Le Blond, 1966; Crampin and Dore, 1970; Wunsch, 1975; Muller, 1976; Ruddick and Joyce, 1979 and Holloway, 1984). For $\Delta\rho \sim 0,6 kgm^{-3}$, $H \sim 200m$ and $H_1 \sim 80m$, this corresponds to values of d from $5,8 \times 10^{-5}$ to $0,2 \times 10^{-5} m^{-1}$. The e-folding length of the semi-diurnal internal tide increases from about 17 km ($0,7\lambda$) to 541 km (23λ). Since the oceanic eddy viscosity is inappropriate for a shelf environment and the effects of breaking waves are excluded from this parameter, a value of 10^{-2} to $10^{-3}m^2s^{-1}$ ($d \sim 0,6$ to $1,8 \times 10^{-5}m^{-1}$ and e-folding length $\sim 2,3$ to 7λ) is suggested on the shelf. However, this only accounts for viscous damping and excludes bottom friction. It would be more realistic to double (cf. Le Blond, 1966) the value suggested (that is, $d \sim 1,2$ to $3,6 \times 10^{-5}m^{-1}$ and e-folding length $\sim 1,2$ to $3,5\lambda$). Accounting fo an inverse dependence on $\frac{H_1 H_2}{H}$ for viscous attenuation and an inverse dependence on $\frac{H_2}{2}$ for bottom friction, the damping coefficient is taken as

$$d = B \cdot \frac{(H+2H_1)}{H_1 H_2} \qquad (63)$$

where B is generally chosen as $10/\lambda$ such that $d^{-1} \sim \lambda$ for $H \sim 100$ m (Le Blond, 1966; Petrie, 1975; Holloway, 1983; Sandstrom and Elliott, 1984). Damping does not only dissipate energy, it also slows the wave down through a decrease in frequency. Nevertheless, this effect is small compared to that due to the decreasing depth as the wave propagates up the shelf. The former effect is neglected and the latter is roughly modelled for a slowly varying depth $\partial_x H << \frac{H}{\lambda}$. Wunsch (1969) theoretically described internal waves on a sloping bottom in a constant-N fluid. Cacchione and Wunsch (1974) studied this situation experimentally. In this section, the two-layer model is used because, as seen earlier, it is more appropriate and it yields a simpler result.

Intensification. In the absence of dissipation and reflection, the energy flux is constant across the shelf. However, it can be shown that with decreasing depth, the wavelength, phase speed and group speed decrease while the energy density and amplitude increase. Using constant depth solutions for slowly-varying depth,

$$\text{from Eq. 19} \quad \frac{c(x_2)}{c(x_1)} = \frac{c_g(x_2)}{c_g(x_1)} = \left(\frac{H_1(x_2)H_2(x_2)H(x_1)}{H_1(x_1)H_2(x_1)H(x_2)}\right)^{0,5}$$

$$\text{from Eq. 38} \quad \frac{T(x_2)}{T(x_1)} = \left(\frac{H_1(x_1)H_2(x_1)H(x_2)}{H(x_1)H_1(x_2)H_2(x_2)}\right)^{0,25} \tag{64}$$

$$\text{from Eq. 19} \quad \frac{\hat{U}(x_2)}{\hat{U}(x_1)} = \left(\frac{H_1(x_1)H_2(x_1)H(x_2)}{H(x_1)H_1(x_2)H_2(x_2)}\right)^{0,75}$$

These expressions are applied judiciously on the shelf where $H_1 < H$, $\partial_x H_1 << \frac{H_1}{\lambda}$ and $\partial_x H << \frac{H}{\lambda}$. The special cases of constant H_1 or sloping $H_1 = \varepsilon H$ are often useful. In the case of constant H_1:

$$\frac{T(x_2)}{T(x_1)} = \left(\frac{H_2(x_1)H(x_2)}{H(x_1)H_2(x_2)}\right)^{0,25} \tag{65}$$

and in the case of sloping $H_1 = \varepsilon H$, ε constant:

$$\frac{T(x_2)}{T(x_1)} = \left(\frac{H\ (x_1)}{H\ (x_2)}\right)^{0,25} \tag{66}$$

The thermocline off Cape Point rises towards the coast with increasing ε (Section 2.1 and Fig. 2.4b). The intensification factor therefore takes a value somewhere between that predicted by Eq. 65 and 66. Intensification of the wave counteracts the drain of energy through damping. These two effects are approximately independent and may be added linearly. Empirical dissipation rates implicitly describe the combined damping-intensification effect.

Turbulent Breakdown. Unless the internal tide is damped to extinction before it reaches the coast, catastrophic breakdown must occur on the shelf (in analogy to breaking waves on a beach). Such breakdown results in turbulent mixing and exchange across the pycnocline. The internal tide may become unstable as a result of shear instabilities or advective instabilities. Largier (1986) briefly reviews these two mechanisms.

Shear instabilities are due to the velocity shear field associated with the internal tide becoming supercritical in terms of the gradient Richardson Number

$$Ri = \frac{-g}{\rho_o} \frac{\frac{\partial \rho_o}{\partial z}}{\left(\frac{\partial u}{\partial z}\right)^2} \qquad (67)$$

If $Ri \leq Ri_{cr}$, then the shear $\frac{\partial u}{\partial z}$ overcomes the stratification $\frac{\partial \rho_o}{\partial z}$, vortices grow on the wave and turbulence results. Woods and Wiley (1972) discuss the evolution of these 'billow' mixing events (Kelvin-Helmholtz instabilities). If energetic enough, these billows coalesce and result in a new mixed layer with a maximum thickness $D_{max} \sim \frac{2\rho_o}{g\Delta\rho} \overline{(\Delta u)^2}$, where $\overline{(\Delta u)^2}$ is the mean square velocity shear over one wavelength, if all the dissipated kinetic energy of the wave is contained in the increased potential energy of the density structure (Turner, 1981). However, only part of the kinetic energy is taken up as potential energy: Thorpe (1973) and Thompson (1980) suggest that about $^1/_4$ of the energy released is taken up: thus $D_{max} \sim \frac{\rho_o}{2g\Delta\rho} \overline{(\Delta u)^2}$. This discussion is continued and developed in Section 7.1

Advective instabilities occur as the wave slows down and the amplitude increases. Eventually the local particle velocities ($\sim T\sigma$) may exceed the phase speed ($\frac{\sigma}{k}$) and a piece of dense water is advected forward of the wave crest. The density inversion leads to overturning and turbulent mixing. The end product of these Rayleigh-Taylor instabilites is a new mixed layer similar to that due to Kelvin-Helmholtz instabilities. Orlanski and Bryan (1969) show this mechanism to be a significant contributor

to internal wave breaking. The stability criterion, which relates to the wave slope Tk, has a critical value of about 0,34 (Thorpe, 1978). The slope will only exceed this value in exceptional cases of constructive interference of very large waves. However, on encountering shoaling topography T and k increase (Eq. 64). Therefore, it is expected that these advective instabilities will account for internal tide breaking as it approaches the theoretical singularity at the coast (cf. Fig. 3.3). From laboratory work of waves over shoaling bathymetry, Cachionne and Wunsch (1974) suggest that interface slopes in excess of 0,15 are unstable.

Conclusion. One would expect a wave on a shallow, gradual shelf to be damped more rapidly than it intensifies. It is unlikely to produce breakdown of the structure. Conversely a wave on a deep, steep shelf will be intensified more rapidly than it is damped. It is likely to result in structural breakdown. However, internal tides propagate through a background of transient motions and mean currents. Breakdown usually occurs as an amorphous, broad-band process due to the linear and non-linear interaction of all the dynamic components. Nevertheless, in the absence of other dynamics, Thorpe (1978, 1979) considers shear-induced and sloped-induced instabilities as end-points on a theoretical stability curve in wave-slope versus wave-shear space. The stability curve for transition-layer flow is drawn in Fig. 5.13 (from Munk, 1981).

5.4 The Cape Point Internal Tide

Application of Models. The models discussed in Section 5.2 can be applied to the internal tide off Cape Point and compared with empirical data. A simplified bathymetry (Fig. 5.14) is expected to account for the gross features of the generation process. This topography is prescribed by H_{OC} = 3 500 m, H = 200 m, $\delta \sim 0,07$ and ℓ = 60 km. The structure can be taken as two-layered and horizontally uniform with $\Delta\rho \sim 0,4$ kg m^{-3}, $H_1 \sim 80$ m and $N_O \sim 0,005$ s^{-1} for the period before 22 June. From

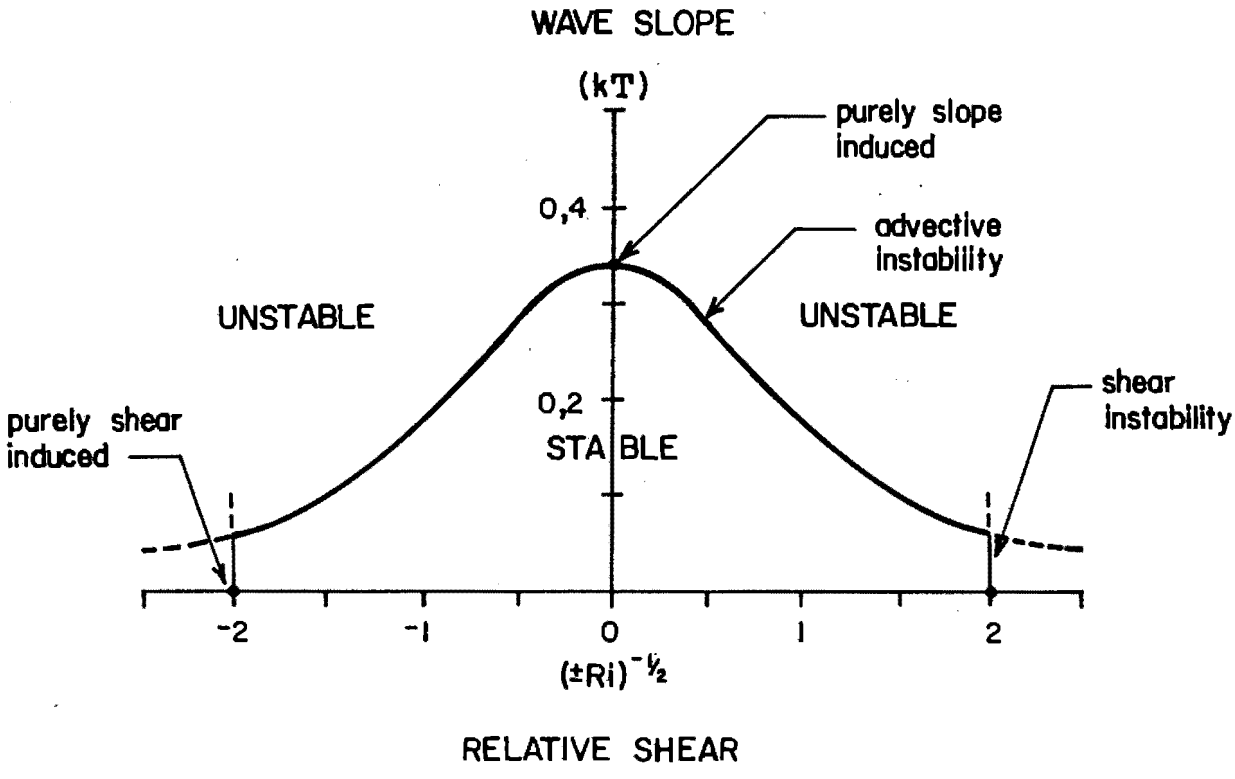

FIGURE 5.13: Stability curve for internal waves for a transition layer profile. Waves may become unstable owing to excessive shear (Kelvin-Helmholtz instability) or excessive slope (Rayleigh-Taylor instability).

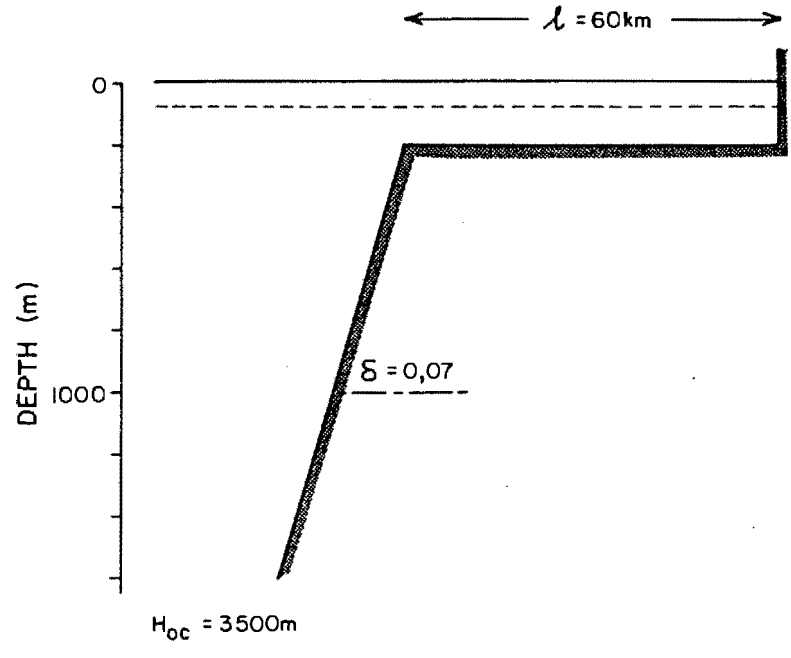

FIGURE 5.14: Model shelf profile which approximates the bathymetry about 20 km east of Cape Point Study Area. The shelf width is taken as for the study area and includes False Bay.

Fig. 5.3, with R = 0,4 and S~1,9 (Eq. 50) this interfacial wave is a valid representation of the first mode internal tide, which is expected to dominate on the continental shelf.

Following Rattray (1960), the tidal amplitude ratio $\frac{T}{A}$ is plotted for constant H_1, against a length ratio $\frac{\ell}{\ell_w}$ where ℓ_w is a horizontal length-scale of the wave (Eq. 47). For given $R = \frac{H_1}{H}$ and $R_{OC} = \frac{H_1}{H_{OC}}$, the internal tide response increases as the interface weakens, the interface deepens or the shelf widens (Fig. 5.15). For the chosen values, the length ratio is $\frac{\ell}{\ell_w}$=12,3. For a flat shelf (Eq. 45) this corresponds to an excessive response $\frac{T}{A}$ ~40 but for a sloping shelf (Eq. 46) this corresponds to a realistic $\frac{T}{A}$ = 5. The internal tide response $\frac{T}{A}$ is weakly dependent on the choice of H_{OC} but decreases strongly for increased H (Eq. 45 and 46).

Following Prinsenberg et al. (1974), an amplitude is predicted for the oceanward tide in a constant-N ocean. Choosing N~0,003 s^{-1} as representative of the above case, Eq. 48 gives $\frac{T_{OC}}{A}$ ~6, which is similar to the sloping-shelf prediction from Rattray (1960).

Following Baines (1982), and taking $\delta \to \infty$ as for Rattray, the internal tide response $\frac{T}{A}$ may be plotted against a length ratio $\frac{\ell}{\ell_{wv}}$ for given R and R_{OC}, where

$$\ell_{wv}^2 = \frac{g'H_1H_2}{(\sigma^2-f^2)H} = \frac{H_2}{H}\,\ell_w^2$$

In Fig. 5.15 this model is plotted relative to ℓ_w; for the chosen values, $\frac{\ell}{\ell_w}$ = 15,9 and $\frac{\ell}{\ell_w}$ = 12,3. A baroclinic response $\frac{T}{A}$ = 2,6 is predicted. The effect of finite slope δ is to decrease $\frac{T}{A}$ (Eq. 52 and Fig. 5.4).

Since Rattray (1960) unrealistically neglects damping (Section 5.3) and includes an interfacial wave reflected from the coast, his solution predicts much larger T than that due to Baines (1982). For A ~1 m, typical of spring tides at Cape

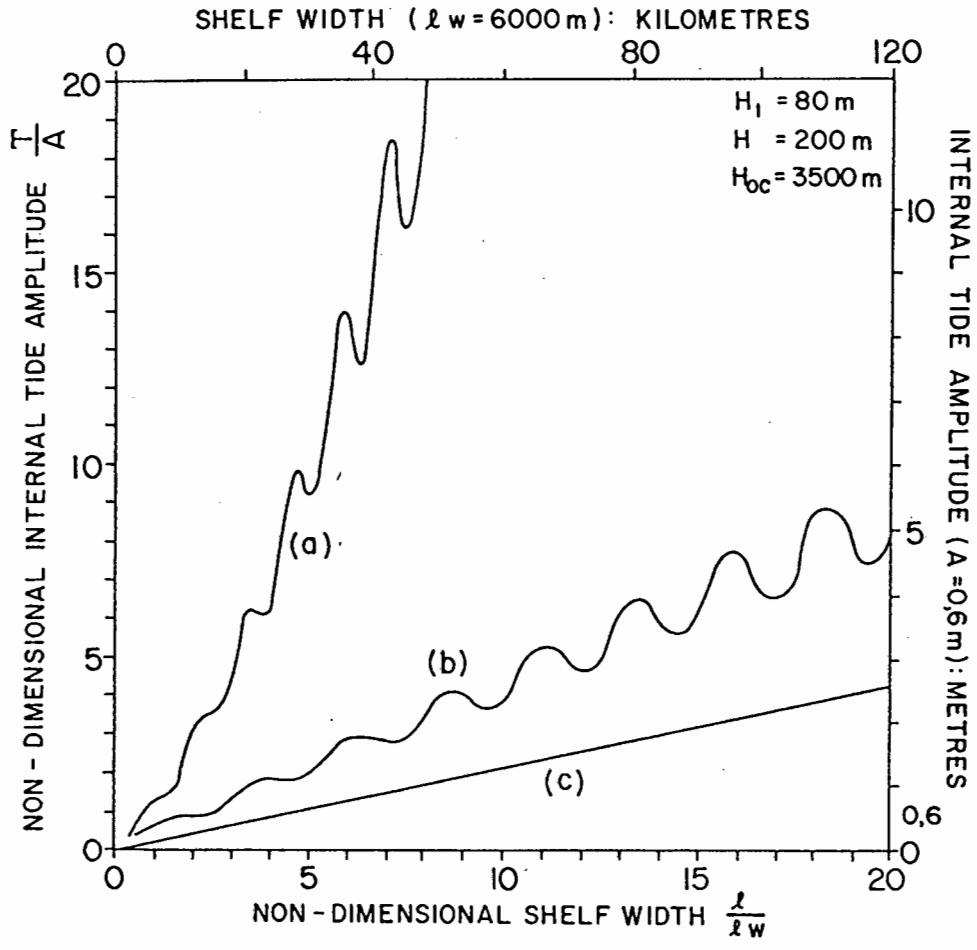

FIGURE 5.15: Predicted tidal amplitudes from (a) Rattray (1960) for a flat shelf; (b) Rattray (1960) for a sloping shelf and (c) Baines (1982) for a flat shelf (γ = 1). The models, discussed in Section 5.2, are applied for a typical Cape Point scenario with interface strength $\Delta\rho$ = 0,6 kgm^{-3}.

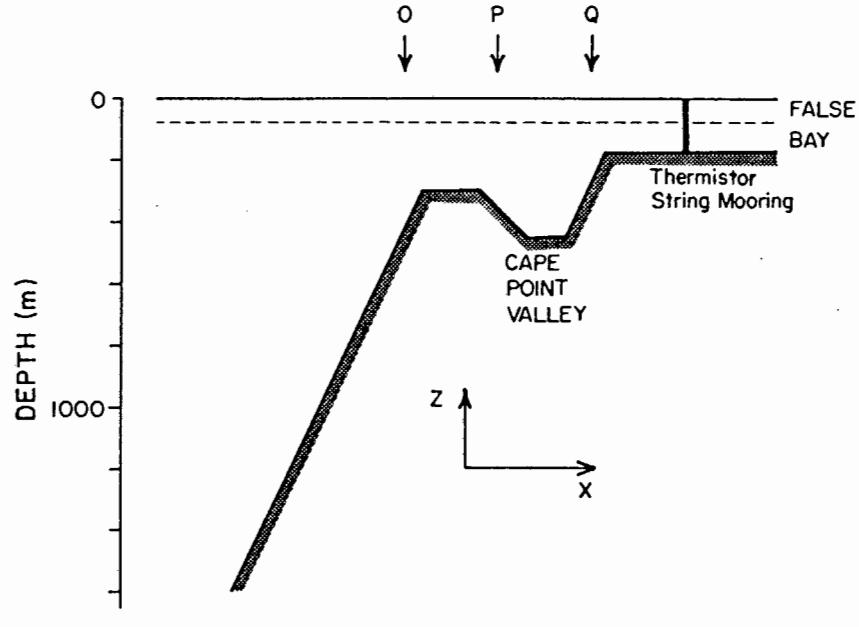

FIGURE 5.16: Model shelf profile which approximates the bathymetry offshore of the Cape Point mooring. The presence of Cape Point valley results in three separate generation sites O, P and Q (cf. Fig. 5.6).

Point, Baines (1982) predicts an internal tide of 2,62 m for a vertical step (γ=1). On propagating from the shelf edge (x_s) to the mooring (x_m) the wave is damped (Eq. 61 and 63) and intensified (Eq. 65):

$$T(x_m) = T(x_s) \cdot \exp \frac{-10(\bar{H}+2H_1)}{H_1 \bar{H}_2 \lambda} (x_m - x_s) \cdot \frac{H_2(x_s)H(x_m)}{H(x_s)H_2(x_m)}^{0,25}$$

where $\bar{H}$ and $\bar{H}_2$ are mean values over the distance $(x_m - x_s)$.

The mooring in 116 m depth is about 1,5 λ distant so that $T(x_m) = 0,466 \cdot 1,179 \cdot T(x_s) \sim 1,44$ m. This is clearly much less than the large amplitudes recorded at the mooring (Section 4.2).

Introduction of Cape Point Valley. It is suggested that the simple profile of Fig. 5.14 is inappropriate and leads to severe underestimation of the tide. The contours of body force plotted in Fig. 5.6 suggest that the internal tide shoreward of Cape Point Valley should be described by a sum of three components corresponding to generation at three sites: the shelf-edge (O), the outer valley wall (P) and the inner valley wall (Q), as depicted in Fig. 5.16. Landsat imagery (Fig.3.3 and 3.4) confirms that the monitored tide originates from the valley. Whether these components interfere constructively or destructively depends on the phase differences between the three components. Ideally O, P and Q would be separated by $\frac{\lambda}{2}$ and the three components would be in phase. This is expected to occur at Cape Point Valley for certain stratification (λ is a function of stratification, Eq. 19). From Eqs 58, 61, 63 and 65, the resultant tide at Q will be

$$T = \gamma_O \Delta_O \phi \; \Psi_O \; e^{-10(H+2H_1)/H_1 H_2} \cdot \frac{H_{2O}}{H_O} \frac{H_Q}{H_{2Q}}^{0,25}$$

$$- \gamma_P \Delta_P \phi \; \Psi_P \; e^{-5(H+2H_1)/H_1 H_2} \cdot \frac{H_{2P}}{H_P} \frac{H_Q}{H_{2Q}}^{0,25}$$

$$+ \gamma_Q \Delta_Q \phi \; \Psi_Q \qquad (68)$$

The same stratification parameters as above are used, with topography $H_- = 3\ 500$ m, $H_O = 300$ m, $\gamma_O \sim 0,5$, $H_P = 450$ m, $\gamma_P \sim 0,3$, $\gamma_Q \sim 0,5$ and $H_+ = 180$ m (Fig. 5.16). The barotropic flow is synoptic and, taken as uniform $\Psi_O = \Psi_P = \Psi_Q = 10\ m^2 s^{-1}$:

$$T = (0,5 \cdot 1,652 \times 10^{-3} e^{-0,227} \cdot 1,072 + 0,3 \cdot 0,630 \times 10^{-3} \cdot e^{-0,103} \cdot 1,103 + 0,5 \cdot 2,018 \times 10^{-3}) 116,11 \cdot 10$$

$$= 2,21 \text{ m}$$

Including a non-vertical step ($\gamma \sim 0,5$) in the model topography of Fig. 5.14, the interfacial tide has an amplitude of 1,55 m for a barotropic flow of 10 $m^2 s^{-1}$ at the shelf-edge, and an amplitude of 1,07 m one wavelength from the shelf-edge. Therefore, the effect of the valley profile is to double the barotropic-to-baroclinic coupling. Huthnance (1981) suggests that bottom damping is weak near the shelf-edge because the tidal characteristic (in a continuously stratified ocean) has not yet reflected from the bottom. If bottom dampling is neglected, then $d = \frac{10H}{H_1 H_2 \lambda}$ and Eq. 68 predicts T = 2,27 m, which is not much greater.

Using Eq. 59, with $\Delta x = 60$ km, one obtains $\Psi \sim 9\ m^2 s^{-1}$ for a 1 m amplitude, which corresponds to spring-tide surface elevations. However, the shelf around Cape Point is not smooth and the analytical model of Battisti and Clarke (1982) is not valid. A mooring in 282 m water depth off Slangkop (S, Fig. 2.1) recorded semi-diurnal tidal currents of about 3 to 4 cm s^{-1} (G Nelson, unpublished data, 1985). This would suggest a mean barotropic flow of $\Psi \sim 10\ m^2\ s^{-1}$ and spring-tide values $\Psi \sim 20\ m^2\ s^{-1}$. This is the best possible estimate of barotropic flow over the valley. Maximum spring-tide interfacial amplitudes at Q are thus over 4,6 m. On propagating to the mooring, a further $\frac{\lambda}{2}$, the internal tide converges (owing to convex bathymetry), intensifies and is damped.

$$T(x_m) = \sqrt{2}\ \left(\frac{100}{180}\ \frac{116}{36}\right)^{0,25}\ e^{-0,293} \cdot T(Q)$$

The predicted maximum spring-tide at the mooring is about 6 m. Maximum tides in excess of 10 m amplitude are recorded at the mooring during the spring-tides of May and June. If bottom friction is neglected a maximum of 7 m is predicted. Significant uncertainty is introduced by the choice of representative γ, $\Delta\rho$, H_1 and particularly Ψ. The predicted values are low but may conceivably be reconciled with the observed values by an optimum choice of γ, $\Delta\rho$, H_1 and Ψ. Barotropic flows of about 30 $m^2\ s^{-1}$ would account for the observed amplitudes. This corresponds to U_b ~10 cm s^{-1} (Fr ~0,2) at the shelf-edge and U_b~ 15 cm s^{-1} (Fr~0,3) over the canyon. Neglecting the canyon one needs barotropic flow of about 60 $m^2\ s^{-1}$ to account for the observed maxima; the corresponding U_b ~30 cm s^{-1} and Fr ~0,6 are unrealistic.

Factors Requiring Attention. As discussed in Section 5.2, simple internal tide generation models are capable of predicting only the gross features of the internal shelf tide. The detail of the topography, the stratification and the local barotropic flow, during the process of generation, may contribute substantially to the solution. In addition, various assumptions have been made. The four most important assumptions are revisited in order to account for the small amplitude predicted by the model.

1. Zero Reflection at the Coast: Internal shelf tides are strongly dissipated as they propagate coastwards (Section 5.3). It has thus become accepted practice to model internal shelf tides with zero reflection from the coastal boundary. This condition is not always well satisfied. Considering Rattray's (1960) solutions (Fig. 5.15), even fractional reflection should significantly increase internal tide amplitudes on the continental shelf (particularly for narrow shelves and near the coast, where the reflected energy has been dissipated to a lesser extent). The Landsat image for 6 January 1979 (Fig. 3.4) displays a group of slicks which appear to be reflected from the steep western

edge of the Cape Peninsula (Δz ~200 m in less than 2×10^4 m; this slope would be super-critical (Largier, 1986) for a temperature gradient in excess of about 1^oC per 10 m). It can be expected, therefore, that the shelf west of the Cape Peninsula will experience unconventionally large tides. The Cape Point mooring could also receive substantial reflected internal tide energy.

2. Two-layer Structure: As discussed in Sections 2.3 and 4.6, a constant-N structure will contain half the energy of a two-layer structure with the same internal tide amplitude T and bulk density difference $[\rho(-H)-\rho(0)]$. It is thus expected that, given constant energy transfer at the shelf-edge, a continuously stratified ocean would contain a greater amplitude internal tide than the corresponding two-layer ocean (i.e. the two-layer approximation leads to underestimation of T). This effect may be particularly significant since, following Fig. 5.3 (Baines, 1982), the chosen model stratification is only marginally two-layer.

3. Linear Model: With measured amplitudes of about 12 m in about 120 m water depth, the internal spring tides should be modelled non-linearly.

4. Constant Depth Interface: The above prediction was calculated by assuming H_1 constant. But in Section 2.1, two features were identified: coastal upwelling fronts ($H_1 \to 0$) and a sub-surface shelf-edge front. Upwelling is mostly absent in winter and is not accounted for here. However, the shelf-edge front is a semi-permanent feature (Fig. 2.4b) which weakens in winter. Judging from the amplitude of the tides measured at the mooring, this shelf-edge front was either seaward of the core generation regions (Fig. 5.6) or it had a sufficiently smooth gradient that it did not effect the efficient generation and propagation of internal tides. If one were to replace the 80 m thermocline with a 70 m thermocline at the mooring dipping

to a 100 m thermocline at the shelf-edge, then the generation would be enhanced (Eq. 58) but the intensification would be weakened (Eq. 64). The result is essentially the same: amplitudes of 6 m to 7 m are predicted. If H_1 were much deeper than 100 m at the shelf-edge, which is unlikely (Fig. 2.4b), then the predicted tide would be significantly larger (Fig. 5.10).

Evaluation of model. The characteristic intermittency of baroclinic tides is a consequence of time-varying density structures and dissipation rates. However, the intermittency displayed at Cape Point occurs on a shorter time scale. This is ascribed to changes in sub-tidal ambient currents which alter the interference of the three components. Cross-shelf flows will doppler shift the tides and long-shelf flows will advect waves from less efficient generation sites up-canyon or down-canyon of the profile modelled above. This intermittency is thus testimony to the above multiple generation process.

The model presented above is conceptually correct but suffers from significant uncertainty as a result of inexact estimates of $\Delta\rho$, H_1, γ and Ψ (Sub-Section 7.2.3). Underestimation is especially due to the assumptions of a non-reflective coast and of a two-layered structure. Further error is due to the assumptions of linearity and constant H_1. Although valid as $\frac{T}{H} \to o$ (or $Fr \to o$) and $S \to \infty$ these particular data reflect maxima $\frac{T}{H} > 0,1$ and minima $S \sim 2$. Baines and Fang (1985) compare linear theory with laboratory data for continuously-stratified and two-layer fluids. The two-layer theory only exhibited qualitative agreement for $Fr \sim 0,5$ and significant differences were observed for $Fr > 1$ owing to substantial advection and associated internal hydraulic jumps. With continuous stratification, linear theory is valid to greater values of Fr. Solutions involving continuous stratification are given by Rattray et al. (1969), Baines (1973, 1974, 1982) and Baines and Fang (1985). Future attention should be given to an equally simple prediction of quasi-interfacial or non-interfacial internal tide generation which includes a reflective coast.

5.5 Discussion of Energy Values

The energy of the internal tide on the SW Cape shelf can be compared with the results of other studies of semi-diurnal internal tides on continental shelves. The empirical energy values obtained through spectral analysis, a 2-layer model and a constant-N model (Section 4.6) are listed in Table 5.1 together with several other estimates taken from the literature. The values which were calculated from the mooring records, are translated to shelf-edge values through the approximations of the Section 5.3. The uncertainty involved in using such crude approximations is large so that one is only able to obtain an order of magnitude estimate. Also included in Table 5.1 is an energy estimate (Eq. 38) based on the mean interfacial tidal amplitude (2,5 m) predicted by constructive multiple generation (Section 5.4). Expressions given by Baines (1974 and 1982) severely underestimate the energy (cf. T in Section 5.4) and are not considered. Apart from the Wunsch and Hendry (1972) estimate, the energy values are all within one order of magnitude. These studies were all executed in areas where internal tides are significant, and usually dominant. Many other sections of continental shelf would have less energetic internal tide activity and would not attract studies of internal tides.

Global estimates of mean barotropic tidal energy vary from 0,2 kJm^{-2} (Munk and McDonald, 1960), to 2,2 kJm^{-2} (Henderschott, 1973) and to 4 kJm^{-2} (Le Blond and Mysak). Taking 0,6 m as the root mean square tidal amplitude at Cape Point, a local value of 0,9 kJm^{-2} is calculated from Eq. 44. From Table 5.1 it appears that the internal tide energy density is between 10% and 30% of the surface tide. Converting to energy fluxes, the local surface tide of period 12,42 hr across a shelf 60 km wide corresponds to 1,2 kWm^{-1}. Expecting equal internal tide energy to be radiated from the shelf-edge towards the ocean and towards the shelf and expecting some input to the stratified continuum, the values from Table 5.1 suggest that between 20% and 30% of

	LOCATION	ENERGY DENSITY ($J.m^{-2}$)	GROUP SPEED (ms^{-1})	ENERGY FLUX ($W.m^{-1}$)
Literature (References)				
Wunsch and Hendry (1972)	slope	-	-	6(?)
Petrie (1975)	slope	1 700	-	800
Schott (1977)	-	-	-	110
Hendry (1977)	ocean	90	2,78	300
Gordon (1979)	slope	-	-	300
James (1982)	slope	1 270	1,41	1 790
Baines (1982)	shelf-break			30 to 7 000
Huthnance and Baines (1982)	slope	-	-	~1 000
Sandstrom and Elliott (1984)	shelf-break	1 387	~1	1 387
Holloway (1984)	shelf (125 m)	-	-	327
	shelf (70 m)	-	-	7
Cape Point Mooring (Calculation Methods)				
Two-layer ($T\sim5$ m, $\Delta\rho\sim0,4$ kgm^{-3})		76	0,4	30
Constant-N ($T\sim5$ m, $N^2\sim8\times10^{-5}s^{-2}$)		96	0,3	29
Spectral (Table 4.2)		170	0,3	50
Cape Point Shelf-Edge (Calculation Methods)				
Extrapolation (Section 5.3) [Damping, Intensification, Convergence]		40 to 340	0,5 to 0,7	20 to 240
Prediction (Section 5.4, $T\sim2,5$ m) [Model of Generation]		20	0,5	10
Suggested Internal Tide		200	0,7	140
Surface Tide		900	-	1 200
Percentage Energy Transfer		22	-	12

TABLE 5.1: Comparison of reported energy values, for continental shelf tides, with estimates for the non-summer internal tide at the Cape Point mooring and with estimates of shelf-edge energy. The last three entries compare the suggested shelf-edge internal tide energy with the energy of the surface tide. It should be noted that these values are order of magnitude estimates with poor precision.

the surface tide flux is transferred to the internal tide. Since the local tide seems to be of average energy, and the energy conversion rate seems to be as expected (Wunsch, 1975), the local energy flux estimate (~300 Wm^{-1}) should be a realistic approximation of a global mean shelf value. Expecting $1,5 \times 10^{8}$ m of shelf-edge (Inman and Brush, 1973), the total shelf will account for about 10^{11}W, as compared with 5×10^{11}W suggested by Bell (1975) for the internal tide generation in oceanic areas. Added together these estimates support Wunsch's (1975) suggestion that internal tides remove energy at about 10% of the rate that energy is lost by the moon.

CHAPTER 6
THE SUB-TIDAL SIGNAL

In the same way that the tidal signal has been accounted for, the inertial signal may be expressed in terms of a simple, linear, two-layer model (Sub-section 6.1.1). With the help of this model, a few clear inertial events can be identified in the temperature record (Sub-section 6.1.2).

In addition, this chapter addresses sub-inertial forced changes in the interfacial depth. One-dimensional models of mixed layer deepening are considered (Sub-section 6.2.1) and identifiable deepening events are accounted for in terms of wind-driven inertial motions (Sub-section 6.2.2). It is found that these events are largely a result of wind-driven shear at the base of the mixed layer.

6.1 The Inertial Signal

The time-series plots (Section 4.2) and spectral plots (Section 4.4) reflect the presence of inertial motions. Following Pollard (1970), Pollard and Millard (1970), Kundu (1976), Pollard (1980), Krauss (1981), Price (1983), Jensen (1983), D'Asaro (1985a) and D'Asaro (1985b), it is expected that upper ocean inertial motions are generally driven by the local wind stress on the surface. These essentially horizontal currents are an important, and sometimes dominant, feature in shelf dynamics. The inertial events recorded by the thermistors, presumably due to the presence of a horizontal temperature gradient (Section 4.2), are found to correlate with significant wind events. The nature of the motions is such that they are clearly wind-forced. In Sub-section 6.1.1 some of the relevant theory is briefly discussed. The few clear observations are interpreted in terms of these models (Sub-section 6.1.2). In conclusion, it is expected that the current records would contain a strong inertial signal.

6.1.1 Theory of Wind-driven Near-inertial Motions in the Surface Mixed Layer

The action of wind on the sea surface is shown analytically to be effective in generating a geostrophic flow, a transient non-oscillatory transverse flow (Ekman transport) and an inertially rotating flow (Pollard, 1970). Non-steady, wind-generated turbulence will be dealt with in Section 6.2.1. For winds of short duration (several inertial periods), which are discussed here, the geostrophic response is weak and is neglected in the following. In order to discuss the 'inertial' response a simple damped slab model (Pollard and Millard, 1970, Pollard, et al., 1973, Kundu, 1976, Gill, 1982 and D'Asaro, 1985b) is presented. The transient Ekman response is included in this model.

The mixed layer above the thermocline is assumed to move as a slab. In other words, the density (temperature) and horizontal velocities are independent of depth for $-H_1 < z < o$. The eddy viscosity is effectively infinite in the mixed layer and zero at the free-slip interface (thermocline). No momentum is transferred to the deeper slabs. Neglecting horizontal gradients and advection, the equations include a linear damping term $r\underline{u}$. A wind stress $\underline{\tau} = (\tau_x, \tau_y)$ is applied at the surface.

$$\frac{\partial u}{\partial t} - fv = \frac{\tau_x}{H_1 \rho} - ru$$

$$\frac{\partial v}{\partial t} + fu = \frac{\tau_y}{H_1 \rho} - rv \qquad (69)$$

The e-folding time r^{-1} is of the order of 2 to 10 days with both Pollard and Millard (1970) and D'Asaro (1985b) choosing $r^{-1} = 4$ days to obtain optimum simulation (Kundu, 1976, has $r^{-1} = 2$ days). Solution of these equations is given by Gold (1908, cited by Gill, 1982) for constant stress τ (Pollard, 1970, discusses spatially variable wind fields), for $r = 0$ and at a time t after the wind was switched on:

$$u = \frac{\tau_y}{\rho f H_1} + \frac{1}{\rho f H_1}(\tau_x \sin ft - \tau_y \cos ft)$$

$$v = \frac{-\tau_x}{\rho f H_1} + \frac{1}{\rho f H_1}(\tau_x \cos ft + \tau_y \sin ft) \qquad \text{for } 0<t<T \quad (70)$$

The underlying layers remain at rest. When the wind stress is switched off (at time T), the first terms (Ekman transport) fall away. The inertially rotating terms remain and are damped ($r^2 << f^2$ for realistic simulation):

$$u = \frac{1}{\rho f H_1}(\tau_x[\sin ft - \sin f(t-T)] - \tau_y[\cos ft - \cos f(t-T)])e^{-r(t-T)}$$

$$v = \frac{1}{\rho f H_1}(\tau_x[\cos ft - \cos f(t-T)] + \tau_y[\sin ft - \sin f(t-T)])e^{-r(t-T)} \qquad \text{for } t>T \quad (71)$$

D'Asaro (1985b) shows that inertial oscillations are excited by changes in the stress rector (τ_x ,τ_y) or the mixed layer depth H_1. One can usually ignore $\partial_t H_1$ but it is conceivable that in the presence of a significant wind stress, a large-amplitude and shallow internal wave may drive a significant inertial response. Both Stern (1975) and D'Asaro (1985b) show an 'inertial resonance' in an expression for currents driven by winds of frequency σ, as $\sigma \to f$.

The energy of these horizontal motions is all kinetic energy. While the wind is active the energy is a function of time due to the successive generation ($2\pi n < tf < (2n+1)\pi/2$) and destruction ($(2n-1)\pi/2 < tf < 2\pi n$) of the inertially rotating current vector.

$$E = KE = \frac{1}{2}\rho H_1 (u^2 + v^2)$$

$$= \frac{(\tau_x{}^2 + \tau_y{}^2)}{\rho H_1 f^2} \cdot (1-\cos ft) \qquad \text{for } 0<t<T. \quad (73)$$

For times after the wind has been switched off, the energy decays due to the damping coefficient r.

$$E = \frac{(\tau x^2 + \tau y^2)}{\rho H_1 f^2} \cdot (1 - \cos f T) \cdot e^{-r(t-T)} \quad \text{for } t>T.$$

From the above model one can conclude that winds with a rapid (of the order of half an inertial period) change in direction or strength will be effective in changing the amplitude and phase of inertial motions in the surface layer. Such wind changes may occur as frequently as the decay time of inertial motion (~4 days). Therefore, in modelling inertial currents, it is often necessary to vector-add successive responses - that is, inertial currents depend on the **history** of the local wind.

In reality the eddy diffusivity is non-zero at the base of the mixed layer and inertial energy propagates from the surface through the mixed layer and into the thermocline. Largier (1986) presents the inertial oscillation as a limiting form of an internal wave ($f \leq \sigma \leq N$); through this it is clear from Eq. 7 and 8 that the vertical group velocity should be proportional to $N(z)^{-1}$. Inertial energy propagates very rapidly (time scale $<< T_f = \frac{2\pi}{f}$) through the mixed layer ($N(z) \to 0$) but on encountering large $N(z)$ at the thermocline the group velocity decreases significantly, taking several days to penetrate a thermocline layer (Pollard, 1980, finds values of 0,03 m to 3 m per day; Kundu, 1976, suggests about 25 m per day). As expected, large coherence between upper layer current measurements decreases sharply at the thermocline. Clearly strong velocity shear at the base of the mixed layer is expected. Turbulent breakdown and deepening, which may result, are discussed in Section 6.2.

Horizontal scales, initially set by atmospheric forcing, rapidly decrease to ocean scales (Kundu, 1976, finds a wavelength of 60 km on the Oregon shelf). Small horizontal group speeds (Pollard, 1980 finds values of 1 to 20 km/day) imply that inertial responses are local features which require local or near-local wind data in order to attempt a prediction. The frequency of inertial waves has been found to be slightly (usually 5% but up to 20%) higher than the inertial frequency. Pollard (1970), Kundu (1976) and Kunze (1985) confirm this tendency through observation and theory.

Pollard (1980) considers the loss of energy from the inertial motions. The damping coefficient approach, adopted here, relies on a choice of r. Jensen (1983) cites several references from which it appears that r is greater on the shelf where bottom stress may account for more rapid decay (Blackford, 1978). Values from 3×10^{-6} s^{-1} to 7×10^{-6} s^{-1} are suggested. For this study, a value of 4×10^{-6} s^{-1} (e-folding time of about 3 days) is chosen as representative of the shelf away from the coast (100 to 300 m). The significant currents measured below the mixed layer by Kundu (1976) on the Oregon shelf prompted further investigation. Kundu (1984) suggests that rapidly varying wind forcing is capable of pumping inertial energy downward from the coast-surface corner. The presence of the coast provides the spatial inhomogeneity necessary for this vertical dispersion. In these coastal areas wind-driven sub-thermocline amplitudes may be as much as 50% of amplitudes in the upper mixed layer. Krauss (1979) describes the inertial waves in a channel of finite width and infinite length. In addition to the surface layer inertial currents described above, the onset of a geostrophic current, due to sea surface slope, gives rise to sub-thermocline inertial waves which are 180° out of phase. In either case the response at depth will lag the response of the mixed layer.

6.1.2 Interpretation of Observed Inertial Motion

Temperature is a poor monitor of inertial motions. Nevertheless the records from Cape Point do indicate the presence of inertial energy. A perusal of current-meter records (usually below the thermocline) confirms the presence of inertial currents and supports Kundu's (1984) suggestion that sub-thermocline inertial energy can be large in coastal waters. These current-meter records, as well as wind records at Olifantsbos (Figure 1.1), were obtained from the Sea Fisheries Research Institute.

Little quantitative information can be obtained from the data but qualitative results are well represented by the model. At least three significant events were recorded during the first

deployment. The frequency of the spectral peak, due to these events, is poorly resolved and cannot be assigned a precise value (~21hr period). Each event was associated with some structural change - presumably due to inertial shear at the base of the mixed layer. Other non-mixing events are expected but were not clear, probably due to the lack of a horizontal temperature gradient. Although residual currents from a previous wind pulse should be included in a model of a new event, it assumed that these residual currents are negligible relative to the strong events investigated.

On 19 May, northerly winds increased to about 20 ms^{-1} before rotating anti-clockwise on 20 May with the passing of an intense cold front (Figure 6.1). The time scales appear to be conducive to significant generation of inertial motion. Using a drag coefficient of $1,8 \times 10^{-3}$ (Large and Pond, 1981), the formulation of the previous sub-section, with H_1~45 m, suggests currents of the order of 0,2 m s^{-1} in the mixed layer. Although increasing in strength, the pre-frontal wind peak lasts for about an inertial period and it is probable that the rapid post-frontal backing of the wind is the more efficient generator. Hints of inertial frequency dynamics are found in the temperature record from 20 May (Fig. 4.1) and lasting for several days (not necessarily due to this single event). The currents at 101 m describe an inertial rotation on 21 May. There appears to be a day's lag between the arrival of energy at the shallow thermistors (mixed layer) and its arrival at the deep thermistors (below the thermocline).

Two intense cold fronts passing between 21 and 24 June (Fig. 6.1) precede severe breakdown and deepening of the structure. The characteristic pre-frontal northerly winds (~20 m s^{-1}) back to westerlies with the passing of the front. The absence of inertial temperature fluctuations does not exclude the presence of strong inertial currents above the thermocline. After deepening (23 to 26 June, Appendix (a)), inertial responses are observed below the thermocline at the deepest

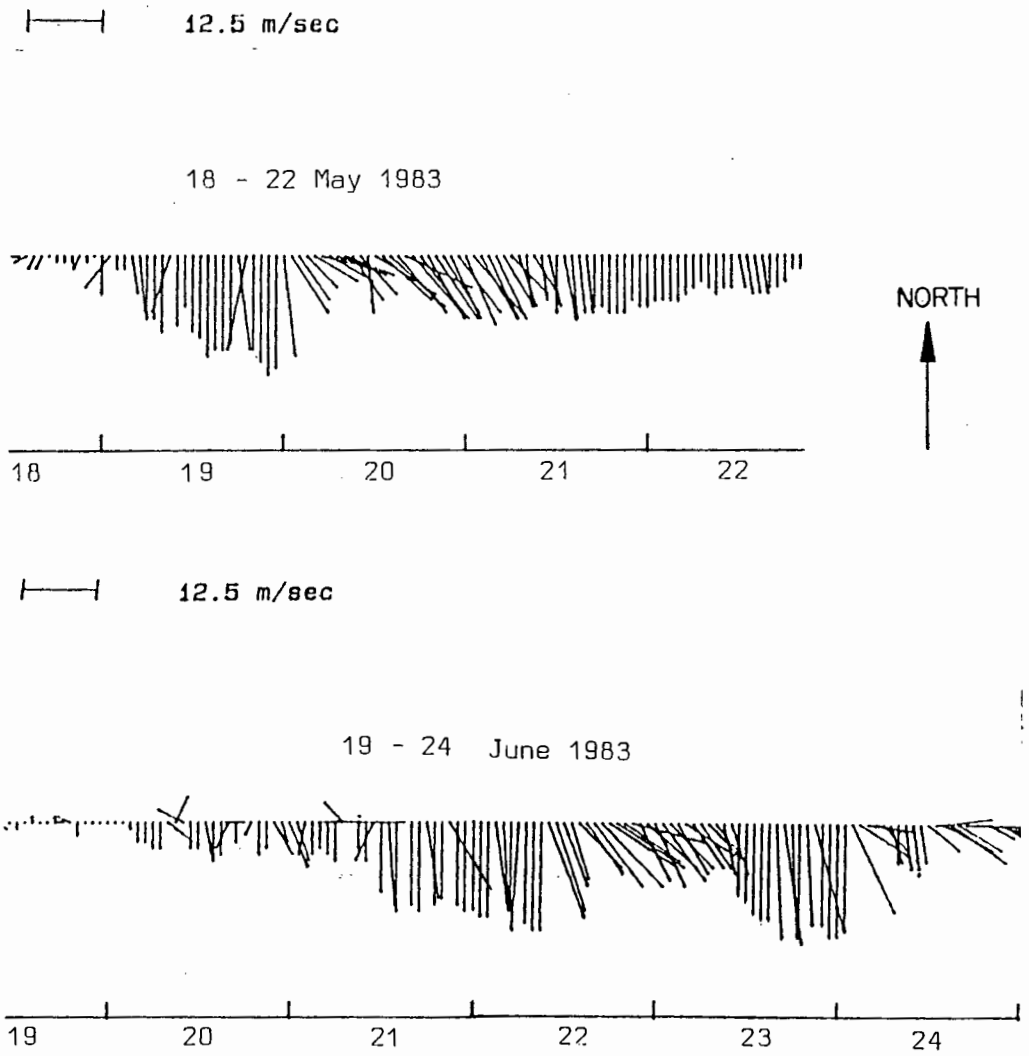

FIGURE 6.1: Typical winter-time 'north-west' wind events associated with the passage of mid-latitude cyclones (courtesy of G Nelson, unpublished data).

thermistor (95 m) and at the current meter (101 m). A lag of several hours is recorded between the two depths. The sub-thermocline current response is of the order of 0,05 m s^{-1}. Similar inertial energy is detected after a weaker cold front with rapid backing (3 and 4 July). The response at the deepest thermistor leads that detected by the current meter by half a day.

The temperature spectra of the second deployment display a marked decrease of the inertial peak with depth. Although weak, the temperature signal indicates several inertial events due to passing cold fronts. These frontal winds were recorded on 27-28 August, 1-2 September, 11-12 September and 15-16 September (Appendix (b)). Inertially rotating currents are suspected at these times from an inspection of current-vectors at 85 m (8 m below the thermistor string), which is probably in or below the thermocline. It is expected that the two periods of persistently strong 'south-easters' from 7 to 9 September and from 22 to 24 September would also have generated inertial motions. In this case, the Ekman transport gives rise to coastal upwelling (Boyd, et al.,1985) and the model presented above is not appropriate on the inner shelf. The winds during the third deployment are predominantly quasi-steady south-easters that result from the South Atlantic High ridging in south of the continent (typically in spring and summer). A new thermocline above the thermistor string (Section 4.3) hinders the downward propagation of the inertial motions.

Unfortunately, prediction of wind-driven motions is made difficult by the lack of local wind data. From Figure 1.1 and Section 2.1 it is clear that the coastal site at Olifantsbos is under the influence of the peninsula topography and may record much weaker winds than the mooring site. Further, a strong wind shear exists for 'south-easters' with the winds off Cape Point consistently stronger than further north (Jury, 1984). The Olifantsbos south-easter wind strengths of 12 m s^{-1} probably correspond to winds of 15 to 20 m s^{-1} at the mooring site and double the wind stress. This will lead to stronger inertial motions and stronger upwelling off Cape Point.

6.2 Mixed-Layer Deepening Events

In the temperature spectrum (Figs 4.8, 4.10 and 4.11) there is a shoulder at low frequencies (several days). Although components of this signal are due to a wide variety of dynamics corresponding to a very broad band of frequencies, it is the episodic mixing events which are of interest in this thesis. A few examples are found in the time-series plots of data. In Sub-section 6.2.1 some of the contemporary theory on mixed layer deepening is discussed. This enables one to understand the observed events, which are considered in Sub-section 6.2.2. These thermocline-penetrating events closely follow intense wind events, as would be expected.

6.2.1 Theory of Mixed Layer-Deepening

Mixed layer models are almost exclusively one-dimensional, that is, horizontal gradients and advection are not considered. In these models two crucial hypotheses are used (Garwood, 1979); (1) mixing within the turbulent boundary layer, and at its base, occurs in response to local atmospheric forcing (wind stress and heat flux); (2) the mechanical heat budget is the key to prediction.

In general, discussion centres on fluxes of momentum and heat across the surface and across the base of the mixed layer. Bulk models thus consider the mixed layer as a slab (Pollard, et al., 1973; Niiler, 1975; Davis, et al., 1981, amongst others) with uniform density (temperature) and mean velocity. Mixed layer depth and temperature are related to surface wind stress and heating by assumed parameters which describe the turbulent energy production and partition. At this stage it is useful to distinguish between mechanically generated turbulence and convective turbulence (Turner, 1981) in order to compare the scales of the processes. Convective effects, which are not limited by rotation, dominate mixed layer depth variations on a seasonal time scale (Krauss and Turner, 1967). However, effects due to

surface wind stress will dominate on a short time scale, of the order of an inertial period (Pollard, et al., 1973). The subsequent discussion is concerned with this 'event' time scale. Further, it is assumed that the periods between events are such that the cooling results in 'non-penetrative' convective turbulence (Gill and Turner, 1976). Therefore, each wind-driven deepening event is analysed by neglecting surface heating. Niiler (1977) also neglects dissipation and proceeds to identify four consecutive dynamic stages following the onset of surface wind stress (Niiler and Krauss, 1977, present a more general model which includes heating and dissipation terms). Essentially, the increase of potential energy of the structure (Π) together with ability of the mixed layer to store turbulent energy (Ω) are equated to the production of turbulent energy by surface shear (∇) and the production of the turbulent energy by shear across the base of the mixed layer (Σ). The four stages, reviewed by Turner (1981), are:

1. Intially (Ω) balances (∇): H_1 ~ few metres; t ~ few minutes.
2. Soon (Π) balances (∇): H_1 ~10 to 15m; t ~ $\frac{10}{N}$ ~ half hour.
3. Then (Π) balances (Σ): H_1 ~20 to 35m; t ~ $\frac{\pi}{f}$ ~ten hours.
4. Eventually (Π) balances (∇): slow erosion may continue.

In essence, a steady background shear field exists as a result of ∇ combined with an interactive internal wave field. D'Asaro (1985a) obtains an oceanic background value of Ri~2,5 and Oakey and Elliott (1982) obtain a mixed layer value of Ri<1 near the surface increasing to Ri ~4 towards the base of the mixed layer. Added to this is an episodic, energetic shear at the base of the mixed layer, due to wind-driven inertial motion (Section 6.1.1). Once the layer is deeper than 10 or 15 m, it is these events which seem to bring about the significant structural changes (Pollard, et al., 1973; Kundu, 1976; Krauss, 1981; Oakey and Elliott, 1982; Jensen, 1983; D'Asaro, 1985a; D'Asaro, 1985b; Gregg, et al., 1986). Further, Oakey and Elliott (1982) suggest that persistent density (salinity)

structure which extends well into the mixed layer is evidence that the lower half of the 'mixed layer' is **not** being continually mixed by surface-generated turbulence. This should be considered together with Turner's (1981) comment that strong evidence exists for a gradient region below the interface, which is indirectly mixed by surface stirring.

Ultimately, the mixed layer is deepened by sub-critical Ri at its base. However, the controversy continues regarding the relative contributions to shear from mean flow (inertial motions), surface-generated turbulent flow and internal waves (Garwood, 1979). The model of Davis et al. (1981) employs two parameters m_o and m_s which describe the contributions of surface-generated turbulence and internal shear-generated turbulence, respectively, to the increase of potential energy. It was found that m_o determines the limits of deepening and m_s governs the rate of response to a wind. Tuned for data from MILE, the 'best fit' was obtained for $m_o = 0,39$ and $m_s = 0,48$. Zero-shear models ($m_s = 0$) would seem to be appropriate for areas of moderate and fairly continuous wind stress (and consequently fairly shallow mixed layers). In contrast, models which only consider shear ($m_o = 0$) are probably good approximations in areas of intense wind events, and in particular when the winds rotate inertially (e.g. cold fronts). In such cases the mixed layer may deepen rapidly and well beyond shorter-period, remote, surface-generated turbulence.

In this work, the emphasis is on dominant and short-time (order of a day) response of a pre-existent mixed layer (of the order of 10 to 20 m) to wind. Consequently the mean surface heat flux is taken as zero (convective mixing is excluded) and the surface-generated turbulence is taken as having negligible effect. This choice is supported by the eventful nature of the local wind field (Section 2.1): cold fronts in winter and 'south-easters' in summer. Pollard et al. (1973) provide a simple and reliable model based on wind-driven inertial motions (including Ekman transport) and a Richardson Number criterion. A modified version of this model is described below.

The wind-driven currents, described in Section 6.1, are modelled by Eq. 70 and 71 in the mixed layer and are taken as zero below the mixed layer. The stratification is chosen as in Eq. 49: a mixed layer, of temperature T_m and depth H_1, overlies a stratified layer, of temperature $(T_n + \Gamma z)$ and depth H_2 (Fig. 6.2). Pollard et al. (1973) discuss the choice of a closure term relating the momentum and buoyancy fluxes. A Richardson Number criterion is chosen, in particular for zero heat flux. While deepening is active (H_1 increasing) the flow is marginally stable and $Ri = Ri_{cr}$, a critical value. Following Turner (1973), Mellor (1973, cited by Niiler and Krauss, 1977) and Thompson (1980), the gradient Richardson number has $Ri_{cr} = 0,25$. In contrast, Abarbanel (1984) suggests the use of $Ri_{cr} = 1$ for finite amplitude motions. It is necessary to consider the contexts and qualifications implicit in these suggestions. In this work, the value $Ri_{cr} = 1$, used with a bulk Richardson number Ri_o (as discussed by Pollard et al., 1973), is indicative of both onset and decay of mixing.

$$Ri_o = \frac{g}{\rho} \frac{\Delta\rho}{(\Delta u)^2} \frac{D_u^2}{D_\rho} \tag{74}$$

where $\Delta u \equiv \hat{u}$ is the velocity shear for deterministic dynamics,
D_u is the vertical length associated with Δu,
D_ρ is the vertical length associated with $\Delta\rho$,
Ri_o is a finite difference approximation of the gradient Richardson number Ri (Eq. 67).

The critical Richardson number receives further attention in Section 7.1.1.

The wind-driven velocity shear $\hat{u}_w$ is given by Eq. 70 and 71 since $u = v = 0$ in the lower layer. The maximum velocities are obtained while the wind is active. If the wind persists for $t = \frac{\pi}{f}$ then maximum deepening is achieved at this time. Further deepening is limited by rotation (Davis et al., 1981). The initial stratification is defined by H_{1o}, T_{m_o}, $\Delta T_o = T_{m_o} - T_{n_o} + \Gamma H_{1o}$ and Γ (Fig. 6.2); the final stratification is H_1, T_m, ΔT and Γ. A constant temperature-salinity relationship is expected and accounted for in the coefficient of thermal expansion α

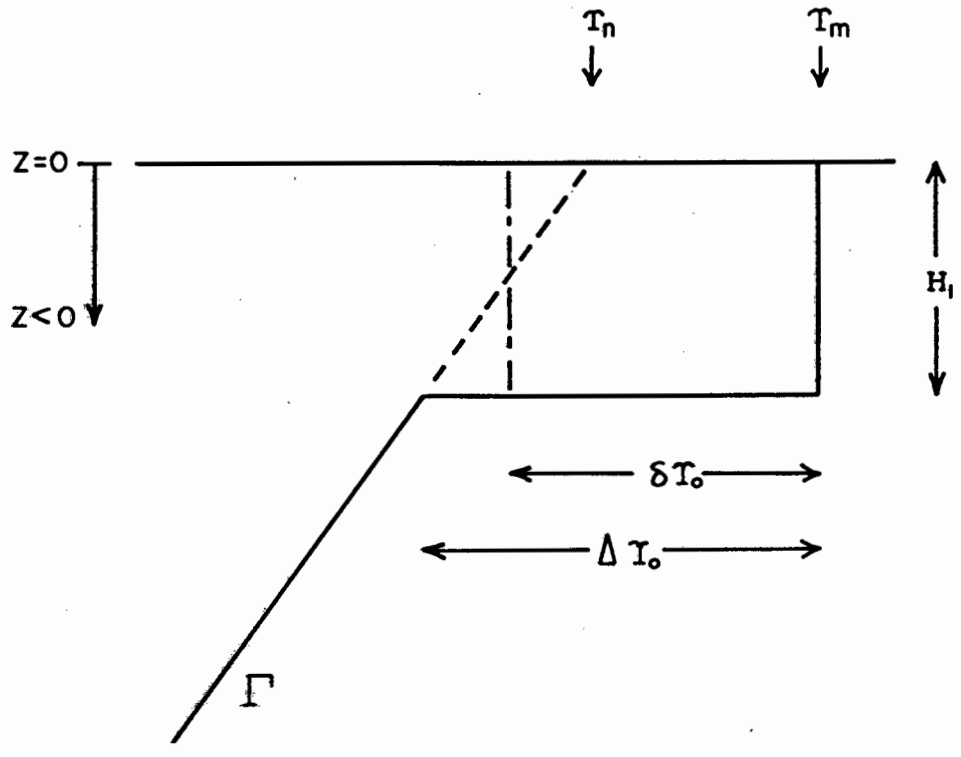

FIGURE 6.2: The model temperature profile used to investigate deepening of the mixed layer. A mixed layer of temperature T_m is separated from a continuously-stratified lower layer, of linear gradient Γ, by an interface of ΔT_o.

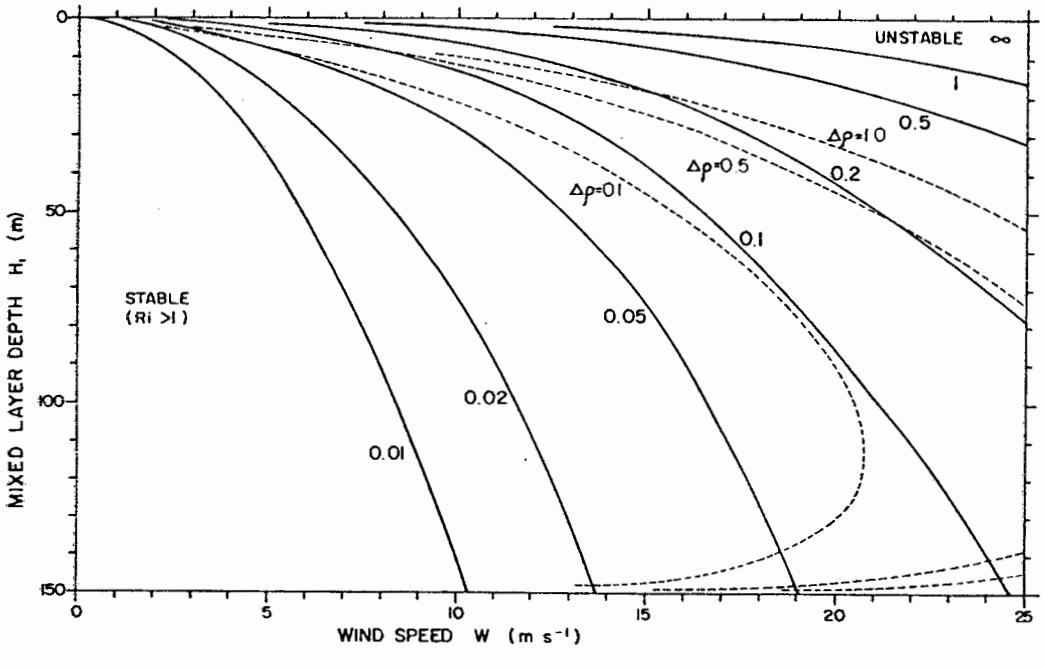

FIGURE 6.3: Wind-driven velocity $\tau/\rho f H_1$ (ms^{-1}) plotted as a function of interfacial depth H_1 and wind speed W, using drag coefficients for 10-metre winds as given by Large and Pond (1981). Given a water depth H = 150 m, dashed lines are drawn for Ri_w =1, $\hat{u}_w = 2\tau/\rho f H_1$ and $\Delta\rho$ as depicted. The interface is stable for larger H_1 and smaller W.

(Fig.4.18, Sub-Section 4.6.1). Although taking zero net heat flux during the event, a net historical heat flux is considered. This appears as 'extra temperature'

$$\delta T_o = \left(T_{m_o} - T_{n_o} + \frac{1}{2}\Gamma H_{1_o}\right) = \Delta T_o - \frac{1}{2}\Gamma H_{1o}$$

in the mixed layer. After deepening ($H_{1o}+H_1$) this 'extra temperature' in the mixed layer (Fig. 6.2) will be $\delta T = \frac{H_{1\,o}}{H_1}\,\delta T_o$. The introduction of $\delta T_o \neq 0$ to the simple model of Pollard et al. (1973) is important since it caters for the contribution of non-penetrative cooling to deepening of the mixed layer (e.g. Sub-section 6.2.2). The inclusion of a stratified bottom layer is of little significance in calculating the fluid velocity response to wind-forcing (Sub-section 6.1.1), but it is essential in the mixing model since the interfacial temperature jump ΔT increases through erosion of the underlying stratified layer.

$$\Delta T = \left(\frac{1}{2}\,\Gamma H_1 + \frac{H_{1o}}{H_1}\,\delta T_o\right) \qquad (75)$$

A further feature of this stratified bottom layer is the removal of momentum by internal waves radiating from the turbulent interface. Kantha (1977) discusses the effect of this on the entrainment rate. Turner (1981) suggests that these waves may help to explain the gradient region directly below the interface. The effect is not accounted for in this model.

The bulk Richardson number (Eq. 74) is used as a finite difference approximation of the gradient Richardson number (Eq. 67). In this expression, the bulk stratification $\Delta\rho$ and velocity shear Δu are clearly defined by field data and/or analytical models (Sub-section 6.1.1). The choice of the vertical scales D_ρ or D_u, associated with the stratification or shear, appears to be the critical issue on which this model departs significantly from Pollard et al. (1973) who use the mixed layer depth H_1 in order to scale both $\Delta\rho$ and Δu. In this model a separate empirically-observed scale D_ρ is used with $\Delta\rho$ in order that a broad thermocline may become unstable easilier than

a sharp quasi-interfacial thermocline. In the absence of an empirical density profile the value of D_ρ would default to the vertical scale D_u chosen for Δu. The use by Pollard et al. (1973) of the mixed layer depth H_1 as a scale for Δu would be justified if the base of the mixed layer was a fixed boundary. In reality, the upper levels of the bottom layer are dragged along with the surface layer (gradient region below interface) and the bulk gradient of velocity also depends on the depth H_2 of the bottom layer. This is particularly the case for coastal seas where it is expected that inertial energy leaks into the bottom layer (Section 6.1). The wind-driven velocities in the lower layer are out-of-phase with those in the upper layer. The velocity shear $\hat{u}_w = (u_1-u_2)_w$, with u_1 from Eq. 70 or 71 and $u_2 = 0$, should be increased to allow for non-zero u_2. In addition this shear should be modelled as a two-layer flow with the vertical scale $\frac{H_1H_2}{H}$ equally dependent on the depth of either layer (refer to Section 2.3).

The wind-driven bulk Richardson number Ri_w, which is plotted in Fig. 6.3 for $\hat{u}_w = \frac{2\tau}{\rho f H_1}$ (maximum of inertial oscillation plus Ekman transport), is therefore

$$Ri_w = \frac{g\Delta\rho}{\rho\hat{u}_w^2} \frac{H_1^2H_2^2}{D_\rho H^2} \qquad (76)$$

Substituting for maximum $\hat{u}_w$ from Eq. 70 and for $\Delta_\rho = \rho\alpha\Delta T$ from Eq. 75

$$Ri_w = \frac{g\alpha(\Gamma H_1^2+2H_{1O}\Delta T_O-\Gamma H_{1O}^2)\ H_1^3H_2^2f^2\rho^2}{4(1+\varepsilon)\tau^2(1-\cos ft)\ D_\rho H^2}$$

where $\alpha = \frac{1}{\rho}\frac{\partial\rho}{\partial T}$ is the coefficient of thermal expansion.

ε is the ratio of inertially rotating currents in the upper layer to those in the lower layer (due to the existence of a coast); its value is $\varepsilon<<1$.

Breakdown occurs for $Ri_w<1$ and turbulent mixing, originating as Kelvin-Helmholtz billows, results in the final profiles of ρ and u taking similar shape and strength (Thorpe, 1973, cited by Turner, 1981); in other words $D_\rho = D_u = \frac{H_1 H_2}{H}$ after mixing. Turbulence and erosion of the interface proceeds for as long as $g'\frac{H_1 H_2}{H} / \hat{u}_w^2 \leq 1$. One can then solve for H_1 by taking $Ri_w = 1$ with $D_\rho = H_1 H_2 / H$. The maximum deepening effect is obtained after a time $t = \frac{\pi}{f}$. In order to make Eq. 77, 78 and 79 solvable without excessive manipulation, it is suggested that the ratio $\frac{H_2}{H} = \frac{H-H_1}{H}$ be taken as a constant $(\frac{H_2}{H})_o$. If H_1 increases by a significant amount, one can repeat the calculation with an improved estimate of the final value $\frac{H_2}{H}$ (that is, an iterative procedure). The solution for H_1 is not strongly dependent on this ratio which appears to the power of 0,5 or 0,25 in the solution. It should be noted that these expressions become invalid as the singularity ($H_2=0$) is approached. When H_2 decreases to the order of the bottom boundary layer thickness, the simple two-layer model is no longer appropriate. In reality, one would expect this region of invalidity to correspond to a well-mixed water colum $H_1 \equiv H$. Away from this singularity, H_1 is given by:

$$H_1^4 + \left(\frac{2H_{1o} \cdot \Delta T_o}{\Gamma} - H_{1o}^2\right) H_1^2 = \frac{4H(1+\varepsilon)\tau^2(1-\cos ft)}{gH_2 \alpha \Gamma \rho^2 f^2} \qquad (77)$$

For the case of $\delta T_o = 0$, as in Pollard et al. (1973),

$$H_1 = \left(\frac{4H(1+\varepsilon)\tau^2(1-\cos ft)}{gH_2 \alpha \Gamma \rho^2 f^2}\right)^{0,25} \qquad (78)$$

For the case of $\Gamma = 0$, two homogeneous layers,

$$H_1 = \left(\frac{2H(1+\varepsilon)\tau^2(1-\cos ft)}{gH_2 \alpha \cdot \Delta T_o H_{1o} \rho^2 f^2}\right)^{0,5} \qquad (79)$$

In all of the above α is given an empirically-determined value in order to account for salinity differences (e.g. Fig. 4.18). In the quadratic expression (Eq. 77), the real solution is given by the positive root.

In this model and subject to the conditions above, mixed layer depth and temperature are thus obtained from an initial state with a given wind stress and zero heat flux, without the use of arbitrary parameters. The model is deterministic.

6.2.2 Interpretation of Observed Deepening Events

Of the sub-inertial events discussed in Sections 4.2 and 4.3, it is only the first two which are adequately represented and only the second which is clearly discernible as a deepening event typical of the onset of winter. During the second deployment the thermistor string provides inadequate coverage of the thermocline itself. The third deployment, although subject to wind-driven motions, is characterized by surface heating and multiple thermoclines which are beyond the scope of the above simple model.

The first event (see p. 46) is recorded by the deeper thermistors as a warming from about 9°C to 12°C (down to at least 100 m). At 55 m the sea warms from about 11°C to about 13°C and ultimately to 14°C. GOSSTCOMP temperatures do not show significant decrease until the end of May. It is conceivable that the surface layer could experience at most a 2°C decrease in temperature. From Section 4.3, the base of the mixed layer is about 45 m. A 2°C decrease over the upper layer (45 m) is insufficient to account for a 2°C to 3°C increase over the lower layers ($\geq$55 m). Since net surface heat fluxes are small or negative during the passage of a cold front, this would imply significant oceanic advection of heat into the mooring area. However, the initial response on the evening of 19 May correlates well with the wind strength (Fig. 6.1) and therefore appears to be related to the inertial motions. It is not clear to what extent the ideas of Krauss (1979) and Kundu (1984) will explain mixing at this depth as a result of sub-thermocline inertial motions. But it is clear that in the absence of other dynamics, the simple model used above (even with exaggerated wind stress) would not allow deepening of the mixed layer described by H_1 ~45 m, ΔT

~7°C. A temperature increase, from about 13°C to about 14°C, at the upper thermistors on the evening of 21 May suggests the mixing down of surface-input heat by small-scale surface-generated turbulence at later time (Niiler, 1977). After 3 or 4 days the deeper thermistors record a cooling which is not reflected at the shallower thermistors. The net effect of this prolonged advection-mixing event is a deepening of the thermocline by over 10 m.

The second clear event (see p. 46) occurs in concert with two consecutive cold front wind fields (Fig. 6.1); the first arrives on 21 June, the second on 23 June (that is, separated by about two inertial periods). Nevertheless, the deepening response appears almost immediately on the evening of 21 June. The response is essentially complete within an inertial period and the second storm has negligible effect on the structure (Fig. 6.4). In this case heat is conserved between the estimated before and after profiles (Fig. 6.5) so that the advective input of new water is not expected. Although the thermistor string only records deepening to 95 m, the conservation of temperature calculation indicates that the mixed layer extends to the bottom. However, it is unlikely that mixing would be so effective in deeper water (larger H_2). Therefore the bottom layer at deeper sites further offshore may spread out under gravity and re-occupy the shallower site after the mixing event has decayed (this occurs on 27 June).

The initial structure is approximated by a surface layer depth H_{1O} = 65 m, a surface layer temperature T_{m_O} = 15,5°C, a quasi-interfacial temperature jump ΔT_O = 4,5°C, a bottom layer temperature gradient $\Gamma \sim 0{,}06°C\,m^{-1}$, a water depth of 116 m, a coefficient of thermal expansion $\alpha \sim 1{,}22 \times 10^{-4}\ °C^{-1}$ and a vertical scale of interfacial stratification D_ρ = 15 m (see Fig. 6.5). The wind event was recorded at Olifantsbos as a fairly constant wind speed of about 15 ms^{-1}. The initial northerly wind persisted for well over $\frac{\pi}{f}$ ~11 hrs, increasing marginally in speed, before it backed to northwesterly (and ultimately westerly) on the afternoon of 22 June. This rotating

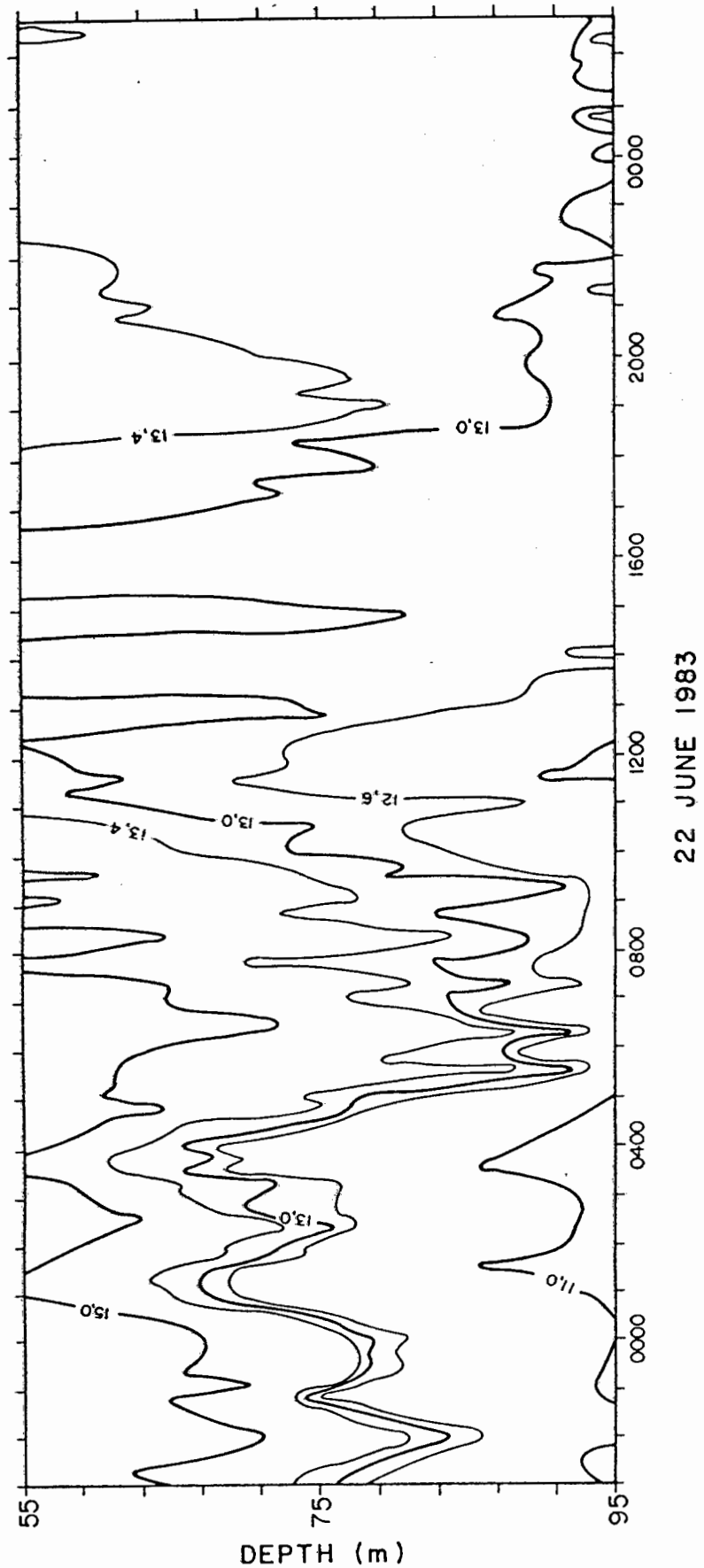

FIGURE 6.4: The change in thermal structure due to the wind event of 21 and 22 June (Fig. 6.1). Internal spring tides have amplitudes up to 12 m on the morning of 22 June. Erosion of the thermocline occurs between noon and midnight on 22 June. The result is an isothermal layer which probably extends 95 m to the surface.

wind field should be particularly conducive to the generation of inertial motions. Following the brief review of local winds (Section 2.1) and the coastal location of Olifantsbos it can be expected that the wind at the mooring site 13 km off Cape Point is subject to an increased wind speed with a more westerly component. A constant 20 ms^{-1} northwesterly wind, active for a period of about $\frac{\pi}{f}$, is input to the model using a drag coefficient of $1,8 \times 10^{-3}$ (as given by Large and Pond, 1981, for stable airflow). This surface stress $\tau = 0,72\ nm^{-2}$ drives mixed layer currents with a maximum velocity (inertial motion plus Ekman transport) of $u_1 = 0,26\ ms^{-1}$ at 90° to the left of the wind (Eq. 70). A current-meter at 100 m, below the interface, recorded inertial currents of less than 0,05 ms^{-1} which would be represented by $\varepsilon \sim 0,4$.

From Eq. 77, and taking $\frac{H_2}{H} = 0,46$, maximum depth of the mixed layer is given as

$$(H_{1max}^{\ 2}) = \frac{-5525 \pm \sqrt{5525^2 + 4 \cdot 2,51 \times 10^7}}{2}$$

and $H_{1max} \approx 54$ m.

In order that H_{1max} exceeds 65 m, a wind speed of about 26 ms^{-1} (or a loss of heat from the mixed layer) would be needed. This is unrealistically large. In other words, the surface mixed layer should not deepen. This is indicated by the value of Ri_w which never goes below the critical value of unity. Eq. 76 yields $Ri_w \sim 3,1$. Nevertheless, the mixed layer depth was observed to increase to about 95 m and it is clear that the wind-driven inertial motions are not capable of doing this alone. The model presented by Pollard et al. (1973) would be even less capable. Nevertheless, the logic suggested by

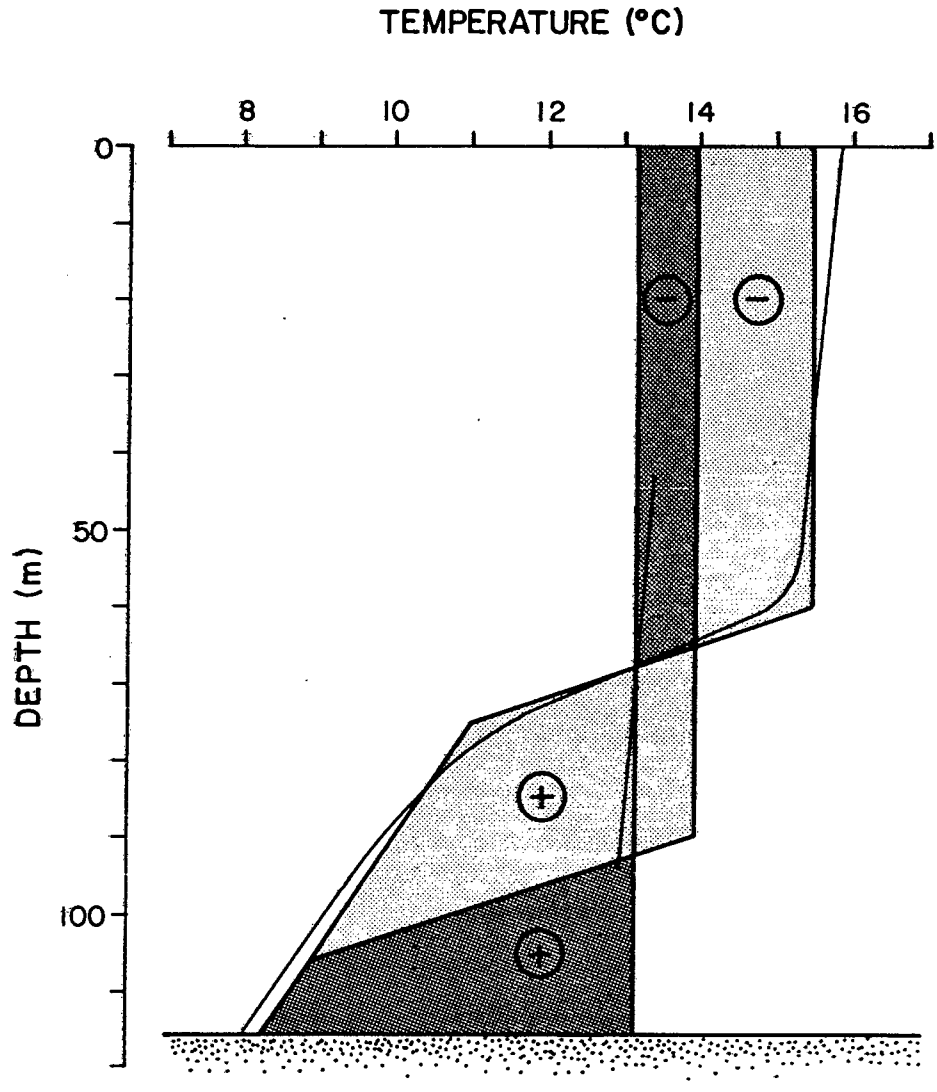

FIGURE 6.5: Model profiles before and after the deepening event of 21 and 22 June. The initial smooth profile is approximated by a mixed layer, a thermocline layer and a stratified lower layer. The thermocline is deepened and strengthened, resulting in a 95 m deep mixed layer. If the whole water column were mixed, in the absence of advection, it would have a temperature of about 13,2°C as indicated.

Pollard et al. (1973) appears to be a correct interpretation of the gross features of 'catastrophic' mixing events. In order to reconcile this theory with the June 1983 observation (and others, Sub-section 7.3.2), it would be necessary to justify an increase in Δu, a decrease in D_u or an increase in Ri_{cr} (Eq. 74). Accepting the above choice of $D_u = \frac{H_1 H_2}{H}$ as appropriate for two-layer dynamics and without any theory to suggest an increase in Ri_{cr}, it appears that Δu has been underestimated. The combination of internal tide shear $\hat{u}_T$ and wind-driven shear $\hat{u}_w$ will be capable of deeper mixing. This idea is explored in Chapter 7.

CHAPTER 7
A MODEL OF COMBINED INERTIAL-TIDAL MIXING EVENTS

The upper layers of the ocean are subject to fluctuations of temperature and salinity (and therefore density) on scales varying from minutes to seasons (and even to interannual) as a result of a continual interaction with the atmosphere. These fluxes of heat and salt are mixed through the ocean by a variety of turbulent processes, either mechanically generated or due to convective forces. In Section 6.2, the formation of a surface mixed layer was accounted for in terms of wind stress on the surface and momentum transfer throughout the mixed layer. The resultant two-layered structure has been formulated in Section 2.3 and used in predicting internal tides in Chapter 5 and inertial motions in Chapter 6.

While reviews of vertical mixing processes (in particular, those by Sherman et al., 1978 and Turner, 1981) reveal the variety and complexity of these processes, a simple approach is adopted in this chapter in order to predict the gross changes in structure on the continental shelf. The importance of events has been recognized (Dillon and Caldwell, 1978; Krauss, 1981) in determining these structural changes. The model below addresses these events (of a scale of hours) and only briefly considers finer-scale dynamics or longer-term fluxes.

From the discussion of theory and observation in Chapters 5 and 6, the internal tide and the wind-driven motions emerge as important agents for shear-driven instabilities. In comparison with this mechanically generated turbulence, convective turbulence is neglected on the event scale. Further, from Section 6.2, the effect of surface waves and surface-driven turbulence have been neglected for a pre-existent mixed layer and a limited time scale. Surface heat fluxes are also dealt with as in Section 6.2 - essentially convective cooling is taken as non-penetrative (an assumption supported by Gill and Turner,

1976). Consequently, it is suggested that for Cape Point, in particular, and quasi-two-layered shelf seas, in general, the majority of mixing across the base of the mixed layer can be accounted for in terms of super-critical velocity shear events. This is in agreement with the theory of Pollard et al. (1973) and the observations of Krauss (1981). However, it is hypothesised that these events are not always due to wind-driven motion alone (Section 6.2) but, in certain circumstances, may be due to super-critical internal tides (Section 5.3) or a combination of these two shear components. Shear due to the remainder of the internal wave spectrum is considered secondary (Sub-section 7.1.2).

Simple, predictive models have been developed for internal tides (Section 5.2) and inertial motions (Section 6.1). Up to this stage turbulence has only been included in the models for the small scales for which it can be handled by a 'viscous' damping parameter (Section 5.3). Tidal and wind-driven currents, formulated in the hypothetical absence of turbulent breakdown, are now used to predict the extent of this turbulent breakdown. Shear-driven turbulent mixing events are investigated deterministically, as controlled by a mechanical energy budget. The two-layer approximation has proved successful in representing the tidal and inertial dynamics. Considering the ease with which it allows one to investigate processes, its use is continued in this chapter. It is specifically appropriate for this purpose of studying thermocline behaviour as an interface but cannot necessarily be used with confidence in the investigation of other stratified dynamics. In Sections 5.2 and 6.1 the stratification of the lower layer was considered to be unimportant - two homogeneous layers were assumed. However, when considering erosion of this lower layer, its stratification must be considered (Section 6.2), since the interfacial strength will increase as the mixed layer deepens. As for the separate tidal and inertial models, this combined mixing model is linear. It is anticipated that the linear superposition of tidal and inertial shear dominates any non-linear interaction between tidal and inertial dynamics.

This model of shear is based on the argument that there exists a critical Richardson number value above which a stratified shear flow will be stable (Turner, 1981). The critical value of the Richardson number, defined generally in Section 5.3 (Eq. 67) and discussed in Sub-section 6.2.1, is chosen as a function of each particular application. In Section 7.1 the effects of super-critical shear are considered for tidal dynamics alone (Section 6.2.1 addressed the mixing resulting from super-critical wind-driven shear alone). The combined effect, due to simultaneous shear, is modelled in Section 7.2. These ideas are applied to the Cape Point data (in particular, the storm of 22-23 June) and are considered for general shelf conditions (Section 7.3). Finally, the scheme is evaluated in terms of its usefulness.

7.1 The Mixing Effect of Tidal Shear

In order to describe shear-instabilities, it is necessary to predict the onset of turbulence and then to determine the nature and extent of the mixing products. It is anticipated that turbulence occurs when $Ri < Ri_{cr}$ and that it will mix until the release of kinetic energy is insufficient to further increase the structural potential energy.

7.1.1 Prediction of Breakdown

The first task is to choose appropriate scales in order to define a bulk internal tide Richardson number Ri_T which approximates a gradient Richardson number at the interface (Eq. 67 and 74), and then to input appropriate values of shear ($\hat{u}_T$, D_u) and stratification ($\Delta\rho$, D_ρ) such that Ri_T is a reliable measure of internal tide stability. From the formulation of the two-layer model (Section 2.3), a vertical length scale $D_u = \frac{H_1 H_2}{H}$ emerges as representative of interfacial dynamics (in particular, consider Eq. 19). This is consistent with the expectation that the interfacial velocity gradient should depend on the depths H_1 and H_2 of the upper and lower layers:

$\frac{\partial u}{\partial z} \sim \frac{\Delta u}{D_u}$ is scaled by $\frac{1}{H_1} + \frac{1}{H_2} = \frac{H}{H_1 H_2}$

where $\Delta u \equiv \hat{u}$ is the velocity shear for deterministic dynamics

D_u is a vertical length associated with Δu.

Since one cannot expect a quasi-interfacial profile of given $\Delta\rho$ to have the same stability as an interfacial profile of the same $\Delta\rho$, it is suggested that an empirically-observed vertical scale D_ρ be used in calculation of the bulk density gradient. In the absence of any empirical knowledge, D_ρ defaults to the value of $\frac{H_1 H_2}{H}$. Thus the bulk internal tide Richardson number is:

$$Ri_T = \frac{g}{\rho_o} \frac{\Delta\rho}{(\hat{u}_T)^2} \frac{H_1^2 H_2^2}{D_\rho H^2} \qquad (81)$$

where $\hat{u}_T = \Delta u$ for internal tide dynamics (Section 2.3).

The values of $\Delta\rho$, H_1 and D_ρ are estimated from profiles of density. The interfacial velocity shear, which is difficult to measure, would be most realistically obtained from a measurement of the vertical displacement due to the interfacial tide. In general, the maximum shear $\hat{U}_T$ is input - this is obtained from the amplitude of the interfacial tide. In Eq.19, $\Delta U \equiv \hat{U}_T$ is expressed in terms of T. Alternatively, in the case of linear stratification (constant or slowly-varying N), $\partial_z u$ from Eq. 9 can be used in place of $(\frac{\hat{u}_T H}{H_1 H_2})$. If no empirical values of T are available then it is necessary to estimate T through analytical models as discussed in Chapter 5. The dependence of $\hat{U}_T$ on $\Delta\rho$, H_1 and T is plotted in Fig. 7.1 for given water depth and tidal frequency. Dashed lines are drawn to indicate where $Ri_T = 1$ for given tidal amplitude. For typical values of T<10 m, internal tide breakdown at H = 150 m is very unlikely.

Being able to evaluate Ri_T, it is now necessary to determine the critical value Ri_{cr} indicating instability. Turner (1973) predicted that a stratified shear flow should become unstable

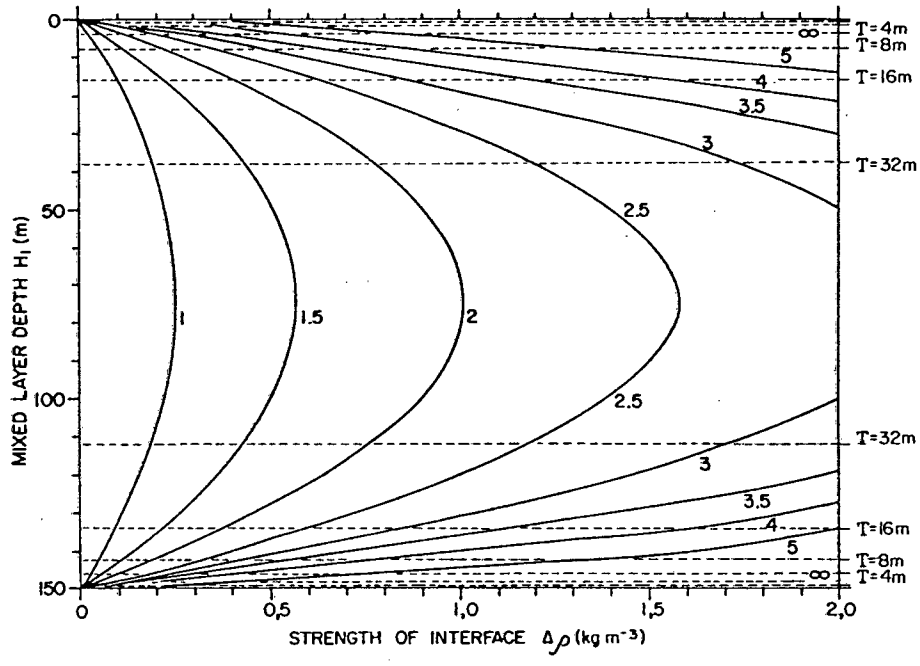

FIGURE 7.1: Interfacial tidal shear $10^2\ \hat{U}_T$ (ms^{-1}) plotted as a function of interfacial depth H1 and interfacial strength $\Delta\rho$; given unit interfacial amplitude T = 1 m, a water depth H = 150 m, semi-diurnal frequency $\sigma = 1{,}41 \times 10^{-4}\ s^{-1}$ and Cape Point latitude $f = 0{,}83 \times 10^{-4}\ s^{-1}$. Tidal shear for greater T is obtained by multiplying these values by T. Dashed lines are drawn for $Ri_T = 1$ and T as indicated on the right-hand axis, decreasing from 32 m to 16 m, 8 m, 4 m, 2 m and 1 m. The interface is stable for H_1 near to H/2.

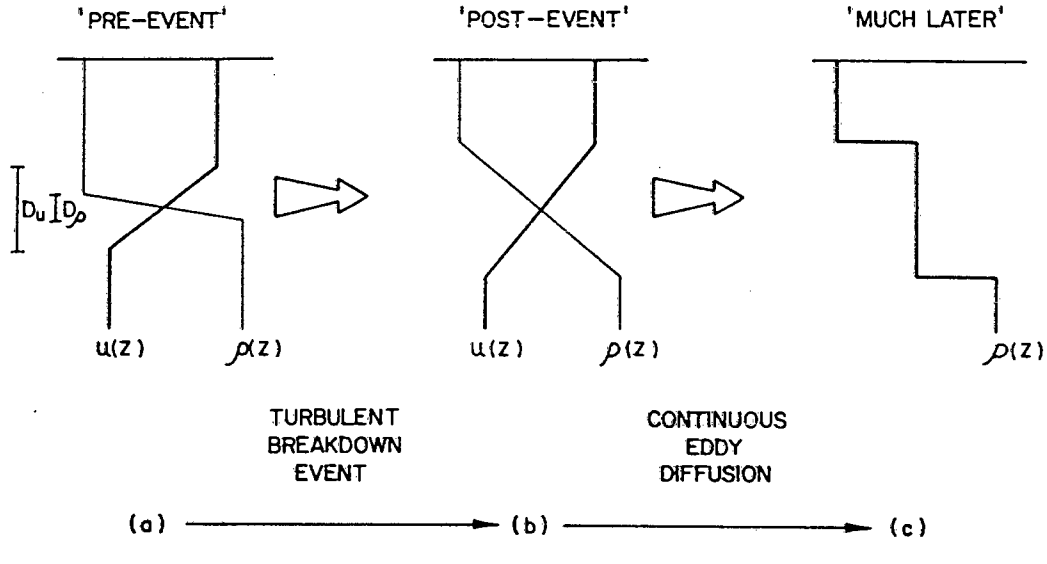

FIGURE 7.2: An idealization of the mixing effect of internal tides. On breakdown of the wave, the thermocline shear layer is rapidly broadened: (a) to (b). This energetic event is followed by less energetic but continuous diffusion which tends to smooth out the linear gradient and results in a splitting of the interface.

when the gradient Richardson number is locally $Ri<0,25$ (also Thompson, 1980). This is supported by the measurements of Eriksen (1978). Through a statistical argument, Padman and Jones (1985) show that the most probable Richardson number due to an internal wave field in the seasonal thermocline may be much lower than the bulk Richardson number based on mean shear. Nevertheless, Desaubies and Smith (1982) and D'Asaro (1985a) suggest that the bulk expression can be used as a fairly sensitive indicator of breakdown and mixing. A critical value of unity (suggested by Abarbanel, 1984, for finite amplitude disturbances) is chosen to be used with Ri_T. This is the same criterion that Pollard et al. (1973) used to close their model of wind-driven deepening (cf. Section 6.2) and their discussions of overall stability, erosion mechanism and gross energetics support this choice.

7.1.2 Shear due to Remainder of Internal Wave Field

Before proceeding, it is necessary to estimate the shear due to the remainder of the internal wave field. It is presumed that only the first mode internal tide needs to be considered. Higher modes are neglected following observations that the first mode, which approximates an interfacial wave, accounts for at least 50% of the energy (Chapters 4 and 5). In other words, the first mode amplitude T, is significantly greater than amplitudes T_n. This is obviously true for an interfacial structure. Considering the opposite extreme, a constant-N structure, vertical shear $\partial_z U_n \propto (n\pi/H)T_n$ is obtained from Eq. 9 and it is thus necessary that $T_n < \frac{1}{n} T_1$ for $\partial_z U_n < \partial_z U_1$. This is generally well-satisfied for a bounded fluid, such as shelf seas, where the higher order modes are rapidly damped (Baines, 1982). Further, only modes with an odd number of zero-crossings will have u=o and $\partial_z u$ maximum at the interface. Only these (n=1,3,5,...) are relevant to this investigation of thermocline dynamics. The higher order modes, which may provide super-critical shear and mixing away from the interface, serve to improve the two-layeredness of the profile.

Higher frequency internal waves have also been excluded from these deterministic events. In particular, the large-amplitude group of waves or solitons (discussed in Sections 4.2, 4.4 and 5.3), which are superimposed on the tidal signal, are of sufficiently high frequency that their inclusion in a tidal damping parameter (Section 5.3) seems justified. This is supported by Le Blond (1966), who finds that short-waves damp very rapidly. Considering the non-tidal amplitudes recorded (Section 4.2) and Eq. 9, it is clear that other frequency waves need not be included in a sum of dominant shear. Their random and ubiquitous nature, however, make them continually available as a trigger for marginally unstable tidal or inertial shear.

7.1.3 Products of Mixing

Energy budget. Having predicted instability, it is now necessary to consider how the turbulent mixing will alter the vertical profiles. Thorpe (1973, cited by Thompson, 1980) found that the final profiles of density and velocity had the same width and much the same shape. Further, Thompson (1980) concludes that little momentum is removed by smaller-scale internal waves and the mixing is local, contained within a layer as defined below. Mixing across the interface occurs when $Ri_T<1$; in general the vertical scales D_ρ, which is small for an interfacial approximation, and $D_u = \frac{H_1 H_2}{H}$ change to a common vertical scale $D = (\frac{H_1 H_2}{H})_{final}$, over which u and ρ vary linearly. The extent of mixing and the thickness D of the gradient layer (thermocline) are determined by the amount of potential energy ΔE_p gained from a certain loss of kinetic energy ΔE_k. Thompson (1980) concludes that $\frac{\Delta E_p}{\Delta E_k}=\frac{1}{4}$ which supports the observation of Thorpe (1973). Sherman, et al. (1978) suggest that an efficiency of 15% would be a good rule of thumb.

From Thompson (1980), the kinetic energy per unit area is

$$E_k = \int \frac{1}{2} \rho_o \cdot u(z)^2 \cdot dz, \qquad (82)$$

and the potential energy per unit area is

$$E_p = \int \rho(z) \cdot g \cdot z \, dz \tag{83}$$

so that any initial profiles of density $\rho(z)$ and velocity $u(z)$ could be used, however, attention is limited to linear quasi-interfacial profiles as described above. If the predicted D is less than D_ρ, then no mixing is expected; therefore $D>D_\rho$ and $D>D_u$. As a first step the lower layer is assumed homogeneous (as in Sections 5.2 and 6.1) in order to allow simpler calculation of D. This is justified by Turner (1973) and Sherman et al. (1978) who declare that Kelvin-Helmholtz instabilities can only thicken an interface to a modest degree. Further, the numerical calculations in Section 7.3 confirm that $(D-D_\rho)$ and the associated $\delta\rho = \rho\alpha(D-D_\rho)\cdot\Gamma$ are small.

Consequently, the decrease of kinetic energy is

$$\Delta E_k = \frac{1}{12} \rho_o (D-D_u) \overline{\hat{u}_T^2} \tag{84}$$

(where the overbar denotes a mean value of $\hat{u}_T^2$),
and the increase of potential energy is

$$\Delta E_p = \frac{1}{24} g \cdot \Delta\rho (D-D_\rho)^2. \tag{85}$$

Expecting a conversion efficiency of 25%,

$$\frac{\Delta E_p}{\Delta E_k} = \frac{g \cdot \Delta\rho \cdot (D-D_\rho)^2}{2\rho_o (D-D_u)\overline{\hat{u}_T^2}} = \frac{1}{4} \tag{86}$$

(this is clearly a version of the flux Richardson number), the new thermocline thickness is given by D where:

$$(D-D_\rho)^2 = \frac{1}{2} \frac{\rho_o \overline{\hat{u}_T^2}}{g \cdot \Delta\rho} (D-D_u). \tag{87}$$

If $D_u = D_\rho = 0$, as for a true interface, this result reduces to the expression given in Section 5.3.

$$D = \frac{\rho_o \overline{(\hat{u}_T)^2}}{2g\Delta\rho}$$

Although smaller scale processes may further mix this layer (e.g. well-mixed layers measured by Woods and Wiley, 1972), laboratory experiments (e.g. Thorpe, 1973) indicate that when Kelvin-Helmholtz billows collapse, due to gravitational instability, nearly linear gradients are produced (Turner, 1981). A schematic (Fig. 7.2) portrays the development of the velocity and density profiles.

Generally, it is expected that $D_\rho \sim D_u$ as a result of previous shear instabilities. This is particularly the case for small values of D_ρ and D_u. Munk (1981) shows simply that, for internal wave profiles, the Richardson number takes a minimum value at maximum N, since $\partial_z u$ varies roughly proportional to N(z). Therefore, one can expect the thermoclince to have a history of Kelvin-Helmholtz 'events'.

Use and Definition of Ri_T: For breakdown due to tidal shear, two different versions of a Richardson number have been defined for two different purposes. The bulk internal tide Richardson number Ri_T (Eq. 81) is used to predict shear instability. The energy internal tide Richardson number $Ri_{TE} = \frac{\Delta E_p}{\Delta E_k}$ (Eq. 86) is used to estimate thickness of the turbulently mixed layer. The simplest valid use of these criteria is to allow mixing to turn on if $Ri_T < 1$ and to allow this mixing to continue until D is such that $Ri_{TE} = \frac{1}{4}$. These shear instabilities are characteristically self-limiting (Sherman, et al., 1978; Turner, 1981) however, should D approach H then one can expect the full water column to be mixed such that a constant-N model would become appropriate. In this discussion, final structure is predicted from an initial structure in terms of two-layer theory. In many cases this final structure will not be quasi-interfacial and no prediction is made on how it may develop after the event.

Once the mixing is started it is allowed to continue to completion, that is, the limit when $\Delta E_p = \frac{1}{4} \Delta E_k$. It is assumed that enough kinetic energy may be temporarily loaned from the spectrum of internal motions so that energy thresholds may be disregarded. In other words, it is only the gross changes in E_p and E_k which are related in the criterion $Ri_{TE} = \frac{1}{4}$. This approach appears justifiable since the "billows" grow to a height of about $\frac{1}{Ri_T} \frac{D_u^2}{D_\rho}$ (Sherman, et al., 1978), which is of the order of D, and so small-scale insufficiencies may be ignored.

The velocity shear associated with internal waves is periodic in space and time such that 'patchy' mixing may result with unstable crests being separated by patches of stable shear (Fig. 7.3). For a sinusoidal wave, as assumed (Eq. 19 and Chapter 5), a crest value $(Ri_T)_{max} = \frac{1}{4}$ would correspond to subcritical $Ri_T<1$ over $\frac{2}{3}$ of the wave. Under the constraints of vertical stratification and the action of horizontal velocity shear, these actively mixing patches will spread horizontally and should rapidly coalesce into a continuous mixed layer (Woods and Wiley, 1972). More patchy instabilities $(Ri_T)_{max} \sim 1$ are generally smaller and influenced to a greater extent by molecular diffusion. Consequently, they will dissipate their momentum more rapidly than they can diffuse their buoyancy character (Thompson, 1980) and it is reasonable to expect that these localized patches of mixing may decay rapidly with negligible effect on the gross structure. In this work, only internal waves with $(Ri_T)_{max} < \frac{1}{4}$ will be treated as having a significant effect on the gross structure.

Solution for D. Subject to the above discussion, Eq. 87 can be solved for

$$\overline{\hat{u}_T^2} = \frac{1}{2} \hat{U}_T^2$$

and the result can be investigated,

$$D = D_\rho + \frac{1}{2} \Lambda + \frac{1}{2} \left(\Lambda^2 + 4\Lambda \left(D_\rho - D_u \right) \right)^{0,5} \qquad (88)$$

where $\Lambda = \frac{1}{4} \frac{\rho_o \hat{U}^2}{g \Delta \rho}$ is a length scale corresponding to Ri_{TE} or mean Ri_T

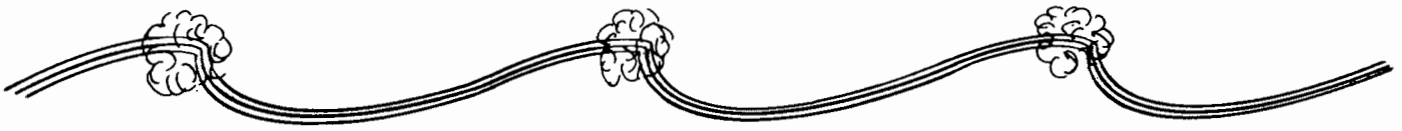

(a)

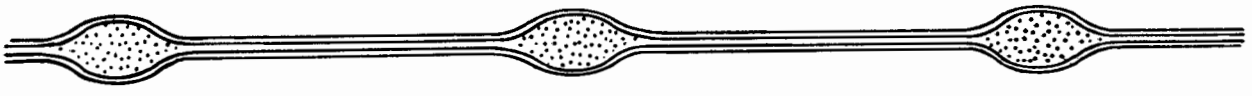

(b)

FIGURE 7.3: An idealization of the effect of marginal instability, resulting in (a) mixing only at the crests (or troughs) of the internal wave and (b) patches of mixed water on the thermocline.

Therefore the horizontally continuous layer is predicted to mix to a thickness D corresponding to the mean square tidal shear $\frac{1}{2}\hat{U}_T^2$. If $D_\rho = D_u = 0$ then this expression reduces to Λ, which is Turner's (1981) interfacial thickness for a mean interfacial shear $\frac{1}{2}\hat{U}^2$ and 25% energy conversion.

For the special case of initial profiles with $D_\rho = D_u$

$$D = D_\rho + \Lambda. \tag{89}$$

In comparison with this special case, the general case $D_u < D_\rho$ will be characterized by increased kinetic energy as a result of smaller D_u. Therefore

$$D > D_\rho + \Lambda, \tag{90}$$

The opposite general case of $D_u > D_\rho$ will be characterized by decreased kinetic energy as a result of greater D_u. Therefore

$$D < D_\rho + \Lambda \tag{91}$$

For the second, weaker general case, it should be noted that solutions only exist for $D_u \leq D_\rho + \frac{1}{4}\Lambda$; at this limit the two roots of the quadratic Eq. 87 converge to $D = D_\rho + \frac{1}{2}\Lambda$. It is suggested that values of D_u which are much larger than D_ρ will tend to be decreased since velocity shear outside of the stratified interface is supercritical. Resultant mixing and decrease of D_u will probably also decrease $\hat{U}_T$ in order to conserve kinetic energy.

From Eq. 81 and the above definition of mean Ri_T, the interfacial length scale Λ can be related to the maximum Ri_T found at the crests and troughs, $(Ri_T)_{max} = \frac{1}{2}(Ri_T)_{mean} = Ri_{TE}$.

$$\Lambda = \frac{1}{4(Ri_T)_{max}} \cdot \frac{D_u^2}{D_\rho} \tag{92}$$

so that for critical $(Ri_T)_{max} = \frac{1}{4}$ the length scale Λ can be replaced by $\frac{D_u^2}{D_\rho}$ in Eq. 89, 90 and 91. Smaller values of Λ, corresponding to larger $(Ri_T)_{max}$, are suspected of suffering from patchiness and, as discussed above, are not considered as significant 'layer-thickening events'. For smaller values of $(Ri_T)_{max}$, this Λ will increase and so will D. Therefore, as expected, the tidal mixed layer will be thicker for smaller Ri_T. This can also be shown by expressing Eq. 88 in terms of $(Ri_T)_{max}$ as given by Eq. 81,

$$D = D_\rho + \frac{1}{8(Ri_T)_{max}} \frac{D_u^2}{D_\rho} + \frac{1}{2} \frac{1}{16(Ri_T)_{max}^2} \frac{D_u^4}{D_\rho^2} + \frac{1}{(Ri_T)_{max}} \frac{D_u^2}{D_\rho}(D_\rho - D_u)^{0,5}$$

For critical $(Ri_T)_{max}$ and $D_\rho = D_u$ one obtains $D = 2D_\rho$.

Formulation in terms of Temperature. In order to combine these with the temperature profile as formulated in Section 6.2.1, the local temperature-salinity characteristics are assumed constant so that one only need consider temperature in order to follow

density (Section 4.6). In other words, temperature is considered as a conservative property on the time-scale of these events. Using the definition of the thermal coefficient of expansion α in Eq. 29, the interfacial length scale (Eq. 88) is expressed as

$$\Lambda = \frac{1}{4} \frac{\hat{U}^2}{g\alpha\Delta T}$$

and the Richardson number (Eq. 81) is

$$Ri_T = \frac{g\alpha\Delta T}{\hat{u}_T^2} \frac{H_1^2 H_2^2}{D\rho H^2}$$

Conservation of energy (Eq. 87), in terms of temperature, is

$$(D-D_\rho)^2 = \frac{1}{4} \frac{\hat{U}_T^2}{g\alpha\Delta T} (D-D_u)$$

7.2 The Combined Effect of Inertial and Tidal Shear

Working on the assumption that the gross structural changes of a quasi-interfacial thermocline are accounted for in terms of wind-driven inertial motions and internal tides, the two end-points of a continuum have been formulated. In Section 6.2.1 expressions were developed for the case of an ocean devoid of internal tides. In Section 7.1.3 expressions were developed for the case of an ocean unmoved by the wind. In this section these two situations will be superimposed in order to account for an ocean in which both internal tides and wind-driven motions are present. It is necessary to decide on whether the combined shear will act to deepen the mixed layer or whether it will merely thicken the interface. One can then predict the extent of the change in strucure. With reservation, a third shear component is introduced to account for ambient shear. This is only valid for small mean flow and constant water type because the associated advection of changing water structure and the

advective removal of mixing products makes this whole model fundamentally incorrect. There is a temptation to introduce a fourth component due to Langmuir circulations (Pollard, 1977) but it is not yet clear what the role of this mechanism is in restructuring density gradients (Turner, 1981). Therefore the Langmuir shear expected at the base of the mixed layer is not included on the premise that this shear is generally smaller than those due to inertial or tidal dynamics.

7.2.1 Prediction of Breakdown

In order to combine the shear, the components must be treated as vectors. For this purpose x and u are defined to be cross-shelf and y and v are defined to be long-shelf (as in Section 5.2). For tidal shear $\underline{\hat{u}}_T = (\hat{u}_T, \hat{v}_T)$ the orientation is fixed in the x-dimension so that $\hat{v}_T = 0$. The inertial shear $\underline{\hat{u}}_W = (\hat{u}_W, \hat{v}_W)$ is determined from the angle of the wind stress (τ_x, τ_y) by Eq. 70 and 71. The orientation of $\underline{\hat{u}}_W$ is a function of the time since switch-on time t = 0. However the phase difference between the tidal shear and the wind-driven shear is not crucial since the wind-driven motions are synoptic over an distance of the order of the wavelength of the interfacial tide. In other words, when the wind-driven shear parallels the tidal shear there will be a tidal crest or trough available within the wind-driven region. The damping of inertial motion over the short time required for maximum interference (less than half an inertial period) is considered negligible.

The maximum shear which brings about maximum mixing (cf. Pollard et al., 1973) may occur either when the wind-driven shear interferes constructively with the tidal shear or when the inertially-rotating component of wind-driven motion parallels the Ekman component of wind-driven motion. If the latter, which is perpendicular to the wind, is greater, then the tidal shear contributes negligibly to structural breakdown. Referring to Eq. 19 and 70, this is the case if

$$\frac{2\tau}{\rho f H_1} \geq \frac{1}{\rho f H_1} \left(\tau_y + \tau_x \sin ft - \tau_y \cos ft\right)_{max} + 0,7 \frac{g' k \sigma}{\sigma^2 - f^2} T \quad (93)$$

where the root mean tidal shear has been used (as in Section 7.1.3). In this case, the mixed layer deepens to a depth H_1 as predicted by Eq. 77 in Section 6.2.1.

The remainder of this section considers the case when Eq. 93 is not satisfied. The maximum shear is then due to constructive interference of inertial, Ekman, tidal and ambient components. Re-introducing ε to account for inertial currents in the lower layer (cf. Eq. 76):

$$\Delta u = \frac{1}{\rho f H_1} \left(\tau_y + (1+\varepsilon)(\tau_x \sin ft - \tau_y \cos ft)\right)_{max} + 0,7 \frac{g' k \sigma}{\sigma^2 - f^2} T + \hat{u}_A \quad (94)$$

where $\hat{u}_A$ is an ambient mean shear.

Shear instability is predicted for a subcritical bulk Richardson number $Ri_o < 1$ where, as before, the two-layer shear flow is scaled by $D_u = \frac{H_1 H_2}{H}$ and the density structure is scaled by D_ρ.

$$Ri_o = \frac{g \alpha \Delta T}{(\Delta u)^2 D_\rho} \left(\frac{H_1 H_2}{H}\right)^2 \quad (95)$$

The calculated value of Ri_o will depend on the choice of values for ΔT, Δu, $D\rho$ and H_1. The Richardson number depends linearly on ΔT or $D\rho$ such that a given percentage error in ΔT or $D\rho$ would produce the same percentage error in the calculated value of Ri_o. A given percentage error in Δu, which is squared in the expression for Ri_o, would produce twice the percentage error input through Δu. Dependence on H_1 is more complicated such that the percentage error in Ri_o is twice the difference between the percentage error in H_1 and the error in H_1 as a percentage of H_2. If $H_1 \sim H_2 \sim \frac{H}{2}$ then this dependence is negligible. The value of the Richardson number is characterized, therefore, by a limited error. A numerical example is presented in Section 7.3.1.

7.2.2 Products of Mixing

Breakdown having occurred, it is necessary to determine the form of the structural change. The upper boundary of a quasi-interfacial thermocline is subject to increased random shear owing to turbulence in the surface mixed layer. The lower boundary, in contrast, borders on a stably stratified layer with weak circulation. Therefore it is anticipated that mixing will be more vigorous at the upper edge and that these mixing products will tend to move away into the surface mixed layer, thus deepening the surface mixed layer. This will definitely occur when wind-driven shear dominates and probably when tidal shear is marginally dominant. For shear which is strongly dominated by the tidal component ($0,7\hat{U}_T >> \hat{u}_w$), the turbulent mixing will thicken the thermocline as described in Section 7.1.3 with the combined shear replacing tidal shear in Eq. 88.

This new thermocline will then be more susceptible to a renewed attack by wind-driven shear and deepening of the mixed layer may occur as a second phase. However, emphasis in this section is placed on deepening of the mixed layer, therefore, considering the unlikelihood of tidal shear dominating sufficiently, this case is not investigated further.

For relatively weaker tidal shears, the resultant deepening of the mixed layer occurs in the same way as for inertial shear alone (Section 6.2.1). Turbulence occurs if $Ri_o < 1$ and proceeds for as long as $Ri_o \leq 1$. If initially $D_\rho > D_u = \frac{H_1 H_2}{H}$, it is conceivable that before D_ρ has been sharpened to D_u, the mixing will cease and no deepening will result. During active turbulent erosion of the base of the surface mixed layer both velocity shear and stratification are scaled by $\frac{H_1 H_2}{H}$. Therefore the maximum extent of deepening (cf. Eq. 76) is given by H_1 when

$$Ri_D = \frac{g \cdot \alpha \cdot \Delta T \cdot \frac{H_2}{H} H_1}{(\Delta u)^2} = 1 \qquad (96)$$

Before proceeding further this Richardson number is investigated. With $\frac{\Delta\rho}{\rho}$ in place of $\alpha \cdot \Delta T$ and Δu given by $(\frac{2\tau}{\rho f H_1}) + 0,7\ U_T$, the value of the bulk Richardson number Ri_D is plotted as a function of surface wind stress τ and internal tide amplitude T in Fig. 7.4 and a function of interface strength $\Delta\rho$ and depth H_1 in Fig. 7.5. Superimposed on these graphs are dashed lines indicating the relative contributions of $\hat{u}_T = 0,7\hat{U}_T$ and $\hat{u}_W = 2\tau/\rho f H_1$ to the total shear Δu; the value of $VR = \hat{u}_W/\hat{u}_T$ is plotted.

In order to manipulate Eq. 96 into an equation for H_1, the dependence of Δu on H_1 has to be determined. Although the internal tide requires a horizontally continuous thermocline in order to propagate in from its source, this mixing event is rapid (on a time-scale of less than a tidal period) and the arrival of new velocity shear is unimportant. However as the thermocline moves away from its original depth the effective tidal shear must decrease. Owing to the lack of laboratory or field data, and the lack of a philosophy, the tidal shear is conveniently assumed to decrease with H_1 in the same way that the wind-driven shear does (and likewise for any weak ambient shear). The assumption, that tidal and inertial energy do not go to zero during deepening, is partially supported by Fig. 6.4 in which a tidal signal is perceptible during the mixing event on 22 June 1983. Therefore the combined shear is given by

$$\Delta u = \frac{H_{1O}}{H_1} (\Delta u_O) \qquad (97)$$

during deepening. The equation for H_1 will thus take the same form as Eq. 77 provided that, once again, the ratio $\frac{H_2}{H}$ is taken as a constant in order to facilitate the solution of Eq. 96. If H_1 increases by a significant amount, one can iterate by solving a second time with $\frac{H_2}{H}$ given by an improved value of H_1. It was noted in Section 6.2.1 that $\frac{H_2}{H}$ appears to the power of $\frac{1}{4}$ in the solution so that an exact numerical value is not critical.

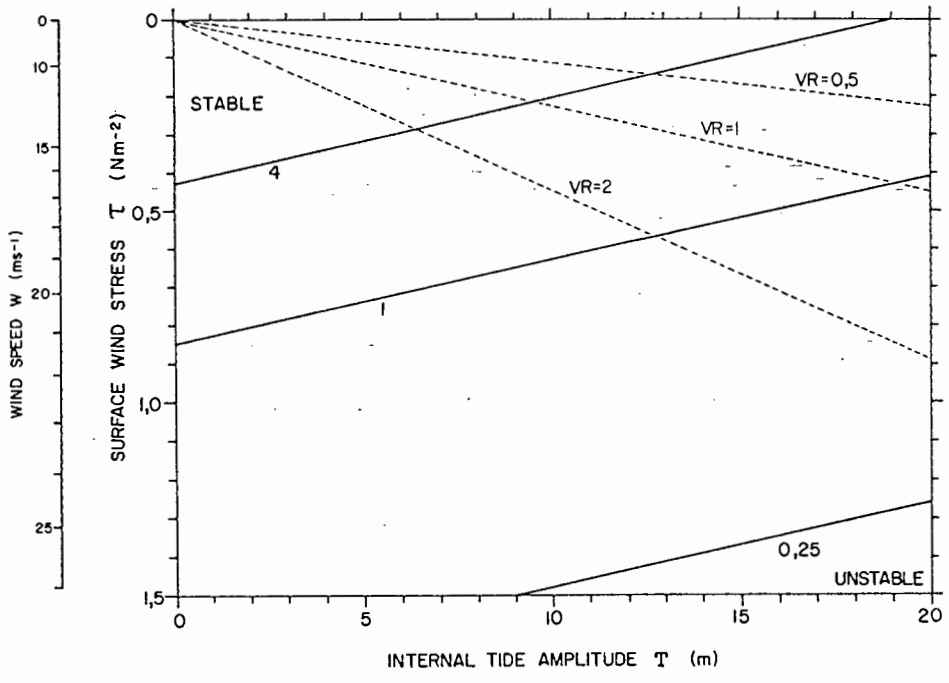

FIGURE 7.4: The Richardson Number Ri_D as a function of wind stress τ and internal tide amplitude T; given interfacial strengh $\Delta\rho$ = 0,5 kgm^{03}, interfacial depth H_1 = 50 m and water depth H = 150 m. Ri_D = 1 is taken as critical. Dashed lines are plotted for the ratio VR of wind-driven to tidal velocity shear.

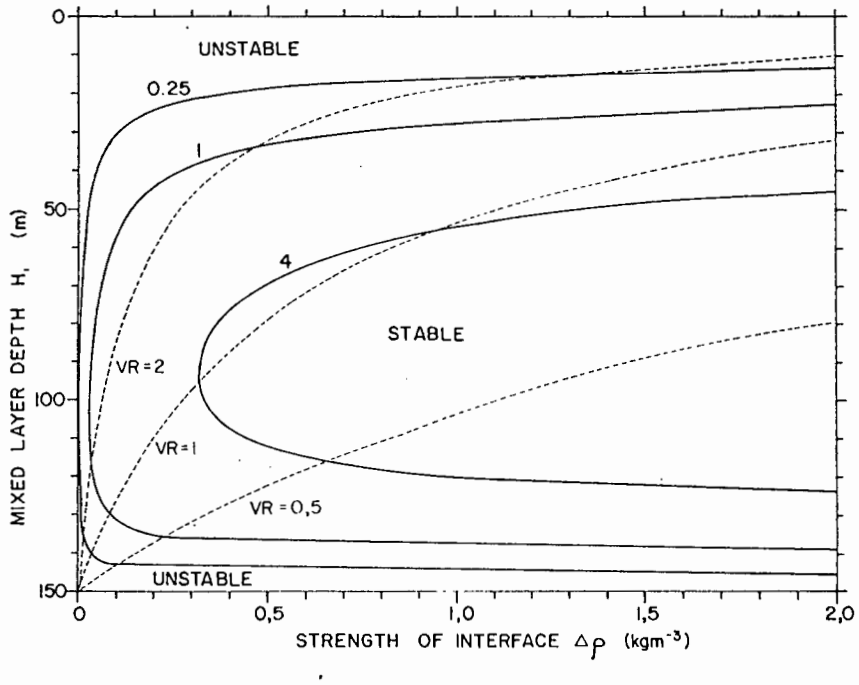

FIGURE 7.5: The Richardson number Ri_D as a function of interfacial depth H_1 and interfacial strengh $\Delta\rho$; given water depth H = 150 m, wind speed W = 15 m/s (τ = 0,33 Nm^{-2}) and internal tide amplitude T = 10 m. Ri_D = 1 is taken as critical. Dashed lines are plotted for the ratio VR of wind-driven to tidal velocity shear.

Eq. 96 can now be written as a quadratic in H_1^2

$$H_1^4 + \left(\frac{2H_{1o}\Delta T_o}{\Gamma} - H_{1o}^2\right) H_1^2 = \frac{2H_{1o}^2(\Delta u_o)^2}{\Gamma g \alpha \cdot \left(\frac{H_2}{H}\right)} \qquad (98)$$

and can be solved for H_1. The calculated value of H_1 depends on the choice of values for H_{1o}, Δu_o, ΔT_o and Γ. The sensitivity of Ri_D, from which Eq. 98 is derived, is displayed in Figs. 7.4 and 7.5. In order to investigate the sensitivity of the solution of Eq. 98 to small changes in the empirically observed variables, one can determine the derivatives of H_1 with respect to H_{1o}, Δu_o, ΔT_o and Γ. Taking the ratio $\frac{H_2}{H}$ (which appears on the right-hand side of Eq. 98) as constant, these derivatives are easily calculated and are clearly small. The small change in H_1, however, causes a feedback by changing $\frac{H_2}{H}$ which was approximated constant in the solution of Eq. 98. For small H_1 this feedback is small so that successive iterations converge rapidly on the solution. But as H_1 increases, the feedback increases so that small changes in the ratio $\frac{H_2}{H}$ can lead to large changes in the solution for H_1. In the limit $H_1 \to H$ and $H_2 \to 0$, a singularity is reached and the feedback swamps the solution. This result is not unrealistic because as the interface approaches the bottom, not only is interfacial shear increased but bottom-generated turbulence erodes the base of the interface. In reality, one could not expect a shallow sea interface to survive within 10 m of the bottom. Mathematically, nevertheless, the problem is ill-conditioned as $H_1 \to H$ because small changes in any of the input values may cause a large change in the solution for H_1. This result can be obtained directly from derivatives of H_1 with respect to H_{1o}, Δu_o, ΔT_o and Γ, where the ratio is not a constant but a function of H_1. A numerical example is discussed in Section 7.3.1.

In the case of zero net historical heat flux $\delta T_o = 0$, as for Eq. 78, the solution to Eq. 98 is

$$H_1 = \left(\frac{2H_{1o}^2(\Delta u_o)^2}{\Gamma g \alpha \left(\frac{H_2}{H}\right)}\right)^{0.25} \qquad (99)$$

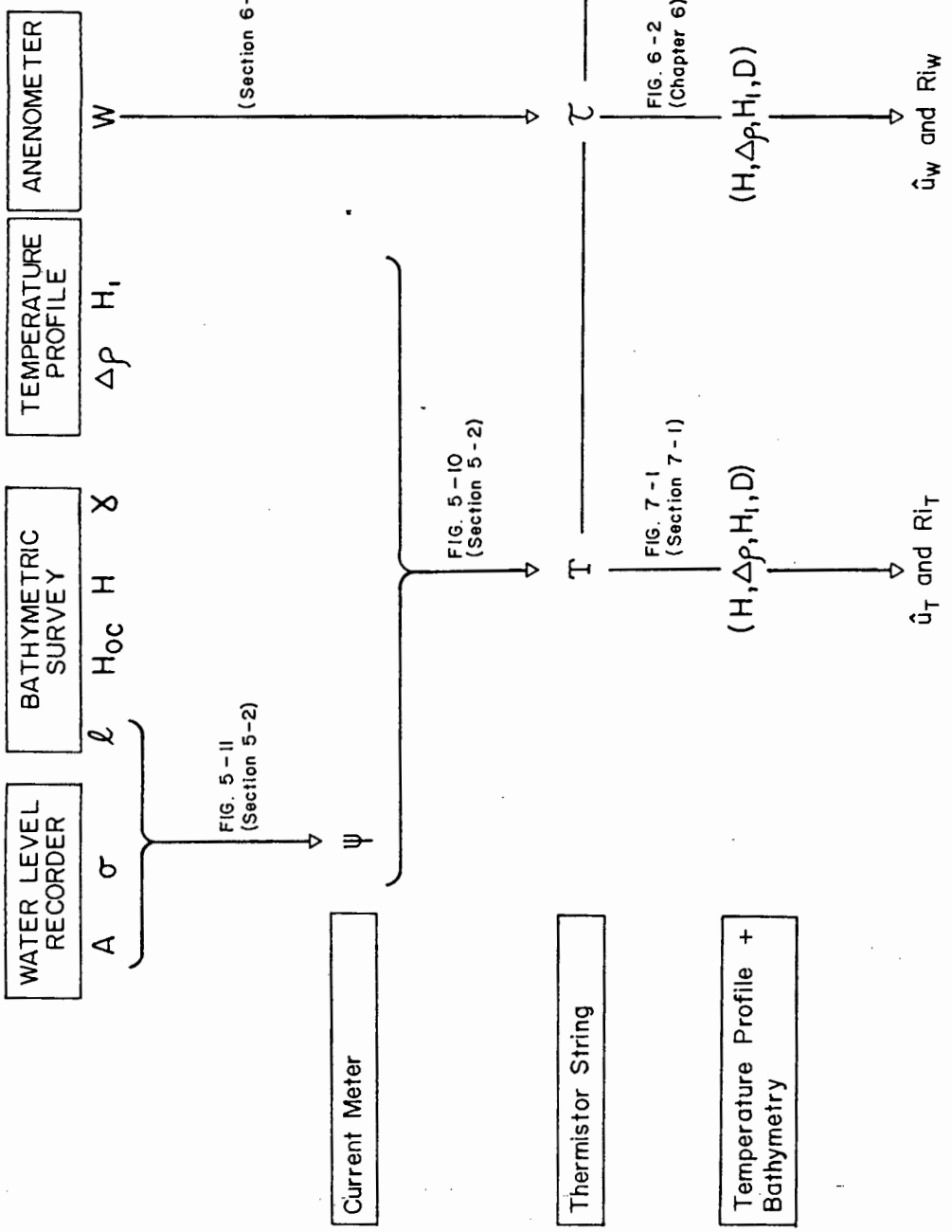

FIGURE 7.6: A flow chart summarizing the use of available empirical data (in blocks) in obtaining estimates of tidal amplitude, velocity shears and stability of the interface. The more steps between the empirical data and the desired prediction, the greater is the uncertainty of the prediction. Each step has been described in the sections which are referenced.

For positive net historical heat flux, $\delta T_o > 0$, H_1 is less than that given in Eq. 99. For negative net historical heat flux, $\delta T_o < 0$, H_1 is greater than that given in Eq. 99. For a well-mixed bottom layer, $\Gamma \to o$ and

$$H_1 = \left(\frac{H_{1o}(\Delta u_o)^2}{\Delta T_o \cdot \Gamma g \alpha \cdot (\frac{H_2}{H})} \right)^{0,5} \qquad (100)$$

7.2.3 Practical Considerations

Assuming that the velocity and density profiles are well approximated by this interfacial model, the greatest source of uncertainty lies in estimating the velocity shear Δu. In comparison, the stratification ($\Delta \rho$ and H_1) is easily estimated from CTD profiles. Although the best values of Δu should be obtained from direct measurement, in practice it is seldom easy to resolve the inertial and interfacial tidal velocities from the spectrum of frequencies and vertical modes in the ocean. It is suggested that acceptable values of Δu are obtained with much less difficulty via the various expressions presented in this thesis. The relevant inputs of field data and appropriate use of models have been summarized in a flow chart (Fig. 7.6).

The internal tide is best estimated by a vertical array measuring temperature as a function of time or space. Interpolating the record, as in Fig.4.2, a clear estimate of the internal tide amplitude T is obtained. Given T, Eq. 19 allows a reasonably confident estimate of $\hat{U}_T$, the amplitude of the tidal velocity shear. In the absence of any such arrays, the internal tide amplitude can be crudely estimated with the model presented in Section 5.2. In particular, Eq. 58 predicts the amplitude of the interfacial tide given knowledge of the ambient stratification, the shelf-edge topography and the surface amplitude of the barotropic tide at the coast. Eq. 61 and 65 or 66 allows one to estimate the amplitude at a distance from the shelf-edge. More complicated expressions, which should model the internal shelf

tide more accurately, are referred to but put aside in favour of the simple model which can be easily and realistically applied. It is interesting to note that since $T \propto (\Delta\rho)^{-0,5}$, the tidal shear $\hat{u}_T$ is independent of the strength of the interface (Eq. 19, and 58; also Fig. 7.1).

The inertial velocity shear is best estimated from an accurate wind record as discussed in Section 6.1.1; Eq. 70 and 71 can be used for an event of approximately constant wind strength. For variable wind an iterative finite difference scheme can be used easily to obtain a reasonably confident estimate of $\hat{u}_W$ as a function of time (Pollard and Millard, 1970). Close to a coastal boundary, it appears that inertial energy is reflected into the lower layer and may be measured as a velocity of up to half the strength and out-of-phase with the velocity of the upper layer (Section 6.1.1). This may account for an increase of up to 50% in the predicted value of $\hat{u}_W$.

The ambient sub-inertial velocity shear $\hat{u}_A$ must be obtained from field measurement. It is re-emphasized that this contribution must be small. Further it is only the component $\hat{u}_A$, which is parallel to $\hat{u}_T$ and $\hat{u}_W$, that is relevent to the above calculations.

7.2.4 Associated Fluxes of Contaminants

One of the important consequences of these structural changes is the significant vertical exchange of the conservative properties of the water. The discussion of density stratification has been reduced to a discussion of the semi-conservative property of temperature. Of equal importance is the associated property of salinity. In addition, the fluxes of nutrients essential for primary production are of central importance to marine ecology. These nutrients are usually available from the sediment at the base of the water column and are spread evenly through the partially mixed bottom layer. The interfacial thermocline inhibits flow of these nutrients to the euphotic zone which is

mostly contained in the surface layer. Depletion of some of these surface layer nutrients (e.g. nitrogren compounds) may be the controlling factor for primary productivity and thereby also for productivity at higher trophic levels.

In the case of dominant tidal shear, some of the nutrient-rich bottom water is mixed with some of the nutrient-depleted surface water in forming a modestly endowed tidal mixed layer. This thickened thermocline layer will be ecologically important if it intersects with the euphotic zone or if the internal tides after the mixing event are of sufficient amplitude that it intersects periodically with the euphotic zone.

Since the response time of primary productivity is significantly longer than the time-scale of these events, the nutrient concentration is considered once it has homogenised over the tidal mixed layer. The concentration B_m over this layer is then

$$B_m = \frac{1}{D} \int_{-H_1-\frac{D}{2}}^{-H_1+\frac{D}{2}} B(z)dz \qquad \text{for } -H_1-\frac{D}{2}<z<-H_1+\frac{D}{2} \tag{101}$$

where $B(z)$ is the nutrient concentration before the event. These nutrients are available in the tidal mixed layer and are also 'leaked' to the surface layer by continuous mixing processes (quantified by eddy diffusion coefficients).

In the case of dominant inertial shear, the nutrient input is direct to the surface layer and is immediately available for primary production. An amount of nutrients, per unit surface area,

$$P = \int_{-H_1}^{-H_{1O}} B(z)\, dz \tag{102}$$

is input to the surface layer as a result of the interface being eroded from depth H_{1O} to depth H_1. Once spread uniformly, the surface layer will have a concentration

$$B'_m = \frac{1}{H_1} \int_{-H_1}^{0} B(z)\, dz \qquad \text{for } -H_1 < z < 0. \tag{103}$$

This uniform concentration may possibly not occur owing to differential depletion in the light-filled upper levels. The injection of nutrients P into the surface layer is schematically represented in Fig. 7.7 against a background of continuous eddy diffusion.

7.3 Application and Evaluation of the Combined Shear Model

The deepening effect of wind-driven shear is usually dominant but in some cases it is insufficient to account for the increases in mixed layer depth. The deepening event at Cape Point on 21 and 22 June is the case in point (Section 6.2.2). Large amplitude internal tides coincided with a strong northerly wind immediately prior to the surface mixed layer deepening from about 60 m to over 90 m. This case study led to the investigations of the previous two sections (Sections 7.1 and 7.2), which suggest that internal tides should be included in estimates of mixed layer deepening resulting from wind-driven events on any continental shelves characterized by significant internal tide energy.

In Sub-section 7.3.1 the June 1983 deepening event at Cape Point will be predicted by this model. The same wind event at neap tide would not have led to breakdown (Section 6.2).

Sub-section 7.3.2 includes examples from historical data sets off Cape Point (Section 2.1). Some well-stratified Agulhas Bank profiles will also be discussed in terms of this model.

7.3.1 An Example from the Cape Point Data

Before an analysis of the combined effect of wind and tide on the structure of 21 June (see p. 135), it is interesting to consider each effect in isolation. The effect of wind-driven

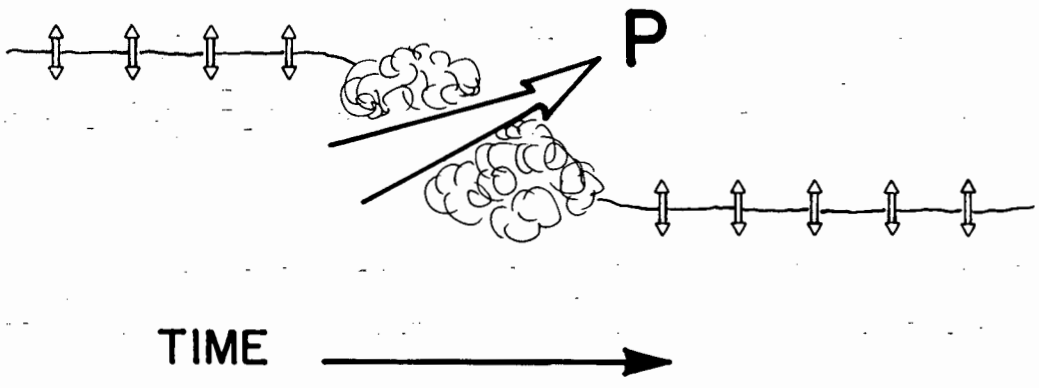

FIGURE 7.7: A schematic of a turbulent mixing event, which injects an amount P of contaminant into the surface layer and deepens the interface, as compared with continuous, two-way diffusion mechanisms.

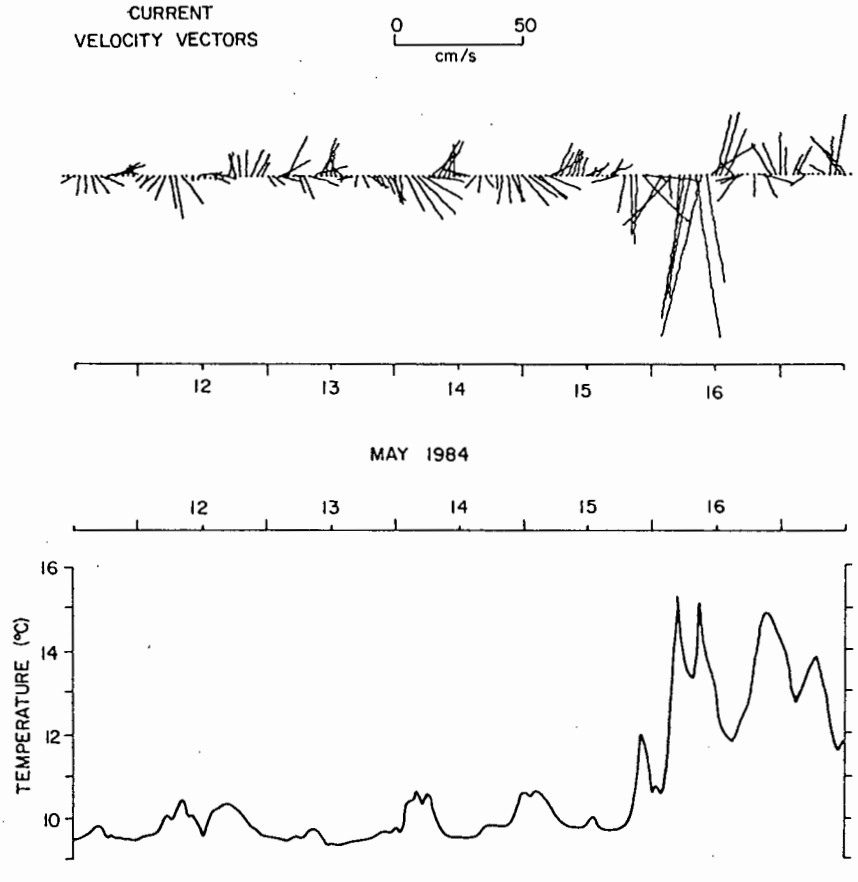

FIGURE 7.8: The response recorded at 103 m depth following extreme winds during mid-May 1984. Strong inertial oscillations, in the lower layer, on 13 and 14 May are followed by an exceptional current pulse and temperature increase on 15 and 16 May.

shear alone is discussed in Sub-section 6.2.2. It is found that the Richardson number is always supercritical and no deepening of the mixed layer may occur.

The interfacial velocity shear due to internal tides is expressed in terms of the tidal amplitude (Eq. 19). Amplitudes of as much as 12 m were recorded during previous spring-tides. The interpolated data (Fig. 6.4) indicates similarly large internal tides immediately preceding the mixing event. Expecting $T = 12$ m the maximum interfacial shear is $\hat{U} = 0,20$ m/s and the root mean square shear is $\hat{u} = 0,14$ m/s. From Eq. 81 the tidal Richardson number is 16 and extensive turbulent breakdown is extremely unlikely. Even if the shear flow did lead to mixing, the effect, as predicted by Eq. 88, is negligible $\Lambda = 1,82$ m. No solution exists for D since the kinetic energy released by the waves is simply insufficient to increase the potential energy of the structure.

Combining the effect of these two shear components, the interface becomes marginally unstable and, owing to the introduction of the $\frac{H_2}{H}$ ratio in Sub-sections 6.2.1 and 7.1.1., this instability is able to penetrate deep into the lower layer. The wind, essentially a north-westerly, drives maximum shear in a north-east orientation which parallels the shear of the internal tide (cf. Eq. 93). The combined shear (including bottom layer inertial currents $\varepsilon \neq 0$) adds up to about 0,5 ms^{-1} for winds of 21 ms^{-1} and internal tides of 12 m. This may be increased further by ambient shear (which seems to be absent), Langmuir circulations (Pollard, 1977) or by barotropic tidal current shear in the bottom boundary layer (if H_1 increases sufficiently). The two-layer Richardson number Ri_o in Eq. 95 takes a marginal value of 1,17 for the parameter values as given in Sub-section 6.2.2. Varying one input while keeping the others fixed, the following results are obtained as a measure of sensitivity:

Ri_o varies from 1,04 to 1,30 as ΔT varies from 4,0° to 5,0°C
Ri_o varies from 0,97 to 1,45 as Δu varies from 0,55 to 0,45m/s

Ri_o varies from 1,07 to 1,30 as $D\rho$ varies from 16,5 to 13,5m
Ri_o varies from 1,11 to 1,20 as H_1 varies from 70 to 60m

Within these ranges, the most unstable case corresponds to $Ri_o \sim 0,74$ and the most stable case corresponds to $Ri_o \sim 1,83$ which are both of order unity. Knowing that if mixing starts D_ρ will increase to $\frac{H_1 H_2}{H}$ and Ri_o will decrease, it is probable that this marginal value indicates full-scale breakdown. The extent of the mixing, which is given by Eq. 98, is dependent on new kinetic energy being input at the surface and being available for release at the interface.

Substituting the values of Sub-section 6.2.2 into Eq. 98, the maximum depth of the mixed layer is from

$$H_{1\,max}{}^2 = \frac{-5525 \pm \sqrt{5525^2 + 4 \cdot 6,80 \times 10^7}}{2}$$

and thus $H_{1\,max} = 77$ m.

This is a significant increase in H_1 and suggests that the calculation is repeated with $\frac{H_2}{H} \sim \frac{1}{3}$. Pre-empting a further increase, the ratio $\frac{H_2}{H} \sim 0,27$ is chosen: Eq. 98 then leads to a prediction of $H_{1\,max} = 89$ m. Further iterations do not converge and the mixed layer is predicted to extend to the bottom (116 m). The thermistors record a mixed structure to at least 95 m while a one-dimensional heat budget indicates that the mixed layer extended to the bottom (Section 6.2.2 and Fig. 6.5). A few days later (27 June) a thermocline has reappeared at about 95 m; this is probably due to the inflow of bottom water from further offshore. In deeper water, a solution $H_1 < H$ is found to Eq. 98 for the conditions during 21 to 23 June. If the offshore interface is shallower than 116 m, then a density-driven flow may restore the bottom layer at the mooring.

At a water depth of 122 m, the iterations converge on a solution of H_1 = 95 m for the conditions as already discussed (Section 6.2.2: H_{1O} = 65 m, ΔT_O = 4,5°C, Δu_O = 0,50 ms^{-1}, Γ = 0,06°C m^{-1}). This suggests that the mixed coastal boundary region extends to a position between the 116 m and 122 m isobaths. In a water depth of 150 m, H_1 is predicted to be 73 m in these conditions (for an infinite water depth, the interface would only be deepened to 58 m - this is comparable to the predictions of Pollard et al., 1973).

For the cases where $\frac{H_2}{H}$ is small, the feedbacks, involved in iterative solution of Eq. 98, are significant. Using a water depth of 122 m to provide a numerical example:

H_1 varies from 72 to 122 m as Δu varies from 0,45 to 0,55 m s^{-1}
H_1 varies from 85 to 122 m as ΔT varies from 5,0 to 4,0°C
H_1 varies from 80 to 122 m as H_{1O} varies from 60 to 70 m
H_1 varies from 87 to 122 m as Γ varies from 0,07 to 0,05°C m^{-1}

It is thus obvious that, near to the singularity $H_2 \to 0$, one cannot predict the depth H_1 with much confidence unless the input values are given with less than 1% uncertainty. Nevertheless, it is valuable to be able to make a qualitative statement that the water column will be mixed to great depth ($\gtrsim$0,8 H) and and possibly to the bottom. For shallower interfaces (in this example, $H_1 \lesssim$ 90 m) a reasonable confidence is attached to the prediction - this can be shown by evaluating the derivatives of H_1 as discussed in Section 7.2.2.

The introduction of the ratio $\frac{H_2}{H}$ and the inclusion of shear due to internal tides, which are excluded from more conventional models (e.g. Pollard et al., 1973), are central to the success of this prediction. While one well-documented example provides insufficient numerical confirmation, it does confirm the concept that deepening of coastal mixed layers should be scaled by $\frac{H_1 H_2}{H}$

rather than by H_1. Further, where significant internal tides exist, their shear must be included in predictions of breakdown (in this example inertial currents, Ekman transport and internal tides contributed equally to the interfacial shear, VR~0,5).

As with the models of the individual components, this combined model usually suffers from uncertainty due to a lack of empirical data on wind speed at sea, internal tide amplitude and initial density structure. Fortunately, the uncertainty associated with the prediction of $H_{1\,max}$ is decreased by the presence of a fourth power in Eq. 98. Uncertainty increases and validity decreases as $H_1 \rightarrow H$ and the singularity ($H_2 \rightarrow 0$) is approached. For $H_2 \lesssim 10$ m (bottom boundary layer thickness) the model should not be used predictively. The locations for which this is the case are included in a coastal boundary region which was excluded from the models at the beginning of the thesis. This coastal mixed region therefore extends further seaward with deepening of the mixed layer in winter.

7.3.2 A Discussion of Previously-Recorded Deep Mixing Events

A survey of some of the temperature profiles recorded off Cape Point (Fig. 2.4 and Boyd et al., 1985) shows that these deep mixing events may be an annual occurrence. Unfortunately the monthly profiles are on a time scale much longer than the event scale under investigation and therefore meaningful hindcasting estimates are not possible. Nevertheless, the wind events are identified and related to the phase of the spring-neap tide cycle.

A surface mixed layer of about 25 m in July 1958 is deepened to about 80 m by September (Fig. 2.4). The following year the 25 m mixed layer depth in April is increased to about 100 m in June. Taking H_1~100 m, ΔT~5°C, H~150 m and coefficient values as in Subsection 7.3.1, an interfacial velocity shear of Δu ~0,45 m/s would have been responsible for the profile recorded in June 1959 (Fig. 2.4). With ε taking a smaller value further

from the coast (Chapter 6) and during negligible tides (neap-tide) this mixed layer depth would correspond to winds of about 27 to 28 ms^{-1}. In the presence of internal spring-tides a more probable sustained 23 ms^{-1} would be sufficient. Weather records for 1959 were not available.

In 1975, Boyd et al. (1985) report a winter mixed layer of over 60 m off Cape Point. It is possible that the surface mixed layer was deeper during July for which there is no data. In 1977 a mixed layer depth of about 95 m was recorded in August and September (Fig. 2.4). Further offshore at station 52-08 an advective event, interpreted as an intrusion of cold Atlantic Ocean Central Water, invalidates the one-dimensional approach. The pre-August deep mixing event at station 52-06, which is at the 1983 mooring site, would only occur if Δu were sufficient to erode a $5^{o}C$ thermocline at a depth of 95 m in a water depth of 130 m. During September the structure was profiled to only 90 m; it is possible that, at this time, the water column was mixed to the bottom. This would be expected if the September station were shallow (H of the order of 100 to 120 m). Estimates of wind speed, extracted from daily synoptic weather maps (issued by the Weather Bureau, Department of Transport), increase to 40 knots during the passage of a mid-latitude cyclone on 16 August. This 21 m/s wind coincides with a spring-tide (A = 0,8 m). Anticipating mean tidal shear of 0,15 m/s and taking $\varepsilon \sim 0,4$, the total interfacial shear would be 0,4 m/s which corresponds to $Ri_D \sim 1$ (Eq. 96). A similar shear event earlier in winter would not deepen as effectively owing to the greater buoyancy (heat content) of the surface mixed layer. Heat loss to the atmosphere during the period between these two event is most important in decreasing the strength and stability of the interface.

A further case of deep mixing was recorded during explosive cyclogenesis ('bomb', Hunter, 1987) in mid-May 1984. From 12 to 17 May several intense frontal systems passed Cape Point. The frontal systems preceding the 'bomb' were effective generators

of inertial motions at 103 m (Fig. 7.8), which is clearly in the bottom layer. These strong inertial currents (up to 0,2 m/s) indicate even stronger currents in the surface layer ($\varepsilon << 1$, Chapter 6). This wind-driven shear on 14 and 15 May is added to by significant shear due to internal spring tides ($A \sim 0,85_m$) generated on 14 May. Expecting a quasi-interfacial thermocline of 6°C, the total shear would be more than sufficient to mix the water column throughout. The temperature increase from 9,5°C to 15°C at 103 m during the night of 15 May. It is not clear whether the 'bomb' itself, or the preceding fronts, was the most effective mixing force but anomalously strong southward currents on 16 May must surely correlate to the freak winds associated with the bomb. In deeper water it is unlikely that the surface mixed layer would have deepened beyond 100 m since the velocity shear is smaller (greater $D_u = \frac{H_1 H_2}{H}$ and smaller ε). Therefore, as the winds and currents subside, density gradients will return cool water to the base of the water column (below 100 m).

The Agulhas Bank: It is tempting to briefly discuss the intense, advectively-imposed thermoclines found to the east of the study area, on the Agulhas Bank (Swart and Largier, 1987). This discussion is presented more fully by Largier and Swart (1987). Considering instaneous events, the mechanism for thermocline production is not of concern. On the inner shelf ($H \sim 100$ m) off Mossel Bay a summertime interface of $\Delta\rho \sim 1,5$ kgm^{-3} at $H_1 \sim 25$ m would seem susceptible to winds in excess of 18,5 ms^{-1} (Pollard *et al.*, 1973). But in place of $D_\rho = H_1$ one should use an the empirical value $D_\rho \sim 10$ m and for D_u one should use $\frac{H_1 H_2}{H}$. The same thermocline is thus only susceptible to wind in excess of 22 ms^{-1} which are much less common (Hunter, 1987). A suggested interface, of $\Delta\rho \sim 1$kgm^{-3} at $H_1 \sim 40$ m, in winter would correspond to winds of 21 ms^{-1} and in the hypothetical absence of advective effects, this mixed layer depth should be maintained during winter off Mossel Bay. Internal tides, generated along the eastern edge of the bank, are of small amplitude and may be neglected (Largier and Swart, 1987).

Monthly transects along a line south of Cape Infanta (to the west of Mossel Bay and east of Cape Agulhas) have been reported by Shelton (1986) and seasonal transects by Eagle and Orren (1986). The strongly interfacial structure ($\Delta\rho \sim 1,5$ kgm^{-3}), $H_1 \sim 30$ to 50 m and $D_\rho \sim 10$ to 20 m) found in summer is completely mixed in winter. With a summer surface layer temperature of about 21°C and bottom layer temperature of about 10°C, the conservation of temperature (in the absence of advection) implies a mixed temperature of 14° to 16°C throughout a water depth of 80 to 100 m. However, the Agulhas Bank structure is characterized by advective processes (Swart and Largier, 1987) which invalidate this approach. Empirical winter temperatures are usually about 16°C throughout the water column. Further east, where the interface survives the winter, the deepened surface layer is also about 16°C (Schumann and Beekman, 1984). The bottom layer, which is usually mixed, maintains a temperature of 10°C.

Interfacial velocity shear would be required to overcome this 6°C or ~0,9 kgm^{-3} interface. Eq. 100 is not suitable in this two-layer case because of the advection of both surface and bottom water. As the surface layer is deepened, the interface will not weaken - the temperature difference will remain at about 6°C during deepening. Using Eq. 96, a velocity shear of 0,46 ms^{-1} is required to deepen the interface at 50 m depth in 100 m water depth. With an internal spring tide shear $\overline{\hat{u}_T^2}$ ~0,1 ms^{-1} and $\varepsilon \sim 0,5$ a wind speed of 19 ms^{-1} (or less for unstable conditions; Large and Pond, 1981) should suffice. As the interface deepens further $\frac{H_1 H_2}{H}$ decreases and smaller Δu is required but $\hat{u}_W \propto \frac{1}{H_1}$ is weaker for given wind speed. Nevertheless a wind speed of 20 ms^{-1}, with internal spring tides, should be capable of deepening the 6°C thermocline at any depth. In 80 m water depth, Ri_D will go subcritical more easily - the interface at 50 m requires a shear of only 0,40 ms^{-1} for deepening. At these shallower locations, further from the shelf-edge, the internal tide may have been significantly damped so that critical wind speeds should be similar to those further offshore.

In essence, one can expect that the water column on the shallow (H<100 m) Agulhas Bank off Cape Infante will be totally mixed during winter. In other words, the coastal boundary layer spreads from less than 5 km in summer to as much as 100 km offshore during winter.

CHAPTER 8
CONCLUSION

The cross-thermocline transport of water and its properties, due to internal waves, may be separated into smaller-scale, continuous, parametrizable diffusion and larger-scale, semi-deterministic turbulent events. While the background diffusive fluxes may contribute significantly to longer-term mean effects, attention has been focussed on the reversible and irreversible deformations of the seasonal thermocline on a time scale from hours to days. Within this context, it is only necessary to consider the internal tides and inertial oscillations.

Spectral analysis of the thermistor string data from the Cape Point mooring yields the three characteristic upper ocean peaks at inertial frequency, tidal frequency and near-buoyancy frequency (Levine, 1983). The high frequency peak, which alone accounts for about 5% of the variance of the internal wave field, is treated as a sink of internal tide energy and thus partially explains the strong tidal damping (e-folding over one or two cycles) on continental shelves. The internal tide, strongly displayed as vertical displacement of isotherms at the thermocline, accounts for the majority (over 50%) of the recorded temperature variance. The inertial oscillations, rotationally restored internal waves, are essentially horizontal motions which produce a weak temperature signal in the presence of weak or intermittent horizontal gradients. Therefore the data analysis presented in Chapter 4 is primarily a comment on tidal dynamics and secondarily a comment on sub-inertial forced changes to the vertical structure.

An empirical orthogonal function analysis confirms that these dominant signals (and especially the internal tide) are characterized by low vertical wavenumbers on the continental shelf. The vertical structure over the depth range of the thermistor string consists, almost exclusively, of the first two principal components; the tide accounting for the majority of mode 1 and the sub-inertial events accounting for the majority of mode 2.

The first mode internal tide, which accounts for over two-thirds of the variance of the semi-diurnal tidal peak, may be justifiably approximated by an interfacial wave.

This two-layer approximation, employed by Rattray (1960) and theoretically deduced by Baines (1982), is continued in the expressions developed for generation, propagation and dissipation of the internal tide. Suggesting resonance across Cape Point Valley, interfacial tides of amplitudes of the order of 7 m are expected at the mooring following optimum springtide generation. Unfortunately, the temporally varying density structure (on time scales as rapid as the tide itself) and spatially varying barotropic forcing (on rather small scales for a narrow, irregular shelf) conspire to produce large uncertainty. The modelling exercise is successful, however, in providing insight to the reasons for anomalously large internal tide amplitudes recorded on a narrow shelf. The maxima (over 12 m amplitude) recorded at the mooring would be more closely reproduced by a continuously stratified model which accounted for partial reflection of the internal tide at the coast. A second severe restriction on the model is the use of linearsized equations - amplitude: water depth ratios $\frac{T}{H}$ ~0,1 are near the limit of such linear formulation. Nevertheless, the simplified linear, interfacial model used in Chapter 5 allows one to obtain easily a reasonable first approximation which is invaluable in the absence of empirical data.

The empirical estimates of shoreward energy flux (about 140 Wm^{-1}) are too large to be dissipated by quasi-continual processes such as non-linear transfer to other internal waves, viscous attenuation (Reynold's stresses) and bottom attenuation. Therefore turbulent breakdown could be expected as or before the wave approaches the coast. The singularity, as the thermocline encounters the shoaling bottom, is excluded from this analysis but breakdown at this apex may be expected

(Cachionne and Wunsch, 1972) in the absence of earlier shear instability. With maximum interfacial shear of about 0,20 ms^{-1} corresponding to the spring internal tides, the possibility and effect of shear instabilities are investigated for semi-interfacial structure. The model presented in Section 7.1 is controlled by a Richardson number criterion (cf. Pollard et al., 1973). While breakdown may occur readily for weaker stratification in shallower water, the new tidal mixed layer is generally contained to within a few metres of the original interface. In the case of a strongly turbulent upper layer and a significantly stratified lower layer the tidal mixed products are expected to be incorporated into an extended surface mixed layer. Both Kantha (1977) and Turner (1981) suggest that these remotely-generated interfacial waves should receive attention concerning their role in enhancing turbulent deepening of the thermocline.

It is now well accepted that the wind-driven inertial oscillations, in association with Ekman transport, are important agents in deepening the surface mixed layer. These wind-driven currents, which are only hinted at by the thermistor data, may be well simulated by input of reliable wind data to the model of Pollard (1970). Wind-driven deepening of the surface mixed layer is then predicted by the simple but successful model of Pollard et al. (1973). The observed sub-inertial events (Sections 2.1, 4.2 and 6.2) are found to correspond to a coastal upwelling feature, an advective input of warm Agulhas water and/or a wind event conducive to this thermocline-deepening process. The adoption of the two-layer approximation is equally valid for these dynamics, in particular, Pollard and Millard (1970) presented a reliable 'slab' model. Irrespective of this approximation, the resultant interfacial shear depends strongly on the measured wind speed (wind stress is proportional to wind speed squared). Although theory exists for reducing wind to the 10 m reference level, little information is available for converting coastal records to open sea values. Nevertheless, this wind-driven interfacial shear is a major factor accounting

for rapid deepening of the surface mixed layer following the wind events associated with mid-latitude cyclones characteristic of winter.

From these earlier chapters (4 to 6) it is clear that both internal tides and wind-driven motion may result in significant shear instabilities which lead to deformation of the seasonal thermocline. The penultimate chapter, which considers the combined effect of these two sources of shear, is the crux of the thesis. Within the discussion centred on the Richardson number criterion, the crucial issue is the choice of appropriate vertical scales D_u and D_ρ for velocity and density structure. The conventional choice of H_1 (mixed layer depth) as a common scale for prediction of breakdown and extent of mixing is replaced by a two-layer scale $\frac{H_1 H_2}{H}$. Mixed layers are generally shallow ($H_1 < \frac{H}{2}$) and the introduction of the ratio H_2/H is of limited effect. However for deeper mixing, H_2/H becomes increasingly smaller until, near the limit ($H_2 \to 0$), shear-induced mixing may no longer be self-limiting. This is a radical conceptual change from the ideas of Turner (1973; 1981) and Pollard et al. (1973). It stems from the decision to account for the proximity of the thermocline to the lower boundary on the continental shelf and results in enhanced shear and turbulence as this boundary is approached. The singularity as $H_2 \to 0$ is not considered analytically. There is a change-over from interfacial dynamics to boundary layer dynamics before the singularity is reached - the result being a mixed water column characteristic of shallow seas (smaller H). A few such deep mixing events are handled and, for the well-described event of June 1983, it is explicitly clear that both internal tide and wind-driven shear need to be included. The inclusion of tidal shear is most important for deeper interfacial dynamics (greater H_1)on continental shelves where internal tides are significant (that is, amplitudes of a few metres or more).

Throughout these above models, the key criteria of simplicity, applicability and representivity have been closely followed in the attempt to predict internal tides and the associated thermocline breakdown due to "symbiosis" with wind-driven shear. The

internal wave field was represented by two semi-deterministic components in preference to the Garrett and Munk style statistical model which has been used extensively in recent internal wave research. In addition to being simpler, this approach allows one much more insight to the dominant linear processes within the internal wave continuum. Adoption of a constant-N model would have been no more involved but, following Baines (1982) and Pollard and Millard (1970), it would have been less representative. However, as the opposite extreme to interfacial structure it would be a useful complementary exercise in determining the limits of response for a real continuously-stratified water column. Likewise the inclusion of second-order non-linear terms would contribute considerably to the results for larger amplitude dynamics and possibly would reveal a substantial non-linear interaction between the dominant tidal and inertial oscillations. In order to do this the tidal-inertial baroclinic dynamics should be formulated and solved as one.

In conclusion, the achievements of this thesis should be evaluated. The Cape Point internal tide, which in a sense is anomalous, is conceptually modelled with success. Further, easily-applied predictive expressions for general internal shelf tide generation, propagation and dissipation have been formulated. With reference to the data collected at the Cape Point mooring, however, these expressions provide a numerical underestimation of maximum springtide amplitudes. This lack of agreement could be anticipated when consideration is taken of the sources of uncertainty.

Linear combination of internal tide and inertial shear, while being conceptually elementary, provided some useful answers to the speculations of Kantha (1977) and Turner (1981). Within this exercise the choice of vertical length scales was crucial - the chosen scale suggesting enhanced thermocline erosion as the bottom is approached. For thermoclines deep relative to effective wind stress, internal tide shear may be essential whereas for thermoclines shallow relative to effective wind stress, the internal tide shear is usually of little consequence.

It is hoped that these findings, if too rough to be applied predictively, will at least be of value in providing an insight into cross-thermocline exchange on a time scale of hours to days. As part of larger conceptual or analytical ecosystem or pollution models, it is anticipated that this work may contribute in some very small way to management and preservation of 'healthy seas'.

REFERENCES

ABARBANEL, H D I (1984). Stability of inviscid stratified flows under non-linear perturbations. In: *Internal Gravity Waves and Small-Scale Turbulence*, P Müller and R Pujalet (eds). Hawaii Inst. Geophysics, 263-276

ANDREWS, W R H and HUTCHINGS, L (1980). Upwelling in the southern Benguela Current. *Prog Oceanogr.* 9, 1-81.

APEL, J R (1981). Non-linear features of internal waves as derived from the SEASAT imaging radar. In: *Oceanography from Space*, J F R Gower (ed). Plenum. pp 525-533.

APEL, J R, BYRNE, H M, PRONI, J R and CHARNELL, R L (1975). Observations of oceanic internal and surface waves from the Earth Resources Technology Sattelite. *J. Geophys. Res.*, 80, 865-881.

APEL, J R, BYRNE, H M, PRONI, J R, SELLERS, R (1976). A study of oceanic internal waves using satellite imagery and ship data. *Remote Sensing of the Environment*, 5, 125-135.

AUBREY, D G and EMERY, K O (1983). Eigenanalysis of recent United States sea levels. *Cont. Shelf Res.*, 2, 21-33.

BAINES, P G (1973). The generation of internal tides by flat-bump topography. *Deep-Sea Res.*, 20, 179-205.

BAINES, P G (1974). The generation of internal tides over steep continental slopes. *Phil. Trans. R. Soc. Land.*, A277, 27-58.

BAINES, P G (1981). Satellite observations of internal waves on the Australian North-west shelf. *Aust. J. Mar. Freshwater Res.*, 32, 457-463.

BAINES, P G (1982). On internal tide generation models. *Deep-Sea Res.*, 29, 307-338.

BAINES, P G and FANG, X-H (1985). Internal tide generation at a continental shelf/slope junction: a comparison between theory and a laboratory experiment. *Dyn. Atmos. Oceans*, 9, 297-314.

BANG, N D (1972). General Report: Finer Structure Studies 1965-1970. *Unpublished personal report, CSIR Oceanogr. Res. Unit., Univ. Cape Town.*

BANG, N D (1973). The Southern Benguela System: Finer Oceanic Structure and Atmospheric Determinants. *Ph.D. thesis, Univ. Cape Town*, 181 pp.

BANG, N D (1974). Observational indications of the behaviour of internal waves approaching the sea surface outcrop of their transmitting interface. *Proces-Verbaux*, 13, 103 (abstract only).

BANG, N D and ANDREWS, W R H (1974). Direct current measurements of an oceanic frontal jet in the upwell regime west of Cape Town. *J. Mar. Res.*, 32, 405-417.

BATTISTI, D S and CLARKE, A J (1982). A simple method for estimating barotropic tidal currents on continental margins with specific application to the M_2 tide off the Atlantic and Pacific coasts of the United States. *J. Phys. Oceanogr.* 12, 8-16.

BELL, T H, Jr (1975). Topographically generated internal waves in the open ocean. *J. Geophys. Res.*, 80, 320-327.

BENDAT, J S and PIERSOL, A G (1971). *Random Data: Analysis and Measurement Procedures.* Wiley-Interscience, New York, 407 pp.

BLACKFORD, B L (1978). Wind-driven inertial currents in the Magdalen Shallows, Gulf of St Lawrence. *J. Phys. Oceanogr.*, 8, 653-664.

BOYD, A J (1986). Frontal features at the ends of the Benguela upwelling area in summer. Poster presentation *Benguela '86 International Symposium*, Univ. Cape Town.

BOYD, A J, TROMP, B B S and HORSTMAN, D A (1985). The hydrology off the South African south-western coast between Cape Point and Danger Point in 1975. *S. Afr. J. Mar. Sci.*, 3, 145-168.

BREKHOVSKIKH, L M, KONJAEV, K V, SABININ, K D and SERIKOV, A N (1975). Short-period internal waves in the sea. *J. Geophys. Res.*, 80, 856-864.

BRISCOE, M G (1975). Internal waves in the ocean. *Rev. Geophys. Space Phys.*, 13, 591-598.

BROWNE, M W (1983). Principal components: a review. *Proceedings of the Seminar on Principal Components Analysis in the Atmospheric and Earth Sciences*, CSIR, Pretoria, 17-23.

CACCHIONE, D and WUNSCH, C (1974). Experimental study of internal waves over a slope. *J. Fluid Mech.*, 66, 223-239.

CAIRNS, J L (1967). Asymmetry of internal tidal waves in shallow coastal waters. *J. Geophys. Res.*, 72, 3563-3565.

CARSON, R (1950). *The Sea around Us*. Panther Books, London, 256 pp.

CHERESKIN, T K (1983). Generation of internal waves in Massachusetts Bay. *J. Geophys. Res.*, 88, 2649-2661.

CLARKE, A J and BATTISTI, D S (1981). The effect of continental shelves on tides. *Deep-Sea Res.*, 28A, 665-682.

COX, C S (1962). Internal waves. In: *The Sea* Vol. 1, M N Hill (ed), Interscience, New York, 752-763.

CRAMPIN, D J and DORE, B D (1970). Numerical comparisons of the damping of internal gravity waves in stratified fluids. *Pure Appl. Geophys.*, 79(2), 53-65.

CURTIN, T B and MOOERS, C N K (1975). Observations and interpretation of a high-frequency internal wave packet and surface slick pattern. *J. Geophys. Res.*, 80, 882-894.

D'ASARO, E A (1985a). Upper ocean temperature structure, inertial currents, and Richardson numbers observed during strong meteorological forcing. *J. Phys. Oceanogr.*, 15, 943-962.

D'ASARO, E A (1985b). The energy flux from the wind to near-inertial motions in the surface mixed layer. *J. Phys. Oceanogr.*, 15, 1043-1059.

DAVIS, R E, DE SZOEKE, R and NIILER P (1981). Variability in the upper ocean during MILE. Part II: Modelling the mixed layer response. *Deep-Sea Res.*, 28A, 1453-1475.

DEFANT, A (1961). *Physical Oceanography*. Vol. 2, New York, Pergamon, 598 pp.

DESAUBIES, Y and SMITH W K (1982). Statistics of Richardson number and instability in oceanic internal waves. *J. Phys. Oceanogr.*, 12, 1245-1259.

DE WITT, L M, LEVINE, M D, PAULSON, C A and BURT, W V (1986). Semidiurnal internal tide in JASIN: observations and simulation. *J. Geophys. Res.*, 91, 2581-2592.

DILLON, T M and CALDWELL, D R (1978). Catastrophic events in a surface mixed layer. *Nature*, 276, 601-602.

DINGLE, R V, MOIR, G J, BREMNER, J M, and ROGERS, J (1977). Bathymetry of the continental shelf off the Republic of South Africa and South West Africa. *Marine Geoscience Series 1*, Geological Survey, Dept. of Mines.

DJORDJEVIC, V D and REDEKOPP, L G (1978). The fission and disintegration of internal solitary waves moving over two-dimensional topography. *J. Phys. Oceanogr.*, 8, 1016-1024.

DUNCAN, C P and NELL, J H (1969). Surface currents off the Cape coast. *Investigational Report of the Division of Sea Fisheries of South Africa*, 76, 19 pp.

EAGLE, G A and ORREN, M J (1985). A seasonal investigation of the nutrients and dissolved oxygen in the water column along two lines of stations south and west of South Africa. *Rep. 567, Nat. Res. Inst. Oceanol., CSIR, Stellenbosch*, 52 pp.

EKMAN, V W (1904). On dead-water. *Scientific Results of the Norwegian North Polar Expedition 1893-1896*, 5(15), 1-152.

ERIKSEN, C C (1978). Measurements and models for fine-structure, internal gravity waves and wave breaking in the deep ocean. *J. Geophys. Res.*, 83, 2989-3009.

ERMAKOV, S A, PELINOVSKY, E N (1984). Variation of the spectrum of wind ripple on coastal waters under the action of internal waves. *Dyn. Atmos. Oceans.* 8, 95-100.

EWING, G (1950). Slicks, surface films and internal waves. *J. Mar. Res.* 9, 161-187.

FU, L-L (1981). Observations and models of inertial waves in the deep ocean. *Rev. Geophys. Space Phys.*, 19, 141-170.

FU, L-L and HOLT, B (1982). SEASAT views oceans and sea ice with synthetic aperture radar. *Publ. 81-120, Jet Propul. Lab., Pasadena, Calif.*, 200 pp.

FU, L-L and HOLT, B (1984). Internal waves in the Gulf of California: observations from a spaceborne radar. *J. Geophys. Res.*, 89, 2053-2060.

GARGETT, A E and HOLLOWAY, G (1984). Dissipation and diffusion by internal wave breaking. *J. Mar. Res.*, 42, 15-27.

GARGETT, A E and HUGHES, B A (1972). On the interaction of surface and internal waves. *J. Fluid Mech.*, 52, 179-191.

GARRETT, C and MUNK, W (1972a). Space-time scales of internal waves. *Geophys. Fluid Dyn.*, 2, 225-264.

GARRETT, C and MUNK W (1972b). Oceanic mixing by breaking internal waves. *Deep-Sea Res.*, 19, 823-832.

GARRETT, C and MUNK, W (1975). Space time-scales of internal waves: a progress report. *J. Geophys. Res.*, 80, 291-297.

GARRETT, C and MUNK, W (1979). Internal waves in the ocean. *Ann. Rev. Fluid Mech.*, 11, 339-369.

GARWOOD, R W, Jr (1979). Air-sea interaction and dynamics of the surface mixed layer. *Rev. Geophys. Space Phys.*, 17, 1507-1524.

GILL, A E (1982). *Atmosphere-Ocean Dynamics.* Academic Press, New York, 662 pp.

GILL, A E and TURNER, J S (1976). A comparison of seasonal thermocline models with observations. *Deep-Sea Res.*, 23, 391-401.

GOLD, E (1908). Barometric gradient and wind force. *Meteorol. Off., M O 190*, H M Stationery Office, London.

GORDON, R L (1978). Internal wave climate near the coast of northwest Africa during JOINT-1. *Deep-Sea Res.*, 25, 625-643.

GORDON, R L (1979). Tidal interactions in a region of large bottom slope near northwest Africa during JOINT-1. *Deep-Sea Res.*, 26A, 199-210.

GOULD, W J and McKEE, W D (1973). Vertical structure of semi-diurnal tidal currents in the Bay of Biscay. *Nature*, 244, 88-91.

GREGG, M C and BRISCOE, M G (1979). Internal waves, fine structure, microstructure and mixing in the ocean. *Rev. Geophys. Space Phys.*, 17, 1524-1548.

GREGG, M C, D'ASARO, E A, SHAY, T J and LARSON, N (1986). Observations of persistent mixing and near-inertial internal waves. *J. Phys. Oceanogr.*, 16, 856-885.

GRÜNDLINGH, M L (1980). On the volume transport of the Agulhas Current. *Deep-Sea Res.*, 27, 557-563.

HALPERN, D (1971). Semidiurnal internal tides in Massachusetts Bay. *J. Geophys. Res.* 76, 6573-6584.

HAURY, L R, WIEBE, P H, ORR, M H and BRISCOE, M G (1983). Tidally generated high-frequency internal wave packets and their effects on plankton in Massachusetts Bay. *J. Mar. Res.*, 41, 65-112.

HENDERSHOTT, M C (1973). Ocean tides. *Eos Trans. AGU*, 54, 76-86.

HENDERSHOTT, M C (1981). Long waves and ocean tides. In: *Evolution of Physical Oceanography*, B A Warren and C Wunsch (Eds), MIT Press, Cambridge, 292-341.

HENDRY, R M (1977). Observations of the semi-diurnal internal tide in the western north Atlantic ocean. *Phil. Trans. R. Soc. Lond.*, A286, 1-24.

HOLLOWAY, P E (1983). Internal tides on the Australian north-west shelf: a preliminary investigation. *J. Phys. Oceanogr.*, 13, 1357-1370.

HOLLOWAY, P E (1984). On th semi-diurnal tide at a shelf-break region on the Australian north west shelf. *J. Phys. Oceanogr.*, 14, 1787-1799.

HOLLOWAY, P E (1985). A comparison of semi-diurnal internal tides from different bathymetric locations on the Australian north-west shelf. *J. Phys. Oceanogr.*, 15, 240-251.

HUNTER, I T (1987). The weather of the Agulhas Bank and the Cape south coast. *M.SC. Thesis, University of Cape Town,* submitted.

HUTHNANCE, J M (1981). Waves and currents near the continental shelf edge. *Prog. Oceanogr.*, 10, 193-226.

HUTHNANCE, J M and BAINES, P G (1982). Tidal currents in the northwest African upwelling region. *Deep-Sea Res.*, 29, 285-306.

INMAN, D L and BRUSH, B M (1973). The coastal challenge. *Science,* 181, 20-32.

JAMES, I D (1982). Tidal currents at two deep-sea moorings near the shelf edge. *Deep-Sea Res.*, 29, 1099-1111.

JENKINS, G M and WATTS, D G (1968). *Spectral Analysis and its Application.* Holden-Day, 525 pp.

JENSEN, T G (1983). Observations of inertial oscillations and vertical mixing during a storm. *Rep. No. 46, Inst. Fysisk Oceanografi, Univ. Copenhagen,* 42 pp.

JURY, M R (1980). Characteristics of summer wind fields and air-sea interactions over the Cape Peninsula upwelling region. *M.Sc. Thesis, Univ. Cape Town,* 131 pp.

JURY, M R (1984). Wind shear and differential upwelling along the SW tip of Africa. *Ph.D. Thesis, Univ. Cape Town,* 161 pp.

KANTHA, L H (1977). Note on the role of internal waves in thermocline erosion. In: *Modelling and Prediction of the Upper Layers of the Ocean,* E B Krauss (ed), Pergamon, Oxford, 173-177.

KRAUSS, E B and TURNER, J S (1967). A one-dimensional model of the seasonal thermocline II: The general theory and its consequences. *Tellus,* 19, 98-106.

KRAUSS, W (1966). *Interne Wellen.* Gebrüder Borntreger, Berlin.

KRAUSS, W (1979). Inertial waves in an infinite channel of rectangular cross section. *Dtsch. Hydrogr. Z.,* 32, 248-266.

KRAUSS, W (1981). The erosion of a thermocline. *J. Phys. Oceanogr.,* 11, 415-433.

KUNDU, P K (1976). An analysis of inertial oscillations observed near Oregon coast. *J. Phy. Oceanogr.,* 6, 879-893.

KUNDU, P K (1984). Generation of coastal inertial oscillations by time-varying wind. *J. Phys. Oceanogr.,* 14, 1901-1913.

KUNZE, E (1985). Near-inertial wave propagation in geostrophic shear. *J. Phys. Oceanogr.,* 15, 544-565.

LA FOND, E C and LA FOND, K G (1967). Internal thermal structures in the ocean. *J. Hydronautics,* 1, 48-53.

LARGE, W G and POND, S (1981). Open ocean momentrum flux measurements in moderate to strong winds. *J. Phys. Oceanogr.,* 11, 324-336.

LARGIER, J L (1986). A review of the theory of oceanic internal waves over the continental shelf. *Rep. T/SEA 8606, Nat. Res. Inst. Oceanol., CSIR, Stellenbosch,* 128 pp.

LARGIER, J L (1987). Linear prediction of interfacial tides on corrugated continental shelves. Pre-print for *Third International Symposium on Density Stratified Flow.* Caltech, Pasadena.

LARGIER, J L and SWART, V P (1987). East-west variation in thermocline breakdown on the Agulhas Bank. In: *Benguela-86*, A I L Payne, J A Gulland and K H Brink (eds), *S. Afr. J. Mar. Sci.*, 5 (in press).

LE BLOND, P H (1966). On the damping of internal gravity waves in a contiously stratified ocean. *J. Fluid Mech.*, 25, 121-142.

LE BLOND, P H and MYSAK, L A (1978). *Waves in the Ocean.* Elsevier, New York, 560 pp.

LEVINE, M D (1983). Internal waves in the ocean: a review. *Rev. Geophys. Space Phys.*, 21, 1206-1216.

LEVINE, M D, DE SZOEKE, R A and NIILER, P P (1983). Internal waves in the upper ocean during MILE. *J. Phys. Oceanogr.*, 13, 240-257.

MARSDEN, R F (1986). The internal tide on Georges Bank. *J. Mar. Res.*, 44, 35-50.

MAXWORTHY, T (1979). A note on the internal solitary waves produced by tidal flow over a three-dimensional ridge. *J. Geophys. Res.*, 84, 338-346.

MAXWORTHY, T, CHABERT d'HIERES, G and DIDELLE, H (1984). The generation and propagation of internal gravity waves in a rotating fluid. *J. Geophys. Res.*, 89, 6383-6396.

McCOMAS, C H and BRETHERTON, F P (1977). Resonant interaction of oceanic internal waves. *J. Geophys. Res.*, 82, 1397-1412.

McCOMAS, C H and MÜLLER, P (1981). The dynamic balance of internal waves. *J. Phys. Oceanogr.*, 11, 970-986.

MELLOR, G L (1973). Analytic prediction of the properties of stratified planetary surface layers. *J. Atmos. Sci.*, 30, 1061-1069.

MÜLLER, P (1976). On the diffusion of momentum and mass by internal gravity waves. *J. Fluid Mech.*, 77, 789-823.

MUNK, W (1981). Internal waves and small-scale processes. In: *Evolution of Physical Oceanography*, B A Warren and C Wunsch (eds), MIT Press, Cambridge, 264-290.

MUNK, W H and MacDONALD, G J F (1960). *The Rotation of the Earth.* Cambridge University Press, Londin, 332 pp.

NANSEN, F (1902). The oceanography of the north polar basin. *Scientific Results of the Norwegian North Polar Expedition 1893-1896*, 3(9).

NELSON, G (1983). Circulation over the shelf zone of the Cape Peninsula region. *S. Afr. J. Sci.*, 79, 147 (abstract only).

NELSON, G (1985). Notes on the physical oceanography and the Cape Peninsula upwelling system. In: *South African Ocean Colour and Upwelling Experiment*, L V Shannon (ed), Sea Fisheries Research Institute, Cape Town, 63-95.

NELSON, G and HUTCHINGS, L (1983). The Benguela upwelling area. *Prog. Oceanogr.*, 12, 333-356.

NELSON, G and SHANNON, L V (1983). Satellite sensed internal wave features off the south-west Cape coast. *S. Afr. J. Sci.*, 79, 147 (abstract only).

NIILER, P P (1977). One-dimensional models of the seasonal thermocline. In: *The Sea* Vol. 6, E D Goldberg, I N McCave, J J O'Brien, J H Steele (eds), John Wiley, New York, 97-115.

NIILER, P P and KRAUSS, E B (1977). One-dimensional models of the upper ocean. In: *Modelling and Prediction of the Upper Layers of the Ocean*, E B Krauss (ed), Pergamon Press, Oxford, 143-172.

OAKEY, N S and ELLIOTT, J A (1982). Dissipation within the surface mixed layer. *J. Phys. Oceanogr.*, 12, 171-185.

OLBERS, D J (1983). Models of the oceanic internal wave field. *Rev. Geophys. Space Phys.* 21, 1567-1606.

ORLANSKI, I and BRYAN, K (1969). Formation of the thermocline step structure by large-amplitude internal gravity waves. *J. Geophys. Res.*, 74, 6975-6983.

OSBORNE, A R and BURCH, T L (1980). Internal solitons in the Andaman Sea. *Science*, 208, 451-460.

PADMAN, L and JONES, I S F (1985). Richardson number statistics in the seasonal thermocline. *J. Phys. Oceanogr.*, 15, 844-854.

PETRIE, B (1975). M2 surface and internal tides on the Scotian shelf and slope. *J. Mar. Res.*, 33, 303-323.

PHILLIPS, O M (1977). *The Dynamics of the Upper Ocean* (2nd edition), Cambridge University Press, Cambridge, 336 pp.

PINGREE, R D and MARDELL, G T (1985). Solitary internal waves in the Celtic Sea. *Prog. Oceanogr.*, 14, 431-441.

PINKEL, R (1981). Observations of the near-surface internal wavefield. *J. Phys. Oceanogr.*, 11, 1248-1257.

POLLARD, R T (1970). On the generation by winds of inertial waves in the ocean. *Deep-Sea Res.*, 17, 795-812.

POLLARD, R T (1977). Observations and theories of Langmuir circulations and their role in near surface mixing. In: *A Voyage of Discovery*, M Angel (ed), Pergamon, Oxford, 235-252.

POLLARD, R T (1980). Properties of near-surface inertial oscillations. *J. Phys. Oceanogr.*, 10, 385-398.

POLLARD, R T and MILLARD, R C (1970). Comparisons between observed and simulated wind-generated inertial oscillations. *Deep-Sea Res.*, 17, 813-821.

POLLARD, R T, RHINES, P B and THOMPSON, R O R Y (1973). The deepening of the wind-mixed layer. *Geophys. Fluid Dyn.*, 3, 381-404.

PRINSENBERG, S J, WILMOT W L and RATTRAY, M, Jr (1974). Generation and dissipation of coastal internal tides. *Deep-Sea Res.*, 21, 263-281.

PRINSENBERG, S J and RATTRAY, M, Jr (1975). Effects of continental slope and variable Brunt-Väisälä frequency on the coastal generation of internal tides. *Deep-Sea Res.*, 22, 251-263.

RATTRAY, M R, Jr (1957). Propagation and dissipation of long internal waves. *Trans. Amer. Geophys. Union*, 38, 495-500.

RATTRAY, M, Jr (1960). On the coastal generation of internal tides. *Tellus*, 12, 54-62.

RATTRAY, M, Jr, DWORSKI, J G and KOVALA, P E (1969). Generation of long internal waves at the continental slope. *Deep-Sea Res.*, 16S, 179-195.

RAYLEIGH (1883). Investigation of the character of the equilibrium of an incompressible heavy fluid of variable density. *Proc. London Math. Soc.* 14, 170-178.

REDFIELD, A C (1958). The influence of the continental shelf on the tides of the Atlantic coast of United States. *J. Mar. Res.*, 17, 432-448.

ROBERTS, J (1975). *Internal Gravity Waves in the Ocean.* Marcel Dekker Inc., New York, 274 pp.

ROTH, M V, BRISCOE, M G and McCOMAS C H, III (1981). Internal waves in the upper ocean. *J. Phys. Oceanogr.*, 11, 1235-1247.

RUDDICK, B R and JOYCE, T M (1979). Observations of interaction between the internal wavefield and low frequency flows in the North Atlantic. *J. Phys. Oceanogr.*, 9, 498-517.

SANDSTROM, H and ELLIOTT, J A (1984). Internal tide and solitons on the Scotian shelf: a nutrient pump at work. *J. Geophys. Res.*, 89, 6415-6426.

SCHOTT, F (1977). On the energetics of baroclinic tides in the North Atlantic. *Ann. Geophys.*, 33, 41-62.

SAWYER, C (1983). A Sattellite Study of Ocean Internal Waves. *NOAA Tech. Memo.*, 70 pp.

SCHUMANN, E H and L J BEEKMAN (1984). Ocean temperature structures on the Agulhas Bank. *Trans. Roy. Soc. S. Afr.*, 45, 191-203.

SCHUMANN, E H and PERRINS, L-A (1982). Tidal and inertial currents around South Africa. *Proc. Eighteenth Coastal Eng. Conf., ASCE, Cape Town,* 2562-2580.

SHANNON, L V (1966). Hydrology of the south and west coasts of South Africa. *Investigational Report of the division of Sea Fisheries of South Africa*, 58, 22 pp.

SHANNON, L V (1985). The Benguela ecosystem. Part 1. Evolution of the Benguela, physical features and processes. *J. Oceanogr. Mar. Biol. Ann. Rev.*, 23, 105-182.

SHANNON, L V, NELSON, G and JURY, M R (1981). Hydrological and meteorological aspects of upwelling in the southern Benguela Current. In: *Coastal and Estuarine Sciences, 1, Coastal Upwelling*, F Richards (ed), AGU, 146-159.

SHELTON, P A (1986). Fish spawning strategies in the variable southern Benguela Current region. *Ph.D. Thesis, Univ. Cape Town*, 327 pp.

SHELTON, P A and HUTCHINGS, L (1982). Transport of anchovy *Engraulis capensis* Gilchrist, eggs and early larvae by a frontal jet current. *J. Cons. perm. int. Explor. Mer.*, 40, 185-198.

SHERMAN, F A, IMBERGER, J and CORCOS, G M (1978). Turbulence and mixing in stably stratified waters. *Ann. Rev. Fluid Mech.*, 10, 267-288.

STERN, M E (1975). *Ocean Circulation Physics*. Academic Press, New York, 246 pp.

STOKES, G G (1847). On the theory of oscillating waves. *Trans. Cambridge Philos. Soc.*, 8, 441-455.

SWART, V P and LARGIER, J L (1987). Thermal structure of Agulhas Bank water. In: *Benguela 86*, A I L Payne, J A Gulland and K H Brink (eds)., *S. Afr. J. Mar. Sci.*, 5, (in press).

THOMPSON, R O R Y (1980). Efficiency of conversion of kinetic energy to potential energy by a breaking wave. *J. Geophys. Res.*, 85, 6631-6635.

THORPE, S A (1973). Turbulence in stably stratified fluids: a review of laboratory experiments. *Boundary-Layer Meteorol.*, 5, 95-119.

THORPE, S A (1978). The near-surface ocean mixing layer in stable heating conditions. *J. Geophys. Res.*, 83, 2875-2885.

THORPE, S A (1979). Breaking internal waves in shear flows. In: *Twelfth Symposium of Naval Hydrodynamics, National Academy of Science*, 623-628.

TURNER, J S (1973). *Buoyancy Effects in Fluids*. Cambridge Univ. Press, Cambridge, 367 pp.

TURNER, J S (1981). Small-scale mixing processes. In: *Evolution of Physical Oceanography*, B A Warren and C Wunsch (eds), MIT Press, Cambridge, 264-290.

WAHL, R J and TEAGUE, W J (1983). Estimation of Brunt-Väisälä frequency from temperature profiles. *J. Phys. Oceanogr.*, 13, 2236-2240.

WAINMAN, C K, CRUIKSHANK, S C and BEAUMONT, E D (1986). Data manual: False Bay wind and current patterns, February - May 1985. *Sea Fisheries Research Institute*, Internal Report.

WEIGAND, J G, FARMER, H G, PRINSENBERG, S J and RATTRAY, M, Jr (1969). Effects of friction and surface tide angle of incidence on the coastal generation of internal tides. *J. Mar. Res.*, 27, 241-259.

WOODS, J D and WILEY, R L (1972). Billow turbulence and ocean microstructure. *Deep-Sea Res.*, 19, 87-121.

WUNSCH, C (1969). Progressive internal waves on slopes. *J. Fluid. Mech.*, 35, 131-144.

WUNSCH, C (1975). Internal tides in the ocean. *Rev. Geophys. Space Phys.*, 13, 167-182.

WUNSCH, C and HENDRY, R (1972). Array measurements of the bottom boundary layer and the internal wave field on the continental slope. *Geophys. Fluid Dyn.*, 4, 101-145.

YUEN, C K (1979). *Digital Spectral Analysis.* Pitman, CSIRO, Melbourne, 160 pp.

ZEILON, N (1912). On tidal boundary-waves and related hydrodynamical problems. *Kungl. Svenska Vetensk.-Akad. Handl.*, 47, 1-46.

ZEILON, N (1934). Experiments on boundary tides. *Medd. Goteborgs Hogskolas Oceanogr. Inst.*, B3, 1-8.

APPENDIX (a): Parallel temperature-time plots for the first deployment. The deepest record is correctly positioned but each successively shallower record overreads by 2°C.

APPENDIX (b): Parallel temperature-time plots for the second deployment. The deepest record is correctly positioned but each successively shallower record overreads by 2°C.

APPENDIX (c): Parallel temperature-time plots for the third deployment. The deepest record is correctly positioned but each successively shallower record overreads by 2°C.

APPENDIX (d): Filtered time-series for the temperatures recorded at the shallowest thermistor during the first deployment. Lanczos filters were used with quarter-amplitude points at 25 hr and 10 hr periods.

APPENDIX (e): Filtered time-series for the temperatures recorded at the deepest thermistor during the second deployment. Lanczos filters were used with quarter-amplitude points at 25 hr and 10 hr periods.

APPENDIX (f): Filtered time-series for the temperatures recorded at the deepest thermistor during the third deployment. Lanczos filters were used with quarter-amplitude points at 25 hr and 10 hr periods.

APPENDIX (g): Isotherm migrations as calculated from interpolation of hourly temperature values for the first deployment.

APPENDIX (a)

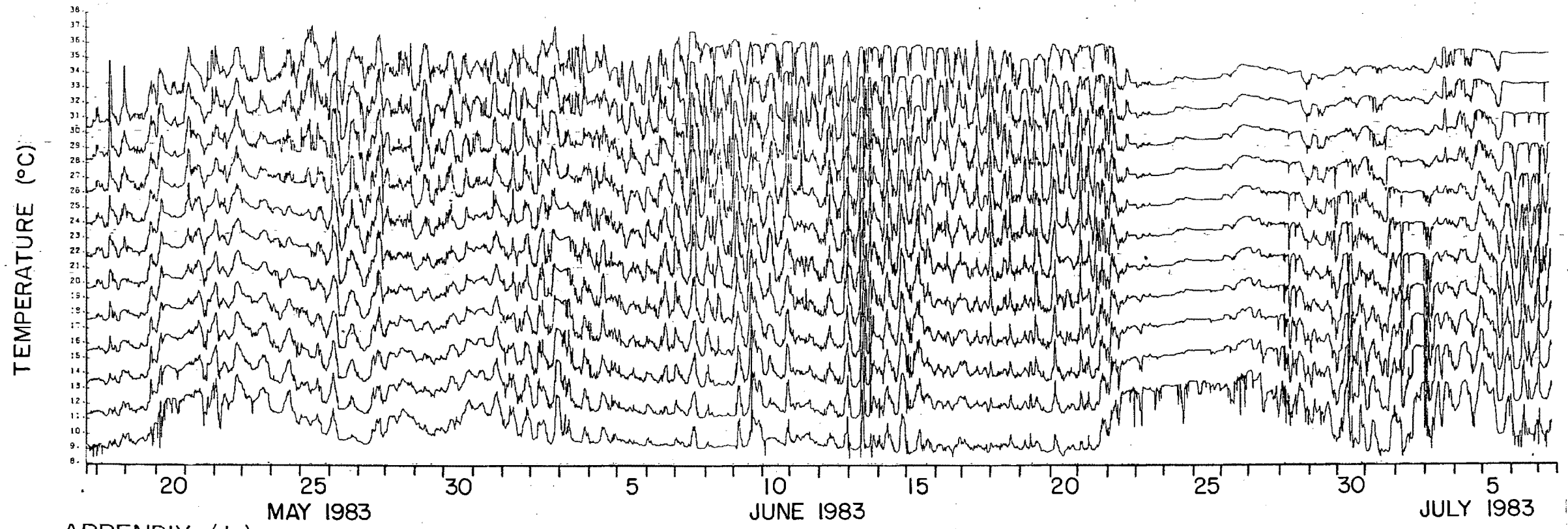

APPENDIX (b)

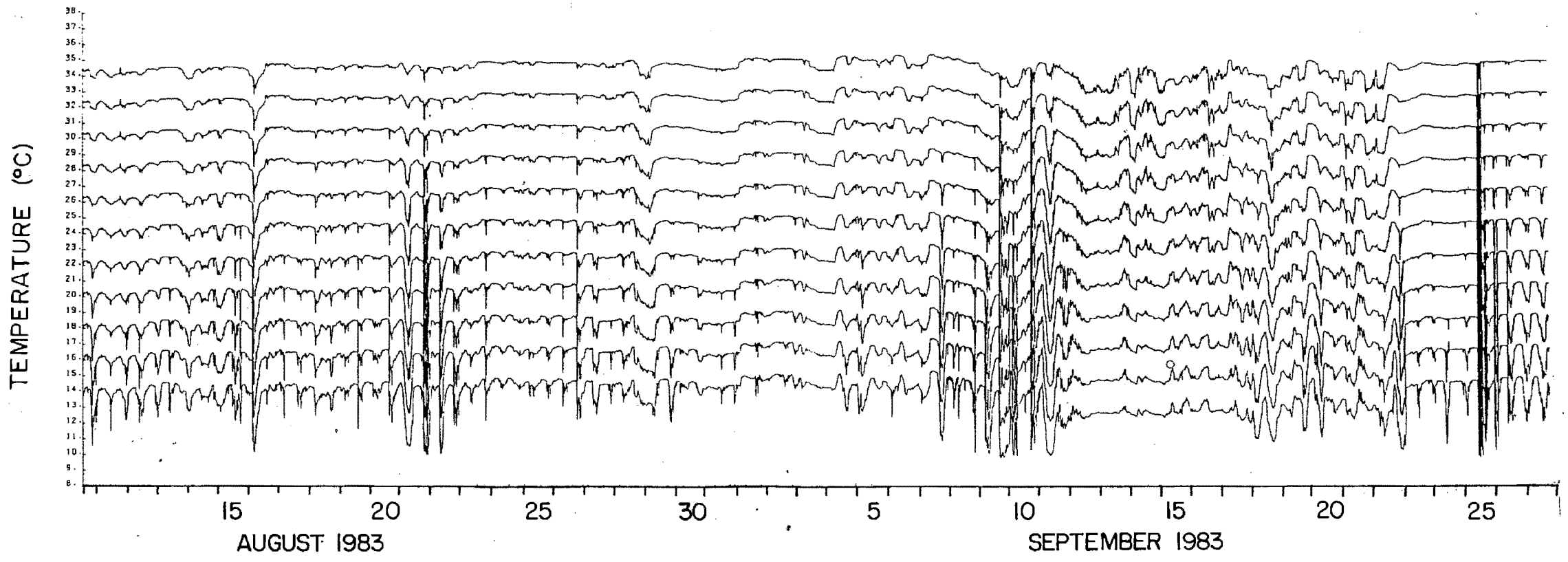

APPENDIX (c)

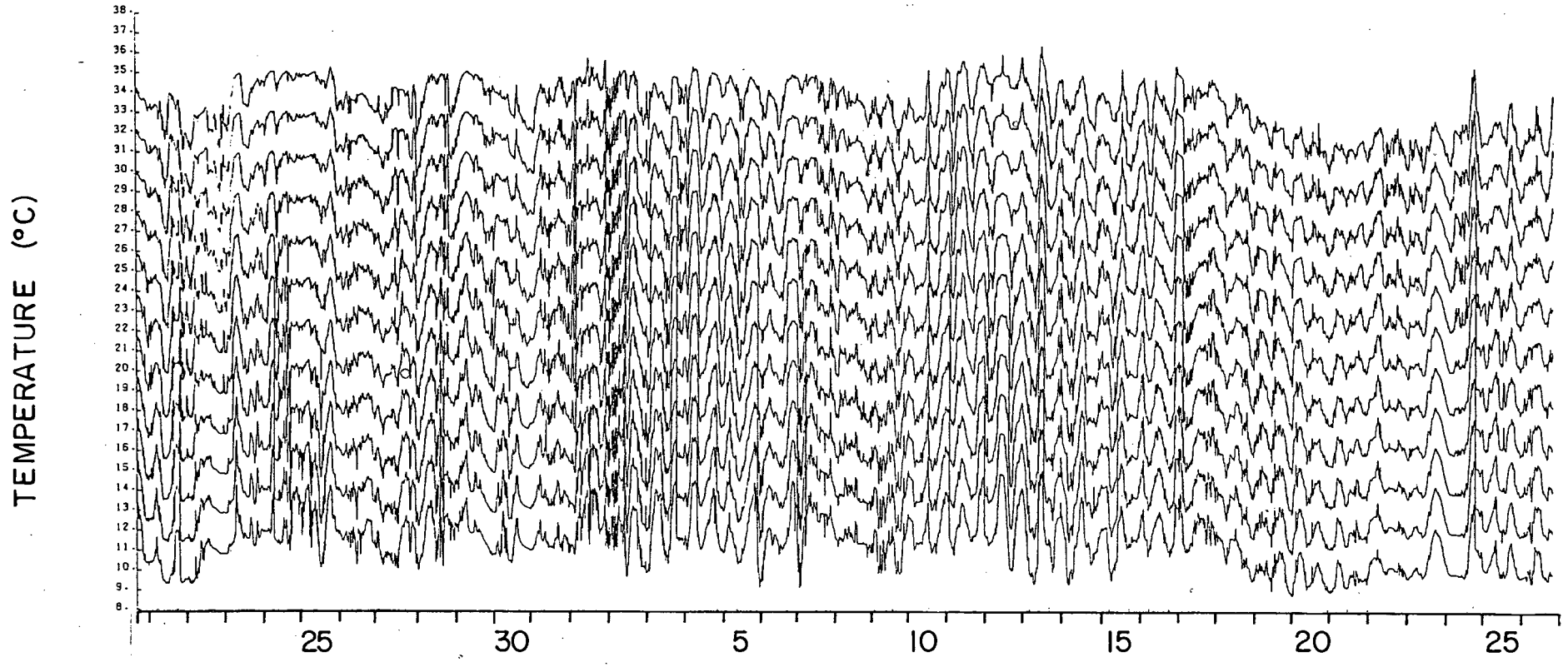

APPENDIX (d)

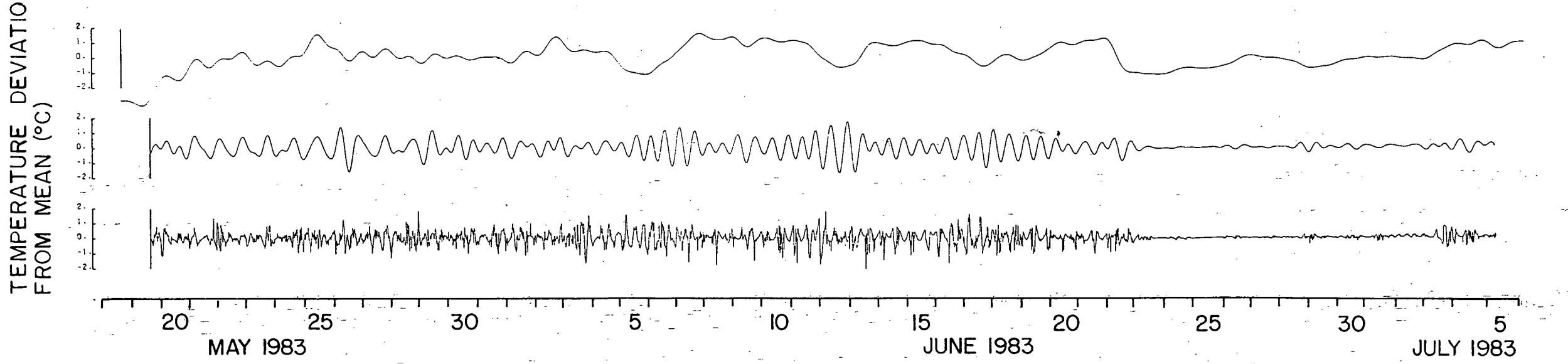

APPENDIX (e)

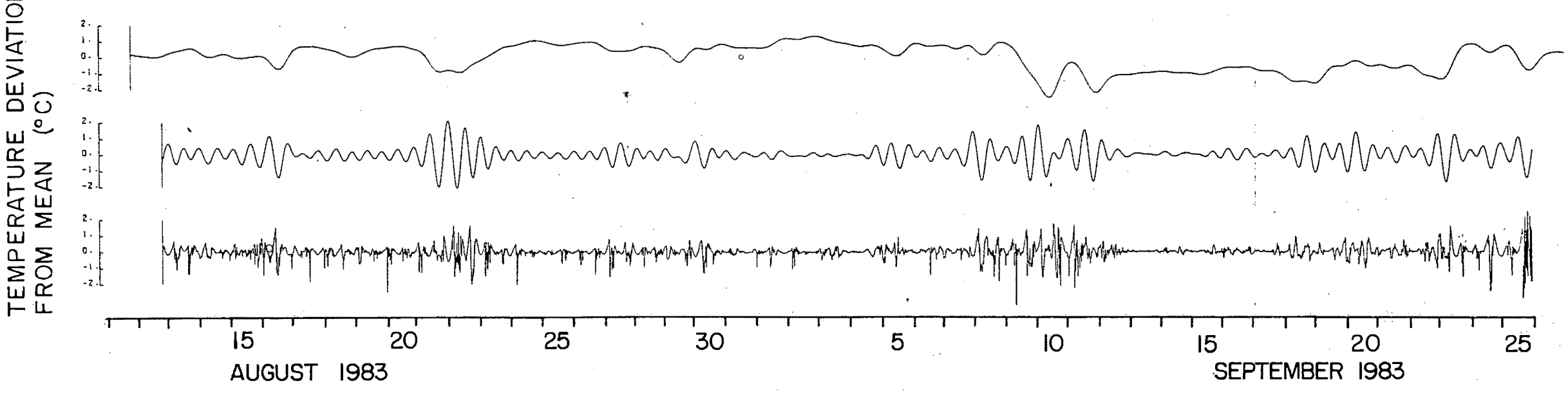

APPENDIX (f)

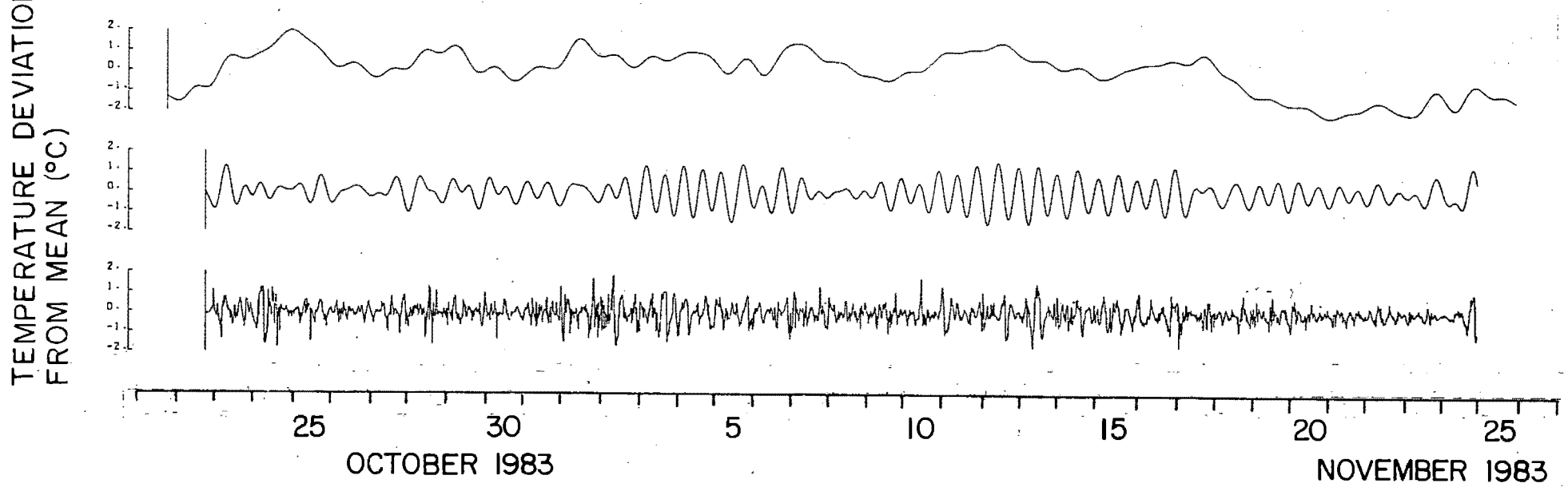

APPENDIX (g)

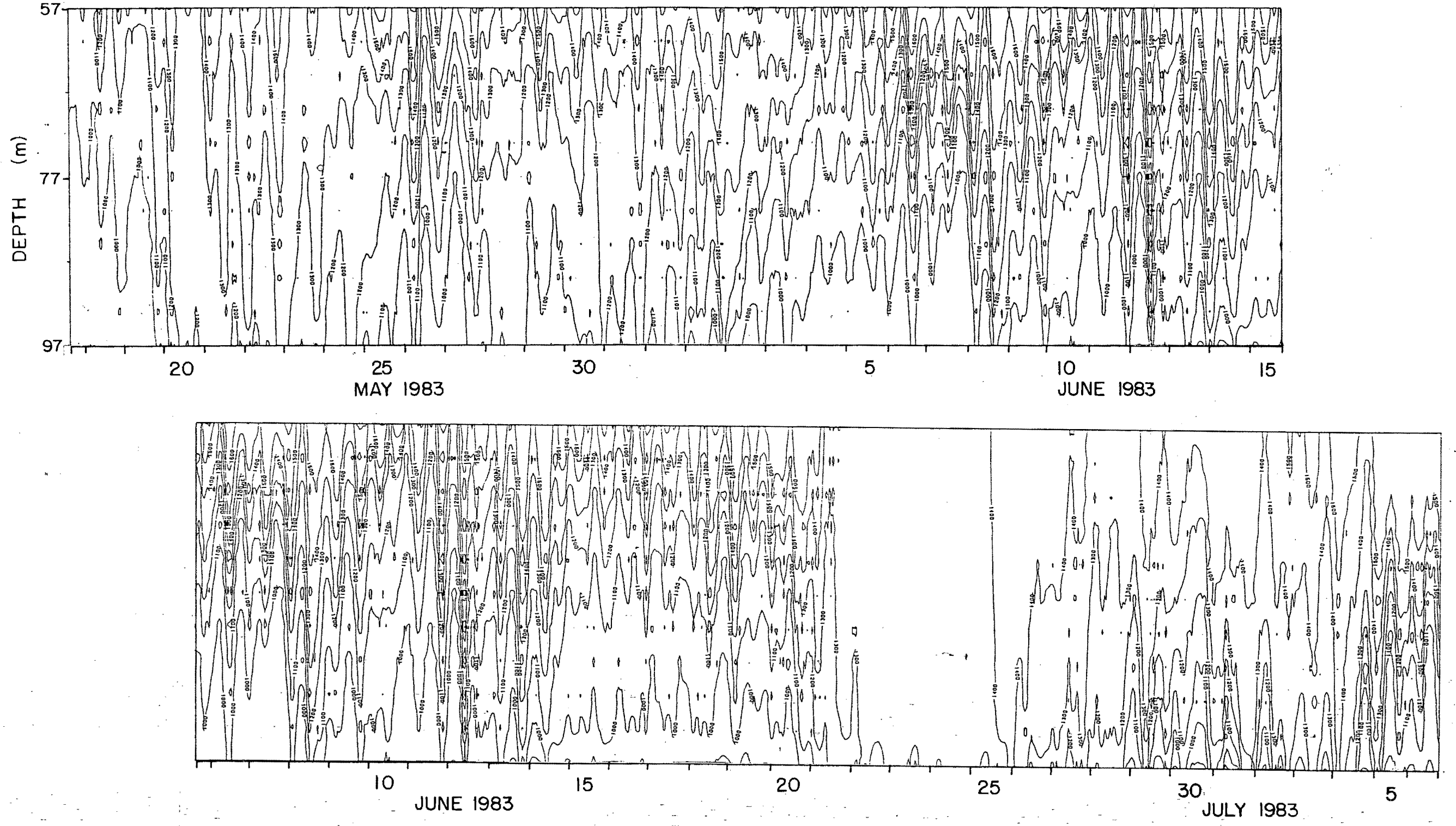
DEPTH (m)
57
77
97
20
25
30
5
10
15
MAY 1983
JUNE 1983
10
15
20
25
30
5
JUNE 1983
JULY 1983